Fatigue of *Electronic Materials*

Scott A. Schroeder
and M. R. Mitchell,
editors

ASTM STP 1153

STP 1153

Fatigue of Electronic Materials

Scott A. Schroeder and M. R. Mitchell, editors

ASTM Publication Code Number (PCN):
04-011530-30

ASTM
1916 Race Street
Philadelphia, PA 19103

Printed in the U.S.A.

Library of Congress Cataloging-in-Publication Data

Fatigue of electronic materials / Scott A. Schroeder and M. R. Mitchell, editors.
p. cm.—(ASTM special technical publication; 1153)
"ASTM publication code number (PCN) : 04-011530-3"
Includes bibliographical references and index.
ISBN 0-8031-1994-1
1. Electronics—Materials—Fatigue. 2. Electronics—Materials—Creep. I. Schroeder, Scott A. II. Mitchell, M. R. (Michael R.), 1941– . III. Series.
TK7871.F37 1994
621.3815'31—dc20 94-38090
CIP

Peer Review Policy

Each paper published in this volume was evaluated by three peer reviewers. The authors addressed all of the reviewers' comments to the satisfaction of both the technical editor(s) and the ASTM Committee on Publications.

The quality of the papers in this publication reflects not only the obvious efforts of the authors and the technical editor(s), but also the work of these peer reviewers. The ASTM Committee on Publications acknowledges with appreciation their dedication and contribution to time and effort on behalf of ASTM.

Printed in Philadelphia, PA
December 1994

Foreword

This publication, *Fatigue of Electronic Materials,* contains papers presented at the symposium of the same name held in Atlanta, Georgia on 17 May 1993. The symposium was sponsored by Committee E–8 on Fatigue and Fracture. Scott A. Schroeder and M. R. Mitchell, both of Rockwell International Science Center, Thousand Oaks, California, served as co-chairmen of the symposium.

Contents

Overview

The first electronic systems developed consisted of circuit components attached to printed circuit boards by mechanical methods. Component leads were either placed through holes in the circuit board, twisted together, or secured with fasteners before soldering. The solder existed only to provide additional electrical and thermal conductivity to the system. Due to the relatively secure methods of component attachment, failure or small cracks in the solder rarely caused electrical system failure. However, relatively recent advances in circuit technology and the need to increase the density of electronic systems have reduced greatly the use of mechanical interconnections. In advanced soldering techniques such as surface mount technology (SMT), the solder is required to provide not only electrical and thermal connection, but mechanical integrity as well. The situation is further complicated by the power and environmental conditions placed upon today's electronic systems. Solder joints are commonly expected to provide an uninterrupted interconnection for several years at relatively high temperatures (0.5 to 0.8 T_m). Degradation of such joints under creep/fatigue conditions has increasingly become a major concern for the electronics community. Failure or even intermittent loss of conductivity in a single solder joint often reduces an entire electronic assembly to an inoperative state.

Considerable research, development, and design-related engineering activity has recently been undertaken by the microelectronics industry to address this problem. This effort has historically been product driven, resulting in material data and test methodologies designed to address specific operating environments and electrical systems configurations. In addition, test methods commonly employed are often developed without a detailed knowledge of mechanics or material science. Current research has roughly grown into three areas: (1) bulk material testing, (2) simulated solder joints, and (3) component testing. Among these areas, methodologies vary widely. Fatigue studies of solder have been undertaken using many different methods, including thin-walled tubes in shear, bulk tension specimens, lap shear joints, and simulated joints in shear. Test parameters such as strain rates, frequency in load control, stress-strain measurement methods, hold times, and thermal/mechanical fatigue effects are equally as varied. The situation for fatigue and reliability testing of entire components is even more complicated due to the variety of proprietary component geometries, operating environments, and in-house mechanical testing expertise. The currently existing database and test methodology is perceived as too complex, difficult to implement and extend to other situations, and is often developed without using existing mechanical testing expertise.

The purpose of the ASTM Symposium on Fatigue of Electronic Materials, the first on this topic, was to assemble a cross section of fatigue practitioners active in the microelectronics area to assess the current state and direction of fatigue/reliability research. A major long-term goal of this symposium and subcommittee activity is to provide a forum for fatigue researchers from a broad spectrum of disciplines and backgrounds within the microelectronics industry to compare and evaluate fatigue test methodologies for eventual development of testing guidelines. Such collaboration has the obvious benefits of providing an industry-wide source for future refinement of fatigue testing methods for electronics and for providing the basis for a more widely applicable database of solder and other electronic material properties.

The first five papers in this STP provide valuable insight into the various methods in use to characterize the fatigue/creep interactions present within solder under typical temperature and loading ranges of electronic systems. These methods incorporate differing experimental and analytical techniques, highlighting the diversity in methods used to analyze fatigue/creep in small components at high homologous temperatures. Within this diversity also exist common approaches for performing fatigue studies where creep, temperature, and hold time effects are prevalent.

The next two papers further detail the complexity of fatigue/reliability testing of electronic component systems. "Test Methodologies to Perform Valid Accelerated Thermomechanical Fatigue Tests of Solder Joints" by D. Frear, N. Sorensen, and J. Martens is an excellent overview of the inherent complexities in accelerated fatigue testing of materials subject to high homologous temperatures and continual microstructural changes. The second paper, A study of the high-cycle fatigue of Kovar, demonstrates that while the focus of fatigue in microelectronics is often on solder alloys, electronic components are complex systems subject to fatigue of various subsystems. The paper by Frear et al. received the "Best Paper" award for this symposium.

The final two papers provide examples of fatigue and creep characterization applied to reliability assessments of actual electronic components. While considerable progress is evident in this area, there remain a number of unresolved issues to consider before truly general, sufficiently detailed design and analysis approaches are available.

The symposium chairmen gratefully acknowledge the authors and reviewers of the manuscripts. Their participation, as well as that of the ASTM staff, has made this publication possible. It is hoped that the subject matter of this symposium will generate cross-disciplinary interest and stimulate cooperative efforts among the organizations active in solder/electronic material research, leading to a forum for test guideline formation.

Scott A. Schroeder
Rockwell Science Center
Thousand Oaks, CA 91360;
symposium chairman and editor

M. R. Mitchell
Rockwell Science Center
Thousand Oaks, CA 91360;
symposium chairman and editor

S. H. Ju,[1] *S. Kuskowski,*[2] *B. I. Sandor,*[1] *and M. E. Plesha*[1]

Creep-Fatigue Damage Analysis of Solder Joints

REFERENCE: Ju, S. H., Kuskowski, S., Sandor, B. I., and Plesha, M. E., **"Creep-Fatigue Damage Analysis of Solder Joints,"** *Fatigue of Electronic Materials, ASTM STP 1153,* S. A. Schroeder and M. R. Mitchell, Eds., American Society for Testing and Materials, Philadelphia, PA, 1994, pp. 1–21.

ABSTRACT: An anisotropic model of continuum damage mechanics has been developed to predict the creep-fatigue life of solder joints. With the help of the finite element method, the stress, strain, and damage fields of the time-dependent and temperature-dependent solder can be obtained. The main advantages of this model include: (1) It can predict the initial crack location and time and the subsequent crack growth paths; (2) The damage analysis is almost the same as in traditional viscoelastic finite element analysis; (3) It can be applied to a complex structure with any loading; (4) It provides a full-field damage investigation of the structure. This damage theory can be used for various solder joints and also can be applied to analyze the creep-fatigue problems of other ductile and temperature-dependent materials. Extensive experiments including uniaxial creep, uniaxial fatigue, tension-torsion, Moiré, and bimaterial tests were performed to validate the new model. These validations and comparisons indicate that this model can predict adequately crack growth paths and fatigue lives of solder joints.

KEYWORDS: anisotropic, continuum damage mechanics, crack, creep, damage, experiment, fatigue, fatigue life, finite element method, isotropic, Moire, stress, strain, time-dependent, temperature-dependent, viscoelastic

Most of the life prediction techniques for solder joints require first finding the stress and strain fields of the structure using only one thermal load cycle and then predicting the life by substituting stresses or strains into an empirical fatigue life formula such as the Coffin-Manson equation (Fig. 1*a*). This method is very easy and simple; however, it has disadvantages: (1) It is only suitable for predicting the life of the initial crack—the stress and strain fields change significantly when the crack grows; (2) It cannot predict the crack growth path; (3) Because of the strong creep effect in solder, stress and strain fields change with time. It is difficult, therefore, to judge whether the stress or strain field should be used. Most likely, exclusive use of just one is not ideal; (4) It is difficult to find a suitable fatigue equation for a loading that includes hold times.

Continuum damage mechanics is another approach that can be used to predict the life of a solder joint without the above disadvantages. During the strain process, defects appear that can be considered damage. Adding this damage into a constitutive equation as an internal variable, we can evaluate the stress, strain, and damage simultaneously (Fig. 1*b*). The advantages of this suggested method are as follows: (1) It can be applied to a very complex

[1]Postdoctoral researcher, professor, and professor, respectively, Department of Engineering Mechanics and Astronautics, University of Wisconsin, Madison, WI 53706.

[2]General engineer, currently at U.S.D.A. Forest Service, Forest Products Laboratory, Madison, WI 53705.

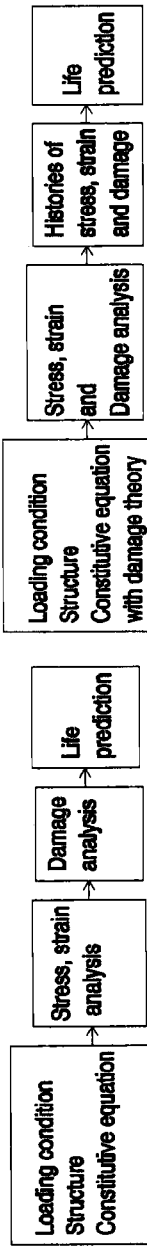

a. Life prediction by conventional methods. Stress and strain are calculated first, then damage is estimated.

b. Life prediction by continuum damage mechanics. Damage, stress and strain are calculated simultaneously.

FIG. 1—*Life prediction techniques.*

structure with any loading; (2) It can be used to locate the initial crack formation; (3) The crack growth path can be computed automatically; (4) It provides for full-field damage (everywhere, not only at the crack tip) investigation of the structure; (5) The procedures of this method are almost the same as those of the conventional finite element method. This is perhaps the most attractive advantage. There are several recognized disadvantages: (1) The theory of continuum damage mechanics is still in development, so no standard formula can be used directly. We need to select a suitable damage equation for a material and experimentally verify the accuracy; (2) The method also requires extensive computer time to determine the solution; (3) To accurately simulate crack closure, complex interface or contact elements must be used; (4) Many material constants are usually included in the damage expression. Some material constants cannot be obtained directly by a uniaxial experimental test, and biaxial tests are required. The most serious disadvantage is probably the first one, so a creep-fatigue damage theory is detailed in this paper.

Creep

Uniaxial Constitutive Relationships

Many simplified uniaxial constitutive relations have been proposed to describe the standard creep curves. The primary and secondary stages of creep are discussed below. Tertiary creep is discussed in the section entitled "Continuum Damage Mechanics."

The first step common to most approaches is to separate the elastic and inelastic parts of the strain rate

$$\dot{\epsilon} = \dot{\epsilon}_e + \dot{\epsilon}_c \tag{1a}$$

The creep strain rate may be written as a function of stress σ, time t, and temperature T

$$\dot{\epsilon}_c = f(\sigma,t,T) \tag{1b}$$

This is usually separable into

$$\dot{\epsilon}_c = f_1(\sigma)f_2(t)f_3(T) \tag{1c}$$

The stress-dependent function can be used as an approximation for the creep rate during steady-state creep. Some suggestions for the stress dependence are

$$f_1(\sigma) = A\sigma^n \quad \text{Norton [1]} \tag{2a}$$

$$f_1(\sigma) = B\exp(\alpha\sigma) \quad \text{Ludvik [2]} \tag{2b}$$

$$f_1(\sigma) = C[\exp(\alpha\sigma) - 1] \quad \text{Soderberg [3]} \tag{2c}$$

$$f_1(\sigma) = D\sinh(\beta\sigma) \quad \text{Nadai [4]} \tag{2d}$$

$$f_1(\sigma) = D[\sinh(\beta\sigma)]^m \quad \text{Garofalo [5]} \tag{2e}$$

$$f_1(\sigma) = A[\langle\sigma - \sigma_y\rangle/\sigma_y]^n \quad \text{Viscoplastic Model 1} \tag{2f}$$

$$f_1(\sigma) = \exp[M(\langle\sigma - \sigma_y\rangle)/\sigma_y] - 1 \quad \text{Viscoplastic Model 2} \tag{2g}$$

where A, B, C, D, M, m, n, α, β, and σ_y are material constants, and $\langle\ \rangle$ means $\langle A\rangle = A$, for $A \geq 0$; $\langle A\rangle = 0$, for $A < 0$.

The time-dependent function can give a good approximation for the creep rate during primary creep; however, it is difficult to deal with cyclic loading using this function. Some suggestions for time dependence are

$$f_2(t) = at^m \qquad \text{Bailey [6]} \tag{3a}$$

$$f_2(t) = (1 + bt^{1/3})\exp(kt) \qquad \text{Andrade [7]} \tag{3b}$$

where a, b, k, and m are material constants.

The creep rate at constant stress usually increases exponentially with temperature [8]; it is therefore convenient to plot strain rate against 1/temperature, thus fitting the creep rate to an Arrhenius-type expression

$$f_3(T) = \exp[-Q/(kT)] \tag{4}$$

where Q is proportional to the slope of ln(strain-rate) versus 1/temperature and is the apparent activation energy of creep, T is the absolute temperature, and k is Boltzmann's constant. Another convenient way of dealing with the temperature effect is to assume that the material constants are functions of temperature.

An appropriate uniaxial creep law dependent on stress, time, and temperature can be obtained by the combination of f_1, f_2, and f_3. The simplest creep expression would take the form

$$\dot{\epsilon}_c = At^m\sigma^n \exp[-Q/(kT)] \tag{5a}$$

or

$$\dot{\epsilon}_c = A(T)t^{m(T)}\sigma^{n(T)} \tag{5b}$$

where m, n, and A are independent of temperature for Eq 5a, but they are functions of temperature for Eq 5b. In practice, we can measure m, n, and A at several temperatures; assume that the strain rate is linear between adjacent temperatures and use interpolation. This interpolation method is used here because it is more accurate than the Arrhenius formula when there is sufficient data. For example, we have m, n, and A at 25 and 50°C and require the strain rate at 40°C. Thus:

1. Find the strain rate at 25°C using the material constants at 25°C.
2. Find the strain rate at 50°C using the material constants at 50°C.
3. Find the strain rate at 40°C by the interpolation of the above two strain rates.

Multiaxial Constitutive Relationships

One explicit form of the secondary creep equation that has been applied widely [9] is

$$\{\dot{\epsilon}_{vp}\} = \gamma\langle\Phi(F)\rangle\frac{\partial F}{\partial\{\sigma\}} \tag{6a}$$

where γ is the fluidity parameter dependent on temperature, Φ is a positive, monotonic increasing function, and $\langle\ \rangle$ indicates that $\langle\Phi\rangle = \Phi$, for $\Phi \geq 0$; $\langle\Phi\rangle = 0$, for $\Phi < 0$.

$F(\sigma)$ is the yielding criterion; a form for orthotropic materials is shown below [10]

$$F = \{\tfrac{1}{2}(\sigma)^T[S_S](\sigma)\}^{1/2} \tag{6b}$$

$$[S_S] = \begin{bmatrix} G+H & -H & -G & 0 & 0 & 0 \\ & H+E & -E & 0 & 0 & 0 \\ & & E+G & 0 & 0 & 0 \\ & & & 2L & 0 & 0 \\ & \text{Symmetric} & & & 2M & 0 \\ & & & & & 2N \end{bmatrix} \tag{6c}$$

where E, G, H, L, M, and N are parameters characterizing the current state of plastic anisotropy. If we set $E = G = H = 1$ and $L = M = N = 3$, the von Mises yielding criterion is obtained.

In this study, Φ is presented as a power function shown in Eqs 7a and 7b, and we use the viscoelastic form (Eq 7b) for solder. The function F is the effective von Mises stress shown in Eqs 8a to 8c

$$\Phi[F(\sigma)] = \{[F(\sigma) - F_0]/F_0\}^n \quad \text{for} \quad F_0 > 0 \tag{7a}$$

$$\Phi[F(\sigma)] = F(\sigma)^n \quad \text{for} \quad F_0 = 0 \tag{7b}$$

$$F(\sigma) = (3S_{ij}S_{ij}/2)^{1/2} \tag{8a}$$

where $S_{ij} = \sigma_{ij} - \sigma_{kk}\delta_{ij}/3$;
or

$$F(\sigma) = [\tfrac{1}{2}\{\sigma\}^T[H_v]\{\sigma\}]^{1/2} \tag{8b}$$

$$[H_v] = \begin{bmatrix} 2 & -1 & -1 & 0 & 0 & 0 \\ -1 & 2 & -1 & 0 & 0 & 0 \\ -1 & -1 & 2 & 0 & 0 & 0 \\ 0 & 0 & 0 & 6 & 0 & 0 \\ 0 & 0 & 0 & 0 & 6 & 0 \\ 0 & 0 & 0 & 0 & 0 & 6 \end{bmatrix} \tag{8c}$$

F_0 is the uniaxial yield stress. For isotropic hardening theory, we have

$$F_0 = H' \int_0^t \dot{\bar{\epsilon}}_{vp}\, dt + F_{0\text{initial}} \tag{9a}$$

$$\dot{\bar{\epsilon}}_{vp} = 2(\tfrac{1}{2}\{\dot{\epsilon}_{vp}\}^T[S_S]\{\dot{\epsilon}_{vp}\})^{1/2} \tag{9b}$$

where the overbar indicates effective strain, and $F_{0\text{initial}}$ and H' are material constants dependent on temperature.

Continuum Damage Mechanics

Isotropic Creep Damage Theory

Continuum damage mechanics was first proposed by Kachanov [*11*] in a mathematical theory for evaluating creep rupture times. Rabotnov [*12*] extended Kachanov's theory and found a one-dimensional isotropic creep damage law shown in Eq 10.

$$\dot{\epsilon}_c = A[\sigma/(1 - w)]^n \tag{10a}$$

$$\dot{w} = B\sigma^m/(1 - w)^k \tag{10b}$$

where w is a damage value between 0 and 1, A, B, n, m, and k are material constants dependent on temperature, and σ is uniaxial stress.

The physical meaning of Eqs 10a to 10c can be illustrated by Fig. 2. A damage value, w, is defined in the body after loading, and the net area of the body A_d changes to $A(1 - w)$. By this definition, we obtain the effective damage stress as

$$\sigma_d = F/A_d = F/[A(1 - w)] = \sigma/(1 - w) \tag{10c}$$

Substituting the effective damage stress into the Norton creep expression [*1*], we get Eq 10a. Hayhurst [*13*] generalized Eqs 10a to 10c for a multiaxial state of stress and derived the equations

$$\dot{\epsilon}_{c_{ij}} = (3A/2)[\sigma_\epsilon/(1 - cw)]^n(S_{ij}/\sigma_e) \tag{11a}$$

$$\dot{w} = B\sigma_d^m/(1 - w)^k \tag{11b}$$

$$\sigma_d = a_1(\sigma_1) + a_2(\sigma_{kk}) + (1 - a_1 - a_2)(\sigma_e) \tag{11c}$$

where

$$S_{ij} = \sigma_{ij} - \sigma_{kk}\delta_{ij}/3 \tag{11d}$$

$$\sigma_e = (3S_{ij}S_{ij}/2)^{1/2} \tag{11e}$$

and σ_1 = maximum principal stress; A, B, m, n, k, a_1, c, and a_2 are material constants.

In the above equations, Hayhurst considered an isochronous surface to be the curve obtained by connecting stress state with equal rupture times. By selecting appropriate values for a_1 and a_2, the isochronous surface can be represented. Two typical isochronous surfaces are shown in Fig. 3. Equation 11a can be also changed to a viscoplastic formula as shown in Eq 12.

$$\dot{\epsilon}_{c_{ij}} = (3A/2)[\langle\sigma_e - \sigma_y\rangle/\sigma_y(1 - cw)]^n(S_{ij}/\sigma_e) \tag{12}$$

Equations 11 and 12 involve the following assumptions:

a. The material under creep strains is incompressible.
b. Damage is isotropic.
c. Material properties are unaffected by material damage.
d. Creep deformation is isotropic under material damage.

Some experiments showed that anisotropic damage has important effects on creep and fatigue damage of some materials, such as copper [*14*]. We take up this question in the next section.

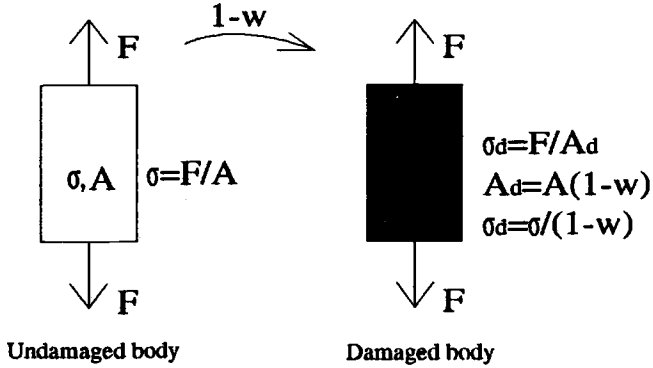

FIG. 2—*Illustration of damage.*

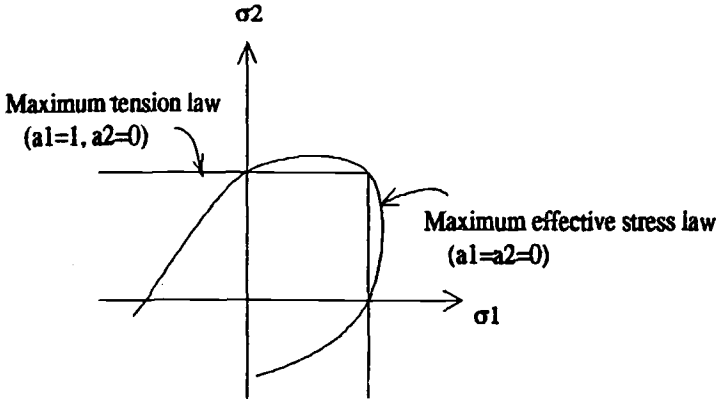

FIG. 3—*Two typical isochronous surfaces.*

Anisotropic Creep Damage Theory

In anisotropic damage theory, the damage measure should be a tensor; it is thus more difficult than isotropic theory in which the damage measure is a scalar. There are few references on this topic [*15–19*]. In this study, an anisotropic creep damage rule was generated which does not require the assumptions in the last subsection.

1. *Definition of a fourth-order damage effect tensor* [M].

First, define a fourth-order damage effect tensor $[M]$ in order to find the effective damage stress vector, $\{\sigma_d\}$, and effective damage strain vector, $\{\epsilon_d\}$.

$$\{\sigma_d\} = [M]\{\sigma\} \tag{13a}$$

$$\{\epsilon_d\} = [M]^{-1}\{\epsilon\} \tag{13b}$$

where $\{\sigma\}$ is the Cauchy stress tensor in the direction of principal damage, and $\{\epsilon\}$ is the small strain tensor in the direction of principal damage.

In the following paragraph, the coordinate system is in the principal damage directions. A transformation matrix can be used to change the coordinate system to an X-Y-Z system.

From this definition, obtain the total internal work as

$$W = \int_V \{\sigma\}^T d\{\epsilon\} = \int_V \{\sigma_d\}^T d\{\epsilon_d\} \tag{13c}$$

Chow and Lu [*15,16*] proved that $[M]$ may be defined as

$$[M] = \begin{bmatrix} \frac{1}{1-D_1} & & & & & \\ & \frac{1}{1-D_2} & & \text{Others} = 0 & & \\ & & \frac{1}{1-D_3} & & & \\ & & & \frac{1}{\sqrt{(1-D_2)(1-D_3)}} & & \\ & & & & \frac{1}{\sqrt{(1-D_1)(1-D_3)}} & \\ & & \text{Others} = 0 & & & \frac{1}{\sqrt{(1-D_1)(1-D_2)}} \end{bmatrix} \tag{14}$$

where D_1, D_2, and D_3 are the principal values of the damage tensor $\{D\}$.

2. *Evaluation of an equivalent damage stress (isochronous surface).*

The equivalent damage stress should be frame-invariant. Usually, we can evaluate it as a function of three effective damage stress invariants, I_{d1}, I_{d2}, and I_{d3}, or two effective damage deviator stress invariants J_{d2} and J_{d3}. We can also use maximum stress (σ_1), minimum stress (σ_2), Mises stress (σ_e), and hydrostatic stress (I_1) to find the isochronous surface defined in Eq 11c. Chow and Wang [*16*] proposed another way to evaluate the isochronous surface. They defined a damage operator [J] that is frame-invariant, and let

$$\sigma_{de}^2 = \tfrac{1}{2}\{\sigma_d\}^T[J]\{\sigma_d\} = \tfrac{1}{2}\{\sigma\}^T[J_d]\{\sigma\} \tag{15a}$$

where

$$[J] = 2\begin{bmatrix} 1 & \mu & \mu & 0 & 0 & 0 \\ \mu & 1 & \mu & 0 & 0 & 0 \\ \mu & \mu & 1 & 0 & 0 & 0 \\ 0 & 0 & 0 & 2(1-\mu) & 0 & 0 \\ 0 & 0 & 0 & 0 & 2(1-\mu) & 0 \\ 0 & 0 & 0 & 0 & 0 & 2(1-\mu) \end{bmatrix} \tag{15b}$$

$$[J_d] = [M]^T[J][M] \tag{15c}$$

μ is a material constant, which can be obtained by pure shear or tension-torsion tests. Since [J] should be positive semidefinite, μ is confined within the range of -0.5 and 1.

3. *Definition of the creep damage evolution model.*

Define the 2nd order damage rate tensor, which is a function of the effective damage stress vector and temperature

$$\{\dot{D}\} = \gamma_d\langle\Phi_d(\sigma_{de})\rangle\frac{\partial\sigma_{de}}{\partial\{\sigma\}} = \gamma_d\langle\Phi_d(\sigma_{de})\rangle\frac{[J_d]}{2\sigma_{de}}\{\sigma\} \tag{16a}$$

where Φ_d is a function of equivalent damage stress, and we can use

$$\Phi_d = (\sigma_{de} - \beta_y)^{n_d} \tag{16b}$$

where β_y is a damage threshold value, which can be deduced the same way as strain hardening is in plasticity theory (we set β_y to zero for solder here), and n_d is a material constant dependent on temperature. For the general case

$$\dot{\beta}_y = 2(\tfrac{1}{2}\{\dot{D}\}^T[J_d]\{\dot{D}\})^{1/2} \tag{16c}$$

$$\beta_y = H_d\int_0^t \dot{\beta}_y\,dt + \beta_{y0} \tag{16d}$$

where β_y is an initial damage threshold value dependent on temperature, H_d is a damage hardening ratio dependent on temperature, and γ_d is a damage parameter controlling the damage rate. It is a function of temperature. Experiments indicate that it may be a constant for proportional loads and may be a function of strain for cyclic loads [*20*].

4. *Evaluation of linear elastic stress-strain expression for damaged material.*

The elastic energy W_e for a damaged material can be written as [*16*]

$$\begin{aligned} W_e &= \tfrac{1}{2}\{\sigma_d\}^T[C_e]^{-1}\{\sigma_d\} \\ &= \tfrac{1}{2}\{\sigma\}^T[M]^T[C_e]^{-1}[M]\{\sigma\} \\ &= \tfrac{1}{2}\{\sigma\}^T[C_{de}]^{-1}\{\sigma\} \end{aligned} \tag{17a}$$

where $[C_e]$ is the fourth-order tensor of linear elastic stress-strain expression for undamaged material

$$[C_{de}] = [M]^{-1}[C_e][M]^{-T} \tag{17b}$$

and

$$\{\sigma\} = [C_{ed}]\{\epsilon_e\} \tag{17c}$$

where $\{\epsilon_e\}$ is linear elastic strain, and $[C_{de}]$ is the linear elastic stress-strain expression for damaged material.

5. *Definition of the strain rate equation.*

$$\{\dot{\epsilon}_{vp}\} = \gamma\langle\Phi(F(\sigma_d))\rangle\frac{\partial F(\sigma_d)}{\partial\{\sigma\}} = \gamma\langle\Phi(F(\sigma_d))\rangle\frac{[M]^T[S_S][M]}{2F(\sigma_d)}\{\sigma\} \tag{18}$$

The creep rate is almost the same as in conventional form (see Eq 6a), and the only difference is that F changes to a function of the effective damage stress tensor (see Eq 13a).

Creep-Fatigue Damage Theory

Damaged solder, and some other engineering materials as well, show a remarkable propensity to heal partially during the application of compressive loads. This phenomenon has been observed and reported by some investigators during the past 20 years [*26,27*], but for our purposes, consider the set of tests reported in Ref *20*. Table 1 and Fig. 4 present results for time to failure for uniaxially loaded solder specimens. In Case 1, a specimen is subjected to a constant tensile stress of 17.24 MPa (2500 psi) and is found to fail after 15.6 h of load application. In Cases 2 through 4, specimens are subjected to multiple cycles of tension-compression with each cycle consisting of 17.24 MPa (2500 psi) tension for 1 h followed by 17.24 MPa (2500 psi) compression for ½, ⅓, and, ⅔ h for Cases 2, 3, and 4, respectively. Conventional wisdom would suggest that little or no damage accumulates during the period of compression. Remarkably, however, the cumulative time that each

TABLE 1—*Time to failure in uniaxial fatigue experiments (63Sn/37Pb solder)* [20].

Case	Period of Tension for One Cycle (hours), $t_{tension}$	Period of Compression for One Cycle (hours), $t_{compression}$	Time to Failure (hours), $t_{failure}$	Cumulative Time that Specimen Supported Tension (hours)
1	15.6	0	15.6	15.6
2	1.0	1/3	34.0	25.5
3	1.0	1/2	73.6	49.1
4	1.0	2/3	138.0	82.8

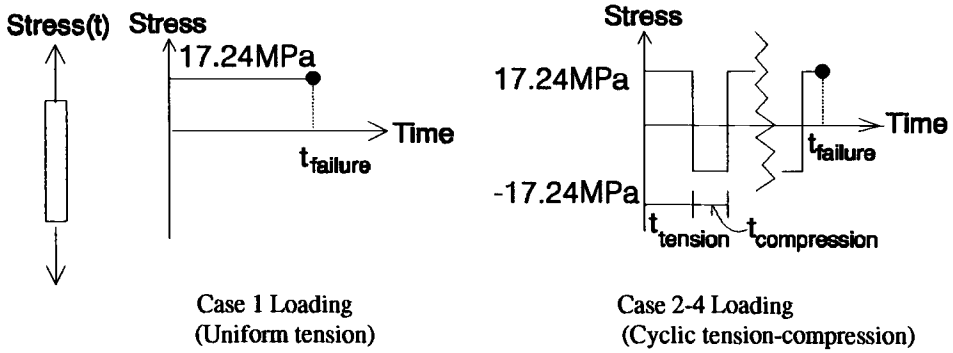

FIG. 4—*Illustration of loading for Table 1.*

specimen can endure in tension shows a strong dependence on the duration of intermittent compressive loading as shown in Table 1. This means that solder undergoes partial, but substantial healing during periods of compression, and that the degree of healing is dependent upon the duration of compression as well as the magnitude of the compression. This healing is probably brought about by strong adhesion that develops across atomically clean microcrack surfaces while they are closed during the application of the compressive load. Its significance has not been previously appreciated in solder mechanics. It has been known qualitatively in the general fatigue area and also applied to the strain range partitioning method, but has not been investigated quantitatively using modern models and analysis. Two approaches can be used in the damage formula to simulate this phenomenon. The first is to decrease the damage rate after compressive stress, and the second is to decrease the damage itself during compressive stress.

The First Approach: Decrease the Damage Rate after Compressive Stress—The damage rules proposed in the previous sections are explicit functions of the current time, stress, and damage; however, the damage rate should also be dependent on the histories of stress and strain. This can be illustrated in Fig. 5. If the damage and stress of loading 1 at time t_1 (Point A) are the same as those of loading 2 at time t_2 (Point B), the damage rates of the two loads should be the same if the damage rate formulas depend only on current stresses and damage. In fact our experiments have shown that damage rates are very different for unidirectional (Fig. 5*a*) and cyclic loads (Fig. 5*b*). For this reason, stress and strain histories must be considered in the creep-fatigue damage rule.

It is extremely difficult to include all stress and strain histories into a fatigue formula; therefore, almost all the fatigue formulas are simplified to fit certain types of cyclic loads. We discuss two famous formulas.

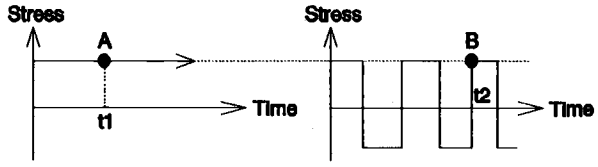

(a) Loading condition 1 (b) Loading condition 2

FIG. 5—*Two different loading histories.*

(1) Paris equation

$$da/dN = C(\Delta K)^n \tag{19a}$$

where a is crack length, N is number of cycles, ΔK is stress intensity factor range in one cycle, and C and n are material constants.

(2) Coffin-Manson equation modified by Engelmaier [*28*]

$$N_f = \frac{1}{2}\left(\frac{\Delta\gamma}{2\epsilon_f}\right)^{1/c} \tag{19b}$$

where N_f is cycles to failure, $\Delta\gamma$ is total shear strain range, ϵ_f is fatigue ductility coefficient, and c is fatigue ductility exponent.

It is clear that the two formulas can only be used for certain types of loading. For example, ΔK and $\Delta\gamma$ are the same for each case in Fig. 6. Using the two formulas, we obtain the same life for both cases; however, they should have different fatigue lives (both mean stress and wave shape should have an effect). Furthermore, we cannot obtain an obvious ΔK or $\Delta\gamma$ for the case of ratcheting in Fig. 7.

Few studies used continuum damage mechanics to solve creep-fatigue problems. Trivadey and Delobelle [*24*] suggested adding the strain rate to the damage evolution equation. Gong and Hsu [*25*] used a threshold stress in the damage evolution equation, similar to the β_y in Eq 16b. We tested both these models, but neither fit all our experiments. In this study, we were unable to generate a comprehensive creep-fatigue damage model, but the first generation model developed here does account for all our experimental results.

The assumption of our model is that the γ_d of Eq 16a is a function of the history of the incremental effective inelastic (creep) damage strain tensor, or

$$\gamma_d = f(\{\Delta\epsilon_d\}^{t=0 \text{ to current time}}) \tag{20a}$$

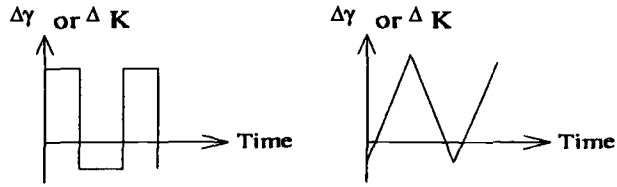

FIG. 6—*Two types of fatigue loading with the same range.*

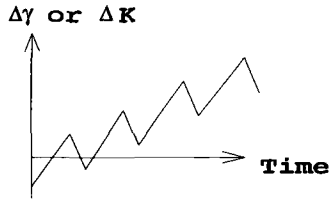

FIG. 7—*Ratcheting* $\Delta\gamma$ *or* ΔK *versus time.*

$\{\Delta\epsilon_d\}$ is a tensor, and we need a frame-invariant scalar from this tensor. In this study, the incremental effective inelastic (creep) damage strain, $\Delta\epsilon_{dp}$, was used, and we obtain

$$\gamma_d = f(\Delta\epsilon_{dp}^{t=0 \text{ to current time}}) \tag{20b}$$

where

$$\Delta\epsilon_{dp} = \Delta t\, 2(\tfrac{1}{2}\{\dot{\epsilon}_{vp}\}^T[M]^{-T}[S_S][M]^{-1}\{\dot{\epsilon}_{vp}\})^{1/2} \tag{20c}$$

Equation 20c is still too complex, and its functional form is not obvious. Especially, it is impossible to deal with the complete $\Delta\epsilon_{dp}$ history. Uniaxial creep and fatigue experiments of 63Sn/37Pb solder indicate the following phenomena.

1. When stress does not change sign (continuous tension, or compression), γ_d can be a constant or in a form shown below:

$$\gamma_d = A(\epsilon_{dp})^r \tag{20d}$$

where A and r can be obtained experimentally

$$\epsilon_{dp} = \int d\Delta\epsilon_{dp} \tag{20e}$$

Note: When r is large, the constant n_d of Eq 16b will be small.

2. When stress changes from tension to compression, the longer the period of compression, the smaller the damage rate after the stress changes to tension again. This means the material partially heals during compression as shown in Table 1. To simulate this phenomenon, we can define a parameter, ϵ_{tot}, and let

$$\gamma_d = A(\epsilon_{\text{tot}})^r \tag{20f}$$

where $\epsilon_{\text{tot}} = \epsilon_{\text{tot\_last\_step}} + \Delta\epsilon_{dp}$ for tension; $\epsilon_{\text{tot}} = \epsilon_{\text{tot\_last\_step}} - p\Delta\epsilon_{dp}$ for compression; where p is a factor that can be obtained by simulating fatigue experiments. If we set p as follows, we obtain results that closely match our experimental results.

$$p = p_0 \frac{\epsilon_{\text{tot}}}{\epsilon_{\text{tot}} + h} \tag{20g}$$

where p_0 is a material constant; $h = \int_{tc}^{t} d\Delta\epsilon_{dp}$; tc is the time when the compression begins; and t is current time. Time from tc to t is the duration of the compression.

For the multiaxial case, ϵ_{tot} can be obtained by the procedures of Table 2. ϵ_{tot} versus time for a uniaxial fatigue case is shown in Fig. 8.

The Second Approach: Decrease the Damage During the Compressive Stress—In this study, assume that parts of the three principal damages are reversible before complete failure (Damage = 1).

1. $D_i^n < 1$ (Incomplete failure: the damage can recover).

$$D_i^{n+1} = D_i^n + \eta_i \dot{D}_i \Delta t \qquad i = 1, 2, 3 \tag{21}$$

TABLE 2—*Procedures to find* ϵ_{tot}.

1. Set $e_1 = e_2 = e_3 = 0$, $h_1 = h_2 = h_3 = 0$ at first time step.
2. Find e_1, e_2, e_3, h_1, h_2, and h_3 at each time step as follows:

```
FOR i = 1 to 3
  IF Ḋ_i ≥ 0 THEN
    e_i = e_i + Δε_dp
    h_i = 0
  ELSE
    p = p_0 e_i / (e_i + h_i)
    e_i = e_i − pΔε_dp
    IF e_i < 0 THEN e_i = 0
    h_i = h_i + Δε_dp
  ENDIF
NEXT i
```

3. Find ϵ_{tot}

```
IF Ḋ_1 ≥ 0 THEN
  ε_tot = e_1
ELSEIF Ḋ_2 ≥ 0 THEN
  ε_tot = e_2
ELSEIF Ḋ_3 ≥ 0 THEN
  ε_tot = e_3
ELSE
  ε_tot = 0
ENDIF
```

NOTE: $\dot{D}_1$, $\dot{D}_2$, and $\dot{D}_3$ are the damage rates in the principal damage directions. ($D_1 \geq D_2 \geq D_3$); P_0 is a material constant.

2. $D_i^n = 1$ (Complete failure: the damage cannot recover).

$$D_i^{n+1} = D_i^n = 1$$

where n is time step; D_i is the principal value of the damage tensor; Δt is the time interval; $\eta_i = 1$ for $\dot{D}_i > 0$; $\eta_i < 1$ for $\dot{D}_i < 0$; and η_i should be a function of the damage tensor. We can set them as constants for simplification.

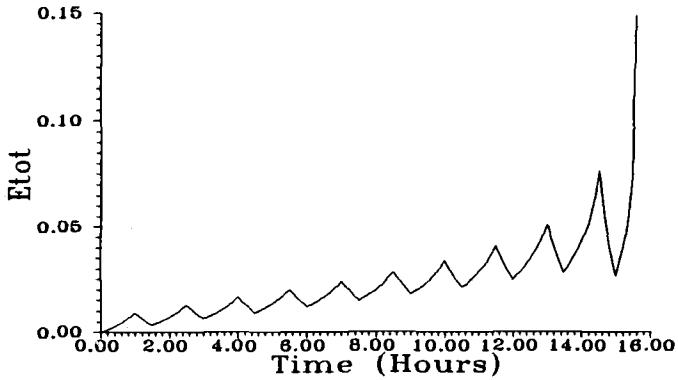

FIG. 8—ϵ_{tot} *versus time of a uniaxial fatigue case. Applied stress is 20.7 MPa (3000 psi) for 1 h and −20.7 MPa (−3000 psi) for ½ h.*

Discussion of the assumption of reversible damage

1. Martin did one-dimensional fatigue experiments in vacuum using various materials [*22*]. In this work, a specimen is fractured in tension, then a compressive force pushes the broken parts together. The load is cycled again into tension, and the specimens break again when the tension load reaches about 70 to 90% of the preceding load at fracture. This means that reweldment (cold welding) occurs during the compressive load. The cold welding effect for ductile metals is discussed in Refs *21* to *23*. These references indicate that up to 90% of the crack area can be rewelded by a compressive load in vacuum. For the above damage theory, the microcracks in the structure should be very small and free of air, and repeated rewelding should be possible.

2. References *22* and *23* indicate that oxygen and moisture decrease the rewelding effect. Therefore, it is difficult to measure the internal reweldment effect of microcracks since microcracks on the surface are instantly exposed to air. For this reason, very little work has been reported on this subject. More typically, the damage for one whole cycle is analyzed, and it is not necessary to measure the damages for tension and compression parts. In this study, we simplify η_1, η_2, and η_3 to material constants (Table 3). A more accurate theory of reweldment under cyclic loads requires further research.

Primary creep recovery is another possible mechanism affecting creep rates and fatigue life, but in our experiments (low-cycle fatigue regime) crack healing is likely to be the dominant mechanism. The primary creep recovery can be modeled by the superposition of viscoelastic or viscoplastic patterns to include the primary creep [*29*]. The superposition method is simple, but it requires too many material constants that need to be found by experiments.

TABLE 3—*Material constants of 63Sn/37Pb solder for creep-fatigue damage formula at 23°C.*

E (N/m^2)	v	γ	n	nd	μ	A	r	p_0	η_1	$\eta_2 = \eta_3$
1.38E10	0.4	1.644E-44	5.2	4.2	−0.1	1.784E-35	0.8	2.5	0.2	0.8
(2.0E6)	(0.4)	(5.4E-21)	(5.2)	(4.2)	(−0.1)	(8.5E-16)	(0.8)	(2.5)	(0.2)	(0.8)

NOTES: unit of strain rate = 1/s (1/h); unit of stress = N/m^2 (psi); E = Young's modulus at low strain rate; v = Poisson's ratio.

TABLE 4—*Summary of the experiments for 63Sn/37Pb solder* [20].

Experiments	Number of Tests, N	Specimen Geometry	Error $\frac{1}{N}\sum_1^N \left\lvert \frac{LE_i - LF_i}{LE_i} \right\rvert$
1D creep tests	29	Fig. 10*a*	14%
1D fatigue tests	14	Fig. 10*a*	24%
Tension-torsion tests	8	Fig. 10*b*	14%
Bimaterial tests	21	One case in Fig. 14	15%
Moiré tests	6	One case in Fig. 15	25%

NOTE: LE_i = The real life of specimen i.
LF_i = The predicted life of specimen i using the creep-fatigue formula.

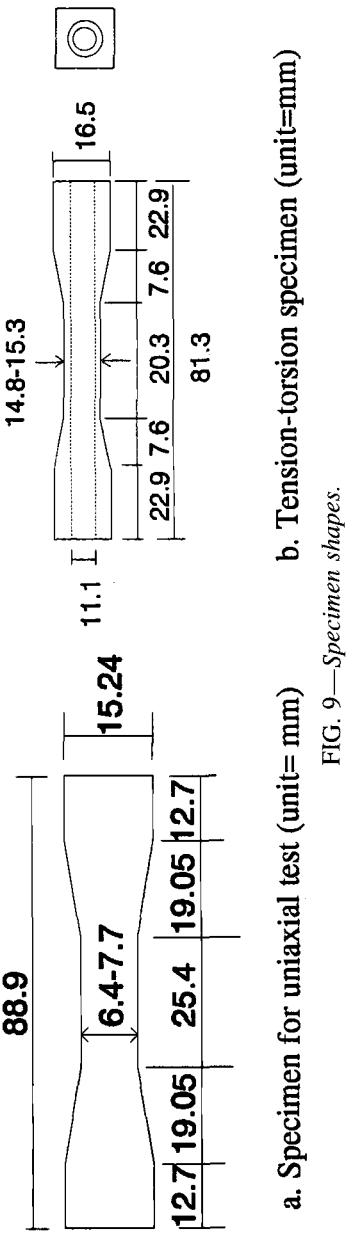

a. Specimen for uniaxial test (unit= mm) b. Tension-torsion specimen (unit=mm)

FIG. 9—*Specimen shapes.*

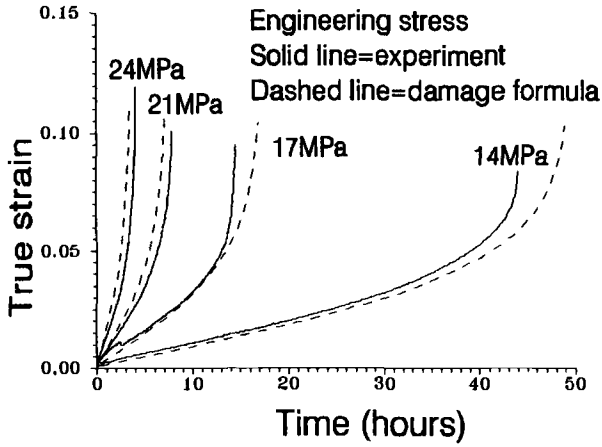

FIG. 10—*Results of creep tests and creep-fatigue damage formula at 23°C.*

The above creep-fatigue formula can be used to predict the structural life for time-dependent and temperature-dependent materials under cyclic loads. A finite element program incorporating this theory has been generated [*20*]. In the next section, experimental results will be used to validate this theory.

Experimental Validation

The main purposes of the experiments are to find material constants and to validate the creep-fatigue damage formula. Experiments include uniaxial creep tests, uniaxial creep-fatigue tests, tension-torsion tests, bimaterial tests, and Moiré tests [*20*], which are summarized in Table 4. Specimens made of 63Sn/37Pb solder by casting [*20*] were tested at 23°C using a servohydraulic testing machine with load cells of 445 and 4450-N capacity under load control. An extensometer with a 12.7-mm gage length was used to measure displacement, and all results of the experiments were recorded on a personal computer. The material

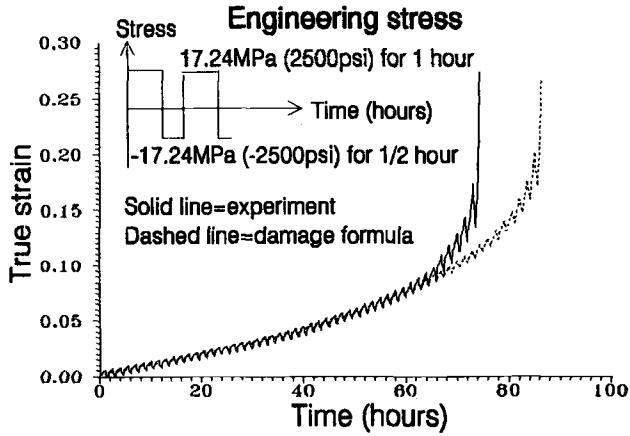

FIG. 11—*Results of one-dimensional fatigue test and creep-fatigue damage formula at 23°C.*

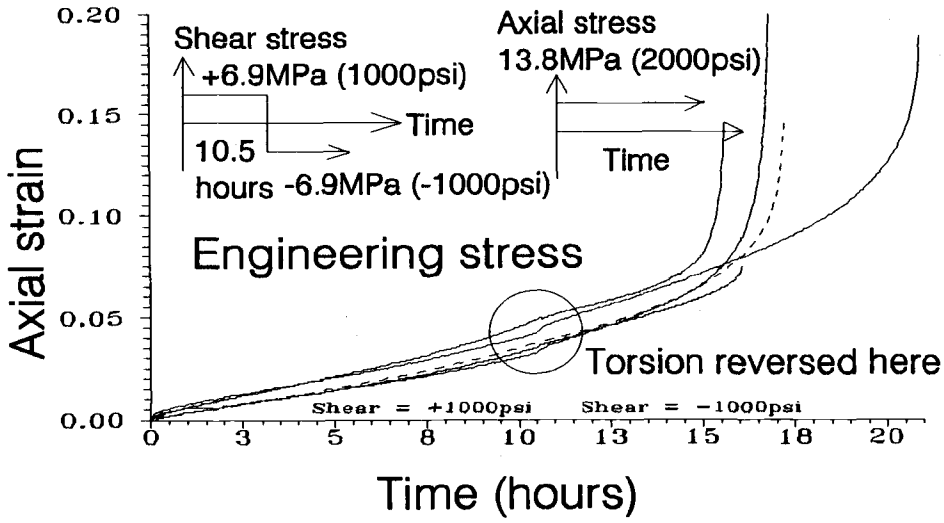

FIG. 12—*Tension-torsion test with a constant axial force and a once-reversed torsional load.*

constants at 23°C are shown in Table 3. Parts of the experiments are shown in Figs. 10 to 15. Figure 10 shows plots of uniaxial creep tests. The results are also simulated by the creep-fatigue damage formula showing good agreement. Figure 11 indicates similar agreement between the experiment and the creep-fatigue damage formula for the uniaxial fatigue test. Figure 12 shows four tension-torsion experimental results of the tubular specimen in Fig. 9. The dashed line obtained from the creep-fatigue damage formula can accurately predict the experimental results. A bimaterial test is illustrated in Fig. 13. The finite element analyses closely simulate the experiments. In addition to life prediction, the creep-fatigue formula can also predict the crack growth path as shown in Fig. 14. The predicted and real crack growth paths are almost the same. Figure 15 shows a similar agreement of Moiré and finite element results for vertical displacement contours. Our experimental results also indicate that material properties derived from experiments with bulk material work well for thin-layer solder joints, if the manufacture procedures and the micro-structure of specimens are the same. Furthermore, material constants for the creep expression derived from pure tension testing can also be applied to models with pure shear and multiaxial stress states using the von Mises criterion.

Conclusions

An anisotropic model of continuum damage mechanics has been developed in this study to predict the creep-fatigue behavior and life of solder joints. With the help of the finite element method, the time-dependent and temperature-dependent stress, strain, and damage fields of solder can be obtained. Experiments including uniaxial creep, uniaxial fatigue, tension-torsion, moiré, and bimaterial tests were performed to validate this model. The results indicate that this model can adequately predict fatigue life and crack growth paths of solder joints for the range of lives and conditions investigated.

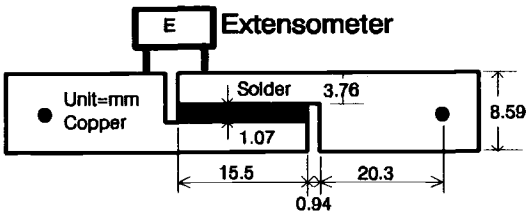

a. Specimen dimension (thickness=1.63mm)

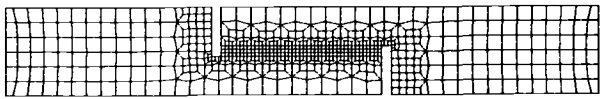

b. Finite element mesh (8-node plane stress element)

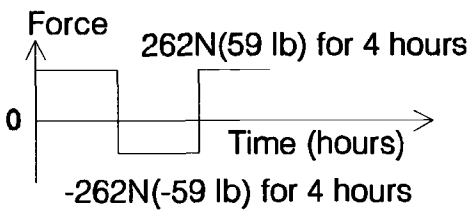

c. Cyclic forces

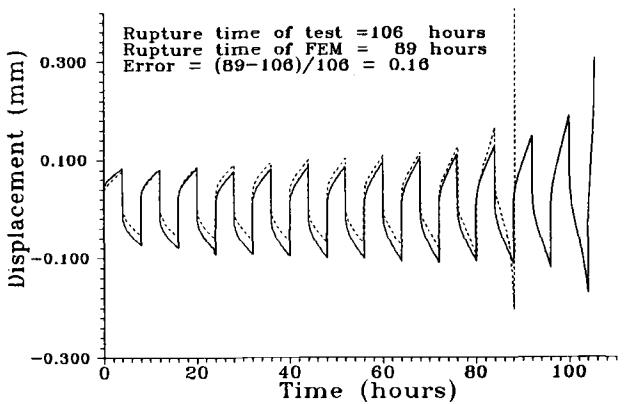

d. Experimental and finite element results
Solid line=experiment, Dashed line=FEM with creep-fatigue damage formula

FIG. 13—*Bimaterial test.*

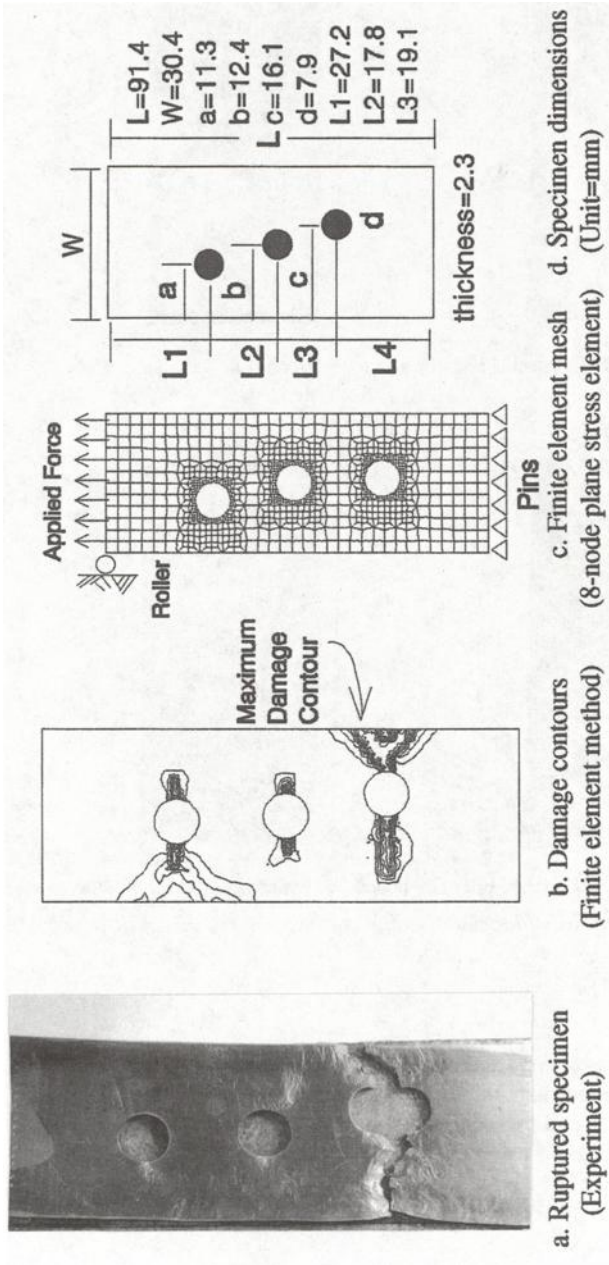

FIG. 14—*Moiré and finite element analyses.*

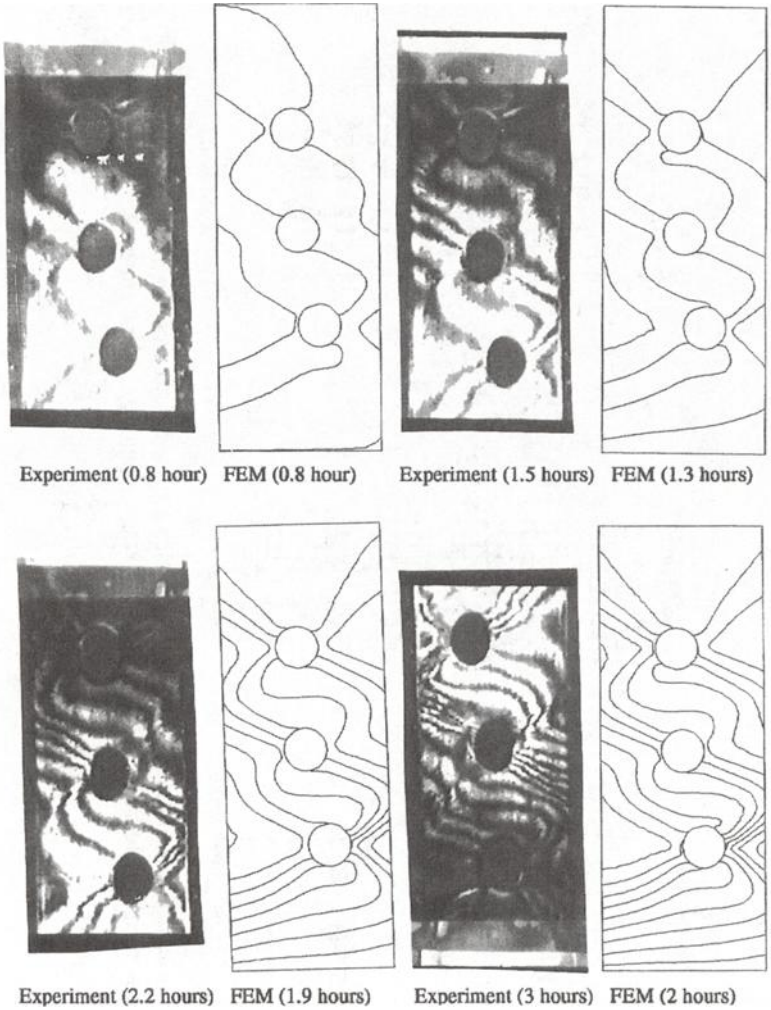

FIG. 15—*Horizontal displacement contours of Specimen 2 (real life = 3.9 h; predicted life = 2.5 h).*

Acknowledgment

This research was supported by the industrial sponsors of the Consortium for Mesomechanics of Electrical Interconnects at the University of Wisconsin-Madison. We thank all the sponsors and the students who assisted in this program. Special thanks go to S. A. Schroeder and M. R. Mitchell of Rockwell International for supplying us the solder used in this study.

References

[*1*] Norton, F. H., *Creep of Steel at High Temperature,* McGraw-Hill, New York, 1929, p. 67.
[2] Ludvik, P., *Element der Technologischen Mechanik,* Springer, Berlin, 1908.

[3] Soderberg, C. R., "The Interpretation of Creep Tests for Machine Design," *Transactions of ASME,* Vol. 58, No. 8, 1936.
[4] Nadai, A., "On the Creep of Solids at Elevated Temperature," *Journal of Applied Physics,* Vol. 8, No. 6, 1937.
[5] Garofalo, F., *Fundamentals of Creep and Creep-Rupture in Metals,* Macmillan, New York, 1965.
[6] Bailey, R. W., "The Utilization of Creep Test Data in Engineering Design," *Proceedings of the Institute of Mechanical Engineers,* Vol. 131, London, 1935, pp. 186–205, 260–265.
[7] Andrade, E. N. da C., "On the Viscous Flow of Metal and Allied Phenomena," *Proceedings of the Royal Society, Series A (London),* Vol. 84, 1910, p. 1.
[8] Sherby, O. D. and Burke, P. M., "Mechanical Behavior of Crystalline Solids at Elevated Temperature," *Progress in Materials Science,* Vol. 13, 1967, p. 325.
[9] Zienkiewicz, O. and Cormeau, I. C., "Visco-Plasticity and Creep in Elastic Solid—A Unified Numerical Solution Approach," *International Journal for Numerical Methods in Engineering,* Vol. 8, 1974, pp. 821–845.
[10] Hill, R., *The Mathematical Theory of Plasticity,* Clarendon Press, Oxford, 1950.
[11] Kachanov, L. M., "Time of the Rupture Process under Creep Conditions," in Russian, *Izvestiya Akademii Nauk SSSR Otdelenie Tekniches Kikh Nauk,* No. 8, 1958.
[12] Rabotnov, Y. N., *Creep Problems in Structural Members,* North-Holland Publishing Co., Amsterdam, 1969, pp. 176–400.
[13] Hayhurst, D. R., "Creep Rupture under Multi-Axial States of Stress," *Journal of the Mechanics and Physics of Solids,* Vol. 20, 1972, pp. 381–390.
[14] Trampczynski, W. A., Hayhurst, D. R., and Leckie, F. A., "Creep Rupture of Copper and Aluminium under Non-Proportional Loading," *Journal of the Mechanics and Physics of Solids,* Vol. 29, No. 5/6, 1981, p. 353.
[15] Chow, C. L. and Lu, T. J., "A Normative Representation of Stress and Strain for Continuum Damage Mechanics," *Theoretical and Applied Fracture Mechanics,* Vol. 12, 1989, pp. 161–187.
[16] Chow, C. L. and Wang, J., "An Anisotropic Theory of Elasticity for Continuum Damage Mechanics," *International Journal of Fracture,* Vol. 33, 1987, pp. 3–16.
[17] Chaboche, J. L., "On the Description of Damage Included Anisotropic and Active/Passive Damage Effect," *Damage Mechanics in Engineering Material,* J. W. Ju, D. Krajcinovic, and H. L. Schreyer, Eds., ASME, New York, November 1990, pp. 153–166.
[18] Ju, J. W., "On Energy-Based Coupled Elastoplastic Damage Theories: Constitutive Modeling and Computational Aspects," *International Journal of Solids and Structures,* Vol. 25, No. 7, 1989, pp. 803–833.
[19] Murakami, S., "Notion of Continuum Damage Mechanics and Its Application to Anisotropic Creep Damage Theory," *Journal of Engineering Materials and Technology, ASME,* April 1983, Vol. 105, pp. 99–105.
[20] Ju, S. H., "Creep-Fatigue Analysis of Solder Joints," Ph.D. thesis, University of Wisconsin-Madison, 1993.
[21] Bay, N., "Cold Welding: Part 1—Characteristics, Bonding Mechanisms, Bond Strength," *Metal Construction,* June 1986, pp. 369–372.
[22] Martin, D. E., "Plastic Strain Fatigue in Air and Vacuum," *ASME, Journal of Basic Engineering,* December 1965, pp. 850–856.
[23] Gilbreath, W. P. and Sumsion, H. T., "Solid-Phase Welding of Metals Under High Vacuum," *Journal of Spacecraft,* May 1966, pp. 674–679.
[24] Trivaudey, F. and Delobelle, P., "High Temperature Creep Damage Under Biaxial Loading—Part II: Model and Simulations," *Journal of Engineering Materials and Technology, ASME,* Vol. 112, October 1990, pp. 450–455.
[25] Gong, L. and Hsu, T. R., "A Constitutive Model for Metal Subjected to Cyclic Creep," *Journal of Engineering Materials and Technology, ASME,* Vol. 113, October 1991, pp. 419–424.
[26] Halford, R., "Cyclic Creep-Rupture Behavior of Three High Temperature Alloys," *Metallurgical Transactions,* Vol. 3, 1972, pp. 2247–2256.
[27] Weinbel, R. C., Tien, J. K., Pollak, R. A., and Kang, S. K., "Creep-Fatigue Interaction in Eutectic Lead-Tin Solder Alloy," *Journal of Materials Science,* Vol. 22, 1987, pp. 3901–3906.
[28] Engelmaier, W., "Fatigue Life of Leadless Chip Carrier Solder Joints During Power Cycling," *IEEE Transactions on Components, Hybrids, and Manufacturing Technology,* Vol. 6, 1983, pp. 232–237.
[29] Pande, G. N., Owen, D. R. J., and Zienkiewicz, O. C., "Overlay Models in Time-Dependent Nonlinear Material Analysis," *Computer & Structure,* Vol. 7, 1977, pp. 435–443.

Chih-Wei G. Kuo,[1] *Shankar M. L. Sastry,*[1] *and Kenneth L. Jerina*[1]

Creep-Fatigue Interactions in Eutectic Tin-Lead Solder Alloys

REFERENCE: Kuo, C. G., Sastry, S. M. L., and Jerina, K. L., **"Creep-Fatigue Interactions in Eutectic Tin-Lead Solder Alloys,"** *Fatigue of Electronic Materials, ASTM STP 1153,* S. A. Schroeder and M. R. Mitchell, Eds., American Society for Testing and Materials, Philadelphia, PA, pp. 22–41.

ABSTRACT: Due to their high homologous temperature, eutectic tin-lead solder alloys subjected to cyclic loading at room temperature experience creep-fatigue interactions. In this study, superposition of fatigue and creep deformation and damage under isothermal conditions in rapidly solidified 63Sn-37Pb with and without reflow and conventional 63Sn-37Pb solder alloy is investigated. For strain-controlled fatigue with mean strain, damage is considered in terms of stress relaxation and cyclic softening. For stress-controlled fatigue with mean stress, the fatigue life is modeled with a cycle-time fraction damage law determined from creep rupture and fatigue life data. The nature of damage was investigated by metallographic examination, cavitation measurements, and fractographic observations. The extent of individual creep and fatigue contributions to the overall life and nature of superposition of creep and fatigue is discussed.

KEYWORDS: creep-fatigue interactions and mechanisms, rapid solidification, stress-controlled fatigue, strain-controlled fatigue, stress relaxation, stress rupture, cavitation, precision density measurements, grain boundary sliding

Eutectic 63Sn-37Pb solder alloy is used extensively for electronic packaging because of a low melting point, excellent wettability, and attractive tensile properties of the near-eutectic Sn-Pb compositions. The reported fatigue failure of solder joints of electronic components is twofold. The primary cause of joint failure is due to the cyclic strain developed as a result of the thermal expansion mismatch between dissimilar materials, for example, between a ceramic chip carrier and a polymeric circuit board during thermal fluctuation [*1,2*]. The other cause of fatigue failure is due to the cyclic stress induced by random or periodic vibration that an electronic component encounters during its service life [*3–6*]. Ambient temperature corresponds to about 0.65 of the melting temperature of near eutectic Sn-Pb solder alloys. Therefore, time-dependent deformation is significant even at room temperature and creep-fatigue interactions must be considered in life prediction calculations.

The phenomenon of creep-fatigue interactions has been the subject of considerable study in recent years, especially in the evaluation of gas turbine blades and nuclear reactor power plant piping [*7*]. Creep-fatigue interactions always lead to shorter lifetime. Crack-initiation-based life prediction under combined creep and fatigue loading conditions has been performed using linear damage rules, frequency-modified Coffin-Manson equations, strain-range partitioning equations, and damage rate equations [*7*]. High-temperature elastic-plastic creep fracture mechanics has been used with limited success for the modeling of crack propagation under creep-fatigue conditions. A linear cumulative damage model has been

[1]Graduate student, professor of metallurgy and materials science, and professor of mechanical engineering, respectively, Materials Research Laboratory, Washington University, Campus Box 1087, One Brookings Drive, St. Louis, MO 63130-4899.

shown to accurately predict total crack growth from the superposition of time-dependent (creep) crack growth and fatigue crack growth in a titanium aluminide alloy [*8*].

Micromechanisms of creep-fatigue interactions include intergranular damage and triple point cracking. One form of intergranular damage is the initiation and growth of grain boundary cracks without the influence of a major crack. Triple point cracking is associated with grain boundary sliding. Several creep fatigue laws or models for these processes have been proposed. The cycle time fraction rule involves linear summation of fatigue and creep damage, where fatigue damage is expressed as a cycle exhaustion ratio for the fatigue component and a time exhaustion ratio for the creep component [*9*]. This Miner-Robinson rule has been adopted in the ASME Boiler and Pressure Vessel Code. Creep damage is determined from stress rupture data, and fatigue damage is determined from fatigue lifetime data. Experimental results for several material systems have shown that the cycle time fraction rule is nonconservative. An alternative ductility exhaustion approach is to recognize that creep ductility is a function of strain rate and to define creep damage as the ratio of strain to ductility [*10*]. The creep-fatigue damage process is considered by some researchers [*11*] to be a fatigue crack propagation controlled problem. Some damage rate equations consider the influence of creep cavity growth ahead of a fatigue crack. In some material systems the effect of sintering of cavities under compressive stress affects creep damage that occurs under tensile stresses [*12,13*]. Cavity formation ahead of the crack tip modifies the crack tip stress fields and the stress intensity parameters that describe fatigue-creep crack growth.

Research on the effects of testing variables on the fatigue life of eutectic Sn-Pb solders has indicated that creep-fatigue interactions are significant. It has been shown that for symmetric fully reversed fatigue tests, the effects of frequency (or strain rate) and hold time on fatigue life are significant [*14–17*]. The fatigue life of eutectic Sn-Pb solders increases as frequency increases or as hold time decreases. These results clearly indicate the important role of creep-fatigue interactions because frequency, strain rate, and hold time have an effect on fatigue life. Studies by Weinbel et al. [*16*] show that as the mean stress is increased, the cyclic creep rate increases and the number of cycles to failure decreases drastically. Knecht and Fox [*18*] were able to isolate the contribution of creep damage from a symmetrical fatigue hysteresis loop. In general, for solder joints connecting stiff leads, the dominant damage mechanism is cyclic shear fatigue. However, Ross and his coworkers [*19*] have found that, for compliant leads, such as flat paks having gull-wing leads, solder joint failure in a thermal cycling condition is caused by a combination of axial tension-compression cyclic fatigue and creep ratcheting at the heel.

In the present study, strain-controlled fatigue life with mean strain is considered as the superposition of stress relaxation and zero mean strain-controlled fatigue. Stress-controlled fatigue life with mean stress is considered as the superposition of stress rupture and zero mean stress-controlled fatigue. Creep-fatigue life was compared to lifetimes under separate fatigue and creep experiments. All the experiments were performed on bulk solder specimens rather than solder joints to separate material and constraint effects. Damage and failure under different loading conditions were studied by precision density measurements, optical metallographic examination of void size and distribution, and grain boundary sliding measurements. Fracture surfaces were examined by scanning electron microscopy to identify the fracture modes.

Experimental Techniques

Material and Specimen Preparation

Three types of eutectic Sn-Pb solder were studied in this investigation: commercial 63Sn-37Pb, rapidly solidified (RS) 63Sn-37Pb, and reflowed (RF) RS 63Sn-37Pb. Commercial

63Sn-37Pb solder powders with powder sizes of 25 to 38 μm were procured from AMT (Advanced Metals Technology, Inc., Branford, Connecticut). The powders were cold pressed to approximately 95% theoretical density and then extruded into 6-mm rods at 100°C with a reduction ratio of 16:1. The rapidly solidified (RS) 63Sn-37Pb solder powders were produced by the induction melting and inert gas atomization process described previously [*20*]. The rapidly solidified powders were sieved, and the −80-mesh (−180-μm) powders were cold pressed and extruded into 6-mm rods. Similar work has been carried out by Fields et al. [*21*] to produce bulk intermetallic compounds commonly found in solder joints. To produce microstructure similar to that found in solder joints, samples of RS 63Sn-37Pb were reflowed. Reflowed samples, RF RS 63Sn-37Pb, were prepared by heating 6-mm-diameter rods in an aluminum mold to 20 ~ 30°C above the melting point and cooling the mold-sample assembly at rates comparable to that encountered in service conditions. A representative temperature-time profile consists of heating the sample at 5°C/min to a maximum temperature of 210°C and cooling at 6°C/min to the ambient temperature.

Mechanical Testing

The geometry of specimens used for tension, creep, and fatigue testing is shown in Fig. 1. Tensile properties of solder alloys were determined from tension tests at 25°C at a strain rate of $2 \times 10^{-3}\,s^{-1}$. Creep-fatigue interactions were studied by stress- and strain-amplitude controlled fatigue tests with and without mean stress/strain as shown in Figs. 2*a* to 2*f*. Creep components in the form of stress rupture and stress relaxation are shown in Figs. 2*c* and 2*f*. Test conditions were designed such that the stress-controlled fatigue with mean stress (Fig. 2*a*) corresponds to the superposition of the stress-controlled fatigue without mean stress (Fig. 2*b*) and the stress rupture test (Fig. 2*c*).

Stress-controlled fatigue without mean stress was conducted per ASTM Practice for Constant Amplitude Axial Fatigue Tests of Metallic Materials (E 466-82). The number of cycles to failure (N_f) was recorded in each test. A triangle waveform was used to apply the stress history, ±21 MPa (±3 ksi) (R ratio of −1) at 0.05 Hz. In stress-controlled fatigue tests with mean stress, the stress reversals were at −14 MPa (−2 ksi) to +28 MPa (+4 ksi), a stress range of 42 MPa (6 ksi) and a mean stress of 7 MPa (1 ksi) (R ratio of −0.5). These conditions resulted in a mean stress creep component of 7 MPa (1 ksi) superimposed on a fully reversed fatigue history. Stress rupture tests were performed at a constant stress of

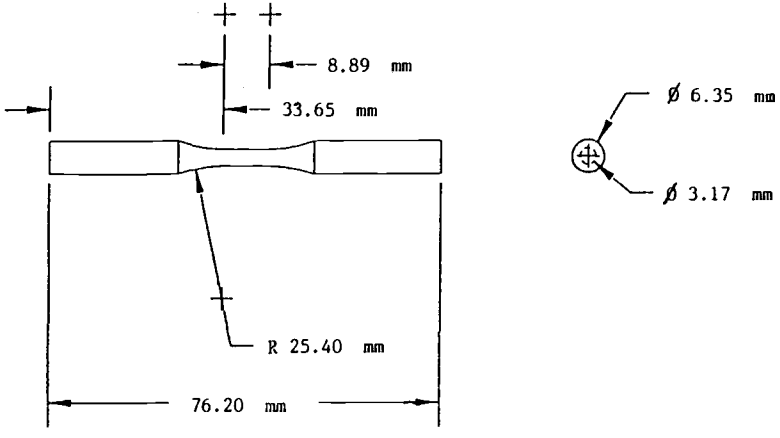

FIG. 1—*Geometry of specimens used for tension and creep-fatigue testing.*

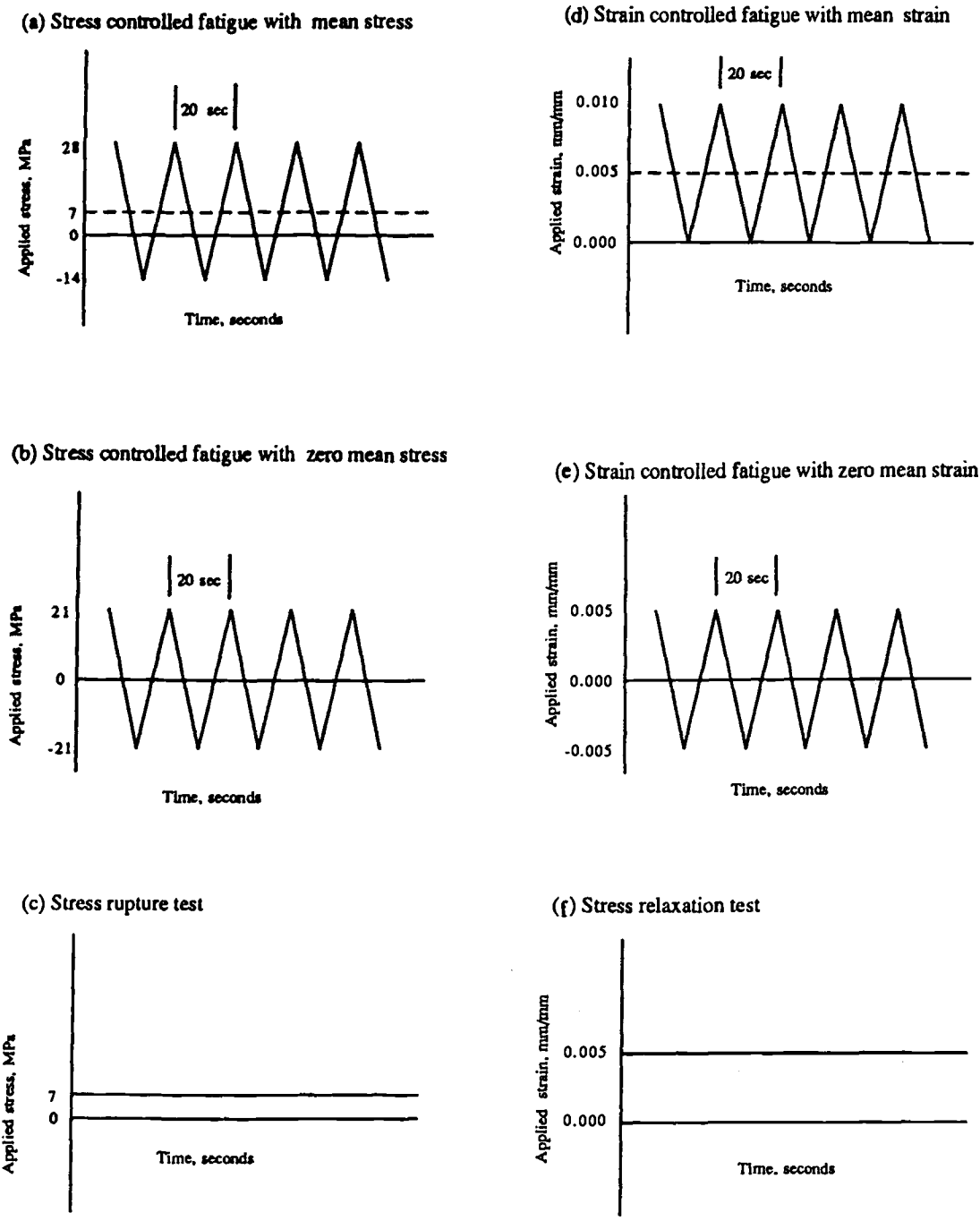

FIG. 2—*Loading conditions used in creep-fatigue tests.*

7 MPa (1 ksi), which corresponded to the mean stress in the stress-controlled fatigue test with mean stress, and the time to failure was determined.

Strain-controlled fatigue without mean strain was conducted per ASTM Practice for Constant-Amplitude Low-Cycle Fatigue Testing (E 606-80). Test conditions were a total strain range of 0.01, zero mean at a strain rate of 0.001 s^{-1} and triangle waveform. The fatigue life was defined as the number of cycles at which the stress at the tension reversal dropped to half of its initial value. Hysteresis loops were recorded at logarithmic intervals. In strain-controlled fatigue with mean strain, the specimens were cyclically deformed with a triangle waveform with a mean strain of +0.005 and a strain range of 0.01. Stress relaxation tests were performed at a strain of 0.005 to determine the time at which the load decreased to 50% of its initial value. Stress relaxation occurs during the hold time of thermal cycling and strain-controlled fatigue. Decrease in stress resulting from stress relaxation reduces mean stress effects in stress-strain analysis and failure determination.

Deformation Characterization

The extent of cavitation was determined by precision density measurements [*22,23*] of slices sectioned close to the fracture end of each specimen. This technique is sensitive to bulk internal cavitation and determines the total volume fractions of cavities. The buoyant fluid used in the measurements can penetrate surface cracks. Therefore, the measurement is not sensitive to surface flaws. An average sensitivity of ± 0.004 g/cm^3 and precision of $+0.04$ g/cm^3 were achieved in the measured density of a 200-mg sample. The longitudinal gage section (parallel to the loading direction) close to the fracture surface was polished, etched, and then examined optically to determine the size, morphology, location, and distribution of voids formed during combined creep and fatigue deformation. Small angle neutron scattering (SANS) was used on a limited number of specimens to determine the applicability of the technique for damage characterization in solder samples. The fracture surfaces were examined with a scanning electron microscope to determine final failure mode.

The extent of grain boundary sliding during creep was determined from optical metallographic examination of surface scribe mark displacement. A specimen similar to that shown in Fig. 1 was ground and polished longitudinally to create a flat surface in the reduced section. The specimen was then etched with a solution of 15 mL acetic acid, 15 mL nitric acid, and 60 mL glycerin at 80°C to reveal the grain structure. Scratches in both the longitudinal and transverse directions were made on the etched surface using a 2000-grit sand paper. Reference spots were located on the surface by optical microscopy at $\times 500$, and micrographs were taken. The specimen was deformed to 20% strain under creep at an applied stress of 10 MPa. The reference spots on specimen surface were located with optical microscopy at $\times 500$, and micrographs were taken of the deformed microstructure.

Results and Discussion

The microstructures of the specimens used in this investigation are shown in Figs. 3*a* to 3*c*. The extruded AMT sample and RS 63Sn-37Pb have a globular tin-rich phase (light area) and a lead-rich phase (dark area), as shown in Figs. 3*a* and 3*b*. The grain structure of RS 63Sn-37Pb is finer than that of AMT 63Sn-37Pb. Reflowed RS 63Sn-37Pb has a lamellar structure with alternate Sn-rich phase and Pb-rich phase, as shown in Fig. 3*c*. The tensile properties of solder alloys at 25°C are summarized in Table 1. Elastic modulus and 0.2% offset yield strength of the solder alloys were determined from load-strain curves [*24*]. The yield strength and ultimate tensile strength increase as the grain structure becomes coarse

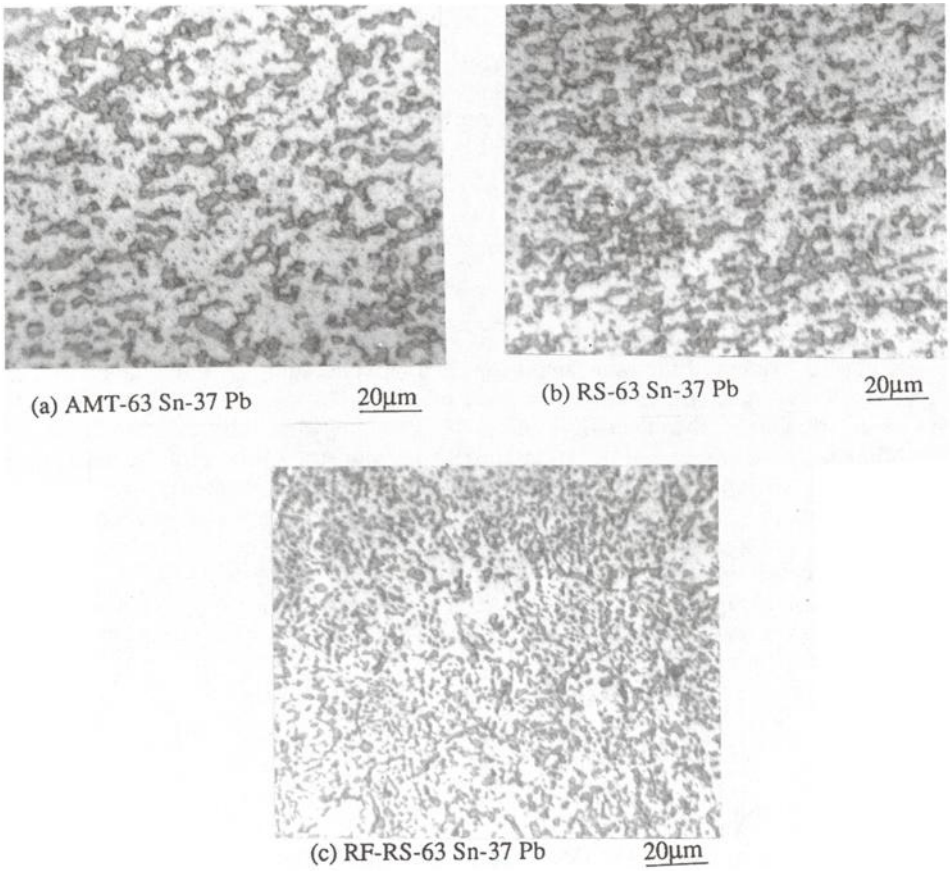

FIG. 3—*Optical micrograph:* (a) *AMT 63Sn-37Pb in as-extruded condition;* (b) *RS 63Sn-37Pb in as-extruded condition;* (c) *reflowed RS 63Sn-37Pb.*

because grain size has an inverse effect in these properties at temperatures above 0.5 melting point as opposed to the effect of grain size at low temperature. AMT 63Sn-37Pb and RS 63Sn-37Pb have similar tensile properties due to similar microstructure.

The number of cycles to failure under stress-controlled fatigue with and without mean stress and the stress rupture life are summarized in Table 2. At the same stress level, solders with higher tensile strengths have longer fatigue lives. The fatigue life is about two orders of magnitude shorter in the presence of a mean stress of 7 MPa than when the mean stress is

TABLE 1—*Tensile properties of eutectic Sn-Pb solders at strain rate of* $2 \times 10^{-3}\ s^{-1}$.

Solder	Yield Strength, MPa	Ultimate Tensile Strength, MPa	Young's Modulus, GPa	Elongation (Reduction in Area), %
AMT-63Sn-37Pb	30	33	11	54 (43)
RS-63Sn-37Pb	29	32	14	42 (34)
RF-RS-63Sn-37Pb	42	46	18	36 (29)

TABLE 2—*Test results for stress rupture at 7 MPa and stress-controlled fatigue at a stress range of 42 MPa, mean of 7 MPa, and frequency of 0.05 Hz, the number of cycles to fatigue failure and the lifetime to rupture for the stress rupture test (data in parentheses show the elongation after fatigue failure due to creep ratcheting).*

Solder	Stress-Controlled Fatigue Mean Stress = 7 MPa	Stress-Controlled Fatigue Mean Stress = 0 MPa	Stress Rupture, σ_c = 7 MPa
AMT-63Sn-37Pb	104 cycles (56%)	15 954 cycles (40%)	6.18×10^3 s
RS-63Sn-37Pb	97 cycles (56%)	12 605 cycles (30%)	$>1.30 \times 10^6$ s
RF-RS-63Sn-37Pb	1164 cycles (48%)	36 662 cycles (16%)	2.86×10^5 s

zero. Nonsymmetric loading in the presence of a mean stress is more damaging than a fully reversed cyclic loading of the same amplitude. In a previous study [*25*], the fatigue life of RS 63Sn-37Pb at the constant stress amplitude of ±28 MPa was found to be 589 cycles. This life is much higher than the fatigue life of 97 cycles shown in Table 2 for a mean stress of 7 MPa and a stress range of 42 MPa. Under nonsymmetric cyclic loading, the fatigue damage due to tension loading is not completely healed during compressive loading. Baik and Raj [*13*] found that 90% of the damage produced in tension can be recovered in compression under creep-fatigue testing conditions.

The stress rupture curves for these three solder alloys are shown in Fig. 4. Based on the tensile strengths, the rupture life for RS 63Sn-37Pb should be similar to that of AMT 63Sn-37Pb. However, because of the fine-grain structure in RS 63Sn-37Pb, there seems to be a threshold stress larger than 7 MPa.

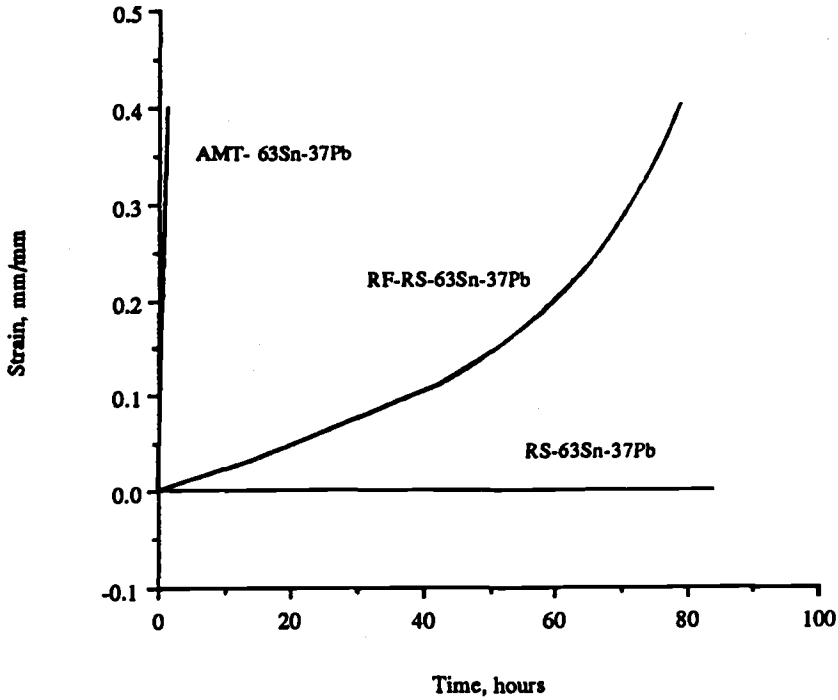

FIG. 4—*Stress rupture test at 7 MPa showing creep strain as a function of time for AMT 63Sn-37Pb, RS 63Sn-37Pb and RF RS 63Sn-37Pb.*

In order to examine the effect of the creep-fatigue interactions, a linear life fraction rule was applied using the following equation

$$D = \frac{N_{cf}}{N_f} + \frac{t_{cf}}{t_c}$$

where

D = total damage assuming that creep and fatigue can be superimposed linearly,
N_f = number of cycles to failure for stress-controlled fatigue with zero mean stress,
t_c = time to rupture in seconds,
N_{cf} = number of cycles to failure under stress-controlled fatigue with mean stress, and
t_{cf} = N_{cf}/frequency, equivalent lifetime in seconds under stress-controlled fatigue with mean stress.

The treatment of creep-fatigue interactions was inspired by Miner's rule [*26*] and the work of Mall, Staubs, and Nicholas [*8*]. The experimental D values are shown in Table 3. If the linear superposition assumption is valid, the creep-fatigue specimen should fail when the total damage, D, reaches unity. However, the failure of solder specimens at D values significantly less than 1 indicates that a linear cycle-time fraction damage rule is not appropriate and suggests that pronounced creep-fatigue interactions are present.

In strain-controlled fatigue tests, the peak stress at tension reversal versus number of cycles is plotted in Figs. 5*a* and 5*b*. The extremely sharp load drop at about 1000 cycles is due to the initiation and propagation of a major crack toward the end of the strain-controlled fatigue life. Stress as a function of time is plotted in Fig. 6 for stress relaxation tests of 0.5% strain. Table 4 gives the strain-controlled fatigue life defined by 50% load drop and the time for stress to reduce to 50% of its initial stress in a stress relaxation test. Specimens with higher tensile ductility have longer strain-controlled fatigue life. Furthermore, all the three solders have short relaxation times, which indicates that mean stress induced by plastic strain rapidly relaxes in these alloys. As a result, the mean strain effect on fatigue life is not as pronounced as the mean stress effect. During strain-controlled fatigue, the fatigue life with mean strain is not significantly different from the fatigue life without mean strain because the stress relaxes so quick that the damage due to the applied strain is not stored and accumulated. No significant difference in the strain-controlled fatigue lives may also be due to the fact that 0.5% mean strain is not large compared to the tensile elongation shown in Table 1.

Creep-Fatigue Mechanisms

Previous studies of creep deformation of eutectic tin-lead solder alloys have shown the stress exponent for creep at 25°C to be 3.2 and activation energy to be 50.6 kJ/mol [*27*]. These values suggest that the dominant creep deformation mechanism of tin-lead solder

TABLE 3—*Evaluation of linear damage under stress-controlled fatigue with mean stress.*

Solder	Total Damage, D
AMT-63Sn-37Pb	0.34
RS-63Sn-37Pb	0.01
RF-RS-63Sn-37Pb	0.11

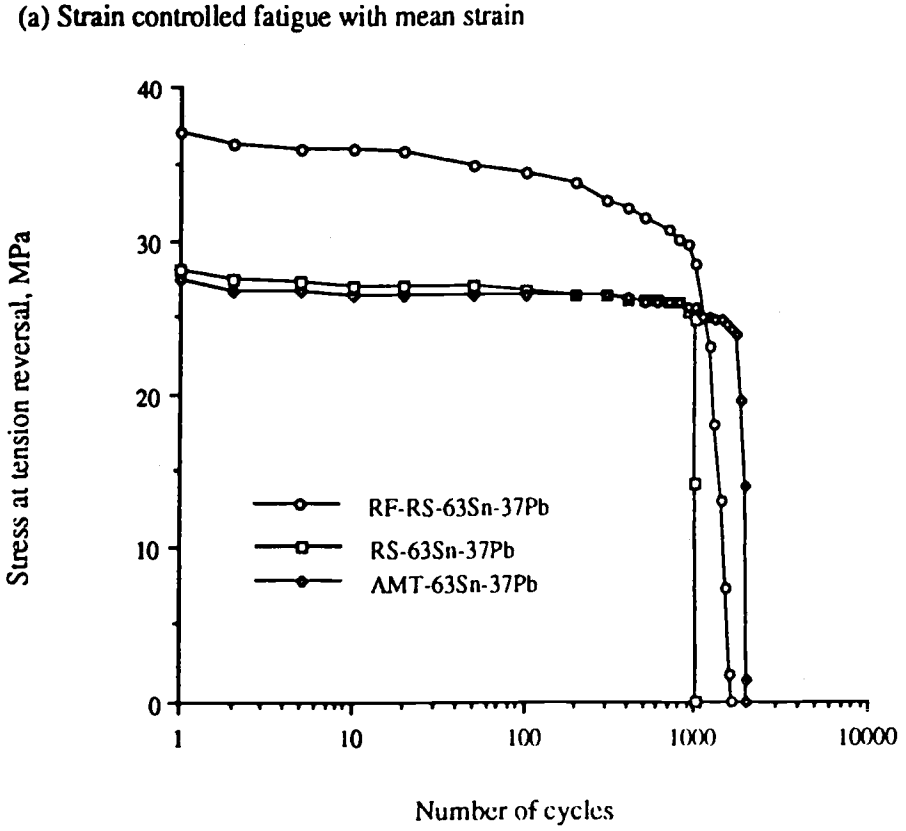

FIG. 5*a*—*The stress at tension reversal versus number of cycles from strain-controlled fatigue with 0.5% strain amplitude and 0.5% mean strain.*

alloys is grain boundary sliding. Corroborative experimental evidence was obtained in the present study from metallographic examination of surface scribe markings before and after creep testing. Figure 7*a* shows the microstructure of RS 63Sn-37Pb and the grid lines engraved on the specimen surface before the creep test. Figure 7*b* shows the microstructure of the same region after the creep test. The offset of grid lines at grain boundaries is clearly seen at locations indicated. Grain boundary sliding during thermal cycling has also been observed in solders used for surface mounting of electronic components [*28*].

Creep-fatigue interaction is a combination of creep and fatigue deformation and damage. Depending on the temperature, frequency, and cycle shape, at least five failure mechanisms have been identified: transgranular or intergranular crack initiation and propagation, "r" type and "w" type cavity formation, and shape instability [*29,30*].

Cavity formation is a common damage mode during high-temperature fatigue and creep. The densities of solder specimens tabulated in Table 5 indicate a significant decrease in density after creep and fatigue deformation such that up to about 2 vol% cavities can form under different test conditions. An attempt was made to measure the amount of cavities present in a fatigued solder sample with small angle neutron scattering (SANS). However, it was found that the neutron scattering due to cavitation could not be separated from the scattering due to Sn/Pb interfaces.

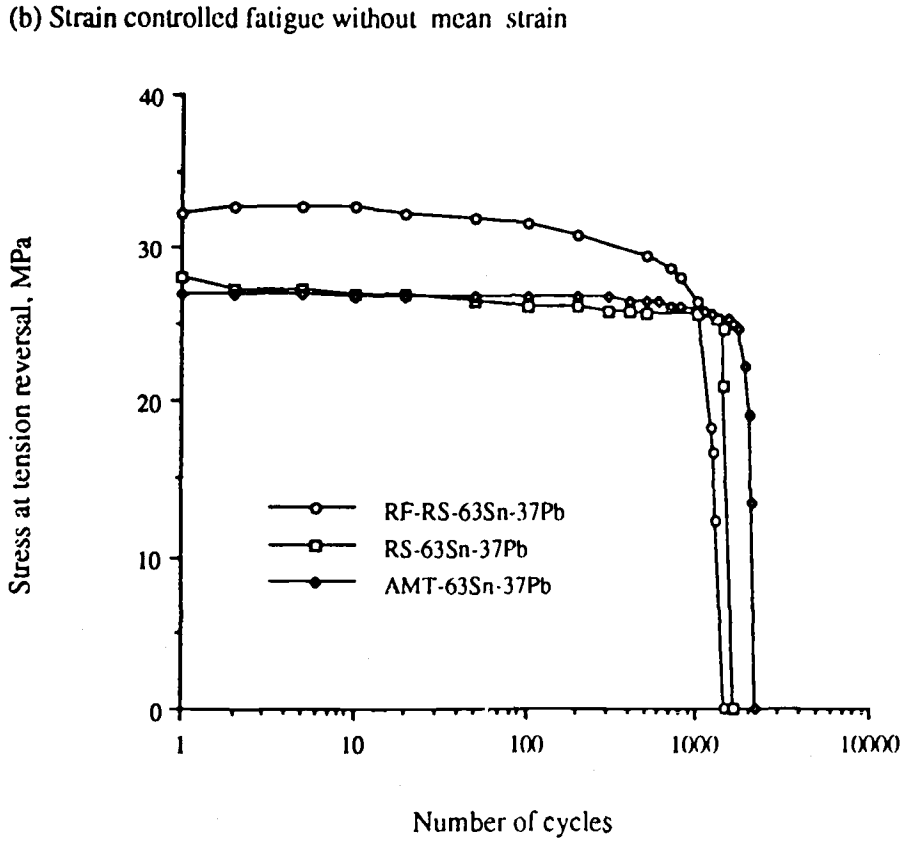

FIG. 5*b*—*Strain-controlled fatigue with 0.5% strain amplitude and zero mean strain.*

The cause of final failure under stress-controlled creep fatigue seems to be different from that under strain-controlled creep fatigue. For stress-controlled fatigue with or without mean stress, the microstructure close to the fracture surface has a large number of spherical voids such as shown in Fig. 8. Figure 9 shows large voids formed by the growth and coalescence of small cavities. In addition to the internal voids, all the specimens tested under stress-controlled fatigue exhibited significant elongation before failure. The specimens exhibited considerable grain coarsening and elongation in the loading direction. The cause of final failure was rupture due to drastic reduction in cross section.

For strain-controlled fatigue with or without mean strain, important features are equiaxed grain structure, surface crack formation, and crack propagation. Figure 10*a* shows secondary surface cracks found in addition to the main crack that caused the final failure. Figures 10*b* and 10*c* show the surface cracks that propagate across the gage section and along grain boundaries. Therefore, final failure of strain-controlled fatigue with or without mean strain is due to propagation of a dominant transverse crack.

Intergranular fracture is also found to be a common feature of eutectic Sn-Pb solder specimens under creep and fatigue tests. Figures 11*a* to 11*c* show the fracture surfaces of RF RS 63Sn-37Pb and RS 63Sn-37Pb after strain-controlled fatigue tests. As shown in Fig. 11*a*, reflowed eutectic Sn-Pb has experienced coarse intergranular fracture. Fine intergranular

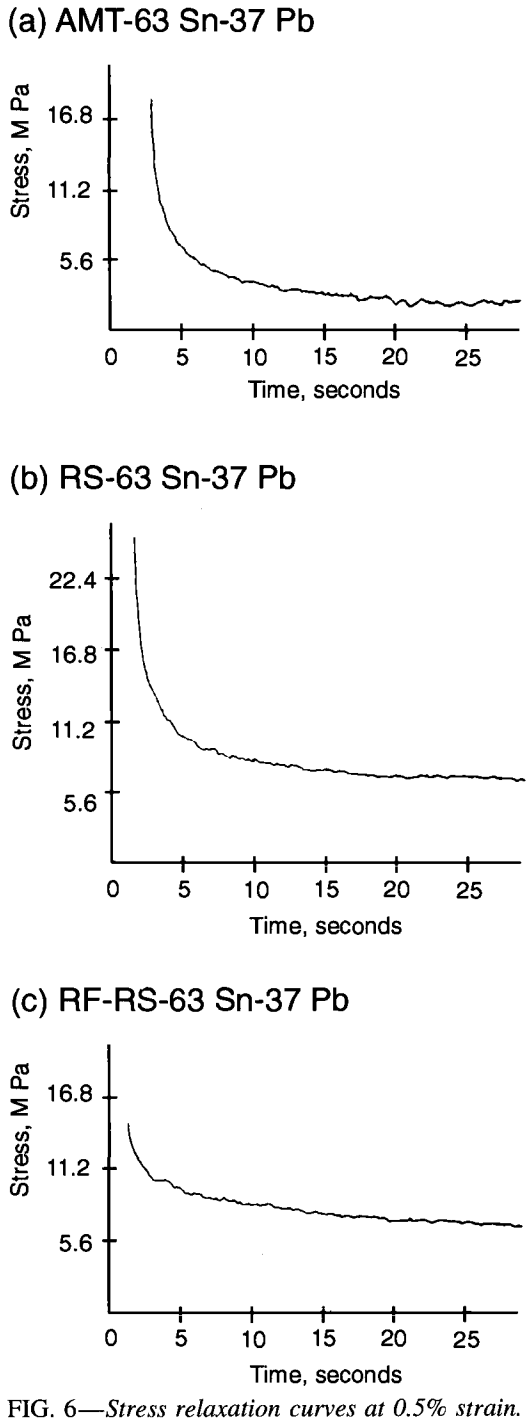

FIG. 6—*Stress relaxation curves at 0.5% strain.*

TABLE 4—*Test results for the stress relaxation and strain-controlled fatigue at a strain range of 0.01 and strain rate of 0.001 $^{-1}$.*

Solder	Strain-Controlled Fatigue Mean Strain = 0.5%	Strain-Controlled Fatigue Mean Strain = 0.0%	Stress Relaxation, ϵ_r = 0.5%
AMT-63Sn-37Pb	1957 cycles	2084 cycles	1.1 s
RS-63Sn-37Pb	1008 cycles	1411 cycles	1.6 s
RF-RS-63Sn-37Pb	1300 cycles	1236 cycles	21.9 s

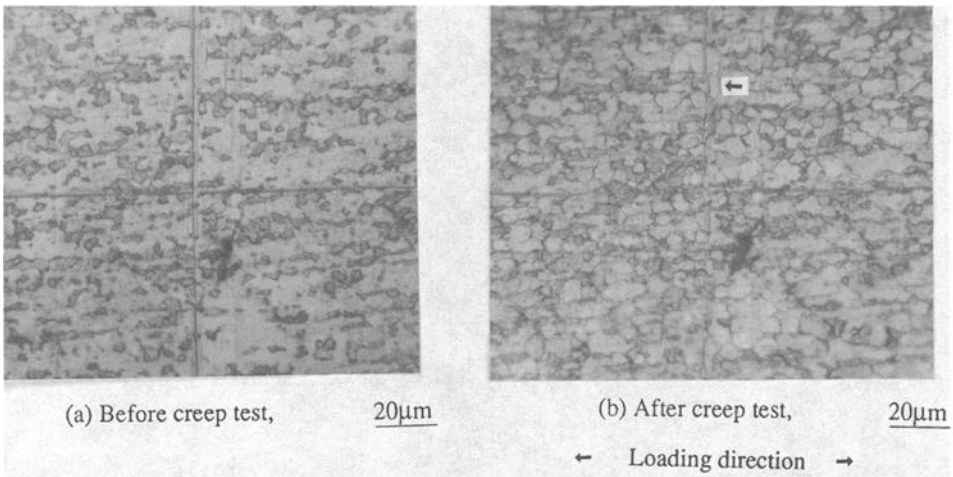

FIG. 7—*Observation of grain boundary sliding under creep in RS 63Sn-37Pb:* (a) *micrograph showing the grid lines engraved on the specimen surface before the creep test,* (b) *micrograph showing the grain boundary sliding after creep test.*

fracture is found in rapidly solidified 63Sn-37Pb as shown in Figs. 11*b* and 11*c*. Secondary cracks are also obvious on these micrographs.

Summary and Conclusions

Creep-fatigue interactions of eutectic Sn-Pb solder alloys were studied by superimposing a creep component in a fully reversed fatigue test. Acceleration of failure due to creep-fatigue interactions is more pronounced in stress-controlled creep fatigue, and samples failed before the total damage in a linear damage summation reached unity. For strain-controlled fatigue with mean strain, the effects of creep-fatigue interactions are not significant because the residual stress due to the mean strain relaxed rapidly and damage was not accumulated.

Grain boundary sliding was observed in eutectic solder deformed in creep. Void formation and intergranular fracture are the common features of specimens deformed under superimposed creep and fatigue. For stress-controlled creep fatigue, the cause of final failure is tension overload, which is due to void coalescence and drastic reduction in cross section. For strain-controlled creep fatigue, the cause of final failure is crack propagation along the grain boundaries and across the gage section.

TABLE 5—*Measured densities in g/cm³ of solder samples under different test conditions.*

Solder	Undeformed Sample	Stress-Controlled Fatigue: mean = 7 MPa; range = 42 MPa; f = 0.05 Hz	Stress-Controlled Fatigue: mean = 0 MPa; range = 42 MPa; f = 0.05 Hz	Stress Rupture, σ_c = 7 MPa	Strain-Controlled Fatigue: mean = 0.5%; range = 1.0%; $\dot{\epsilon} = 1 \times 10^{-3}\ s^{-1}$	Strain-Controlled Fatigue: mean = 0.0%; range = 1.0%; $\dot{\epsilon} = 1 \times 10^{-3}\ s^{-1}$
AMT-63Sn-37Pb	8.44	8.32	8.42	8.29	8.40	8.38
RS-63Sn-37Pb	8.42	8.25	8.39	8.42	8.39	8.39
RF-RS-63Sn-37Pb	8.42	8.26	8.40	8.25	8.37	8.27

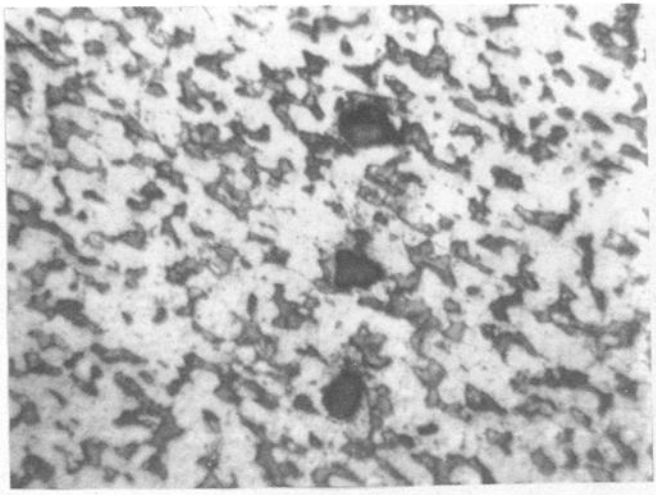

(a) AMT-63 Sn-37 Pb under stress controlled fatigue with zero mean stress

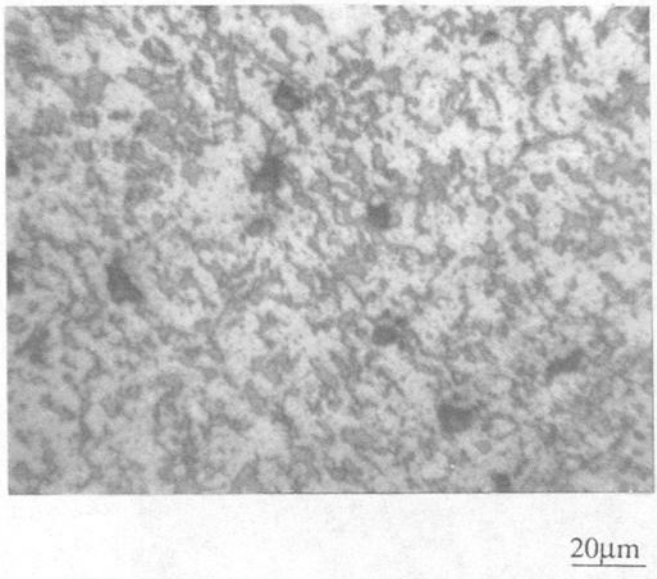

(b) RS-63 Sn-37 Pb under strain controlled fatigue with mean strain

FIG. 8—*Voids of round shape (''r'' type) formed under different test conditions.*

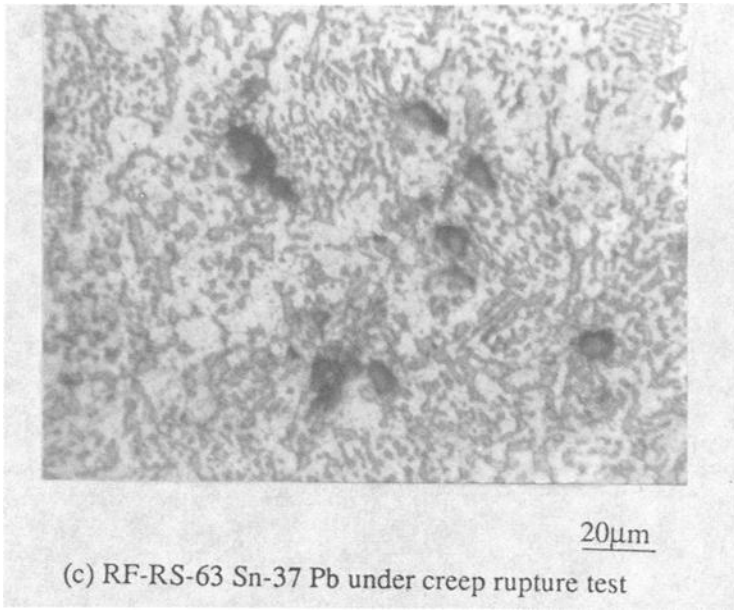

FIG. 8—*(Continued)*

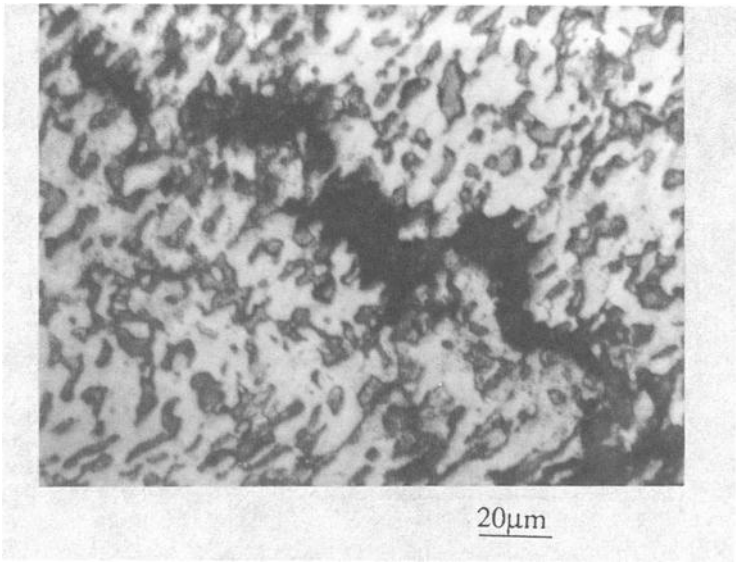

FIG. 9—*Void coalescence to form a bigger void under stress-controlled fatigue with mean stress in AMT-63Sn-37Pb.*

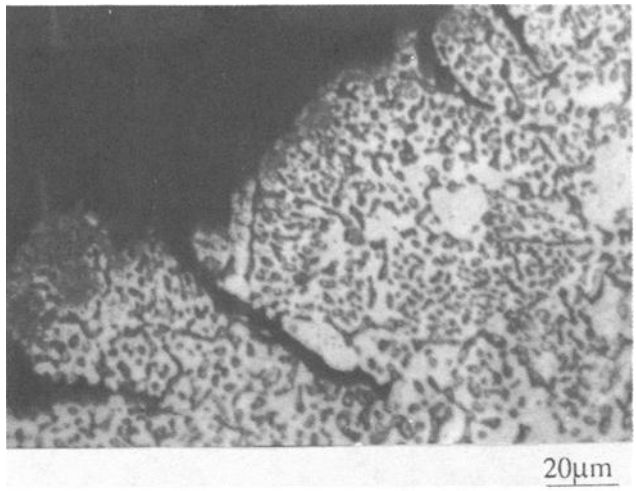

(a) Surface crack found in RF-RS-63 Sn-37 Pb under strain controlled fatigue with zero mean strain

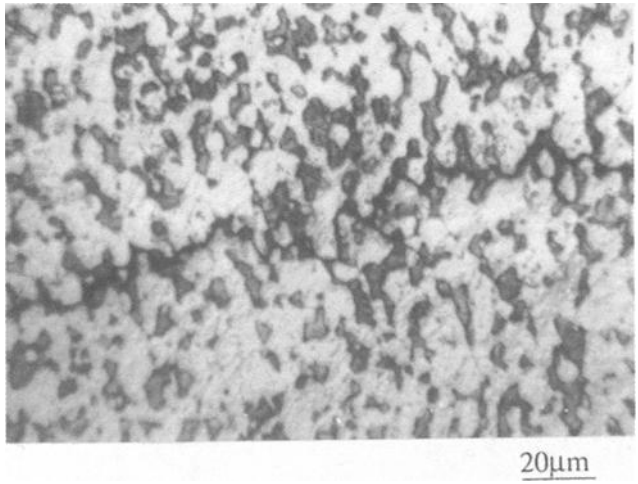

(b) Crack propagation across the gage section of AMT-63 Sn-37 Pb under strain controlled fatigue with mean strain

FIG. 10—*Surface crack which propagates along grain boundaries and across the gage section is the cause of final failure for strain-controlled fatigue with or without mean strain.*

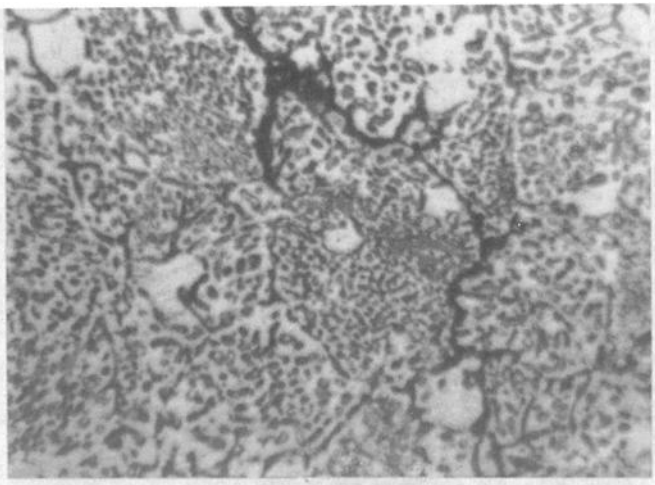

(c) Crack propagation along grain boundary in RF-RS-63 Sn-37 Pb under strain controlled fatigue with mean strain

FIG. 10—*(Continued)*

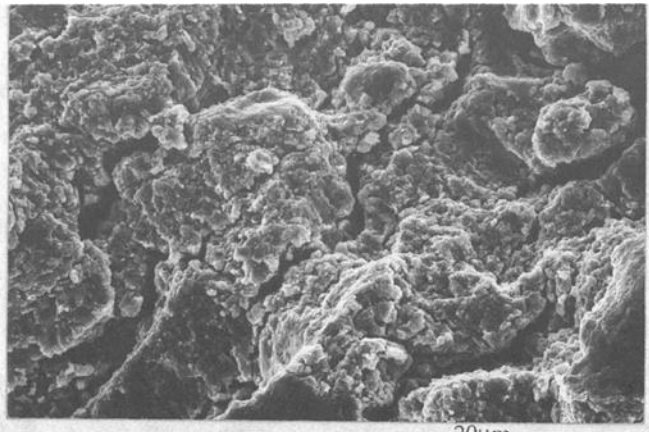

(a) RF-RS-63 Sn-37 Pb under strain controlled fatigue with zero mean strain

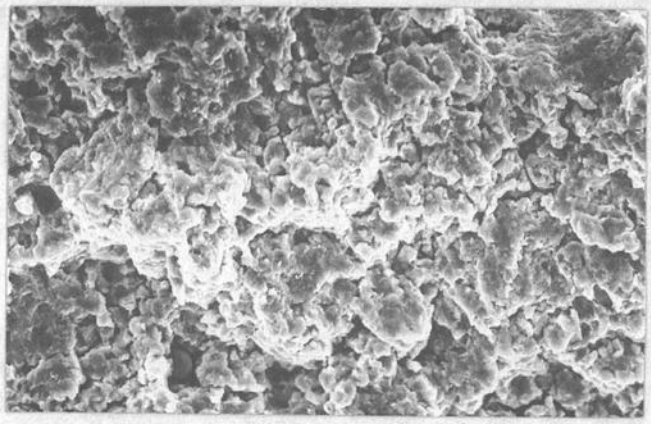

(b) RS-63 Sn-37 Pb under strain controlled fatigue with zero mean strain

FIG. 11—*Intergranular fracture of eutectic solder alloys.*

References

[1] Vaynamn, S., Fine, M. E., and Jeannotte, D. A., "Low-Cycle Isothermal Fatigue Life of Solder Materials," *Solder Mechanics*, D. R. Frear, W. B. Jones, and K. R. Kinsman, Eds., The Minerals, Metals & Materials Society, Warrendale, PA, 1991, p. 155.

[2] Frear, D. R., "Thermomechanical Fatigue in Solder Materials," *Solder Mechanics,* D. R. Frear, W. B. Jones, and K. R. Kinsman, Eds., The Minerals, Metals & Materials Society, Warrendale, PA, 1991, p. 191.

[3] Steinberg, D. S., "Tougher Tests for Military Electronics," *Machine Design,* 25 May 1989, pp. 105–109.

[4] Steinberg, D. S., *Vibration Analysis for Electronic Equipment,* 2nd ed., Wiley, New York, 1988.

[5] Liguore, S., Fields, S., Followell, D., and Perez, R., "Vibration Fatigue of Leadless Chip Carrier Solder Joints," presented at the ASME Winter Annual Meeting, 8–13 Nov. 1992, Anaheim, CA, ASME, New York.

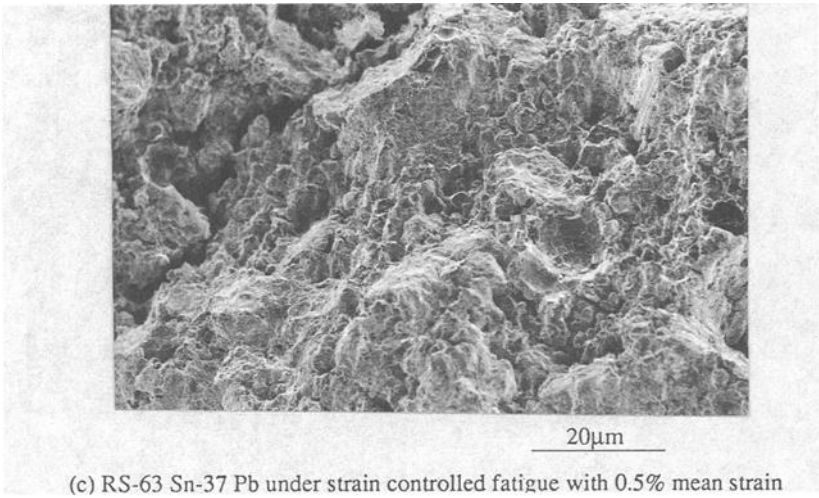

(c) RS-63 Sn-37 Pb under strain controlled fatigue with 0.5% mean strain

FIG. 12—*(Continued)*

[6] Fields, S., Liguore, S., Followell, D., and Perez, R., "High- and Low-Cycle Fatigue Characteristics of Leadless Chip Carrier Solder Joints," presented at the ASME Winter Annual Meeting, 8–13 Nov. 1992, Anaheim, CA, ASME, New York.

[7] Majumdar, S. and Jones, W. B., "How Well Can We Predict the Creep-Fatigue Life of a Well-Characterized Material?" *Solder Mechanics,* D. R. Frear, W. B. Jones, and K. R. Kinsman, Eds., The Minerals, Metals & Materials Society, Warrendale, PA, 1991, pp. 273–360.

[8] Mall, S., Staubs, E. A., and Nicholas, T., "Investigation of Creep/Fatigue Interaction on Crack Growth in a Titanium Aluminide Alloy," *Journal of Engineering Materials and Technology,* Vol. 112, October 1990, pp. 435–441.

[9] ASME Boiler and Pressure Vessel Code, Case N-47-23, Class I, Components in Elevated Temperature Service, Section III, Division I, 1986.

[10] Hales, R., "A Method of Creep Damage Summation Based on Accumulated Strain for the Assessment of Creep-Fatigue Endurance," *Fatigue of Engineering Materials and Structures,* Vol. 6, No. 2, 1983, pp. 121–135.

[11] Majumdar, S. and Maiya, P. S., "A Mechanistic Model for Time Dependent Fatigue," *ASME Journal of Engineering Materials and Technology,* Vol. 102, 1980, pp. 159–167.

[12] Majumdar, S., "Thermomechanical Fatigue of Type 304 Stainless Steel," *ASME PVP,* Vol. 123, 1987, pp. 31–36.

[13] Baik, S. and Raj, R., "Wedge Type Creep Damage in Low Cycle Fatigue," *Metallurgical Transactions,* Vol. 13A, July 1982, pp. 1207–1214.

[14] Solomon, H. D., "Influence of the Cycle Frequency and Wave Shape on the Fatigue Life of Leaded Chip Carrier Printed Wiring Board Interconnections," *Journal of Electronic Packaging, Transactions of the ASME,* Vol. 115, No. 2, June 1993, pp. 173–179.

[15] Weinbel, R. C., Tien, J. K., Pollak, R. A., and Kang, S. K., "Creep-Fatigue Interaction in Eutectic Lead-Tin Solder Alloy," *Journal of Materials Science,* Vol. 22, 1987, pp. 3901–3906.

[16] Weinbel, R. C., Schwarzkopf, E. A., and Tien, J. K., "Effect of Frequency on the Cyclic Creep and Fracture of a Lead-Rich Lead-Tin Solder Alloy," *Scripta Metallurgica,* Vol. 21, 1987, pp. 1165–1168.

[17] Vaynman, S., "Fatigue Life Prediction of Solder Material: Effect of Ramp Time, Hold Time and Temperature," *Proceedings,* 40th ECTC, Las Vegas, EIA, CHMT-IEEE, IEEE Service Center, Piscataway, NJ, May 1990, pp. 505–509.

[18] Knecht, S. and Fox, L. R., "Constitutive Relation and Creep-Fatigue Life Model for Eutectic Tin-Lead Solder," *IEEE Transactions on Components, Hybrids, and Manufacturing Technology,* Vol. 13, No. 2, June 1990, pp. 424–433.

[19] Ross, R. G. Jr., Wen, L. C., Mon, G. R., and Jetter, E., "Solder Creep-Fatigue Interactions with

Flexible Leaded Parts," *Journal of Electronic Packaging,* Vol. 114, No. 2, June 1992, pp. 185–192.

[20] Sastry, S. M. L. et al., "Microstructures and Mechanical Properties of In-Situ Composite Solders," *Proceedings,* NEPCON'92, Anaheim, CA, Cahners Exposition Group, Des Plaines, IL, 1992, pp. 1266–1275.

[21] Fields, R. J., Low, S. R. III, and Lucey, G. K. Jr., "Physical and Mechanical Properties of Intermetallic Compounds Commonly Found in Solder Joints," *Proceedings,* Electronic Components Conference, published by IEEE, 1991, IEEE Service Center, Piscataway, NJ.

[22] Boettner, R. C. and Robertson, W. D., "A Study of the Growth of Voids in Copper During the Creep Process by Measurement of the Accompanying Change in Density," *Transactions of the Metallurgical Society of AIME,* Vol. 221, June 1961, pp. 613–622.

[23] Miller, D. A. and Langdon, T. G., "Density Measurements as an Assessment of Creep Damage and Cavity Growth," *Metallurgical Transactions,* Vol. 11A, June 1980, pp. 955–962.

[24] Kuo, C. G., Sastry, S. M. L., and Jerina, K. L., "Tensile and Creep Properties of In-Situ Composite Solders," *Proceedings,* First International Conference on Microstructure and Mechanical Properties of Aging Materials, P. K. Liaw, R. Viswanathan, K. L. Murty, E. P. Simonen, and D. R. Frear, Eds., The Minerals, Metals & Materials Society, 1993, pp. 409–415.

[25] Kuo, C. G., Sastry, S. M. L., and Jerina, K. L., "Fatigue Deformation of In-Situ Composite Solders," *Proceedings,* First International Conference on Microstructure and Mechanical Properties of Aging Materials, P. K. Liaw, R. Viswanathan, K. L. Murty, E. P. Simonen, and D. R. Frear, Eds., The Minerals, Metals & Materials Society, 1993, pp. 417–423.

[26] Miner, M. A., *Journal of Applied Mechanics,* Vol. 12, 1945, pp. A159–A164.

[27] Sastry, S. M. L., Frear, D. R., Kuo, C. G., and Jerina, K. L., "The Properties of Composite Solders," *The Mechanics of Solder Alloy Wetting and Spreading,* G. F. Yost, F. M. Hosking, and D. R. Frear, Eds., Van Nostrand Reinhold, New York, 1993, pp. 299–352.

[28] Lee, S.-M. and Stone, D. S., "Grain Boundary Sliding in Surface Mount Solders During Thermal Cycling," *Proceedings,* 40th ECTC, Las Vegas, EIA, CHMT-IEEE, IEEE Service Center, Piscataway, NJ, May 1990, pp. 491–495.

[29] Baik, S. and Raj, R., "Mechanisms of Creep-Fatigue Interaction," *Metallurgical Transactions,* Vol. 13A, July 1982, pp. 1215–1221.

[30] Baik, S. and Raj, R., "Creep-Fatigue Interaction in OFHC-Copper," *Scripta Metallurgica,* Vol. 17, 1983, pp. 1087–1090.

David L. McDowell,[1] *Matthew P. Miller,*[1] *and Del C. Brooks*[1]

A Unified Creep-Plasticity Theory for Solder Alloys

REFERENCE: McDowell, D. L., Miller, M. P., and Brooks, D. C., **"A Unified Creep-Plasticity Theory for Solder Alloys,"** *Fatigue of Electronic Materials, ASTM STP 1153,* S. A. Schroeder and M. R. Mitchell, Eds., American Society for Testing and Materials, Philadelphia, 1994, pp. 42–59.

ABSTRACT: Sn-Pb solders exhibit creep-plasticity interaction and significant strain-rate dependence at operating temperatures of electronic circuits. A major problem is fatigue and creep-fatigue interaction due to thermomechanical cycling. Reversed plasticity, creep, and creep-plasticity interactions dominate the behavior for these types of histories. Furthermore, thermal softening plays a strong role in the time dependence of the mechanical behavior. However, classical forms of decoupled plasticity and creep theories have been shown to be quite inferior for modeling cyclic plasticity, creep, and interaction effects. The goals of this study were to: (a) develop a thermomechanical unified creep-plasticity model which can characterize the response of solders, and (b) characterize a selected solder alloy through mechanical testing and correlation with the model across a range of strain rates, temperatures, aging times, and loading-unloading conditions.

Solder alloys in general are mechanically soft and are employed routinely at very high homologous temperatures. The microstructure is often unstable at normal circuit board operating temperatures and the extent of alteration to the microstructure is a function of the applied stress or strain, temperature, etc. Many alloys recrystallize below 77°F (25°C) and therefore can change with time at room temperature.

A program of characterization involving tension tests at various temperatures and strain rates, creep tests, cyclic loading tests, and tension tests after prior high-temperature exposure was pursued to develop a broad-based understanding of the behavior of eutectic Sn-Pb solder, the most commonly used industrial solder alloy. A model for thermomechanical temperature- and rate-dependent behavior of metallic alloys has been developed. Many of the typical, complex behaviors of solders can be addressed with this model, including temperature dependence and strain-rate dependence, creep-plasticity interaction, viscous cyclic strain ratchetting, softening effects due to static thermal recovery, and potential effects of aging (microstructural changes due to exposure at high temperature).

KEYWORDS: unified, creep, plasticity, state variable, rate dependence, temperature dependence, cyclic loading

Some Important Features of Solder Behavior

Solder joints are subjected to a combination of thermal and mechanical cycling. Unfortunately, tin-lead (Sn-Pb) solders exhibit among the most complex inelastic behaviors of high-temperature materials due to the high homologous temperatures of typical applications. As a result, use of classical plasticity and creep models is of very questionable accuracy, particularly for thermomechanical cycling. Some important behaviors include

[1]Professor, graduate student, and undergraduate student, respectively, George W. Woodruff School of Mechanical Engineering, Georgia Institute of Technology, Atlanta, GA 30332-0405.

1. Breakdown of power law strain-rate dependence of inelastic flow.
2. Creep-plasticity interaction.
3. Microstructural aging effects.

Power Law Breakdown

Many studies and analyses reported in the literature concerning solders employ a simple power law creep equation of the uniaxial form

$$\dot{\epsilon}^c = A_0 \exp\left(\frac{-Q}{R_G T}\right) \sigma^n \tag{1}$$

where A_0 and n are creep constants, Q is the activation energy for creep, R_G is the universal gas constant, $\dot{\epsilon}^c$ is the creep strain, σ is the applied stress, and T is the absolute temperature. Such a model provides a useful idealization of the minimum or steady-state creep rate under constant stress conditions as a function of temperature, but is seriously limited in applicability. First, it is well-known that Sn-Pb solders exhibit a creep exponent, n, which increases with the applied stress. For example, for a eutectic Sn-Pb, $n \approx 3$ for $\dot{\epsilon}^c < 10^{-5}\ s^{-1}$ and increases to $n \approx 7$ for $\dot{\epsilon}^c \approx 10^{-3}\ s^{-1}$ [*1*]. This behavior is observed for virtually all solder compositions and is typical of other metallics at high homologous temperature. In contrast to Eq 1, unified creep-plasticity frameworks permit a straightforward description of this phenomenon.

Creep-Plasticity Interaction

Treatment of cyclic plasticity minimally requires introduction of a kinematic hardening variable to represent the Bauschinger effect during load reversal. However, in the regime of viscous deformation, creep behavior is intimately linked to prior and concurrent plasticity and vice versa. For example, the creep rate is affected by the position on a cyclic hysteresis loop in addition to the stress level. Creep of virgin material differs from creep of cycled material at the same stress level, in general. Classical decoupled creep and plasticity models, although temperature dependent, cannot capture this interaction effect without ad hoc modifications.

Microstructural Aging Effects and Temperature-Dependence

Solders typically exhibit significant changes in mechanical behavior after periods of high-temperature exposure. This is particularly true of initially fine-grained material which undergoes grain growth and/or grain boundary migration [*2*]. Such aging effects are not taken into account in most isothermal tensile, creep, and cyclic loading experiments. Moreover, the only means of modifying classical theories of plasticity and creep is by introducing time- and temperature-dependent material parameters, which is in many respects intractable.

Unified Creep-Plasticity Models

Classical models for simultaneous creep and plasticity assume that the inelastic strain rate is composed of additive contributions from decoupled creep and plasticity, i.e.

$$\mathbf{D}^n = \mathbf{D}^p + \mathbf{D}^c \tag{2}$$

where $\mathbf{D}^n$ is the inelastic rate of deformation tensor comprised of the time-independent plastic strain rate, $\mathbf{D}^p$, and the time-dependent creep strain rate, $\mathbf{D}^c$. State variable or unified creep-plasticity (UCP) models effectively address these deficiencies by assuming that plasticity and creep processes are intrinsically coupled. In this case, the inelastic strain rate is specified by the flow rule or kinetic equation

$$\mathbf{D}^n = \mathbf{G}(\mathbf{s},\mathbf{x},T) \tag{3}$$

where s is the deviatoric stress tensor, T is absolute temperature, and x represents a set of internal state variables which reflect the evolving state of the material, i.e.

$$\overset{\nabla}{\mathbf{x}} = \mathbf{f}(\mathbf{s},\mathbf{x},T) \tag{4}$$

where the symbol $\overset{\nabla}{}$ pertains to an appropriate time derivative necessary to preserve objectivity (e.g., Jaumann rate).

Examples of the set $\mathbf{x}$ include backstress, $\boldsymbol{\alpha}$, representative of directional internal stresses, isotropic hardening variable, R, representative of overall dislocation density, and drag stress, $\mathbf{D}$, which attenuates the effective dislocation force versus velocity relationship. Other variables (e.g., damage) may also be introduced if desired [*3,4*]. The framework of the evolution equations is the key to physical consistency and accuracy of the approach. A physically based framework for evolution of internal variables under combined creep-plasticity deformation of metals is of the form

$$\overset{\nabla}{\mathbf{x}} = H\dot{p}\mathbf{N} - R_d(\mathbf{x})\dot{p}\mathbf{x} - R_s(\mathbf{x}) + \frac{\mathbf{x}}{H}\frac{\partial H}{\partial T}\dot{T} \tag{5}$$

where

$$\dot{p} = \sqrt{\mathbf{D}^n:\mathbf{D}^n} = \|\mathbf{D}^n\| \tag{6}$$

Functions H, R_d, and R_s may, of course, depend on temperature as well. The first term on the right-hand side in Eq 5 represents direct hardening associated with the interaction of dislocations with obstacles and with other dislocations (workhardening); $\mathbf{N}$ is the unit vector in the direct hardening direction. The second term represents dynamic recovery, associated with dislocation cross-slip, creation of dislocation cell walls, and ladder and vein dislocation substructures (lower energy configurations) [*5,6*]. The third term represents static thermal recovery, associated with diffusion processes. Description of rate-independent plasticity predominately involves the first two terms, whereas creep involves a competition of the first two terms with the third term. The last term involves the temperature rate effect of rapid accommodation to the isothermal response at each temperature in a nonisothermal history [*7,8*].

Unified creep-plasticity models of this sort have enjoyed widespread development and application to analysis of high-temperature power plant and gas turbine engine components [*9–15*]. The authors are aware of some recent efforts to apply such approaches to solder [*15,16*], but the literature is surprisingly scarce in this regard. In the next section, we will introduce a specific form of this class of models and will demonstrate applicability for correlation of the strain rate- and temperature-dependent deformation behavior of two Sn-Pb solder alloys.

Two Backstress Thermoviscoplasticity Model

Following McDowell [*17*], we introduce a thermoviscoplastic internal state variable model consistent with the foregoing framework. Many of the typical, complex behaviors of solders can be described with this model, including rate dependence, cyclic hysteresis loops, temperature dependence, and thermal softening with exposure at relatively high homologous temperatures. The descriptive features of the model include:

1. Temperature dependence and strain-rate dependence.
2. Creep-plasticity interaction.
3. Competition of hardening and dynamic/static recovery effects.

In this approach, state variables are introduced to represent the internal state of the material at each stage of deformation. These internal or state variables evolve in a manner that reflects both hardening processes that strengthen the material and recovery processes that soften the material. In the absence of consideration of damage effects on deformation, we introduce a minimal set of state variables: a tensorial variable, α, and scalar variables R and D. Backstress $\boldsymbol{\alpha}$ represents directional deformation-induced hardening effects (kinematic hardening), while R and D represent isotropic hardening effects. Temperature dependence resides both in the expression for the rate of inelastic strain (flow rule) and the evolution laws for the internal variables. Likewise, rate dependence is predominately related to the flow rule, but also arises from static thermal recovery (e.g., annealing) terms in the evolution laws of internal variables. As will be demonstrated, this simple model structure can describe both creep and much higher strain rate plasticity behaviors for solder alloys.

The temperature-dependent viscoplastic flow rule is given by

$$\mathbf{D}^n = \sqrt{\frac{3}{2}} A \left(\frac{\langle S_v \rangle}{D}\right)^n \exp\left(B\left(\frac{\langle S_v \rangle}{D}\right)^{n+1}\right) \Theta \mathbf{N} \tag{7}$$

where $\mathbf{D}^n$ is the inelastic rate of deformation tensor (strain rate), $S_v = (3/2)^{1/2}\|\mathbf{s} - \boldsymbol{\alpha}\| - R$ is the viscous overstress, $\mathbf{s}$ is the deviatoric stress defined by $\sigma - 1/3\sigma_{kk}\mathbf{I}$, $\boldsymbol{\alpha}$ is the backstress, R is the yield strength, and D is the drag strength; Θ is a diffusivity parameter defined in Ref *18*

$$\Theta = \exp\left(\frac{-Q}{R_G T}\right) \quad \text{for} \quad T \geq \frac{T_m}{2} \tag{8}$$

$$\Theta = \exp\left(\frac{-2Q}{R_G T_m}\left[\ln\left(\frac{T_m}{2T}\right) + 1\right]\right) \quad \text{for} \quad T \leq \frac{T_m}{2} \tag{9}$$

where Q is the activation energy for viscous flow, T_m is the absolute melting point temperature, and N is the direction of inelastic strain rate, defined by

$$N = \frac{\mathbf{s} - \boldsymbol{\alpha}}{\|\mathbf{s} - \boldsymbol{\alpha}\|} \tag{10}$$

In Eq 7, the Macauley brackets $\langle \quad \rangle$ ($\langle G \rangle = G$ if $G > = 0$, $\langle G \rangle = 0$ otherwise) are used to introduce a yield function of von Mises form in terms of viscous overstress, S_v. The flow

rule in Eq 7 approaches power law creep in the limit as the overstress becomes small and approximates a hyperbolic sine dependence of the strain rate-dependence [*8,17*]. Equation 7 leads to an effective exponent, n_{eff}, in a power law expression [*8*] in terms of (S_v/D) given by

$$n_{eff} = n + B(n+1)\left(\frac{\langle S_v \rangle}{D}\right)^{n+1} \tag{11}$$

where $n_{eff} = \partial \ln \dot{p}/\partial \ln (S_v/D)$. Clearly, $n_{eff} = n$ at low viscous overstress (or applied stress) levels. It is important to note that the strain rate in Eq 7 is a function of the overstress, S_v, rather than the applied stress. Backstress α serves a primary role in establishing anisotropy (Bauschinger effect) essential for the description of the stress-strain response under cyclic loading conditions. Moreover, α introduces an interaction of prior creep deformation with subsequent higher strain rate plasticity and vice versa. The same is true of R and D if these variables are assigned evolution equations that depend on loading history.

We decompose $\boldsymbol{\alpha}$ into two components [*17,19–21*], i.e., $\boldsymbol{\alpha} = \boldsymbol{\alpha}^s + \boldsymbol{\alpha}^*$. The short-range component governs workhardening just after initial yielding, while the long-range component governs the larger strain response. The yield strength, R, is composed of a temperature-dependent component, R^0, and a component, R^{iso}, dependent on the loading history, i.e., $R = R^0(T) + R^{iso}$. The short range backstress is assumed to evolve according to

$$\overset{\nabla}{\boldsymbol{\alpha}}{}^s = C(b\mathbf{N} - \boldsymbol{\alpha}^s)\dot{p} + \left[\omega \frac{\boldsymbol{\alpha}^s}{b}\frac{\chi}{\bar{\chi}}\frac{\partial \bar{\chi}}{\partial T} + \frac{\boldsymbol{\alpha}^s}{C}\frac{\partial C}{\partial T} + \frac{\boldsymbol{\alpha}^s}{b}\frac{\partial b^0}{\partial T}\right]\dot{T} - Cb\Omega^s(\boldsymbol{\alpha}^s)\Theta\boldsymbol{\alpha}^s \tag{12}$$

and the rate of long-range backstress is assumed as

$$\overset{\nabla}{\boldsymbol{\alpha}}{}^* = H^*\dot{p}\mathbf{N} + \frac{\boldsymbol{\alpha}^*}{H^*}\frac{\partial H^*}{\partial T}\dot{T} - H^*\Omega^*(\boldsymbol{\alpha}^*)\Theta\boldsymbol{\alpha}^* \tag{13}$$

Here, $b = b^0(T) + b^{iso}$ is the saturation level of the short range backstress; b^{iso} depends on the loading history, while b^0 is purely temperature dependent. In Eqs 12 and 13, χ is the isotropic hardening variable; C, H^*, and b^0 are temperature-dependent functions, and Ω^s and Ω^* are static thermal recovery functions representative of recovery or "annealing" effects which occur in order to minimize the free energy of dislocation structures. When recovery effects overwhelm hardening, net material softening can occur. Power law forms for the static thermal recovery functions are given by

$$\Omega^s(\boldsymbol{\alpha}^s) = C^s(\alpha^s_{ij}\alpha^s_{ij})^{M^s/2}, \quad \Omega^*(\boldsymbol{\alpha}^*) = C^*(\alpha^*_{ij}\alpha^*_{ij})^{M^*/2} \tag{14}$$

The isotropic hardening variable χ, representative of the increase of dislocation density, evolves according to

$$\dot{\chi} = \mu(\bar{\chi} - \chi)\dot{p} + \frac{\chi}{\bar{\chi}}\frac{\partial \bar{\chi}}{\partial T}\dot{T} - \mu\bar{\chi}\Omega^{\chi}(\chi)\Theta \tag{15}$$

where μ is independent of temperature. The factor ω $(0 < \omega < 1)$ partitions the hardening between the b^{iso} and R^{iso} according to $b^{iso} = \omega\chi$ and $R^{iso} = (3/2)^{1/2}(1 - \omega)\chi$ for $\chi(0) = 0$. Parameter $\bar{\chi}$ represents the saturation level for isotropic hardening. The isotropic hardening independent component, $R^0(T)$, includes strengthening factors such as solid solution strengthening, intrinsic lattice friction, etc. which are independent of dislocation density.

The temperature rate terms contribute to evolution of α and χ even for stresses within the yield surface and are generally necessary to model nonisothermal behavior.

The saturation or asymptotic value of χ is given by

$$\bar{\chi} = \chi_0 \Sigma(T), \quad \Sigma(T) = A_1 - A_2 T + A_3 \exp(-A_4 T) \tag{16}$$

where χ_0 and $A_1 - A_4$ are constants.

Taking into account the variation of elastic constants with temperature, the linearized thermohypoelastic (rate-type) expression is given by

$$\overset{\nabla}{\boldsymbol{\sigma}} = \mathbf{C} : (\mathbf{D} - \mathbf{D}^n) + \mathbf{C}^{-1} : \boldsymbol{\sigma} : \frac{\partial \mathbf{C}}{\partial T} \dot{T} \tag{17}$$

Equation 17 may be separated into deviatoric and hydrostatic stress rates for an isotropic elastic material according to

$$\overset{\nabla}{\mathbf{s}} = 2G \left(\mathbf{D}' - \mathbf{D}^n - \frac{\mathbf{s}}{2} \frac{\partial G^{-1}}{\partial T} \dot{T} \right) \tag{18}$$

$$\dot{\sigma}_{kk} = \frac{E}{1 - 2\nu} \left\{ D_{kk} - 3 \left[\sigma_{kk} \frac{\partial}{\partial T} \left(\frac{1 - 2\nu}{3E} \right) + (T - T_0) \frac{\partial \alpha^T}{\partial T} \right] \dot{T} - 3\alpha^T \dot{T} \right\} \tag{19}$$

where $\mathbf{D}'$ is the deviatoric part of $\mathbf{D}$, and G, E, and ν are the temperature-dependent elastic shear modulus, Young's modulus, and Poisson's ratio, respectively. The temperature-dependent coefficient of thermal expansion is denoted by α^T and should not be confused with backstress, $\boldsymbol{\alpha}$. The presence of temperature rate terms in Eqs 17–19 in addition to the thermal strain rate modify the hypoelastic expression to ensure path independence in $(\boldsymbol{\sigma}, T)$ space. Here, T_0 is a reference temperature for the thermoelastic linearization, i.e., the so-called stress free temperature.

To summarize, the key elements of the model include (1) the flow rule, (2) the kinematic hardening laws for short- and long-range backstresses, and (3) the isotropic hardening law, partitioned between the yield strength, R, and the amplitude of the short-range kinematic hardening variable. All of these equations are significantly coupled, rendering parameter estimation nontrivial. In general, nonlinear parameter estimation schemes of numerical nature designed to minimize some error norm based on comparison with experimental data are suspect, particularly in the usual case of a limited dataset. Since the equations of the theory are highly nonlinear, it follows that certain parameters are sensitive to the variation of others, resulting in potentially unstable trajectories for numerical error minimization schemes for the constants, depending on how far the initial guess is from the final iterate. In the next section, we will describe an essentially noniterative procedure for determining the constants of the theory for Sn-Pb solder to within first order accuracy. This procedure makes liberal use of the link between the different terms in the equations for state variable evolution and distinct regimes of the stress-strain curve, rate-dependence, etc.

Correlation of Experimental Data

In this study, we present correlations of the preceding model with data for 61Sn-39Pb and 62Sn-36Pb-2Ag solder alloys. As these two alloys have somewhat different initial strengths, their model constants differ. Hence, they will be presented distinctly.

Alloy I

Tension test data conducted at four strain rates and five temperatures ranging from −55 to 125°C were available from Adams [*22*] as reported by Busso et al. [*16*] for 61Sn-39Pb near-eutectic solder. Moreover, previous creep studies on Sn-Pb solder had established that the power law creep exponent takes on the value $n = 3$ at low stresses and low steady state creep rates corresponding to grain boundary sliding-controlled deformation [*1,23,24*] and increases exponentially at higher inelastic strain rates.

Here we summarize the procedure used in determining the model constants based on this data. Since all variables of the model have distinct interpretation in terms of physical processes, it is possible to determine the constants of the theory without numerical intervention or iteration, at least to first order. First, it was determined by inspection that the yield strength, R, was relatively small and did not evolve, based on deviation from linearity across a wide range of temperatures; hence, a relatively small value of $R = R^0(T) = 3$ MPa was selected, along with $R^{iso} = 0$ ($\omega = 1$). Next, focus was placed on the nonlinear initial yielding part of the tension test curves to determine transient material workhardening; combined with the cyclic hysteresis loop data of Busso et al. [*16*], it was determined that the transient hardening was essentially entirely kinematic. In addition, cyclic stability was assumed as a first approximation based on the observations of Busso et al. [*16*]; hence, μ is inconsequential, leading to $\chi = \chi(0) = R^{iso} = b^{iso} = 0$ and $b = b^0(T)$. Another observation from the data was that the short range, transient stress-strain behavior associated with initial yielding was of approximately the same duration of inelastic strain for all temperatures and strain rates; accordingly, rate coefficient C in the short-range kinematic hardening law was assessed from the duration of the short-range transient (approximately 1.5 to 2% cumulative inelastic strain). Since this duration of transient behavior depended only weakly on temperature, the selection of a constant C value was reasonable. Saturation level $b^0(T)$ was then determined from the initial yielding transient, assuming no static thermal recovery for the short range backstress; hence $C^s = 0$ and M^s is irrelevant.

The next step was to describe the long-range backstress workhardening rate in the asymptotic regime (i.e., plastic strain levels between 2 and 5%) at the higher strain rates to determine H^* as a function of temperature. Subsequently, the static thermal recovery constants C^* and M^* were determined to fit the decay of the long-range hardening rate over the range of strain rates and temperature. It should be noted that the long-range backstress static thermal recovery term contributes significantly to modeling the primary creep response and could be determined with additional precision by creep experiments if such data were available. In the present formulation, the static thermal recovery terms introduce a rate dependence of the backstress under steady-state creep conditions achieved upon balance between hardening and recovery processes. Finally, the constants A, B, the drag stress, D, and the activation energy, Q, were determined by fitting the overstress versus strain rate- and temperature dependence of tension test data at a strain level just beyond the initial yielding transient (approximately 2% plastic strain) since the evolution equation for α^s was previously established and R has been assigned. Although the activation energy for self-diffusion, Q_s, is a well-known physical constant, the additional temperature dependencies of the model parameters such as $b^0(T)$ and the appearance of the overstress in the flow rule introduce an effective stress-dependent activation energy; hence, Q and Q_s do not necessarily equate.

It should be emphasized that numerical integration was necessary within the framework of this algorithm only at the stage at which static thermal recovery constants were determined. Consequently, the fit to data is expected to be of first order accuracy since error norms were not iteratively minimized in the fitting process. The model constants from this procedure are summarized in Table 1.

TABLE 1—*Constants for Alloy I.*

Constants
$n = 3, A = 1.1 \times 10^3\ s^{-1}, B = 0.001, D = 4$ MPa
$Q = 50$ kJ/mol, $T_m = 468$ K, $R_G = 8.314 \times 10^{-3}$ kJ/mol-K
$C^s = 0, C^* = 1$ MPa^{-6}/s, $M^* = 5$
$R^{iso} = 0$ MPa, $R^0 = 3$ MPa ($\omega = 1, \chi = 0$)
$b^{iso} = 0$ MPa, $b^0(T) = 294 \exp(-0.012T)$ MPa, $C = 250$
$H^* = 13 + 2500 \exp(-0.0132T)$ MPa
$G = 24\,280 - 29T$ MPa, $\nu = 0.37$
$\alpha^T = 24 \times 10^{-6}$ °C^{-1}

The correlation of the tension test data of Adams is shown in Figs. 1 through 4 for various strain rates and temperatures. In all cases, solid lines represent the model results. Clearly, the description by the model is accurate for engineering purposes over the full range of temperatures and strain rates encountered. Figure 5 demonstrates the prediction of the model at cyclically stable conditions for shear strain cycling at several amplitudes at 0.01 Hz and 25°C for another eutectic solder alloy reported by Busso et al. [*16*]. The nonlinear transient work-hardening behavior is represented by the evolution of the short range backstress. Even though the actual alloy exhibited a slight degree of cyclic softening, the predictions in Fig. 5 are reasonable.

Alloy II

Tensile, cyclic creep, and constant load creep tests were conducted in the Mechanical Properties Research Laboratory at Georgia Tech across a range of temperatures and strain

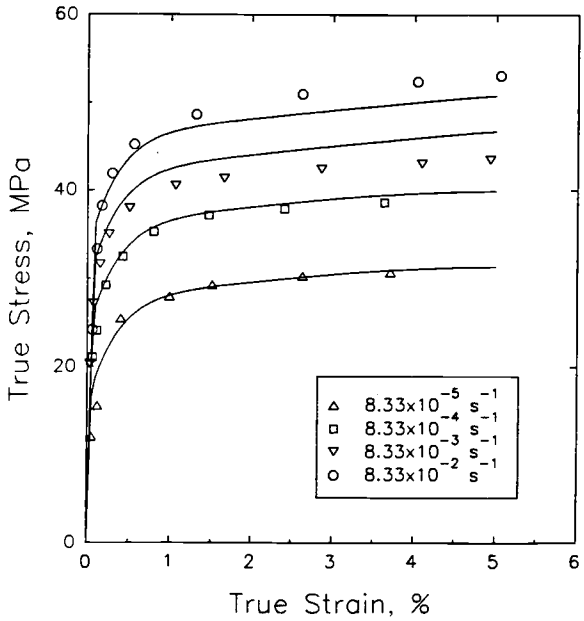

FIG. 1—*Model correlations with data for monotonic uniaxial stress-strain behavior for four strain rates at 22°C (Alloy I).*

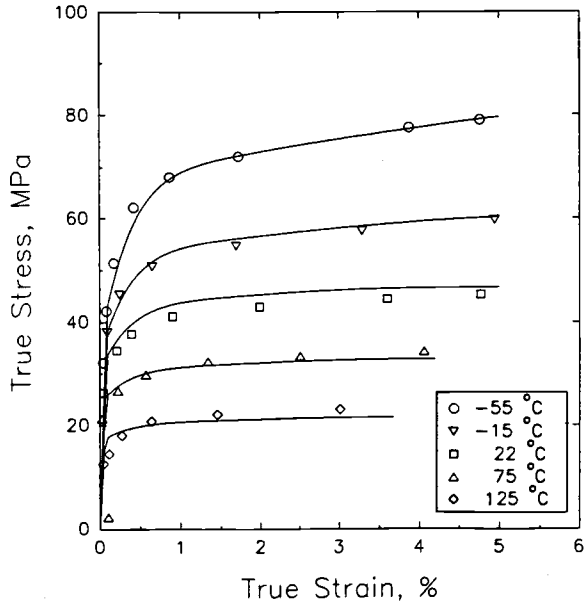

FIG. 2—*Model correlations with data for monotonic uniaxial stress-strain behavior for five temperatures at a strain rate of* $1.67 \times 10^{-2}\ s^{-1}$ *(Alloy I).*

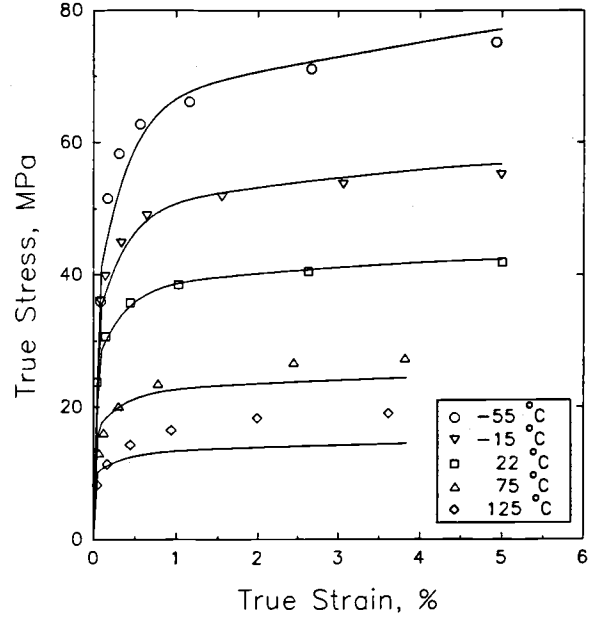

FIG. 3—*Model correlations with data for monotonic uniaxial stress-strain behavior for five temperatures at a strain rate of* $1.67 \times 10^{-3}\ s^{-1}$ *(Alloy I).*

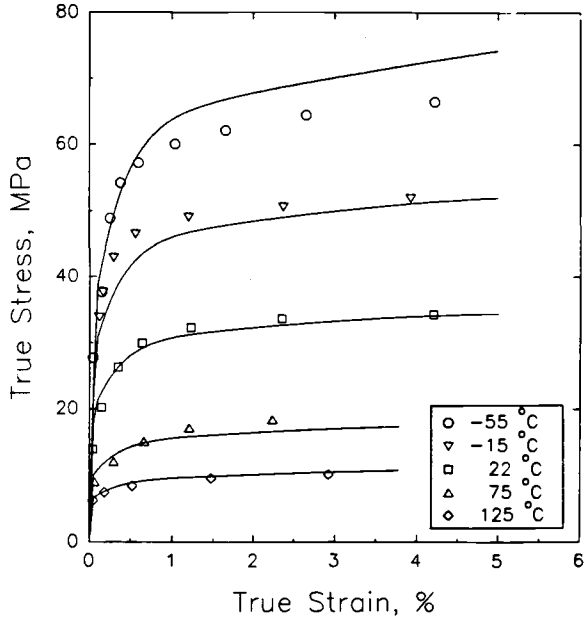

FIG. 4—*Model correlations with data for monotonic uniaxial stress-strain behavior for five temperatures at a strain rate of* $1.67 \times 10^{-4}\ s^{-1}$ *(Alloy I).*

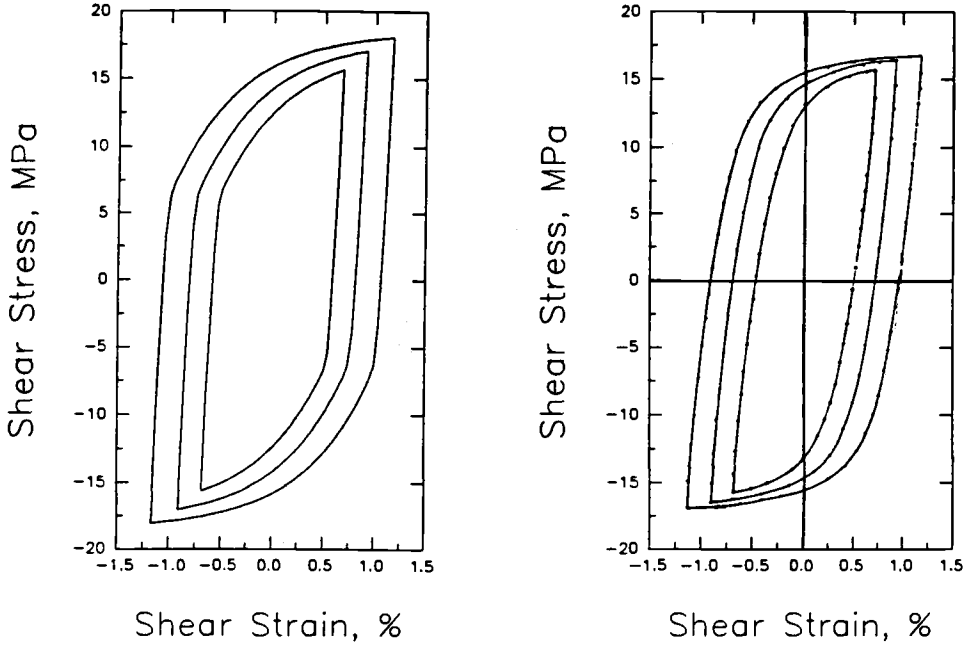

FIG. 5—*Comparison of model predictions (left) with experimental results (right) for cyclically stable uniaxial stress-strain behavior (Alloy I) for several strain amplitudes at 0.01 Hz and 25°C.*

rates on a 62Sn-36Pb-2Ag solder alloy obtained in ingot form and machined into uniaxial specimens as shown in Fig. 6.

This solder alloy exhibited a consistently higher initial flow stress than those of Adams [*22*] or Busso et al. [*16*]. This is likely attributed to the addition of silver to the alloy [*25*] since the melting point and moduli are somewhat elevated in this case. Strengthening effects may be anticipated on the basis of dislocation arguments [*26*]. Neglecting the slight differences in melting point and moduli between Alloys I and II, all model parameters for Alloy II were taken to be identical to those reported in Table 1 as a first approximation with the exception that $R = 9$ MPa, $A = 5 \times 10^3\ s^{-1}$, and $C^* = 600\ MPa^{-6}/s$ as determined by matching both the creep and tension test results just following the initial yielding transient. Without adjusting $H^*(T)$, the higher value of static thermal recovery constant C^* results in more rapid saturation of the long-range backstress at a given strain rate, but this is not of particular concern in this illustrative study.

Figures 7 through 9 show the model correlation for Alloy II for the tension tests at two strain rates at several temperatures and four creep tests at 20°C. The tension tests were conducted in stroke (displacement) control, and hence the initial yielding portion was somewhat inaccurately characterized; furthermore, the strain rate varies somewhat during the initial transient workhardening response, then conforms very closely to the values indicated during the asymptotic plastic flow at strains exceeding 1% or so. Stroke data were correlated with the output of an extensometer mounted on the gage section at room temperature to determine the calibration factor for conversion from stroke to strain. The scatter of stress data in the tension tests may be attributed to test machine noise at the very low load levels of these experiments; the minimum calibrated range of the load cell [500 lb (2225 N)] used in these experiments was an order of magnitude higher than the loads applied to the specimens, so the voltage output signal was near its peak resolution capability. Conse-

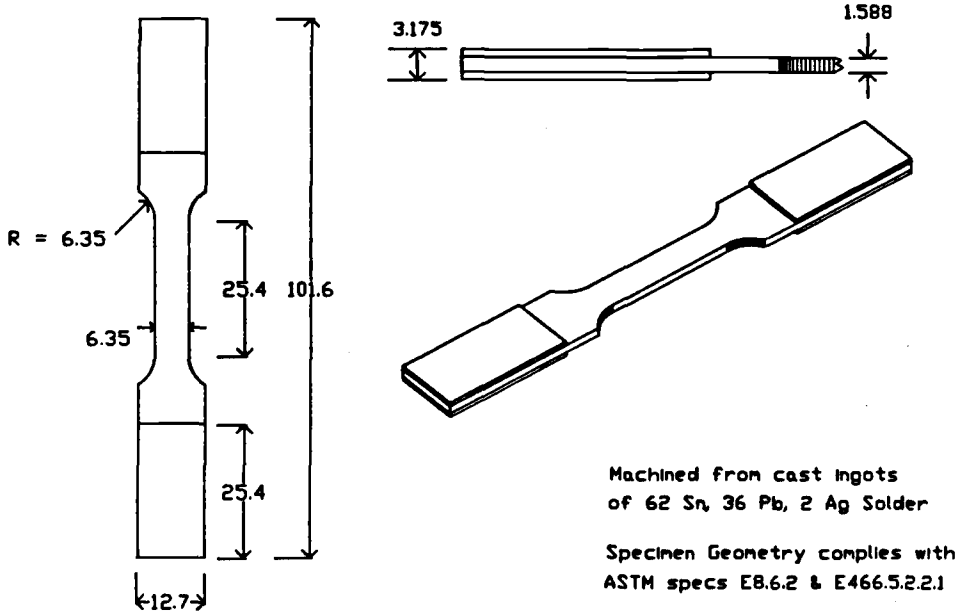

FIG. 6—*Specimens for Alloy II.*

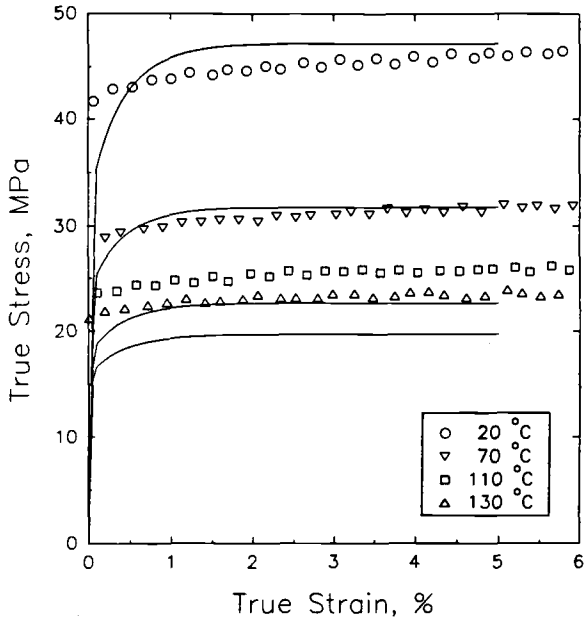

FIG. 7—*Model correlations with data (Alloy II) for stroke-controlled, monotonic uniaxial stress-strain behavior for four temperatures at a strain rate of approximately* 10^{-2} s^{-1}.

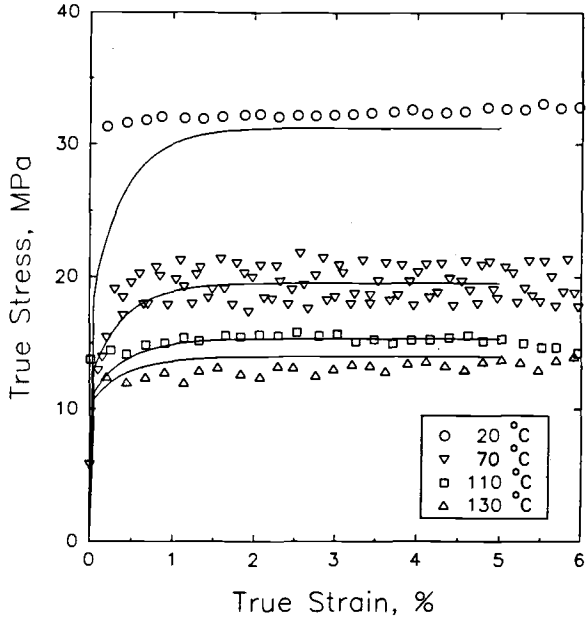

FIG. 8—*Model correlations with data (Alloy II) for stroke-controlled, monotonic uniaxial stress-strain behavior for four temperatures at a strain rate of approximately* 10^{-4} s^{-1}.

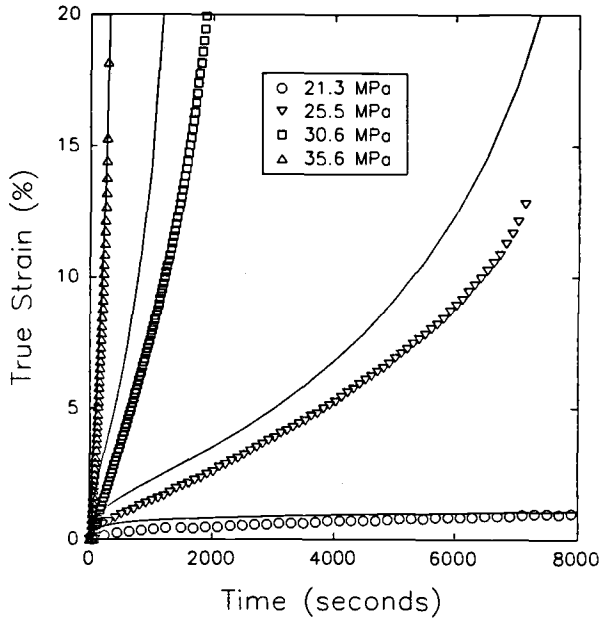

FIG. 9—*Model correlations with data (Alloy II) for strain accumulation during constant load creep at four stress levels at 20°C.*

quently, electronic noise between discrete voltage levels was noticeable, superimposed upon the data. No filtering or smoothing was performed on the data reported in these figures.

The apparent tertiary creep behavior observed in Fig. 9 is due to the fact that the creep tests were constant load, not constant stress, and the true stress increased with cumulative creep strain. The capture of this trend is indicative of the capability of the model to describe viscous behavior over a range of strain rates.

Figure 10 shows the correlation achieved with an experiment involving a two-step sequence of load-controlled cycling at 0.2 MPa/s. The observed ratchetting response has a significant contribution from viscous creep and is well-predicted by the model; integration of the model at much higher stress rates produced significantly less ratchet strain accumulation. Confirmation of model performance for both load- and strain-controlled experiments is very relevant since actual solder joints are subjected to an intermediate control condition.

Aging Effects

Aging effects or microstructural changes due to high-temperature exposure are governed by diffusion kinetics. Aging processes may include irreversible mechanisms such as formation of carbides or intermetallics, precipitate coarsening, grain growth, etc. Solders may exhibit strong temperature path history and aging effects through changes of phase morphology and grain size. However, when the temperature range does not produce an unstable microstructure, behavior approaching temperature path history independence of the inelastic and elastic responses may be observed [*17,27*]. Thus, the presence of temperature rate terms in Eqs 12 through 15 should be regarded as essential for a general theory [*8,17,27*]. Microstructural aging effects may be admitted by additional irreversible evolution of existing state variables such as α and χ, the drag stress, D, or by introducing new state variables descriptive of these effects.

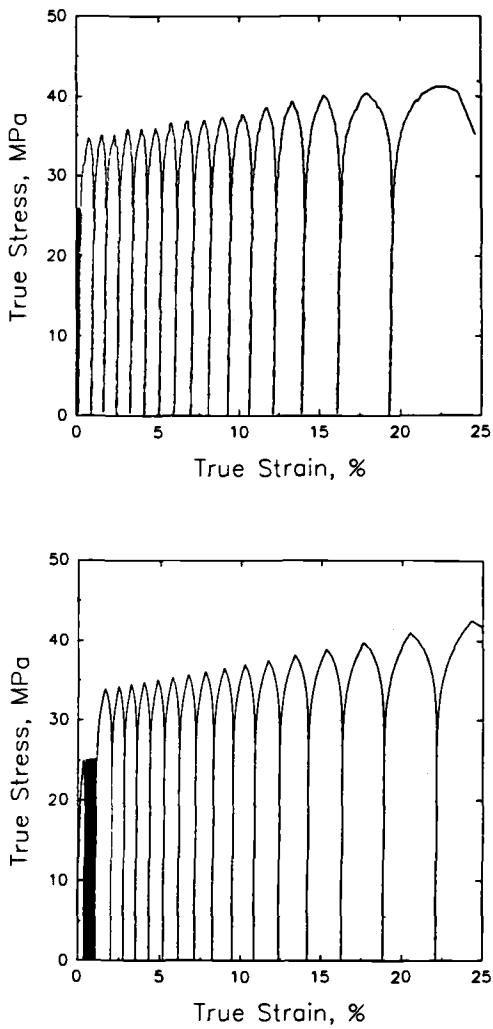

FIG. 10—*Two-step, load-controlled sequence of cyclic loading* ($R = P_{min}/P_{max} = 0$) *at 20°C and an initial loading rate of 0.2 MPa/s (Alloy II). Experimental results (top) and model results (bottom) are comparable.*

Tension tests were conducted at both 20 and 110°C on specimens subjected to 1 and 10 h of stress-free aging at 145°C to assess the influence of microstructural changes with exposure time at elevated temperature. The results are presented in Figs. 11 and 12 for maximum strains on the order of those of interest in cyclic applications. In all cases, a creep strengthening or hardening effect was observed, with a substantial increase in flow stress compared to the virgin material. The kinetics of the aging process are observed to be relatively rapid since little difference is observed between 1 and 10-h results, particularly at lower strain rates. Although further study is required, coarsening of grains is likely responsible for the creep strengthening due, for example, to the grain-size dependence of grain boundary sliding [*1,23,24*] and diffusional creep processes. The current model can be modified to admit

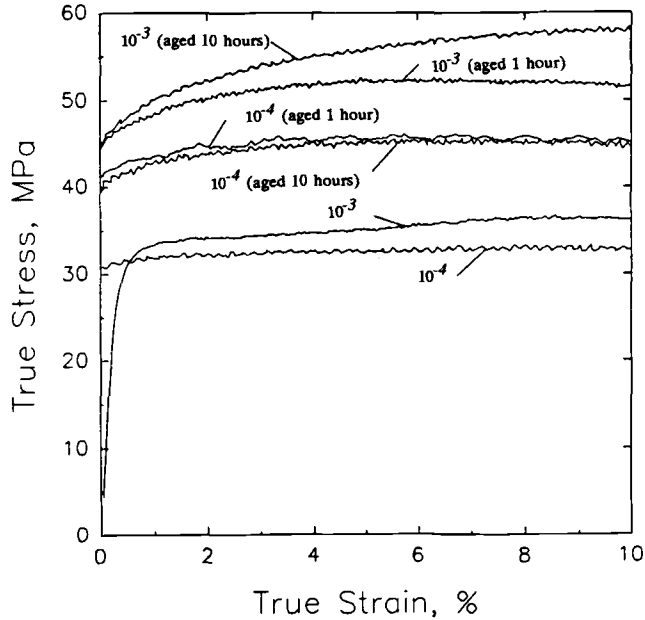

FIG. 11—*Tensile tests at 20°C on specimens aged at 145°C (Alloy II). Approximate strain rates and aging times are indicated. The reference (unaged) stress-strain curves are the lowest two curves.*

coarsening kinetics, although the quantitative link between deformation hardening and coarsening kinetics has not yet been well established experimentally.

For example, we may suggest possible forms for isothermal aging effects on the drag strength or saturation level of isotropic hardening, e.g.

$$D = D^0(T) + D_A(T,t), \quad D_A = D_s \exp\left(\frac{-Q_a}{R_G T}\right) t^{\beta} \tag{20}$$

$$\bar{\chi} = \chi^0(T) + \chi_A(T,t), \quad \chi_A = \chi_s \exp\left(\frac{-Q_a}{R_G T}\right) t^{\beta} \tag{21}$$

where Q_a is the activation energy for diffusive microstructural rearrangement, and χ_s and D_s are constants. Exponent β denotes the time dependence of the aging phenomena. More complex forms, including evolutionary forms, could be introduced. Evolution of D affects strain rate dependence, while evolution of χ primarily affects isotropic strengthening at all strain rate levels.

Discussion and Conclusions

Based on the reasonable correlations achieved for Alloy II with only minor modification of the constants for Alloy I, allowing for the different initial condition (and slight difference of composition) of the former, the correlative capability of the existing framework appears to be acceptable for engineering calculations of solder joints subjected to combined thermal and mechanical loading conditions. It is likely that the quality of the correlation achieved for

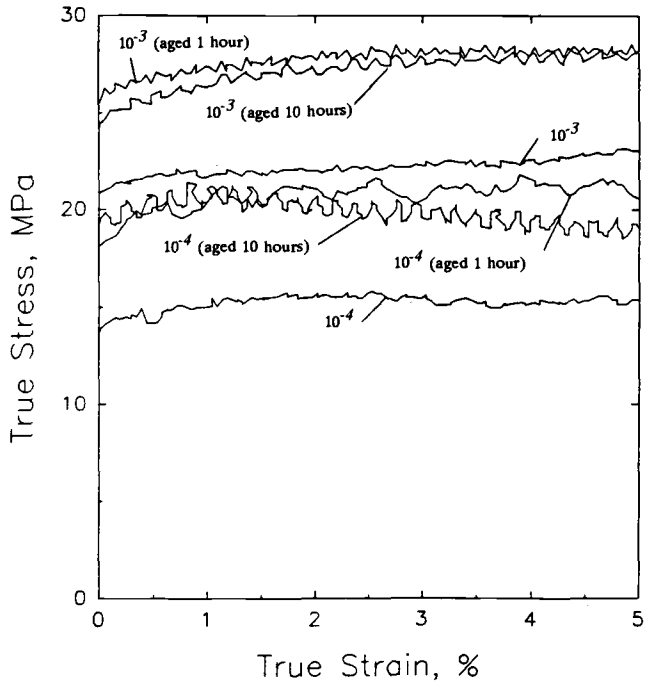

FIG. 12—*Tension tests at 110°C on specimens aged at 145°C (Alloy II). The reference (unaged) stress-strain curves are marked. Approximate strain rates and aging times are indicated. Note the nearly uniform 5-MPa strengthening effect of aging.*

Alloy I without recourse to optimization procedures for curve fitting reflects the intimate physical basis of the model. According to the first-order algorithm employed, different constants or parameters were identified with physically distinct behaviors, enabling their estimation without numerical integration and iteration. It is interesting to consider that for a physically based model, not all regimes of stress-strain-temperature behavior are equally significant in so far as their impact on the overall performance of the model structure. A purely numerical scheme for fitting constants has the disadvantage that the experienced user's knowledge of these regimes and their link to model parameters is not necessarily invoked. The real value of minimizing an error norm to fit constants numerically may be in sorting out mutual dependencies between model constants and parameters which are not apparent upon inspection; such results might suggest that several terms are redundant, for example, in reflecting the same mechanism.

In the experiments reported here, temperature variations were not considered. The model, however, has the capability to model temperature history effects through the inclusion of temperature rate terms in the evolution equations of the internal variables χ and α. As shown by Ohno and Wang [*27*] and McDowell [*17*], temperature-independent C and μ lead to temperature path history independence; this simply means that the material will respond at each temperature as it did in an isothermal experiment at that temperature for a given internal state. On the other hand, exclusion of the temperature rate terms in the evolution of χ and α leads to an implicit degree of temperature path history dependence which is not necessarily indicative of the actual case. The thermomechanical response of OFHC copper, for example, was better correlated by excluding the temperature rate terms [*17*] in all

internal evolution equations except for that of the long-range backstress. Normally, path history dependence is a consequence of an unstable microstructure as exhibited by solder alloys during aging at temperature. However, the last section proposed to incorporate aging effects directly into the evolution equations of the internal variables. In this case, the necessity of the temperature rate terms is an open issue, subject to further study based on thermomechanical fatigue experiments and careful examination of aged microstructures.

Acknowledgments

The authors would like to acknowledge the support of Texas Instruments in development of the thermoviscoplastic model, and of the Georgia Tech Manufacturing Research Center Industrial Advisory Board for the experimental program. The authors are also indebted to Mr. R. L. T. Oehmke for his assistance in the early stages of the experimental program.

References

[*1*] Baker, E., "Stress Relaxation in Tin-Lead Solders," *Materials Science and Engineering,* Vol. 38, 1979, p. 241.

[*2*] Raman, V. and Reiley, T. C., "Cyclic Deformation and Fracture in Pb-Sn Solid Solution Alloy," *Metallurgical Transactions A,* Vol. 19A, 1988, p. 1533.

[*3*] Chaboche, J. L., "Description Thermodynamique et Phenomenologique de la Viscoplasticite Cyclique avec Endommagement," Ph.D. thesis, Universite Paris VI, 1978.

[*4*] Cailletaud, G. and Chaboche, J. L., "Macroscopic Description of the Microstructural Changes Induced by Varying Temperature: Example of IN100 Behaviour," *Proceedings,* ICM3 Cambridge, TP ONERA, 1979, p. 112.

[*5*] Mecking, H. and Kocks, U. F., "Kinetics of Flow and Strain Hardening," *Acta Metallurgica,* Vol. 29, 1981, pp. 1865–1875.

[*6*] Follansbee, P. S. and Kocks, U. F., "A Constitutive Description of the Deformation of Copper Based on the Use of the Mechanical Threshold Stress as an Internal State Variable," *Acta Metallurgica,* Vol. 36, No. 1, 1988, pp. 81–93.

[*7*] Germain, P., Nguyen, Q. S., and Suquet, P., "Continuum Thermodynamics," *ASME Journal of Applied Mechanics,* Vol. 50, 1983, p. 1010.

[*8*] Chaboche, J. L., "Constitutive Equations for Cyclic Plasticity and Cyclic Viscoplasticity," *International Journal of Plasticity,* Vol. 5, No. 3, 1989, pp. 247–302.

[*9*] Chan, K. S., Bodner, S. R., Walker, K. P., and Lindholm, U. S., "A Survey of Unified Constitutive Theories," *Proceedings,* 2nd Symposium on Nonlinear Constitutive Relations for High Temperature Applications, NASA Lewis Research Center, 13–15 June 1984.

[*10*] Walker, K. P., "Research and Development Program for Nonlinear Structural Modeling with Advanced Time-Temperature Dependent Constitutive Relationships," NASA Report CR-165533, NASA Lewis Research Center, November 1981.

[*11*] Freed, A. D. and Chaboche, J. L., "Viscoplasticity: A Thermodynamic Formulation," NASA Technical Memo 102388, 1989.

[*12*] Korhonen, M. A., Hannula, S.-P., and Li, C.-Y., "State Variable Theories Based on Hart's Formulation," Chapter 2 in *Unified Constitutive Equations for Creep and Plasticity,* A. K. Miller, Ed., Elsevier Applied Science, New York, 1987.

[*13*] Miller, A. K., "The MATMOD Equations," Chapter 3 in *Unified Constitutive Equations for Creep and Plasticity,* A. K. Miller, Ed., Elsevier Applied Science, New York, 1987.

[*14*] Krieg, R. D., Swearengen, J. C., and Jones, W. B., "A Physically Based Internal Variable Model for Rate Dependent Plasticity," Chapter 5 in *Unified Constitutive Equations for Creep and Plasticity,* A. K. Miller, Ed., Elsevier Applied Science, New York, 1987.

[*15*] Skipor, A., Harren, S., and Botsis, J., "Constitutive Characterization of 63/37 Sn/Pb Eutectic Solder Using the Bodner-Partom Unified Creep-Plasticity Model," *Proceedings,* 1992 Joint ASME/JSME Conf. on Elec. Packaging, Advances in Electronic Packaging, Vol. 2, W. T. Chen and H. Abe, Eds., 1992, pp. 661–672.

[*16*] Busso, E. P., Kitano, M., and Kumazawa, T., "A Visco-Plastic Constitutive Model for 60/40 Tin-Lead Solder Used in IC Package Joints," *ASME Journal of Engineering Materials and Technology,* Vol. 114, 1992, pp. 331–337.

[17] McDowell, D. L., "A Nonlinear Kinematic Hardening Theory for Cyclic Thermoplasticity and Thermoviscoplasticity," *International Journal of Plasticity,* Vol. 8, 1992, pp. 695–728.
[18] Miller, A. K., "A Unified Phenomenological Model for the Monotonic, Cyclic, and Creep Deformation of Strongly Work-Hardening Materials," Ph.D. thesis, Stanford University, 1975.
[19] Moosbrugger, J. C. and McDowell, D. L., "A Rate-Dependent Bounding Surface Model with a Generalized Image Point for Cyclic Nonproportional Viscoplasticity," *Journal of the Mechanics and Physics of Solids,* Vol. 38, No. 5, 1990, pp. 627–656.
[20] Lowe, T. C. and Miller, A. K., "Improved Constitutive Equations for Modeling Strain Softening, Parts I and II," *ASME Journal of Engineering Materials and Technology,* Vol. 106, No. 4, 1984, pp. 337–348.
[21] McDowell, D. L. and Moosbrugger, J. C., "Continuum Slip Foundations of Elasto-Viscoplasticity," *Acta Mechanica,* Vol. 93, 1992, pp. 73–87.
[22] Adams, P. J., "Thermal Fatigue of Solder Joints in Micro-electronic Devices," M.S. thesis, Department of Mechanical Engineering, Massachusetts Institute of Technology, Cambridge, MA, 1981.
[23] Wong, B., Helling, D. E., and Clark, R. W., "A Creep-Rupture Model for Two-Phase Eutectic Solders," *IEEE Transactions of Composites, Hybrids, and Manufacturing Technology,* Vol. 11, 1988, pp. 284–290.
[24] Riedel, H., *Fracture and High Temperatures,* Chapter 1, Springer-Verlag, Berlin, 1986.
[25] Rohde, R. W. and Swearengen, J. C., "Deformation Modeling Applied to Stress Relaxation of Four Solder Alloys," *ASME Journal of Engineering Materials and Technology,* Vol. 102, 1980, pp. 207–214.
[26] Schmidt, C. G. and Miller, A. K., "The Effect of Solutes on the Strength and Strain Hardening Behavior of Alloys," *Acta Metallurgica,* Vol. 30, 1982, pp. 615–625.
[27] Ohno, N. and Wang, J. D., "Transformation of a Nonlinear Kinematic Hardening Rule to a Multisurface Form under Isothermal and Nonisothermal Conditions," *International Journal of Plasticity,* Vol. 7, 1991, pp. 879–891.

Y.-H. Pao,[1] *S. Badgley,*[1] *R. Govila,*[1] *and E. Jih*[1]

Thermomechanical and Fatigue Behavior of High-Temperature Lead and Lead-Free Solder Joints

REFERENCE: Pao, Y.-H., Badgley, S., Govila, R., and Jih, E., **"Thermomechanical and Fatigue Behavior of High Temperature Lead and Lead-Free Solder Joints,"** *Fatigue of Electronic Materials, ASTM STP 1153,* S. A. Schroeder and M. R. Mitchell, Eds., American Society for Testing and Materials, Philadelphia, 1994, pp. 60–81.

ABSTRACT: Thermal fatigue tests were performed on six solder alloys, i.e., 90Pb-10Sn, 97Sn-2Cu-0.8Sb-0.2Ag, 97Sn-3Cu, 95.5Sn-4Cu-0.5Ag, 95Bi-5Sb, and 63Sn-37Pb to study their stress/strain hysteresis response and corresponding thermal fatigue behavior. The first five solder alloys, with melting temperature ranging from 250 to 310°C, are regarded as high-temperature solders compared to solders with lower melting point, e.g., 63Sn-37Pb (T_M = 183°C). A double-beam joint specimen has been developed for this test. The specimen is made by bonding an Al_2O_3 beam and an Al 2024-T4 beam together at their ends with solder. A method based on the measured stress relaxation data at dwell time has been developed to determine the steady-state creep parameters of the solder. Simplified viscoplastic constitutive equations employing the measured creep properties were assumed for the solder and implemented in a finite element program to evaluate their validity in modeling thermal cyclic behavior. During thermal fatigue, the evolution of the stress/strain hysteresis loop was measured, and the fracture surface was examined with SEM to identify the dominant failure mechanism. The results show that some Sn-Cu alloys have a much better thermal fatigue resistance than the high lead one and can be considered as lead-free alternatives. In addition, the eutectic solder also exhibits a surprisingly longer fatigue life than 90Pb-10Sn solder, which implies that using melting temperature as a guideline for solder selection against operation temperature may need to be modified.

KEYWORDS: solder, creep, thermal fatigue, stress and strain hysteresis response, fracture, finite element methods

Thermal fatigue failure in electronic packages frequently results from cracking in solder joints. For most solder alloys, such as lead-tin (Pb-Sn) based solders, the operating temperature can be as high as 0.5 to 0.8 T_M of the alloys. In such high-temperature regimes, significant amounts of creep and creep-induced fracture can occur, which, when coupled with the fatigue crack growth, becomes a dominant failure mechanism in the solder joints. Thus, understanding the stress/strain hysteresis behavior is critical in characterizing their fracture behavior.

In the present study a solder joint specimen has been used to determine the thermal cyclic stress/strain hysteresis response and thermal fatigue behavior of six solder alloys, 90Pb-10Sn, 97Sn-2Cu-0.8Sb-0.2Ag, 97Sn-3Cu, 95.5Sn-4Cu-0.5Ag, 95Bi-5Sb, and 63Sn-37Pb, in an in-house developed temperature chamber. The study of Pb-free solders reflects the increasing demand in the electronics industry in search of lead solder substitutes [*1,2*]. In this paper, detailed characteristics of stress relaxation and creep of the solder joint were

[1]Research Laboratory, Ford Motor Company, Dearborn, MI 48121-2053.

determined as a function of temperature. The associated secondary creep properties were measured, and the corresponding mechanisms are discussed. From the fatigue experiment, the evolution of stress/strain hysteresis response as a function of thermal cycles was determined and used, together with the fracture surface examination with scanning electron microscopy (SEM), to identify the failure mechanism. The results suggest some tin-copper (Sn-Cu) solders have potential as Pb-free solder substitutes.

Solder Alloys

Six solder alloys were tested: 90Pb-10Sn and 63Sn-37Pb are two commonly used Pb solders, and 95Bi-5Sb, 97Sn-2Cu-0.8Sb-0.2Ag, 95.5Sn-4Cu-0.5Ag, 97Sn-3Cu are commercially available Pb-free solders. Their melting temperatures are listed in Table 1. It is seen that, except for the eutectic 63Sn-37Pb, the other five have their melting temperatures above 250°C and usually are regarded as high-temperature solders. Studies of high-temperature Pb or Pb-free solders are lacking in the literature compared to extensive research activities on solders with low melting temperatures, 130 to 200°C. The four Pb-free solders selected here represented the authors' first attempt in search of Pb-free replacements for high-temperature lead-containing solders.

Specimen and Test Apparatus

The design of the specimen and the test apparatus has been discussed in detail in a previous paper [*3*]. Only a brief introduction is given here. The specimen consists of two beams, Al_2O_3 and Al 2024-T4, jointed at the ends with solder (Fig. 1). It is obvious that under uniform temperature variations both beams are subjected to uniform bending and axial forces. This results in a constant bending curvature in each beam. Assuming uniform shearing in the joint, which has been verified by the finite element analysis treating solder as an elastic/creep material [*4*], the average shear stress and strain can be determined by measuring the elastic response of the beams, e.g., with strain gages.

The specimen is 42 mm long and 5 mm deep. The thicknesses of the Al 2024-T4 and the Al_2O_3 beams are 3 and 1.2 mm, respectively. The solder joint at each end of the specimen is 2 mm wide and 5 mm deep, and the thickness is 0.381 mm (= 15 mils). Prior to making the joint, the areas to be soldered were sputtered with a thin layer of chromium (approximately 200 nm) to increase the adhesion to the beam and a 3-μm-thick copper film for solderability. These areas were then fluxed and pretinned with the same solder used in the test.

Four strain gages (Micro-Measurements WK-13-062AP-350) were mounted on the aluminum beam, two on the inside surface and two on the outside surface, as shown in Fig. 1. The two gages on each surface were connected into a double-quarter Wheatstone bridge. The double-quarter bridge was designed such that the two diagonal active gages measure strains with the same magnitude and the same sign. With this arrangement the output voltage of the bridge is doubled without increasing the noise level. The increase in output signal voltage allows the bridge to resolve smaller strain changes. In addition, a temperature sensor (Micro-Measurements ETG-50A) was bonded on one side of the aluminum to provide

TABLE 1—*Melting temperature of tested solder alloys, °C.*

State	90Pb-10Sn	97Sn-2Cu-0.8Sb-0.2Ag	97Sn-3Cu	95.5Sn-4Cu-0.5Ag	95Bi-5Sb	63Sn-37Pb
Solidus	268	225	227	227	274	183
Liquidus	301	257	310	349	296	183

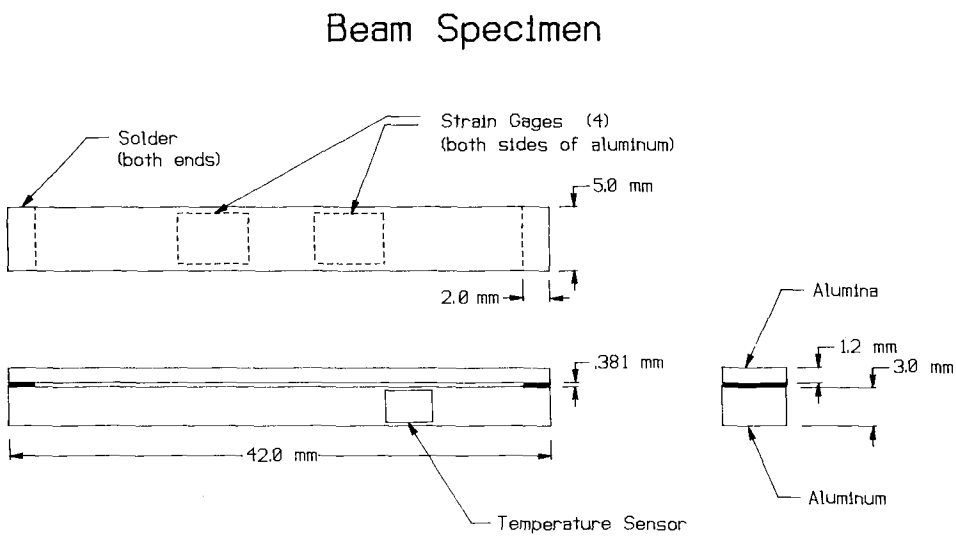

FIG. 1—*A schematic of the specimen, associated dimensions, and location of strain gages and temperature sensor.*

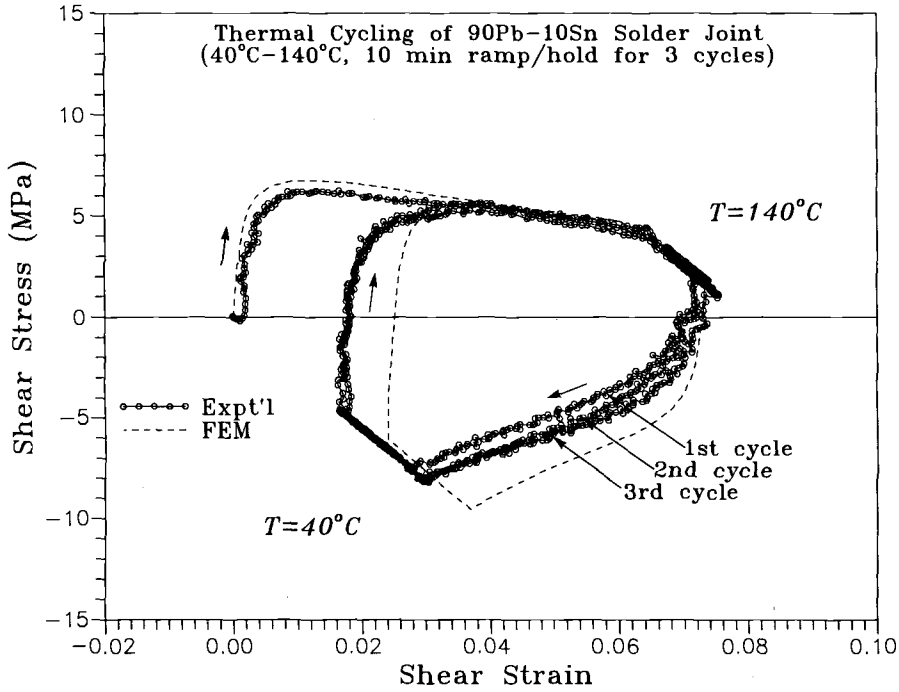

FIG. 2—*Experimental and predicted thermal cyclic shear stress/strain hysteresis loops of 90Pb-10Sn between 40 and 140°C with 10-min hold and ramp.*

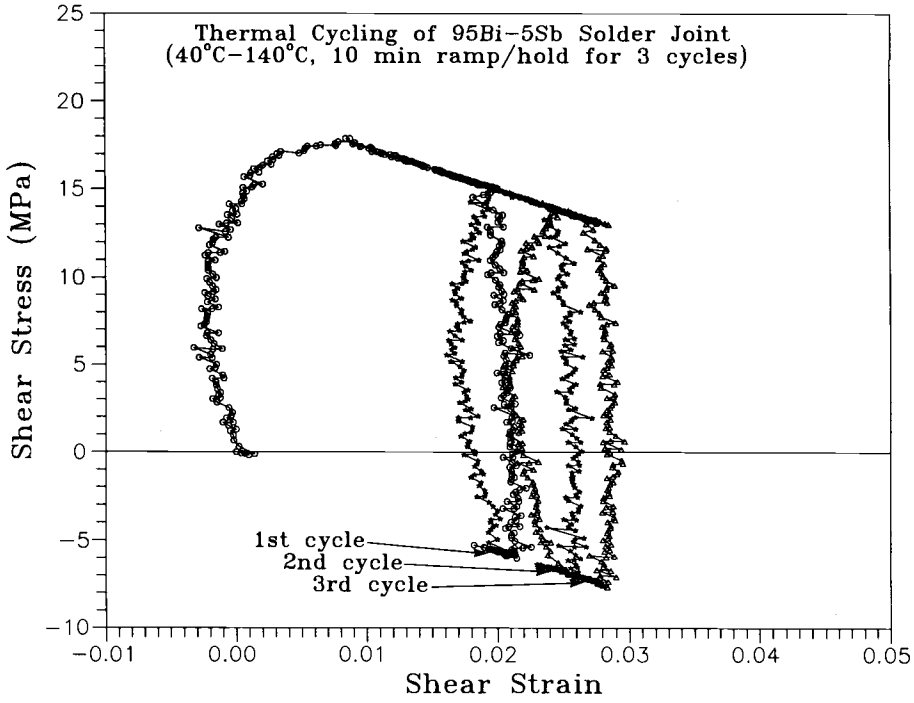

FIG. 3—*Experimental thermal cyclic shear stress/strain hysteresis loops of 95Bi-5Sb between 40 and 140°C with 10-min hold and ramp.*

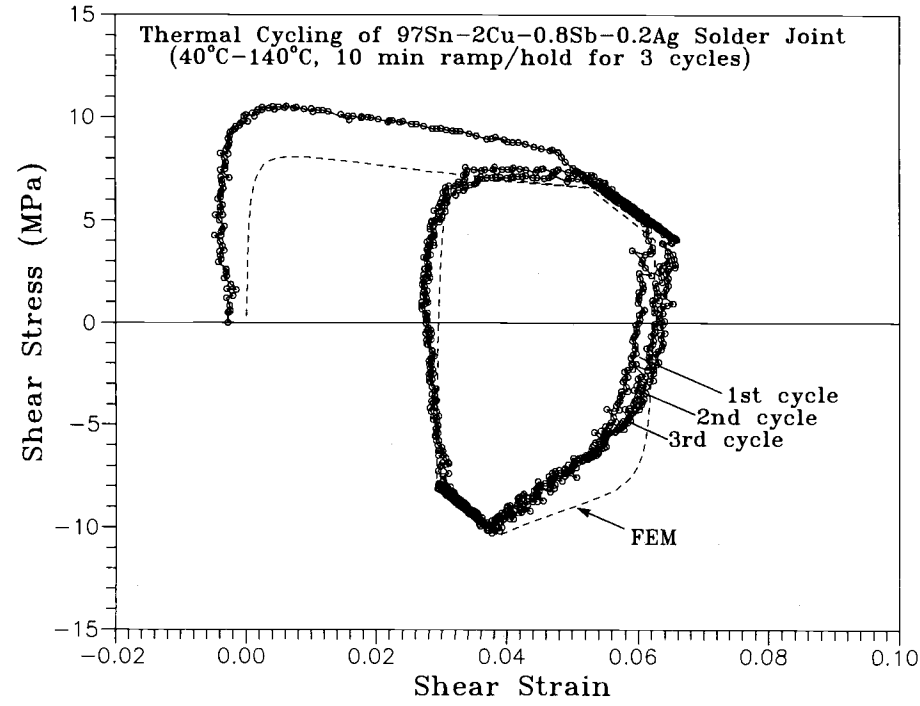

FIG. 4—*Experimental and predicted thermal cyclic shear stress/strain hysteresis loops of 97Sn-2Cu-0.8Sb-0.2Ag between 40 and 140°C with 10-min hold and ramp.*

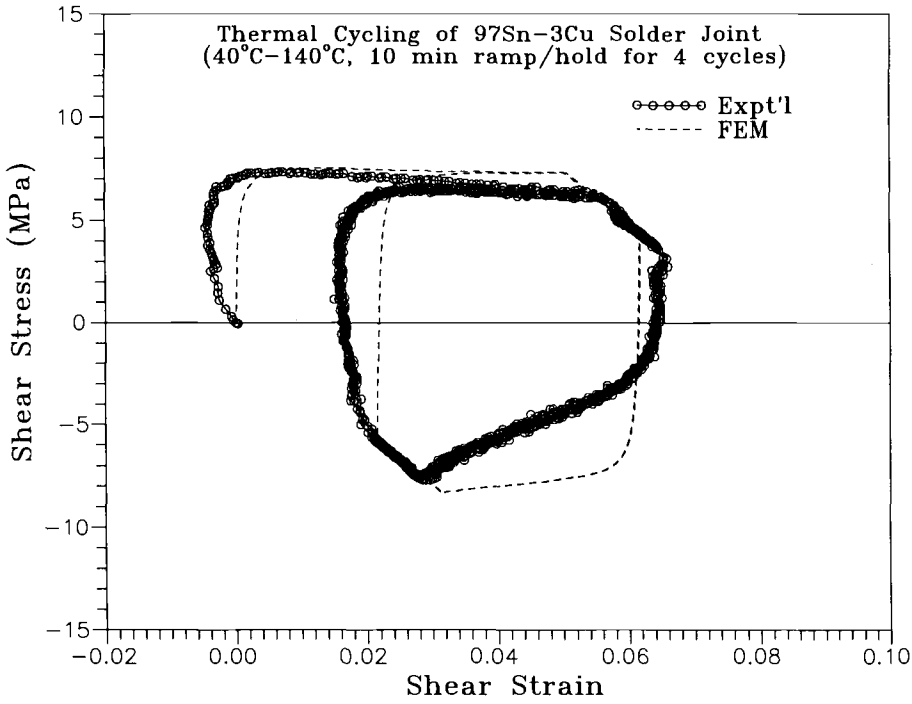

FIG. 5—*Experimental and predicted thermal cyclic shear stress/strain hysteresis loops of 97Sn-3Cu between 40 and 140°C with 10-min hold and ramp.*

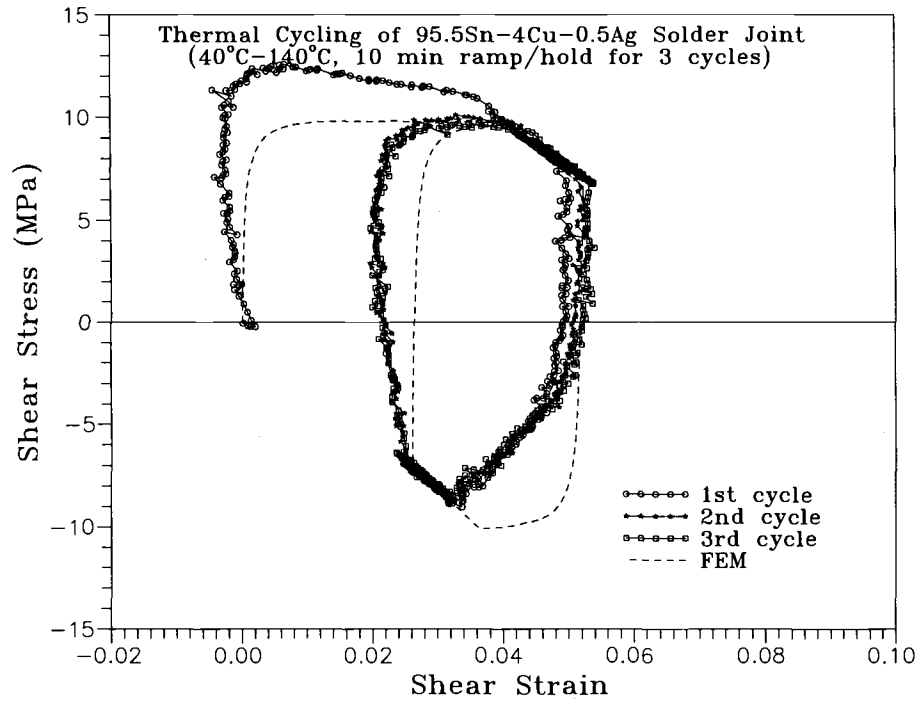

FIG. 6—*Experimental and predicted thermal cyclic shear stress/strain hysteresis loops of 95.5Sn-4Cu-0.5Ag between 40 and 140°C with 10-min hold and ramp.*

feedback to the controller to produce a desired temperature cycle. The temperature profile used in the test is a 40-min cycle between 40 and 140°C with a 10-min dwell and ramp.

The method used to determine the shear stress and shear strain in the solder joint has been delineated by Pao et al. [*3,5*]. The method is based on the simple beam theory and the measured strains on the aluminum beam as input. The temperature chamber developed includes a heating coil and an air cooling fan driven by a controller. The present system can only attain temperatures above 20°C. The chamber is capable of achieving a ramp rate as fast as 1°C/s and any length of hold time and can give a range from 20 to 300°C with accuracy of ± 0.1°C.

Stress/Strain Hysteresis Response and Steady-State Creep Properties

The measured shear stress/strain hysteresis responses of 90Pb-10Sn, 95Bi-5Sb, 97Sn-2Cu-0.8Sb-0.2Ag, 97Sn-3Cu, 95.5Sn-4Cu-0.5Ag, and 63Sn-37Pb are shown in Figs. 2 through 7, respectively, for the first few cycles. The data acquisition rate is one per 5 s. This gives 480 data points per cycle. All the symbols shown in the figure represent raw data from the strain gage records.

As can be seen in the figures, the shear stress tends to stabilize very rapidly within three cycles except for the 95Bi-5Sb solder. The fact that 95Bi-5Sb stabilizes at a slower rate is because of a smaller strain range resulting from the test. In Figs. 2 through 7 it can be seen that both stress relaxation and creep occur simultaneously at the hold time since the system is neither displacement controlled nor load controlled. The initial total shear strain range is 5.6% for 90Pb-10Sn, 0.9% for 95Bi-5Sb, 3.8% for 97Sn-2Cu-0.8Sb-0.2Ag, 5.2% for 97Sn-

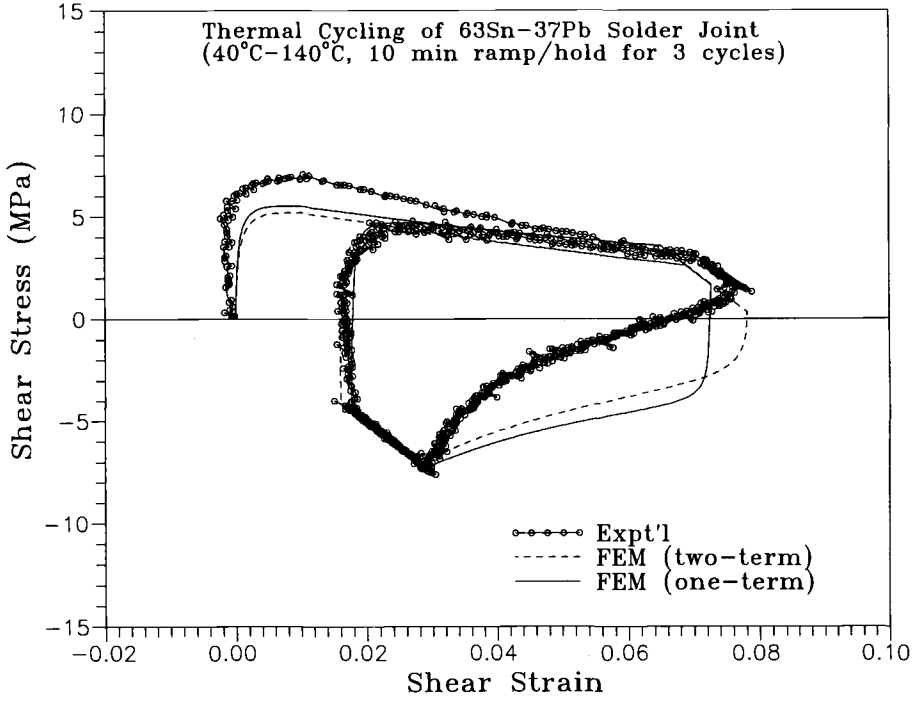

FIG. 7—*Experimental and predicted thermal cyclic shear stress/strain hysteresis loops of 63Sn-37Pb between 40 and 140°C with 10-min hold and ramp.*

3Cu, 3.3% for 95.5Sn-4Cu-0.5Ag, and 6.4% for 63Sn-37Pb, with the corresponding initial shear stress range of 13.2, 22.0, 17.4, 14.8, 18.8, and 12.3 MPa, respectively. Both Pb solders have the lowest stress range and the highest strain range, while 95Bi-5Sb shows the opposite. As far as the Sn-Cu system is concerned, 97Sn-3Cu behaves quite differently from the other two, which are very similar in terms of stress/strain range and the shape of the hysteresis loop. In general, the shape of the hysteresis loop reflects how time-dependent plastic deformation flows during the loading and unloading. It can be seen that except for the two Sn-Cu-Ag solders, the others bear no resemblance in terms of the hysteresis loop. This indicates that these solders have distinct viscoplastic properties, e.g., steady-state creep during hold time or primary creep during loading and unloading.

In a previous study by Pao et al. [5] an effective and accurate method based on the stress relaxation data at the hold time was developed to determine the secondary creep properties of the solder associated with Norton's equation

$$\frac{d\gamma_{crp}}{dt} = B^* \exp\left[\frac{-\Delta H}{kT}\right] \tau^n \tag{1}$$

where $d\gamma_{crp}/dt$ is the shear creep strain rate, n is the stress exponent, ΔH is the activation energy, k is Boltzmann's constant, T is temperature, and B^* is a material constant. The method is based on the assumption that the deformation at the hold time is controlled by steady-state creep. The creep properties determined for 90Pb-10Sn, 97Sn-2Cu-0.8Sb-0.2Ag, 97Sn-3Cu, 95.5Sn-4Cu-0.5Ag, and 63Sn-37Pb are listed in Table 2. The creep properties of 95Bi-5Sb could not be accurately determined because of the lack of sufficient relaxation data at the hold time. A higher stress level or a longer dwell is required.

The magnitude of ΔH for 90Pb-10Sn is in the range from 0.61 to 0.65 eV measured by Lavery [6] on the same solder in the isothermal creep test and is close to that of the dislocation core diffusion of pure Pb, 0.68 eV [7]. The ΔH of 63Sn-37Pb, 0.49 eV, is also in the range reported by Knecht and Fox [8]. It is noted that the activation energy of the Sn-Cu solders decreases with the weight percentage of copper and falls down to 0.06 eV when copper increases to 4%. This implies that the creep process could be athermal, which may be due to short-range copper clustering [9]. The other four solder alloys listed in Table 2 indicate that the range of ΔH and n correspond to a dislocation-controlled steady-state creep (Region III) (see Ref *10*).

The steady-state creep rate of Eq 1 is plotted versus stress in Figs. 8 and 9 for 40 and 140°C, respectively, for the listed five solders. It is seen that 63Sn-37Pb and 90Pb-10Sn show a higher creep rate and are temperature sensitive, while 95.5Sn-4Cu-0.5Ag has a much

TABLE 2—*Creep properties and the associated mechanism for 90Pb-10Sn, 97Sn-2Cu-0.8Sb-0.2Ag, 97Sn-3Cu, 95.5Sn-4Cu-0.5Ag, and 63Sn-37Pb solder alloys.*

Property	90Pb-10Sn	97Sn-2Cu-0.8Sb-0.2Ag	97Sn-3Cu	95.5Sn-4Cu-0.5Ag	63Sn-37Pb
B^*, 1/MPa^{n}s	100.6	3.031	9.10×10^{-4}	4.229×10^{-12}	0.205
ΔH, eV	0.64	0.85	0.51	0.062	0.49
n, 40°C	4.25	8.91	7.99	8.36	5.25
n, 140°C	3.03	7.37	6.30	8.36	5.25
Deformation mechanism	Dislocation core-diffusion	Dislocation glide/climb	Dislocation glide/climb	Athermal, short range Cu clustering	Dislocation glide/climb

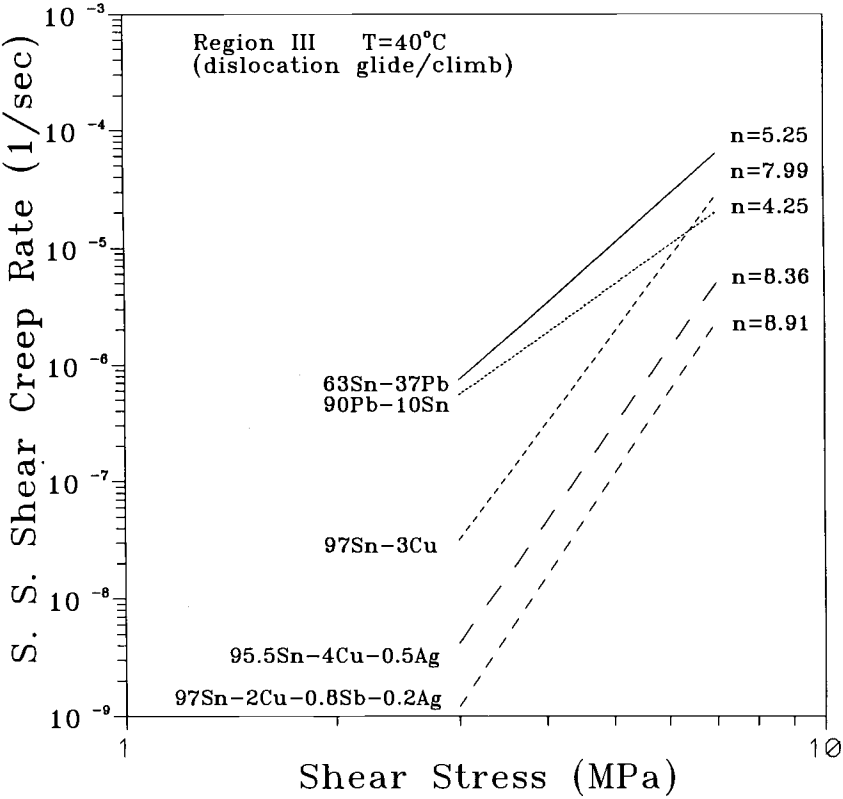

FIG. 8—*Steady-state shear creep rate versus shear stress at 40°C for 63Sn-37Pb, 90Pb-10Sn, 97Sn-3Cu, 95.5Sn-4Cu-0.5Ag, and 97Sn-2Cu-0.8Sb-0.2Ag.*

lower rate and is almost temperature insensitive but has a higher stress exponent as the other two Sn-Cu solders.

Constitutive Equations and Finite Element Modeling

A time-dependent constitutive equation for the solder is formulated to model its thermal cyclic behavior. It is assumed that the total strain rate consists of elastic and inelastic components. As a first approximation, the inelastic part is assumed to be dominated by the steady-state creep, as shown in Eq 1, and the creep properties determined in the test are used in the constitutive equation. The constitutive equation was implemented in a finite element program, ABAQUS [*11*], to model the experiment. The purpose is to study how well Norton's equation, probably the most simplified viscoplastic equation, models the thermal cyclic behavior of the solder joint. The loading imposed is the same as the test, i.e., 40 to 140°C with a 10°C/min ramp rate and 10-min hold time. Only half of the specimen was modeled due to the symmetry in geometry and loading. The model is constructed by eight-noded plane stress elements and consists of 850 elements with 2767 nodes.

The temperature-dependent Young's modulus, E, tangent coefficient of thermal expansion (CTE), and Poisson's ratio of Al_2O_3, Al 2024-T4, and solders are listed in Table 3. As

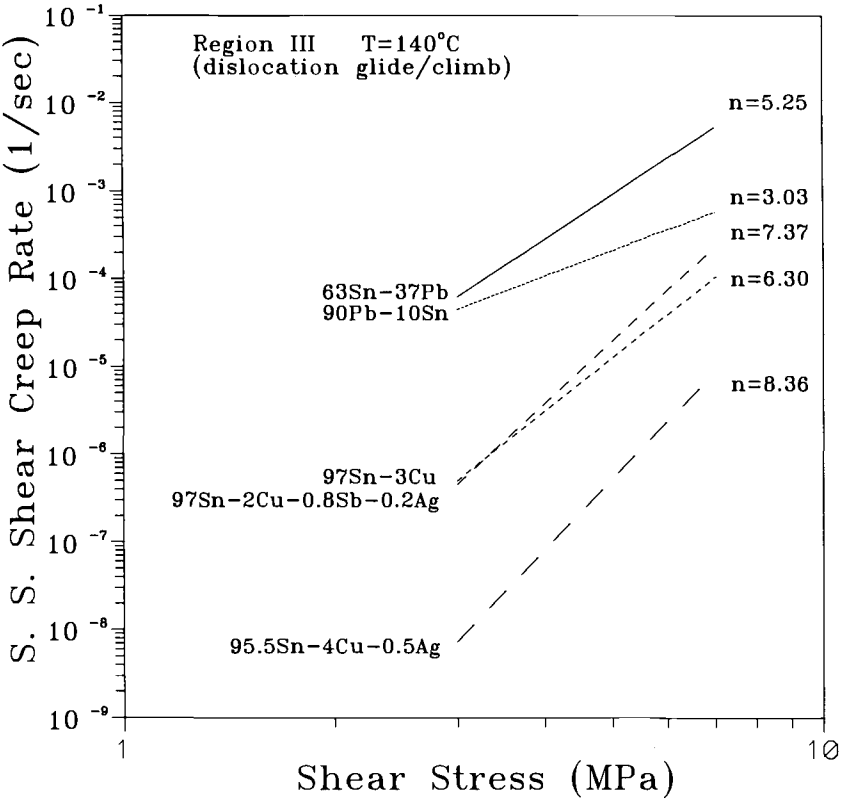

FIG. 9—*Steady-state shear creep rate versus shear stress at 140°C for 63Sn-37Pb, 90Pb-10Sn, 97Sn-3Cu, 95.5Sn-4Cu-0.5Ag, and 97Sn-2Cu-0.8Sb-0.2Ag.*

reported previously [*3*], the temperature dependence of the CTE of Al_2O_3 and Al 2024-T4 were measured between 100 and 300°C. Data for Al_2O_3 below 100°C were taken from the measurement on the same material, i.e., Coors AD-96, by Chanchani and Hall [*12*]. A linear relationship between the CTE and temperature was assumed for Al 2024-T4, and a third-order polynomial was used to fit the data of Al_2O_3. The dependence of Young's modulus for Al_2O_3 and Al 2024-T4 was assumed to follow the form suggested by Frost and Ashby [*7*] as $E(T) = E_0(1 - \beta(T - 300)/T_M)$, where T_M is the melting point (in K) and is 933K for

TABLE 3—*Elastic and thermal properties used in the FE model.*

Solder	*E*, MPa	CTE, ppm/°C	Poisson's Ratio
90Pb-10Sn[a]	21 138 − 26*T*[b]	28.6 + 0.015*T*	0.4
63Sn-37Pb	32 400 − 88*T*	21.1	0.4
97Sn-3Cu[c]	43 472 − 108*T*	20.1 − 0.033*T*	0.33
Al_2O_3	304 604 − 46*T*	$4.9 + 1.7\times10^{-2}T - 6.6\times10^{-5}T + 1.05\times10^{-7}T^3$	0.3
Al 2024-T4	74 141 − 39*T*	18.9 + 0.024*T*	0.35

[a]Assumed to be those of pure lead.
[b]*T* expressed in degrees Celsius.
[c]Assumed to be those of pure tin.

aluminum and 2320K for alumina; β is 0.5 for aluminum and 0.35 for alumina. The elastic modulus at room temperature, E_0, is assumed to be 73 084 MPa for Al 2024-T4 [*13*] and 303 368 MPa for Al_2O_3 [*14*]. The properties of 90Pb-10Sn solder are assumed to be those of pure lead [*7,15*]. For 63Sn-37Pb solder, the dependence of E on the temperature is assumed to follow the relation derived by Wong et al. [*16*], and CTE is assumed to be 21.1 [*17*]. The elastic properties of 97Sn-3Cu, 97Sn-2Cu-0.8Sb-0.2Ag, and 95.5Sn-4Cu-0.5Ag are assumed to be those of pure Sn [*15,18*]. It should be noted that the input of temperature-dependent CTE in ABAQUS is the secant CTE, which is generally not equal to the tangent CTE as measured in the lab and shown in Table 3 [*19*].

The inelastic part of the constitutive equation is implemented in ABAQUS with a user subroutine. Here, the uniaxial Norton's creep law is generalized to multiaxial stress states by converting the pure shear stress and strain into effective stress and strain.

The shear stress contours of solder joint at the start and end of both hold times are examined. It is seen that approximately 90% of the joint is under uniform shearing. Some transverse normal stresses are observed near the edges, but they die out rapidly toward the center of the joint. A fairly uniform and pure shear condition is achieved that validates the experimental assumption of pure shear.

The finite element results of shear stress/strain hysteresis loops at center of the joint are shown in Figs. 2 and 4 through 7 for 90Pb-10Sn, 97Sn-2Cu-0.8Sb-0.2Ag, 97Sn-3Cu, 95.5Sn-4Cu-0.5Ag, and 63Sn-37Pb, respectively. It is seen from Fig. 2 that the size and shape of the loop for 90Pb-10Sn solder compare well with the experiment. However, a shift of the loop during ramp-down is noted. In addition, the predicted stress is slightly larger in the lower temperature regime. Recently, a lower Young's modulus of 90Pb-10Sn, less than half of that of pure lead, was reported by Cole and Caulfield [*20*]. A finite element study shows that Young's modulus has an insignificant effect on stress/strain hysteresis loop because the deformation is essentially inelastic. For 63Sn-37Pb solder, as shown in Fig. 7, the predicted loops match well with the experiment except during ramp-down, where more hardening is predicted. This implies another creep mechanism (e.g., Region II or primary creep) prevailing in the lower stress and higher temperature regime, i.e., the onset of ramp-down. In order to account for this effect, a second creep term based on a modified Region II term taken from Hacke et al. [*21*], with $n = 1.96$, was introduced. This term gives a higher strain rate at lower stress level, as shown in Fig. 10. It is seen in Fig. 7 that some improvement has been achieved.

Figure 4 shows the predicted and experimental results of 97Sn-2Cu-0.8Sb-0.2Ag solder. It is noted that both agree well except at the later stage of ramp-down. The predicted and experimental results for 97Sn-3Cu solder are shown in Fig. 5. It is seen that though both experimental and finite element results show an approximately similar trend: the prediction slightly overestimates the stress level and underestimates the total strain range. Moreover, in Fig. 5, a significant difference is observed during cooling from 140 to 40°C, where the high temperature and low stress response is not modeled well by the current creep law, similar to the case of 63Sn-37Pb. A similar observation can also be made for 95.5Sn-4Cu-0.5Ag in Fig. 6. In spite of these differences, the constitutive model based on steady-state creep seems to be able to capture most of the key features in the thermal cyclic response. Moreover, the finite element results suggest that there exists a second creep mechanism dominating in the higher and lower stress regime.

Thermal Fatigue

The stress/strain hysteresis loops as a function of temperature cycle are shown in Figs. 11 through 16 for all six solders. All solders demonstrate an evolution of the shape and area of

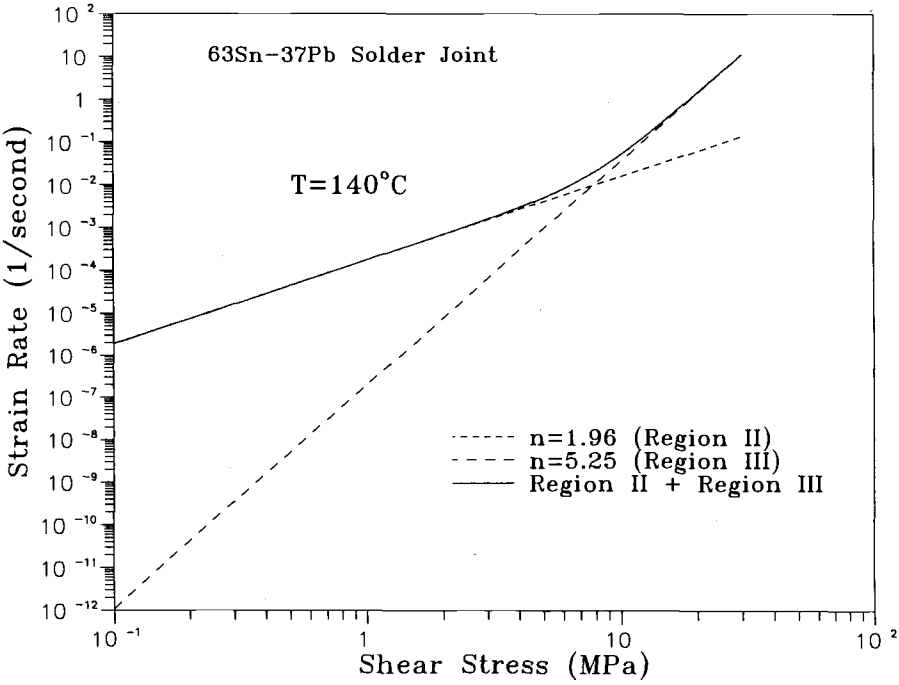

FIG. 10—*Steady-state shear creep rate versus shear stress at Regions II and III for 63Sn-37Pb at 140°C.*

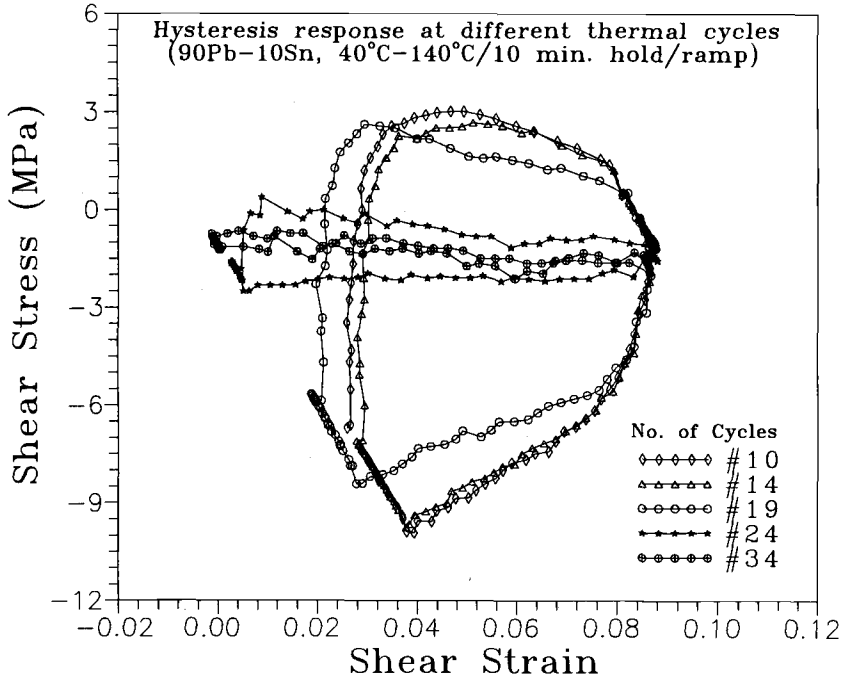

FIG. 11—*Experimental thermal cyclic shear stress/strain hysteresis loops as a function of number of cycles for 90Pb-10Sn between 40 and 140°C with 10-min hold and ramp.*

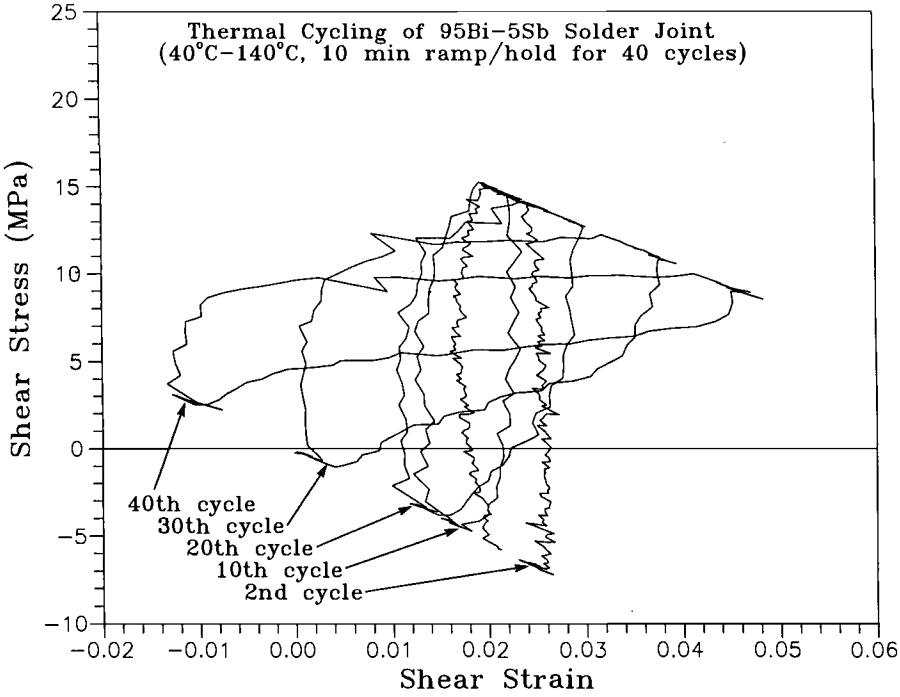

FIG. 12—*Experimental thermal cyclic shear stress/strain hysteresis loops as a function of number of cycles for 95Bi-5Sb between 40 and 140°C with 10-min hold and ramp.*

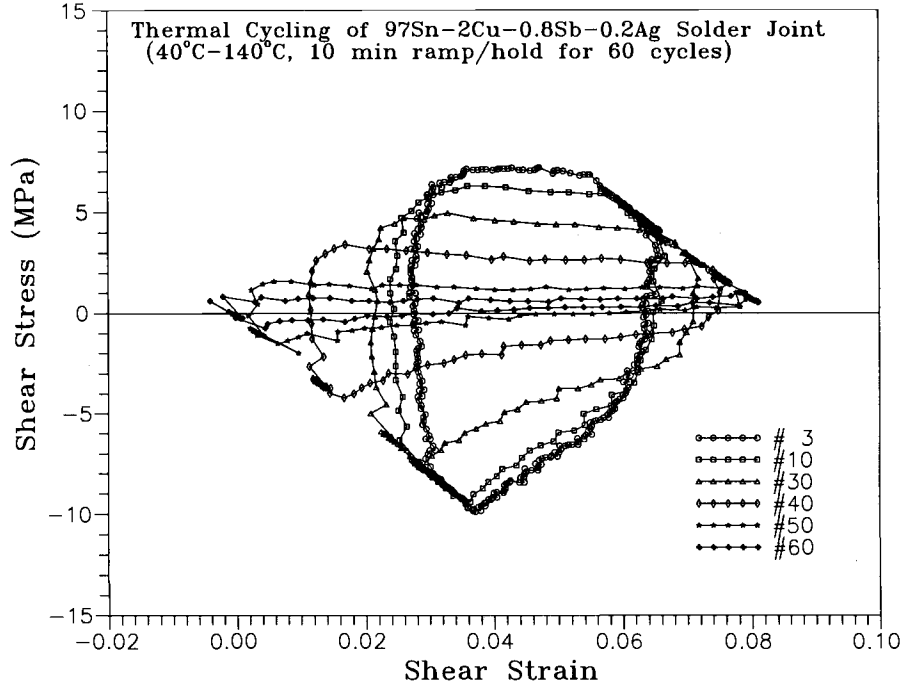

FIG. 13—*Experimental thermal cyclic shear stress/strain hysteresis loops as a function of number of cycles for 97Sn-2Cu-0.8Sb-0.2Ag between 40 and 140°C with 10-min hold and ramp.*

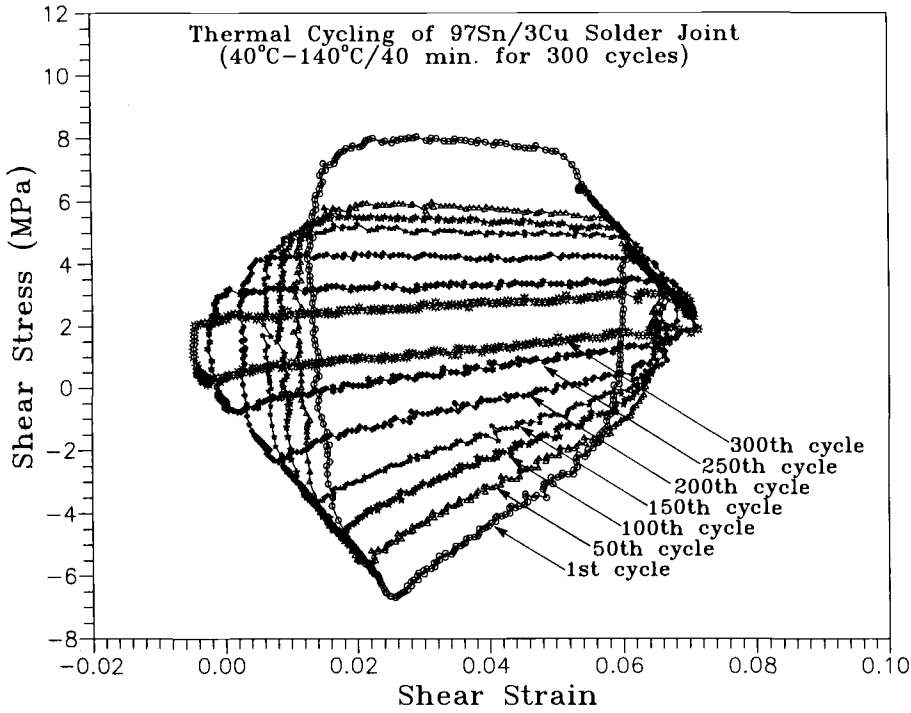

FIG. 14—*Experimental thermal cyclic shear stress/strain hysteresis loops as a function of number of cycles for 97Sn-3Cu between 40 and 140°C with 10-min hold and ramp.*

the loop. It has been shown previously [*22*] that the loops based on the original solder area has little difference from those based on the current area, taking into account the crack length, since the crack growth rate is small compared with the joint width in the first half of the life. It is seen in Fig. 11 that the loops of 90Pb-10Sn remain essentially unchanged up to 14 cycles, after which a clear change in shape follows, e.g., from the 19th through the 34th cycles. During this period of time the solder apparently undergoes a "softening" or "weakening" process. This softening becomes more pronounced when cycling continues, e.g., the 24th and 34th cycles. Examination of fracture surface, shown in Fig. 17, reveals that this weakening is primarily attributed to a large amount of secondary cracks and voids generated during the thermal cycling. These defects cause the material to degrade and are reflected in the hysteresis loops.

Figure 18 shows the fracture surface of 97Sn-2Cu-0.8Sb-0.2Ag. The crack initiated at the Al_2O_3/solder interface and propagated near and parallel to the interface (Fig. 18*b*). A significant amount of secondary cracks are seen in Figs. 18*a*, 18*c*, and 18*d*. The large amount of voids may be due to the outgassing of the flux during joint fabrication. However, viewing through a void due to outgassing shows an evidence of creep-induced voids at the grain boundary (Fig. 18*e*). In addition, fatigue striations are also seen in the figure.

The fracture surface of 63Sn-37Pb after 201 cycles is shown in Fig. 19. The joint is only partly fractured, indicated by the dashed line in Fig. 19*a*. The crack initiated at the Al_2O_3/solder interface and extended into the solder. The fracture morphology is quite different from those of 90Pb-10Sn and Sn-Cu solders in that there are more creep-induced dimples and less secondary cracks and fatigue striations. A magnified view of the thermal fatigue

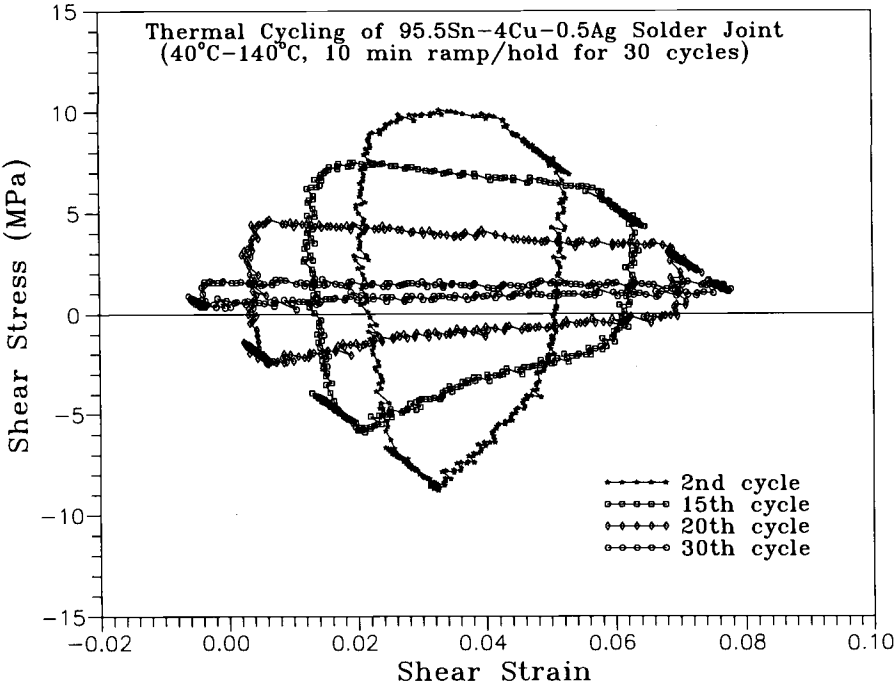

FIG. 15—*Experimental thermal cyclic shear stress/strain hysteresis loops as a function of number of cycles for 95.5Sn-4Cu-0.5Ag between 40 and 140°C with 10-min hold and ramp.*

cracked region (Region I in Fig. 19*a*) and pulled fracture after the test (Region II) is shown in Fig. 20, where the microstructure coarsening is seen in Region I, as compared to Region II. This indicates the coarsening occurred only at the high-strain field near the crack tip.

The number of cycles to failure and the associated failure mechanism as a result of SEM examination are listed in Table 4; 97Sn-3Cu apparently has a much longer life than 90Pb-10Sn, the other two Sn-Cu solders, and 95Bi-5Sb. It is interesting to note that 63Sn-37Pb, though with a lower melting point of 183°C, shows a much higher creep/fatigue resistance than the other solders except for 97Sn-3Cu. This infers that the higher steady-state creep rate of 63Sn-37Pb, as shown in Figs. 8 and 9, does not necessarily suggest that the material would fail at a faster rate. The corresponding mechanism associated with the crack propagation is essentially creep-fatigue coupled.

Conclusions

The technique developed here is particularly useful for studying the thermomechanical response over a wide range of solder alloys and for evaluating their thermal fatigue strength and associated failure mechanism. The experimentally determined hysteresis loops and their evolution as a function of temperature cycle are also important for developing viscoplastic constitutive equations and damage models. The finite element study suggests that there may be a second creep mechanism prevailing in the higher temperature and lower stress regime. The current test results of testing six different solder alloys show that the lower melting point 63Sn-37Pb (T_M = 183°C) has a thermal fatigue life approximately four to ten times

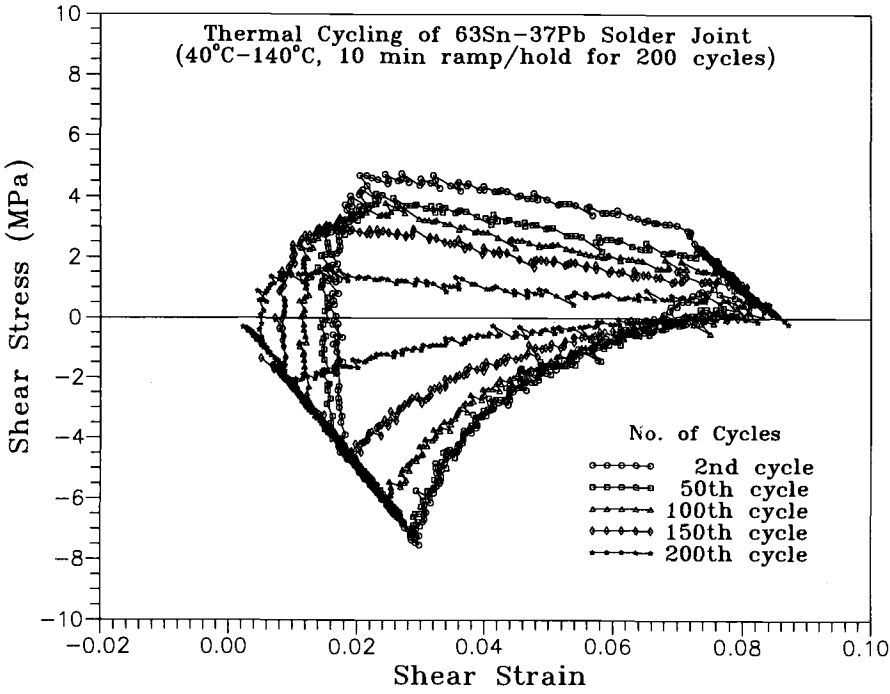

FIG. 16—*Experimental thermal cyclic shear stress/strain hysteresis loops as a function of number of cycles for 63Sn-37Pb between 40 and 140°C with 10-min hold and ramp.*

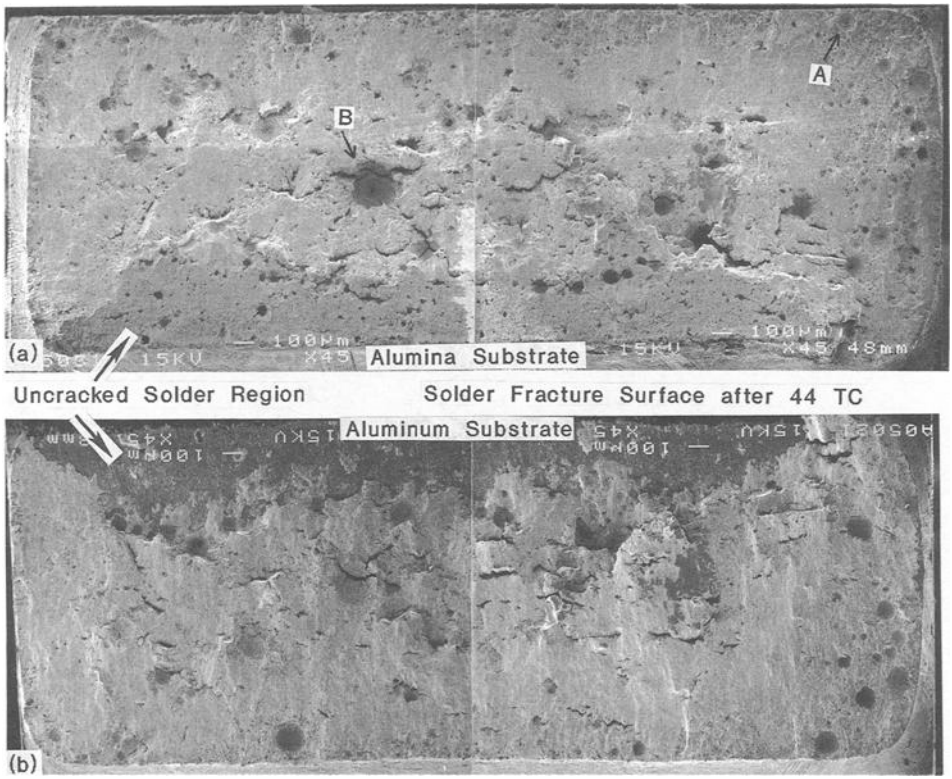

FIG. 17—*Fracture surfaces of 90Pb-10Sn solder joint subjected to thermal cycling between 40 and 140°C with 10-min hold and ramp:* (a) *on alumina beam, and* (b) *on aluminum beam.*

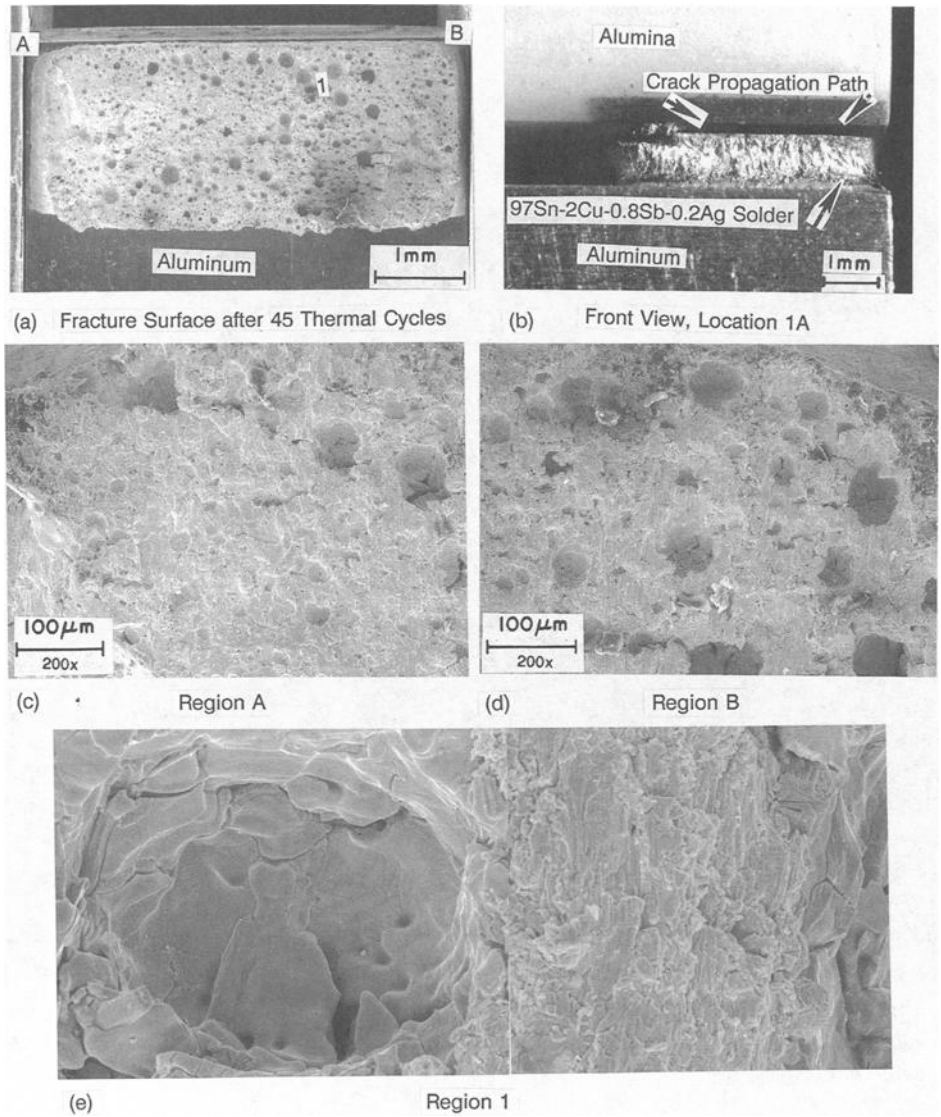

FIG. 18—*Fracture surfaces and front view of 97Sn-2Cu-0.8Sb-0.2Ag solder joint subjected to thermal cycling between 40 and 140°C with 10-min hold and ramp:* (a) *fracture surface on aluminum beam,* (b) *front view showing crack path near the alumina beam,* (c) *magnification of Region A in* (a), (d) *magnification of Region B in* (a), *and* (e) *magnification of Region 1 in* (a).

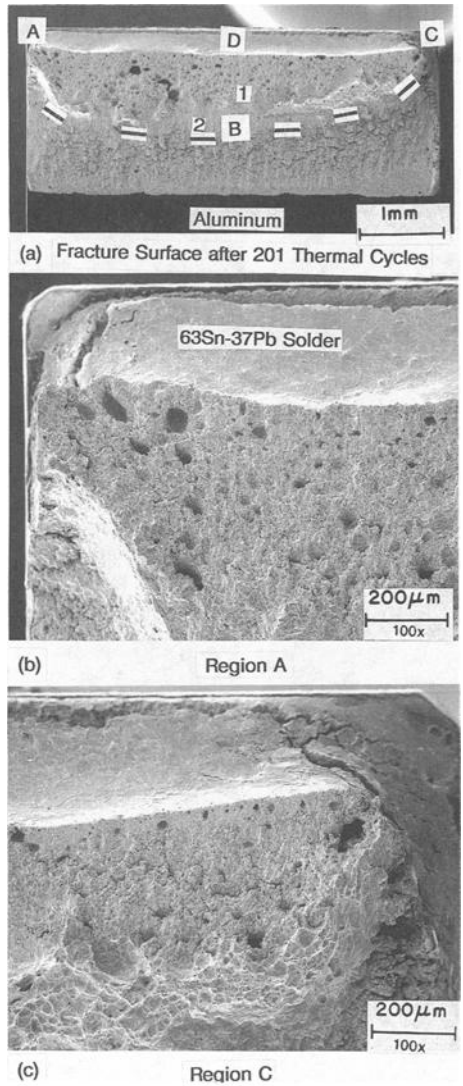

FIG. 19—*Fracture surfaces of 63Sn-37Pb solder joint subjected to thermal cycling between 40 and 140°C with 10-min hold and ramp:* (a) *on aluminum beam,* (b) *magnification of Region A in* (a), (c) *magnification of Region C in* (a).

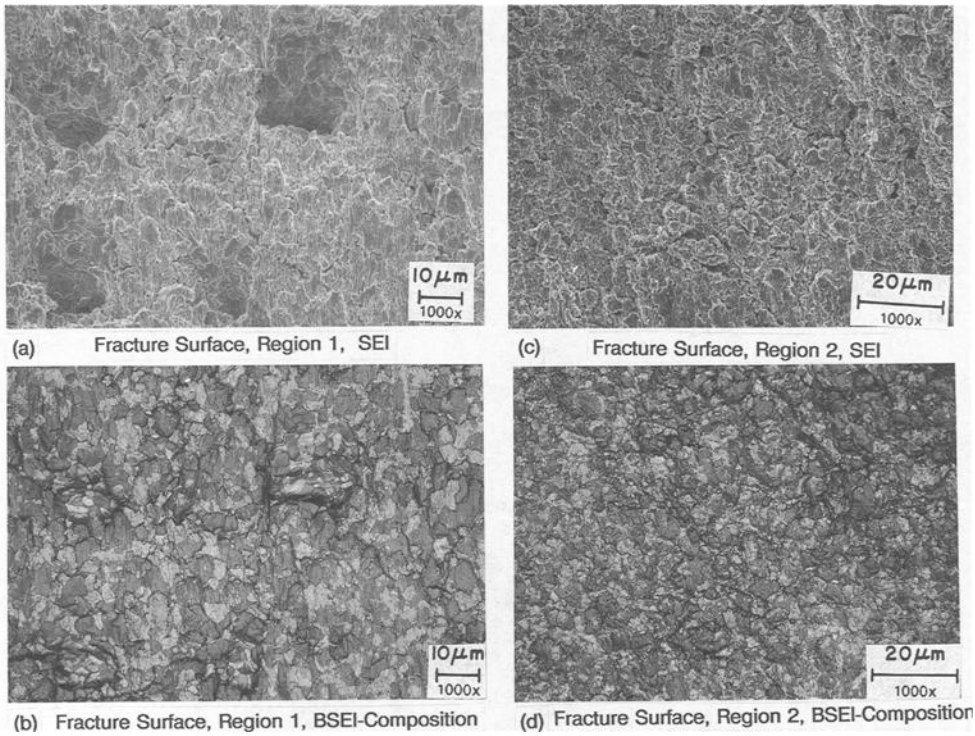

FIG. 20—*Fracture surfaces of 63Sn-37Pb:* (a) *Region 1 in Fig. 19*a *corresponding to the fatigue cracked area,* (b) *back scatter electronic image (BSEI) showing crack-induced coarsened microstructure,* (c) *Region 2 in Fig. 19*a *corresponding to the uncracked ligament, and* (d) *the associated BSEI of Region 2 showing noncoarsened microstructure.*

TABLE 4—*Number of cycles to failure and the associated failure mechanisms.*

Solder	Initial Shear Strain Range, %	Initial Shear Stress Range, MPa	Final Shear Strain Range, %	Final Shear Stress Range, MPa	Number of Cycles to Failure, N_f	Primary Failure Mechanisms
90Pb-10Sn	5.6	13.2	8.8	2.5	20 (interface[a]) 45 (cohesive[b])	Major crack (one end) Trans/intergranular Secondary cracking Creep/fatigue
97Sn-2Cu-0.8Sb-0.2Ag	3.8	17.4	8.2	1.3	60 (interface)	Similar to 90Pb-10Sn One end
97Sn-3Cu	5.2	14.8	7.6	1.5	100 (interface) 300 (cohesive)	Similar to 90Pb-10Sn Two ends
95.5Sn-4Cu-0.5Ag	3.3	18.8	8.1	0.6	30 (interface)	Similar to 90Pb-10Sn One end
95Bi-5Sb	0.9	22.0	5.6	6.8	50 (interface and cohesive)	Major crack (one end) Transgranular Secondary cracking Fatigue only
63Sn-37Pb	6.4	12.3	8.1	3.6	>200 (interface and cohesive)	Major cracks (two ends) Intergranular Secondary cracking Coarsening Creep/fatigue

[a]Interface crack is defined as a crack propagating either along or near the interface between the beam and the solder.
[b]Cohesive crack is defined as a crack propagating in the solder joint and relatively away from the interface.

longer than 90Pb-10Sn, 95Bi-5Sb, 97Sn-2Cu-0.8Sb-0.2Ag, and 95.5Sn-4Cu-0.5Ag, which all have a higher T_M (>250°C). In addition, a Pb-free solder 97Sn-3Cu has been demonstrated to exhibit a more improved creep/fatigue resistance than the 90Pb-10Sn and thus seems to be promising as a Pb solder substitute. However, more studies are needed to assess the fatigue strength at different strain ranges and temperature profiles.

Acknowledgment

The authors wish to thank Litton/Kester Solder for providing 97Sn-2Cu-0.8Sb-0.2Ag samples, Engelhard for providing 95.5Sn-4Cu-0.5Ag, and Multicore Solders, Inc. for providing 97Sn-3Cu. The authors would also like to thank W. L. Winterbottom for valuable discussions and R. Shah for assisting with the data processing.

References

[1] Allenby, B. R. et al., "An Assessment of the Use of Lead in Electronics Assembly—Part 1," *Circuit World*, Vol. 19, No. 2, 1993, pp. 18–24.
[2] Allenby, B. R. et al., "An Assessment of the Use of Lead in Electronics Assembly—Part 2," *Circuit World*, Vol. 19, No. 3, 1993, pp. 25–31.
[3] Pao, Y.-H., Badgley, S., Govila, R., Baumgartner, L., Allor, R., and Cooper, R., "Measurement of Mechanical Behavior of High Lead Lead-Tin Solder Joints Subjected to Thermal Cycling," *ASME Transactions, Journal of Electronic Packaging*, Vol. 114, No. 2, 1992, pp. 135–144.
[4] Pao, Y.-H., Badgley, S., Jih, E., Govila, R., and Browning, J., "Constitutive Behavior and Low Cycle Thermal Fatigue of 97Sn-3Cu Solder Joints," *ASME Transactions, Journal of Electronic Packaging*, June 1993, Vol. 115, No. 2, pp. 147–152.
[5] Pao, Y.-H., Govila, R., and Badgley, S., "Thermal Fatigue Fracture of 90Pb/10Sn Solder Joints," *Advances in Electronic Packaging 1992*, Proceedings of the 1992 Joint ASME/JSME Conference on Electronic Packaging, pp. 291–300.
[6] Lavery, P. R., "An Investigation of the Thermal and Mechanical Properties of High Lead-Low Tin Alloy Solders," M.S. thesis, Dartmouth College, Hanover, NH.
[7] Frost, H. J. and Ashby, M. F., *Deformation Mechanism Maps*, Pergamon Press Ltd., Elmsford, NY, 1982.
[8] Knecht, S. and Fox, L., "Integrated Matrix Creep: Application to Accelerated Testing and Lifetime Prediction," *Solder Joint Reliability: Theory and Application*, J. H. Lau, Ed., Van Nostrand Reinhold, New York, 1991, pp. 508–544.
[9] Conrad, H., 1993, private communications.
[10] Hacke, P., Sprecher, A. F., and Conrad, H., "Computer Simulation of Thermo-mechanical Fatigue of Solder Joints Including Microstructure Coarsening," presented at ASME WAM, 8–13 Nov. 1992, Anaheim, CA, ASME, New York.
[11] *ABAQUS*, Hibbit, Karlsson & Sorensen, Inc., Pawtucket, RI.
[12] Chanchani, R. and Hall, P. M., "Temperature Dependence of Thermal Expansion of Ceramics and Metals for Electronic Packages," *IEEE Transactions on Components, Hybrids, and Manufacturing Technology*, Vol. 13, No. 4, 1990, pp. 743–750.
[13] *Machine Design—Materials Reference Issue*, 1984, April 19.
[14] Manufacturers data, Coors AD-96, Coors Ceramics Company, Grand Junction, CO.
[15] *CRC Handbook of Tables for Applied Engineering Science*, 2nd ed., The Chemical Rubber Co., 1973, pp. 331–332.
[16] Wong, B., Helling, D. E., and Clark, R. W., "A Creep-Rupture Model for Two-Phase Eutectic Solders," *IEEE Transactions on Components, Hybrids, and Manufacturing Technology*, Vol. 11, No. 3, 1988, pp. 284–290.
[17] Lau, J. H. and Rice, D. W., "Solder Joint Fatigue in Surface Mount Technology: State of the Art," *Solid State Technology*, Vol. 28, October 1985, pp. 91–104.
[18] *ASM Metals Handbook*, Vol. 2, 10th ed., American Society of Metals, 1990, p. 1167.
[19] Pao, Y.-H., Jih, E., Artz, B. E., and Cathey, L. W., "A Note on the Implementation of Temperature Dependent Coefficient of Thermal Expansion (CTE) in ABAQUS," *ASME Transactions, Journal of Electronic Packaging*, Vol. 114, No. 4, 1992, pp. 470–472.
[20] Cole, M. and Caulfield, T., "Constant Strain Rate Tensile Properties of Various Lead Based Solder Alloys at 0, 50, and 100°C," *Scripta Metallurgica*, Vol. 27, No. 7, 1992, pp. 903–908.

[21] Hacke, P. L., Sprecher, A. F., and Conrad, H., "Thermo-Mechanical Fatigue of 63Sn-37Pb Solder Joints," *Thermal Stress and Strain in Microelectronic Packaging*, J. Lau, Ed., Van Nostrand Reinhold, New York, 1993.

[22] Pao, Y.-H., Govila, R., Badgley, S., and Jih, E., "An Experimental and Finite Element Study of Thermal Fatigue Fracture of PbSn Solder Joints," *ASME Transactions, Journal of Electronic Packaging*, Vol. 115, No. 1, 1993, pp. 1–8.

S. A. Schroeder,[1] *W. L. Morris,*[1] *M. R. Mitchell,*[1] *and M. R. James*[1]

A Model for Primary Creep of 63Sn-37Pb Solder

REFERENCE: Schroeder, S. A., Morris, W. L., Mitchell, M. R., and James, M. R., **"A Model for Primary Creep of 63Sn-37Pb Solder,"** *Fatigue of Electronic Materials, ASTM STP 1153,* S. A. Schroeder and M. R. Mitchell, Eds., American Society for Testing and Materials, Philadelphia, 1994, pp. 82–94.

ABSTRACT: A micromechanical model of transient and steady-state creep as it applies to near eutectic Sn-Pb solder is presented. The material is described as a two-phase system having individual material properties, coupled by long-range internal stresses. The constitutive equations permit primary creep and the transition to steady state to be simulated by a numerical analysis in which the global mechanical response is dependent on the local stress state.

The creep equations are calibrated through a series of shear strain measurements of thin-walled tubular solder specimens. Comparisons to predictions include cyclic shear strain-controlled experiments, creep relaxation, and combination ramp-hold shear strain and stress control environments. Application to finite element analysis of surface mount interconnects is described.

KEYWORDS: 63Sn-37Pb solder, primary creep, steady-state creep, thin-walled tube, torsion, shear, composite model, finite element methods

A major objective in the electronics industry is to develop a means of evaluating the mechanical response and corresponding reliability of solder joints used in the construction of electronic components. This task is complicated by the complex deformation behavior of the commonly used Sn-Pb near-eutectic solder. Solder joints are routinely employed in environments which repeatedly expose the solder to temperatures above 0.5 of the homologous temperature. In this regime, significant creep, stress relaxation, and microstructural changes occur. In addition, the microstructure is observed to evolve under conditions of thermomechanical fatigue, forming localized heterogeneous coarsened bands [*1,2*]. Large strains are present within the developing bands, leading to an increase in local compliance and eventual failure of the joint.

Various methods have been employed to predict the stress-strain state and reliability of soldered joint assemblies, such as strain range partitioning [*3*], fracture mechanics [*4,5*], combined tension-torsion of bulk solder [*6*], and micromechanical models [*7*]. The success of any method as a predictive tool for the design engineer depends not only on the accuracy of the mechanics involved, but also on the ease at which it can be incorporated into the engineering environment. To provide a usable solution, the constitutive relations must describe the deformation mechanisms in sufficient detail to give an accurate estimation of material response while maintaining the required simplicity for iterative numerical solutions of complex component systems. The goal of this paper is to present a constitutive framework by which the elastic-creep deformation of solder alloys can be calculated for arbitrary

[1]Rockwell International Science Center, Thousand Oaks, CA 91360.

loading paths. While no attempt will be made here to extrapolate to thermomechanical situations, the required temperature dependency is easily incorporated in the model framework.

The approach taken here is similar to that used to model transient creep in simple binary solid solutions [*8,9*]. The system is treated as a composite material with a heterogeneous dislocation structure. Regions of low dislocation density are constrained by harder regions of high dislocation density. In the eutectic solder alloy system, this may correspond to the soft Pb-rich phase and the harder Sn-rich phase of the near-eutectic microstructure. Compatibility is further assumed to be enforced across adjacent phases, giving identical strains in both regions. Strain rates in the two regions are not independent from each other, but are coupled by internal stresses which tend to eliminate any variances in the local rates.

Deformation within each cell consists of distinct elastic and plastic components. For purposes of reproducing experimental results and mathematical simplicity, the plasticity is represented as generalized power-law creep. Transient creep of the system develops until the differing internal stresses within both cells reach steady-state values. The resulting deformation and stress relationships are expressed as either creep (constant applied stress) or fatigue (constant applied strain rate) for comparison with experimental results. A general expression is derived as a subroutine for finite element calculations.

Experimental results for verification and calibration of the composite model were obtained using thin-walled tubular samples of bulk eutectic tin-lead solder. A series of isothermal creep tests at constant shear stress and several ramp-hold tests provided the experimental basis for calibration of the power-law creep component of the constitutive relation. Evaluation of hysteresis of the solder deformation was explored through shear-strain-controlled, low-cycle fatigue experiments.

Experimental Results

Creep

The material used exclusively in this study, electronic grade eutectic solder, was purchased in the form of 1 by 7 by 26-in. (2.5 by 17.8 by 66.0-cm) 50-lb (22.7-kg) bars of nominal composition 63Sn-37Pb. Bars were cast with tin of 99.9% and lead of 99.94% purity or better and conform to government QQ-S-571E, MIL-STD-2000, WS-6536E, and applicable ASTM Standard Specification for Solder Metal (B 32) specifications. Composition of samples removed from the bars was nominally 62.69 wt% tin. Specimen blanks were cut to 1 by 1 by 7 in. (2.5 by 2.5 by 17.8-cm) and single-point machined to 0.500 in. (1.27 cm) outside diameter over the gage section. Specimens were then gun bored to inside

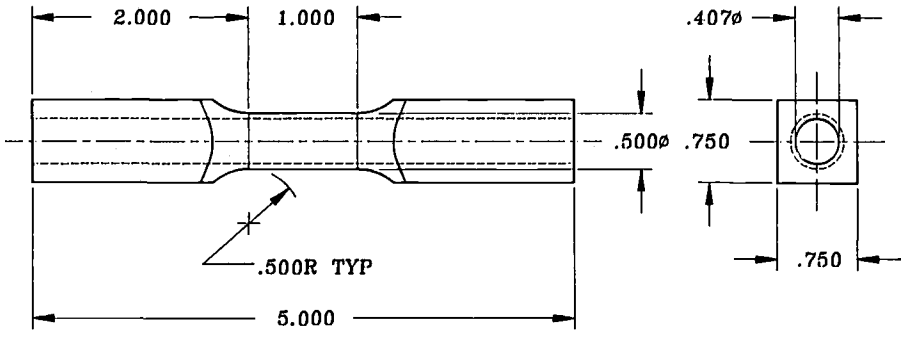

FIG. 1—*Thin-walled tubular solder specimen (dimensions in inches, 1 in. = 25.40 mm).*

diameter of 0.407 in. (1.03 cm), as in Fig. 1. Gage lengths were finished in accordance with the ASTM Standard Practice for Constant-Amplitude Low-Cycle Fatigue Testing (E 606-92). All specimens were aged at 22°C for over two months prior to testing to allow microstructural equilibration.

Due to the large plastic deformations observed for solder, two distinct experimental procedures were used to evaluate the creep response [*10*]. For large shear strains (>3.5%), a specially designed troptometer and loading apparatus (Fig. 2) is used. Results obtained from this method are entirely in the secondary steady state and tertiary creep regimes and are illustrated in Fig. 3.

Primary creep measurements were obtained with the thin-walled tubular specimen loaded at a constant shear stress in a typical axial-torsion servohydraulic test system (Fig. 4). Shear strains were monitored with an axial-torsional extensometer and digitally recorded. Data acquisition rates of 0.02/s were used to fully capture the initial strain transient and any deviations from the programmed torque. The desired torsional load was reached under computer control within 0.1 s and was held constant for the duration of the test. The detail of the torque rise to steady state was recorded and used in the calibration analysis described below. Axial load was relieved throughout the test, thus eliminating any load-induced buckling instability. The relatively low shear strains present did not produce torsional instability, and additional test constraints were not required.

Stress Relaxation and Creep Reversal

Two hold-time creep experiments were performed to evaluate the effect of hold time and stress or strain reversal on creep response in the primary regime. The specimen configuration, torque and shear strain transducers, test control hardware, and data acquisition systems were identical to those of the primary creep experiments. The effect of torque reversal on

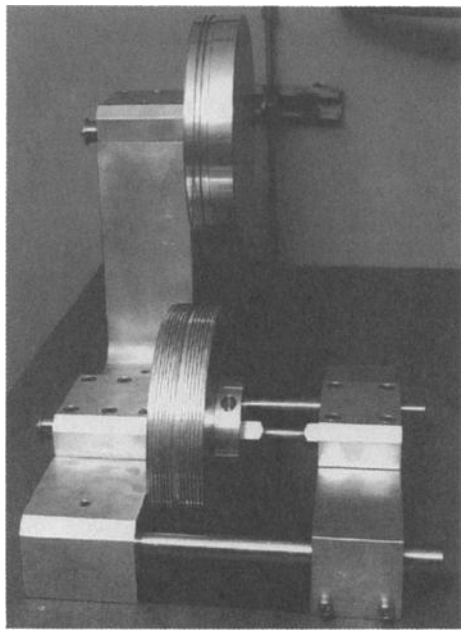

FIG. 2—*Torsional creep apparatus (secondary-tertiary creep).*

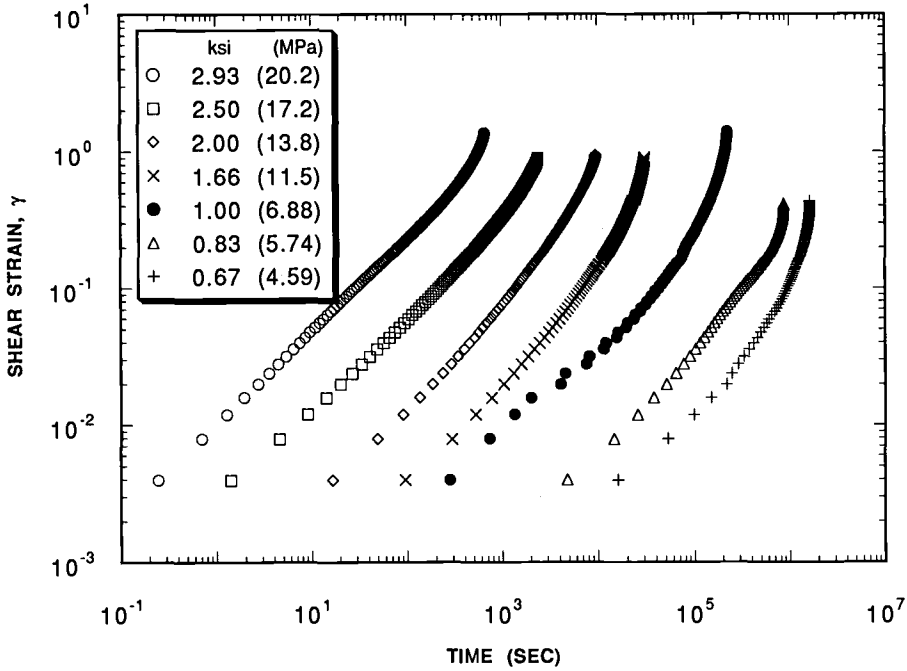

FIG. 3—*Shear strain versus time creep of tubular solder specimens at 22°C.*

creep shear strain was observed by imposing a constant stress amplitude square waveform. A shear-strain-controlled test of similar nature was performed to examine stress relaxation and reversal effects.

Low Cycle Fatigue

Isothermal low-cycle fatigue experiments were conducted on bulk solder specimens identical to those used for the creep experiments. Shear strain rate and magnitude were applied through computer control of an axial-torsional servohydraulic system (Fig. 4). Buckling instability at large strain amplitudes and/or long lifetimes was inhibited by inserting a boron-

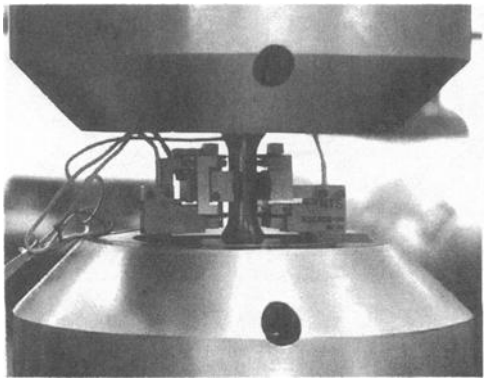

FIG. 4—*Axial-torsional system (primary creep and fatigue).*

nitride-coated polytetrafluoroethylene rod into the tubular solder specimen as described in Ref *10* and by maintaining a state of zero axial force. Test termination and failure were defined as 50% drop in shear stress. Figure 5 shows the first cycle of the low-cycle fatigue tests for selected runs at representative shear strain rate. The purpose here is to describe the hysteresis with the composite-back stress model. The model can be expanded to account for damage propagation and microstructural evolution.

Two-Phase Creep Model

The binary solder system is modeled as a region of low dislocation density (soft Pb-rich phase) surrounded by a region of higher dislocation density (hard Sn-rich phase). Such regions cannot deform independently, but must strain identically to maintain compatibility. The total shear strain rate is therefore identical in both regions and is assumed to take the form

$$\dot{\gamma}_{\text{tot}} = \frac{1}{G_i}\frac{\partial \tau_i}{\partial t} + A_i(\sinh B_i \tau_i)^{m_i} \tag{1}$$

where the subscripts denote the region, G_i is the shear modulus, A_i and B_i are generalized creep coefficients, and m_i is the creep stress exponent. The creep coefficients can be devolved to accommodate temperature variations as

$$A_i \propto \exp\left(\frac{-Q_i}{kT}\right)$$

where Q_i is the creep activation energy for a given mechanism in region i.

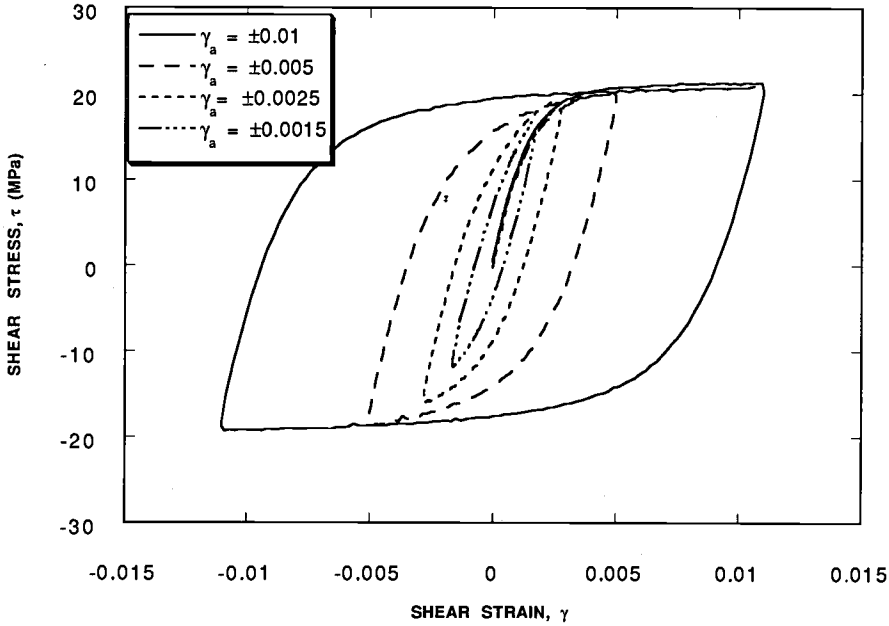

FIG. 5—*First cycle in shear strain control fatigue at 22°C (0.003/s).*

If $\bar{\tau}$ is the shear stress applied to the entire system, and f_1 is the volume fraction of the first phase, $\bar{\tau}$ can be expressed in terms of the local stresses, τ_1 and τ_2, as

$$\bar{\tau} = f_1\tau_1 + (1 - f_1)\tau_2 \tag{2}$$

Combining the shear strain rate and stress relations and solving for the experimental creep condition of constant applied shear stress (i.e., $\partial\bar{\tau}/\partial t = 0$) gives

$$\frac{\partial\tau_1}{\partial t} = \frac{G_1}{1 + \dfrac{G_1}{G_2}\dfrac{f_1}{(1 - f_1)}}[A_2(\sinh B_2\tau_2)^{m_2} - A_1(\sinh B_1\tau_1)^{m_1}]$$

$$\frac{\partial\tau_2}{\partial t} = \frac{G_2}{1 + \dfrac{G_2}{G_1}\dfrac{(1 - f_1)}{f_1}}[A_1(\sinh B_1\tau_1)^{m_1} - A_2(\sinh B_2\tau_2)^{m_2}] \tag{3a}$$

The coupling of the cells in this manner describes the local back stresses generated within the composite system. These back stresses manifest as transient creep until local equilibrium is achieved. It follows that under conditions of nonideal stress or arbitrary stress rate control, the time dependency of the applied stress must be retained (i.e., $\partial\bar{\tau}/\partial t \neq 0$).

$$\frac{\partial\tau_1}{\partial t} = \frac{G_1}{1 + \dfrac{G_1}{G_2}\dfrac{f_1}{(1 - f_1)}}\left[A_2(\sinh B_2\tau_2)^{m_2} - A_1(\sinh B_1\tau_1)^{m_1} + \frac{1}{G_2(1 - f_1)}\frac{\partial\bar{\tau}}{\partial t}\right]$$

$$\frac{\partial\tau_2}{\partial t} = \frac{G_2}{1 + \dfrac{G_2}{G_1}\dfrac{(1 - f_1)}{f_1}}\left[A_1(\sinh B_1\tau_1)^{m_1} - A_2(\sinh B_2\tau_2)^{m_2} + \frac{1}{G_1 f_1}\frac{\partial\bar{\tau}}{\partial t}\right] \tag{3b}$$

For constant applied shear strain rate as specified in the low-cycle fatigue experiments, the local stress increments become

$$\frac{\partial\tau_i}{\partial t} = G_i[\dot{\gamma} - A_i(\sinh B_i\tau_i)^{m_i}] \tag{4}$$

The resulting relationships for shear stress and strain controlled conditions fully describe the stress-strain states in the initial transient and steady-state regimes. Expressed in differential form, a numerically stable computer algorithm can be developed for an incremental solution of any arbitrary shear stress or strain imposed environment.

Model Calibration

Transient and primary creep in the composite cell model responds to the initial change in back stress between the composite cells and is quite sensitive to the shear modulii of the phases and to their volume fractions. In the solder system, the cells are assumed to be represented by the Pb-rich α and Sn-rich β phases as observed in the typical near-eutectic microstructure of Fig. 6. The average volume fraction of the phases, as determined through

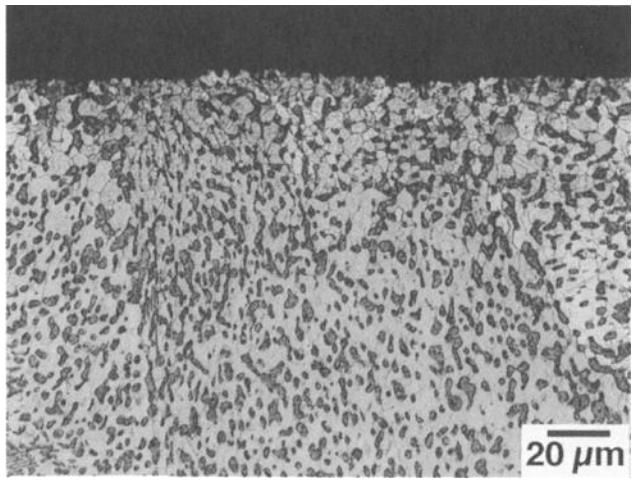

FIG. 6—*Optical micrograph of thin-walled eutectic solder specimen (transverse).*

threshold image analysis of micrographs taken of the experimental specimens, was 0.35 ± 0.03 for the α phase. The shear modulii for the phases were estimated using a rule of mixtures approximation, and phase compositions were determined by the extension of nonequilibrium solidus lines of the tin-lead phase diagram (Fig. 7). The composite model can be adapted to other alloys or deformation mechanisms through the correlation of the model cells to the appropriate microstructural features (phase distributions, grains, or colonies).

Generalized creep coefficients, A_i and B_i, and the creep exponents, m_i, are determined through comparison with the constant-load, torsional creep experiments. Initial estimates for the model parameters were obtained using an optimizing computer subroutine which examined 40 000 possible sets of model parameters using Eqs 2 and 3. Final model values for f and G were adjusted to improve the fit to the experimental primary creep, giving results as

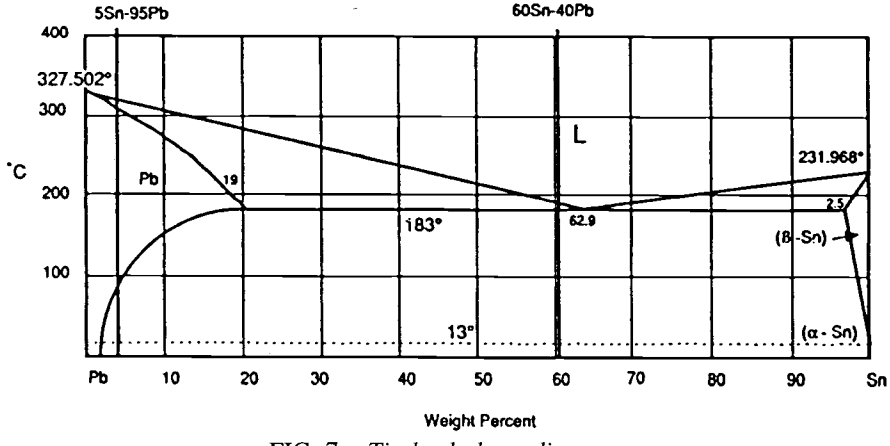

FIG. 7—*Tin-lead phase diagram.*

TABLE 1—*Composite and single-cell model parameters.*

Cell	f	G, GPa	A, s^{-1}	B, MPa^{-1}	m
1 (α phase)	[0.35] 0.33	[10.2] 7.0	2.54×10^{-7}	0.0676	7.0
2 (β phase)	[0.65] 0.67	[15.3] 17.4	7.26×10^{-7}	0.398	1.8
Single-cell	1	14.4	3.81×10^{-6}	0.678	4.38

NOTE: f = volume fraction; G = shear modulus; A, B = generalized creep coefficients; m = creep stress exponent.

shown in Fig. 8. Oscillations observed in the load rise at times below 0.1 s are the result of test system vibration and were included in the model analysis (Eq 3*b*). Final creep material parameters for both single- and two-cell models are shown in Table 1, where the bracketed values are initial estimates based on microstructure. The correlation of the distinct cells to phases of a binary system is not fundamental to the development of the model. Deforming regions may be more accurately represented by other appropriate microstructural features that differ in mechanical response, such as grain boundaries or colonies.

Comparison with Experiment

The objective for developing a back stress model for primary and steady-state creep is to more accurately represent the low-amplitude, mechanical behavior dominant in long life regimes. For purposes of comparison with typical creep models, a single-cell power-law creep model was derived using the steady-state creep rate values from Fig. 3. Two-cell model predictions were generated through iterative solution of Eqs 2, 3, and 4.

A comparison of both creep models with experimental stress relaxation data is shown in

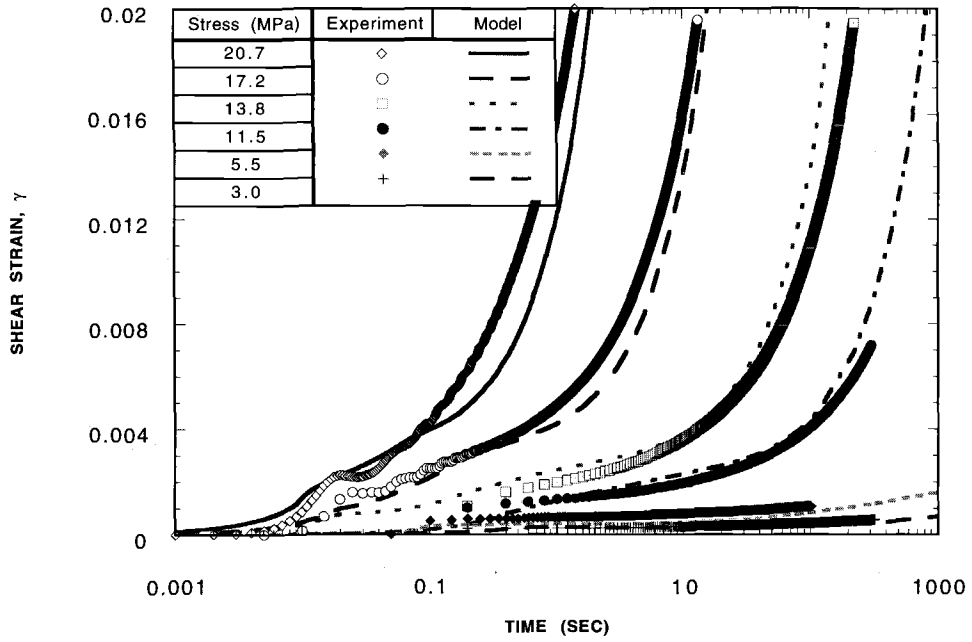

FIG. 8—*Correspondence of model prediction to monotonic torsional creep strain.*

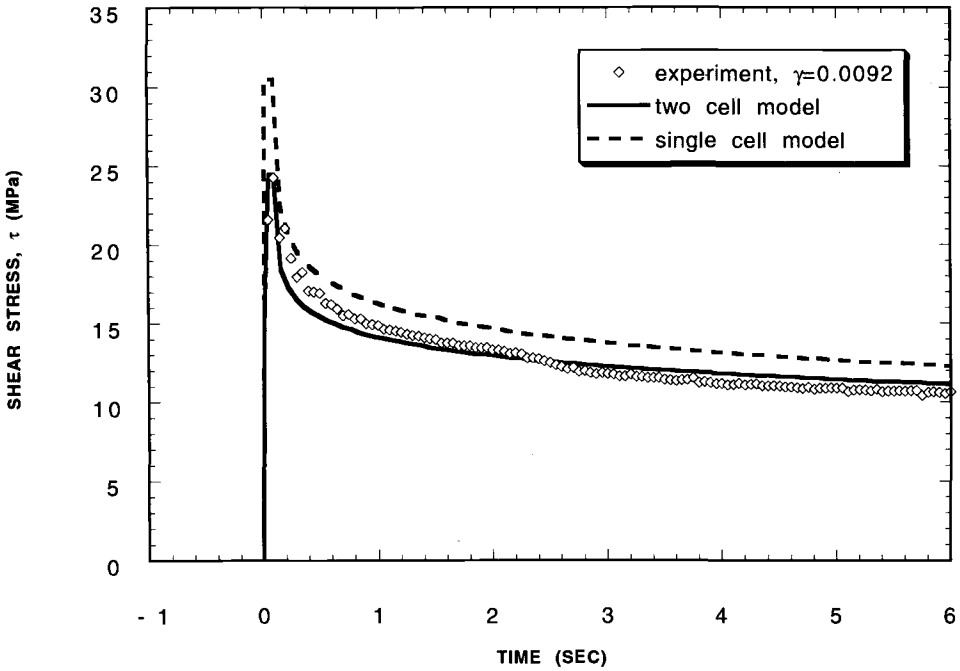

FIG. 9—*Correlation of model results to stress relaxation at* $\gamma = 0.0092$.

Fig. 9. The single-term, steady-state model greatly overestimates the initial stress where the deformation due to primary creep dominates. This behavior is expected from the monotonic creep results of Fig. 8, which show all strains below 0.4% to consist of mostly primary creep for all stress levels.

Fully reversed strain amplitude experiments provide a more revealing test of creep model limits. Figure 10 illustrates the importance of primary creep deformation for stress-controlled cyclic behavior. The early strain rise in the single-cell model is mostly elastic and of the expected magnitude. Comparison of the steady-state to the two-cell model shows that the apparent large elastic deformation observed experimentally is actually primary creep at high strain rates. Including primary creep in the deformation model provides higher strains at fixed stress conditions and lower stresses at fixed strain rates. The two-term model reproduces the asymmetric, stress-sensitive strain behavior that is neglected in the steady-state model.

Extrapolation of the single- and two-cell models to constant strain amplitude conditions emphasizes the importance of incorporating primary creep deformation in long life fatigue. Experimental low-cycle fatigue measurements taken before the onset of damage are compared to model calculations for a representative shear strain amplitude in Fig. 11. The single-cell power-law model anticipates the transition to steady-state deformation and, as a result, overestimates the shear stress amplitude. Small amplitude fatigue experiments are more accurately represented by the two-cell model, which accounts for the inherently large primary creep strain component. The relatively sharp transitions in stress-strain response of the two-cell model result from creep to steady-state transition in the first cell followed by a similar transition in the second cell. Further smoothing of the prediction would be obtained by increasing the constraints beyond two cells.

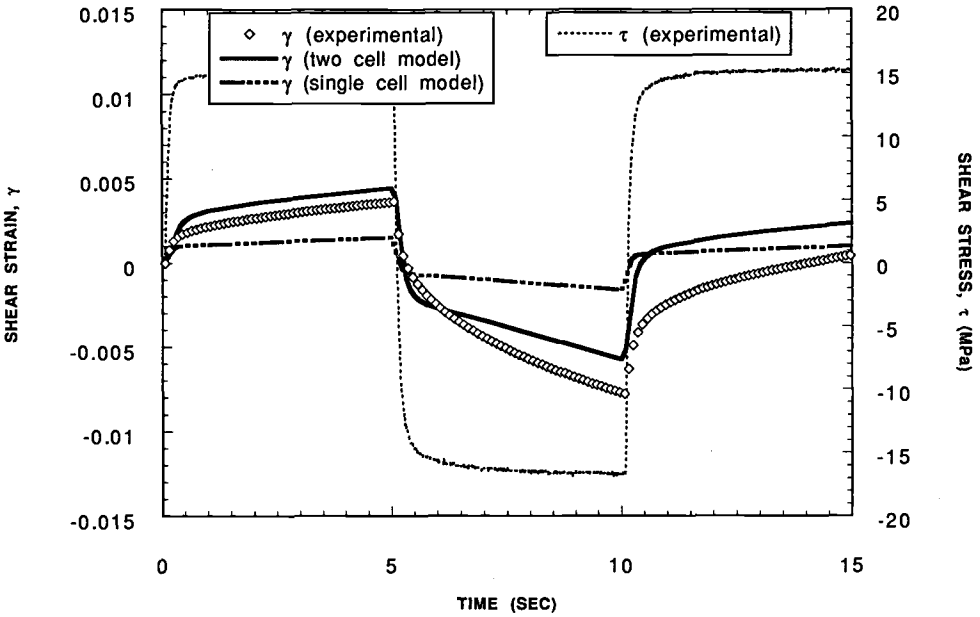

FIG. 10—*Correlation of model results to fully reversed stress hold.*

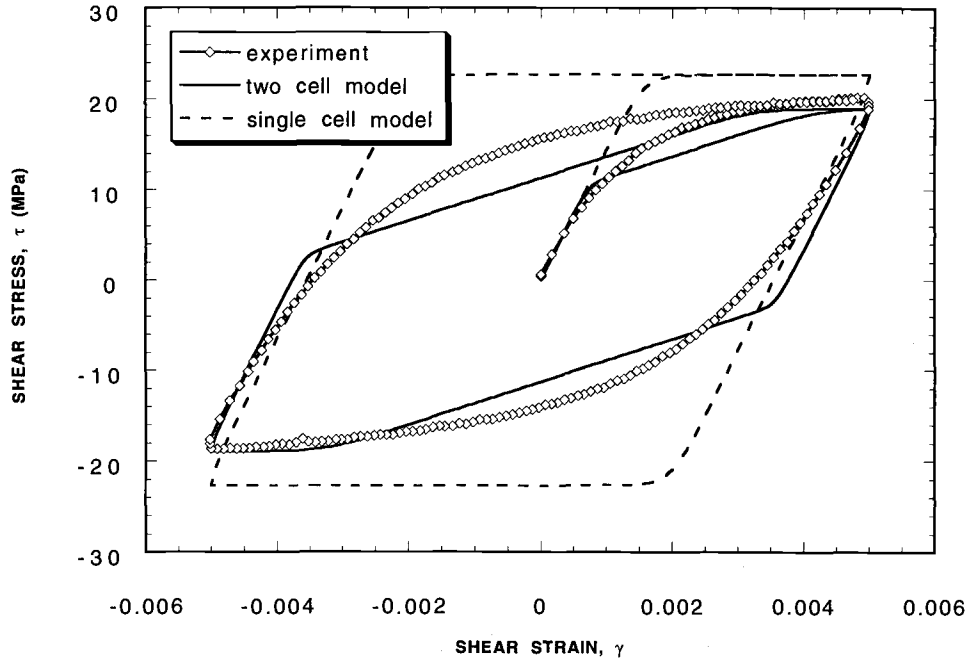

FIG. 11—*Representative correlation of model results to strain-controlled low-cycle fatigue (22°C, 0.003/s).*

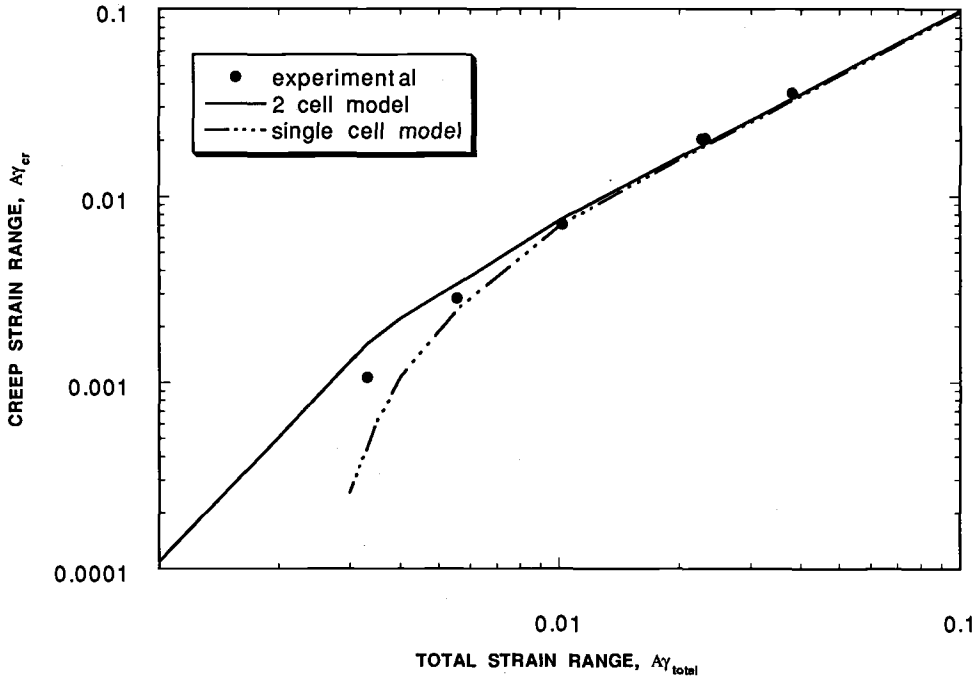

FIG. 12—*Creep and total strain range comparison of single- and two-cell methods for cyclic loading (0.003/s).*

Figures 12 and 13 compare the experimental and calculated shear stress and creep strain ranges for several shear strain amplitudes and rates. For large strain amplitudes, both the single- and two-cell models give identical results for the creep strain range. At small shear strains, the single-cell model overestimates the hysteresis. The single-cell model overpredicts the shear stress range for all strain amplitudes and rates examined (Figs. 13 and 14). The discrepancy in the calculated shear stress range is more pronounced at cyclic strains below 1%.

Use in Finite Element Analysis

A single-cell sine hyperbolic model is a standard feature of finite element solvers in the form of

$$\dot{\epsilon}_{ij}^{\text{creep}} = A(\sinh B\bar{\sigma})^m \exp\left(\frac{-Q}{kT}\right)\frac{\partial\bar{\sigma}}{\sigma_{ij}} \tag{5}$$

where $\bar{\sigma}$ is the effective stress. The two-cell model can be easily implemented in this form without developing special user material subroutines [*11*]. Two geometrically identical finite element meshes are generated and joined at the nodes. Each mesh is given differing elastic and creep properties (using Eq 5) as in the two-cell model. Model parameter B_i and the cell modulii need to be scaled by the volume fraction, and the coefficients A_i and B_i generalized from pure shear to the multiaxial stress-strain state.

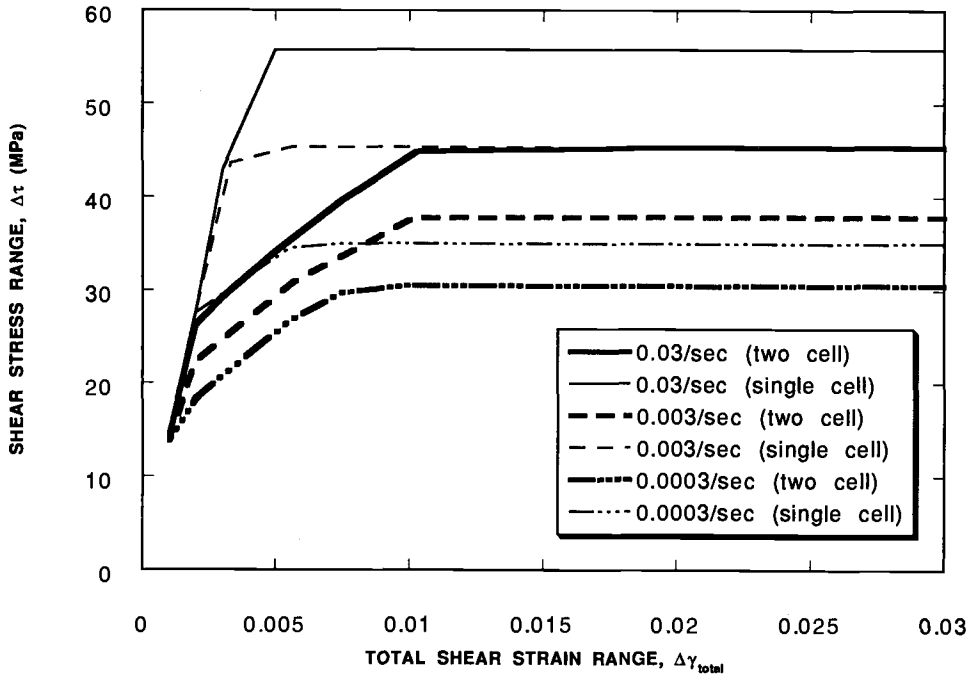

FIG. 13—*Comparison of cyclic shear stress range for one- and two-term models.*

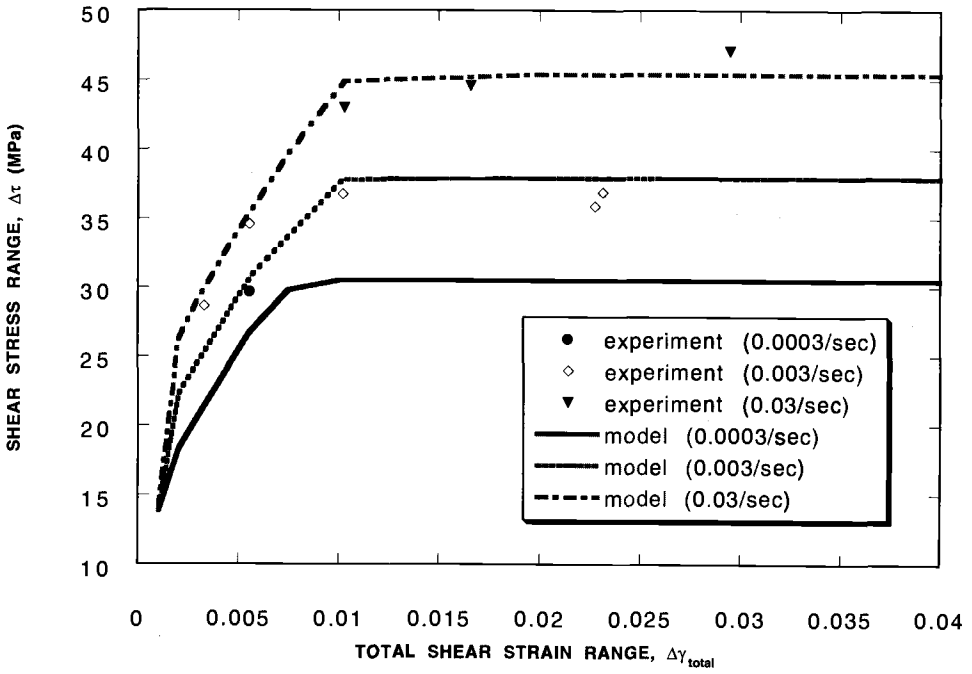

FIG. 14—*Theoretical (two-term model) cyclic shear stress range versus experimental.*

Summary

1. A model based on the elastic and power-law creep deformation of two compatible cells predicts primary creep and the transition to steady state in 63Sn-37Pb solder. Arbitrary stress-strain environments can be simulated.

2. Primary creep dominates at cyclic shear strains below 1% for all examined shear stress levels. Steady-state creep models underestimate strains for fixed stresses and overestimate stresses for fixed strains. Predictions of deformation and fatigue in this regime must account for transient behavior.

3. The model can accommodate thermal excursions by including an exponential term with the appropriate activation energies.

4. The model can be used for finite element analysis using standard sine hyperbolic creep rate expressions.

Acknowledgment

This work was funded by the Rockwell Independent Research and Development Program. The authors are indebted to J. G. Flintoff for assistance in preparation of the manuscript.

References

[1] Tribula, D., Grivas, D., Frear, D. R., and Morris, J. W., "Observations on the Mechanisms of Fatigue in Eutectic Pb-Sn Solder Joints," *Proceedings,* ASME Winter Annual Meeting, Chicago, IL, 27 Nov.–2 Dec. 1988, American Society of Mechanical Engineers, New York.

[2] Frear, D. R., Jones, W. B., and Kinsman, K. R., Eds., *Solder Mechanics: A State of the Art Assessment,* TMS Publications, Warrendale, PA, 1991.

[3] Enke, N. F., Kilinski, T. J., Schroeder, S. A., and Lesniak, J. K., "Mechanical Behaviors of 60/40 Tin-Lead Solder Lap Joints," *IEEE Transactions on Composites, Hybrids, and Manufacturing Technology,* Vol. 12, No. 4, December 1989, pp. 459–468.

[4] Pao, Y. H., "A Fracture Mechanics Approach to Thermal Fatigue Life Prediction of Solder Joints," *IEEE Transactions on Composites, Hybrids, and Manufacturing Technology,* Vol. 15, No. 4, August 1992.

[5] Wong, B. and Helling, D. E., "A Mechanistic Model for Solder Joint Failure Prediction Under Thermal Cycling," *Journal of Electronic Packaging,* Vol. 112, June 1990.

[6] Cortez, R., Fine, M. E., Daniel, I. M., and Jeannotte, D. A., "Torsion and Combined Tension-Torsion Fatigue of 63Sn-37Pb Solder," *Materials Developments in Microelectronic Packaging Conference Proceedings,* Montreal, Quebec, Canada, 19–22 Aug. 1991, pp. 147–154.

[7] Knecht, S. and Fox, L. R., "Constitutive Relation and Creep-Fatigue Life Model for Eutectic Tin-Lead Solder," *IEEE Transactions on Composites, Hybrids, and Manufacturing Technology,* Vol. 13, No. 2, June 1990, pp. 424–433.

[8] Vogler, S. and Blum, W., "Micromechanical Modelling of Creep in Terms of the Composite Model," *Creep and Fracture of Engineering Materials and Structures, Proceedings,* 4th International Conference, B. Wilshire and R. W. Evans, Eds., Institute of Metals, Swansea, U.K., April 1990, pp. 65–79.

[9] Nix, W. D. and Ilschner, B., in *Strength of Metals and Alloys (IC-SMA 5),* P. Haasen, V. Gerold, and G. Kostorz, Eds., Pergamon, Oxford, 1980, p. 1503.

[10] Schroeder, S. A. and Mitchell, M. R., "Torsional Creep Behavior of 63Sn-37Pb Solder," *Advances in Electronic Packaging,* Vol. 2, American Society of Mechanical Engineers, New York, 1992, pp. 649–653.

[11] Owen, D. R. J. and Hinton, E., *Finite Elements in Plasticity: Theory and Practice,* Pineridge Press Limited, Swansea, U.K., 1980, pp. 304–318.

Darrel R. Frear,[1] *N. Robert Sorensen,*[1] *and John S. Martens*[2]

Test Methodologies to Perform Valid Accelerated Thermomechanical Fatigue Tests of Solder Joints

REFERENCE: Frear, D. R., Sorensen, N. R., and Martens, J. S., **"Test Methodologies to Perform Valid Accelerated Thermomechanical Fatigue Tests of Solder Joints,"** *Fatigue of Electronic Materials, ASTM STP 1153,* S. A. Schroeder and M. R. Mitchell, Eds., American Society for Testing and Materials, Philadelphia, 1994, pp. 95–109.

ABSTRACT: Valid test parameters for performing thermomechanical fatigue tests are needed to make reasonable life prediction estimates for solder joints in electronic assemblies. We present the results of three test parameters that can be used to perform accelerated thermomechanical fatigue tests: deformation rate, hold time, and atmosphere. At deformation rates of $2.8 \times 10^{-4}\ s^{-1}$ and slower, the damage mechanism in the solder does not change and is in the form of heterogeneous coarsening at cell boundaries, indicating that this is a valid testing rate. Decreasing the hold time at the temperature extremes to the point where the stress relaxes to zero at the high-temperature portion of the thermal cycle results in the same solder joint behavior as longer hold times. Accelerating the test by changing environment was found to change the damage mechanism and is not a valid means of accelerating thermomechanical fatigue tests for solder joints.

KEYWORDS: solder, thermomechanical fatigue, accelerated test parameters, atmospheric corrosion

The reliability of an electronic assembly is, in part, measured by how long the system lasts in the field. Field life can be limited by the electrical/mechanical interconnections made by the solder joints in the system. The failure of a solder joint can render an entire system inoperable. Strain can be imposed to solder joints when the system encounters temperature fluctuations because the joined components have different coefficients of thermal expansion. The temperature fluctuations occur at a low frequency, such as the diurnal cycles of a system that is turned on and off once a day. This results in a condition of thermomechanical fatigue under which solder joints can fail. It is well established that the microstructure of near eutectic Sn-Pb solder (the alloy commonly used in electronic assemblies) evolves under conditions of thermomechanical fatigue [*1–7*]. The imposed strain localizes into heterogeneous bands in the solder joint. Eventually, cracks form in the coarsened bands and the joint fails.

A number of methodologies have been proposed for determining reliability through lifetime prediction of solder joints under conditions of thermomechanical fatigue. A detailed summary and critical review of these methodologies is found elsewhere [*8,9*]. The most

[1]Sandia National Laboratories, Albuquerque, NM 87185-0340.
[2]Conductus Corp., Sunnyvale, CA 94086.

commonly used technique for life prediction is based upon the Coffin-Manson low-cycle fatigue relationship [*10–13*], which relates fatigue life, N_f, to the applied plastic strains

$$N_f = \left(\frac{\Delta\gamma}{2\epsilon'}\right)^c$$

where N_f is the fatigue life, $\Delta\gamma$ is the applied plastic shear strain, ϵ' is the strain ductility coefficient (empirically derived), and c is an empirically derived constant. Life is estimated by performing fatigue experiments at a variety of strain ranges, then fitting the data on a log-log plot of N_f versus $\Delta\gamma$ to derive the necessary constants (c and ϵ').

A number of variations exist on the Coffin-Manson relationship such as: frequency-modified Coffin-Manson [*14,15*], strain range partitioning [*16*], and figures of merit [*17*]. These methods are all variants of one another and have a common basis in that it is necessary to have experimental data to derive the empirical constants. For the empirical constants to be accurate, a large number of fatigue tests must be performed. An additional time constraint is that thermal cycles on electronic systems are typically on the order of a few cycles a day for up to 30 years of life. Therefore, the tests must be accelerated to provide information in a timely fashion. However, the valid fatigue test must shorten the time to failure of a solder joint without changing the mechanisms that cause the joint to fail.

There are four variables that can be changed to accelerate a thermomechanical fatigue test on a solder joint:

1. Increase the temperature extremes beyond what is typically encountered.
2. Increase the rate at which the temperature and strain are imposed (increase the deformation rate).
3. Decrease the time spent at the temperature extremes (decrease the hold times).
4. Increase the severity of the environment.

The first option is typically used in isothermal fatigue tests for test acceleration. However, the first option is not a viable alternative for thermomechanical fatigue; by changing the temperature extremes, the deformation mechanisms in the solder can change, and the testing results cannot be applied to real use conditions [*18*]. The other three acceleration methods can be used in thermomechanical fatigue tests. However, it has yet to be demonstrated whether these methods of test acceleration cause solder joints to behave in a similar fashion as those in the field.

There is a great deal of variability in test techniques used to perform thermomechanical fatigue of solder joints, which obfuscates comparison of results between studies. We propose a standardized test method for performing thermomechanical fatigue on solder joints. Furthermore, results that show which options are reasonable for accelerating a thermomechanical fatigue test and yet retain the damage mechanisms found in real use conditions are presented. This paper concludes with specific recommendations for performing valid accelerated thermomechanical fatigue tests.

Experimental Procedure

A summary of the thermomechanical fatigue test method and oxide characterization and growth kinetics are given below.

The specimen used to test solder joints is shown in the schematic drawing in Fig. 1. The specimen consists of 18 electrically isolated solder joints that deform nominally in shear when the specimen is gripped on the ends. Strain is imposed upon the solder joints by a

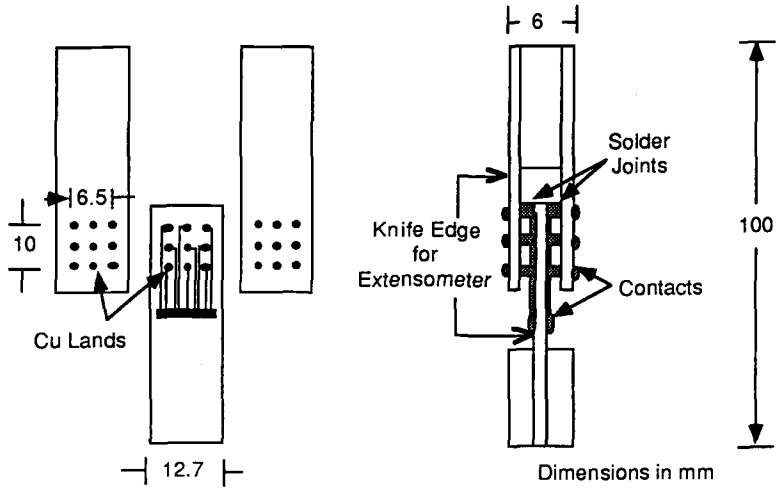

FIG. 1—*Thermomechanical fatigue specimen.*

servohydraulic load frame operated under strain control. Thermal fluctuations are induced by a chamber that fits around the specimen in the load frame. Air circulated around the specimen is heated with resistive heating coils and cooled by vaporized liquid nitrogen. The strain and temperature are digitally controlled by a computer. The temperature extremes are −55° to 125°C at 10% shear strain. A photograph of the test system is shown in Fig. 2.

The thermal cycle consists of a ramp in strain and temperature to the elevated temperature extreme and hold period, a ramp down, and another hold at the low temperature extreme. Failures are monitored electrically using an event detector. An event detector measures spikes in resistance of greater than 500 Ω for periods of time less than 1 μs. Final failure was defined when all 18 joints exhibited spikes in resistance greater than 500 Ω. However, individual joints fail before this point, and tests are interrupted to perform metallography on the samples to observe the failed joints and those that have not yet failed. Event detector data along with load, temperature, and strain are collected and stored digitally. The data are plotted in the form of number of cycles versus solder joint load. An illustration of hysteresis loops from which data were gathered is shown in Fig. 3. The data plotted are: the high-temperature load maximum, low-temperature load maximum, and the load after the high-temperature hold as a function of the number of thermal cycles.

To examine the effect of environment, TMF tests were performed in inert gas (nominally N_2), dry oxygen-rich air, and high-humidity (60% RH) environments. The inert environment consisted of the nitrogen from the cold portion of the thermal cycle continually circulating around the solder joints during the entire test. Dry oxygen (95% pure) was introduced to the specimen at a flow rate of 40×10^4 mm^3 s^{-1} through a piece of TFE-fluorocarbon tubing situated immediately adjacent to the solder joints. The oxygen concentration at the solder joints was about 40%. High-humidity tests were performed by bubbling air through deionized water, which was then circulated around the specimen and resulted in a 60% RH environment.

Experiments were performed at three deformation rates and hold times. These test conditions are summarized in Table 1.

The formation and growth of the oxide film on the solder was followed using a confocal resonance technique [*19*]. Bulk samples of solder were suspended in a chamber during the

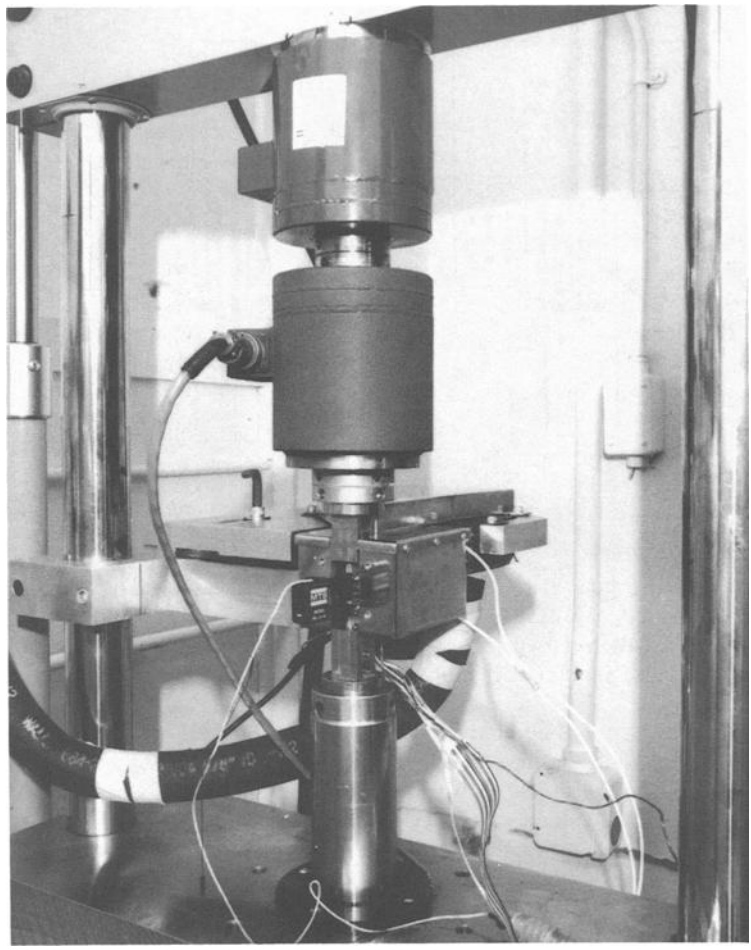

FIG. 2—*The test system used to perform thermomechanical fatigue tests.*

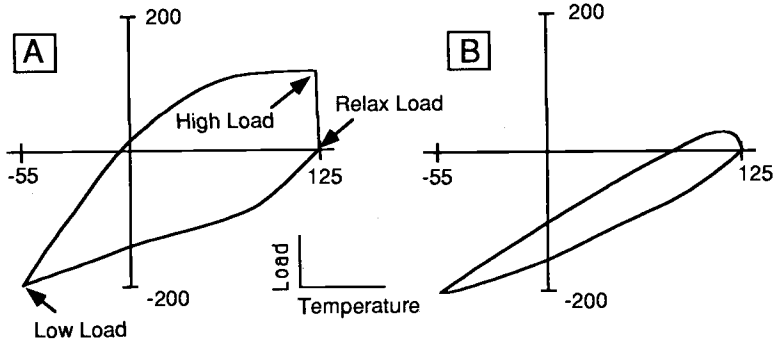

FIG. 3—*Schematic illustration of a hysteresis loop of load versus strain.*

TABLE 1—*Test conditions.*

Test	Deformation Rate, s^{-1}	Hold Time, min	Environment
A	5.6×10^{-4}	0, 3, 6	N_2
B	2.8×10^{-4}	0, 3, 6	N_2
C	2.1×10^{-4}	0, 3, 6	N_2
D	2.8×10^{-4}	3	N_2, dry O_2, 60% RH

thermomechanical fatigue tests and were later analyzed using the confocal resonator to determine oxide composition and thickness. The confocal resonator works by measuring the surface conductivity of a sample. A spherical mirror is placed above a flat sample to form a resonant cavity. A resonant wave is established between the sample and the mirror. By measuring the power of the input versus the reflected wave, information about the surface conductivity of the sample can be obtained [*19*].

Thermomechanical fatigue specimens were sectioned after testing to optically characterize the microstructure. Standard metallographic techniques were used to polish the specimen down to 1 μm. A final polishing/etching step was performed in a slightly acidic colloidal suspension of 0.1 μm alumina to highlight the solder microstructural details.

Results and Discussion

Thermomechanical fatigue tests were performed to examine the effect of accelerating the deformation rate, shortening the hold time, and increasing the effect of the environment on the mechanical and microstructural behavior of 60Sn-40Pb solder. The goal of this study was to determine which parameters could be accelerated and to what extent without changing the failure mode observed in service failures.

Effect of Deformation Rate

Increasing the deformation rate accelerates a thermomechanical fatigue test by shortening the time spent going from one temperature and strain extreme to the other. Thermomechanical fatigue tests were performed at increasingly slower deformation rates until a condition was found where further slowing of the deformation rate did not change the microstructural evolution and mechanical behavior of the solder. Deformation rates of $5.6 \times 10^{-4}\ s^{-1}$, $2.8 \times 10^{-4}\ s^{-1}$, and $2.1 \times 10^{-4}\ s^{-1}$ were examined at a hold time of 6 min at each temperature extreme. Plots of the load versus the number of cycles are shown in Fig. 4.

At the fastest deformation rate of $5.6 \times 10^{-4}\ s^{-1}$, failures occurred after 75 cycles. Slowing the deformation rate by a factor of two to $2.8 \times 10^{-4}\ s^{-1}$ increased the life threefold to 250 cycles. Further decreases in the deformation rate had a negligible effect on the lifetime of the solder joints (Fig. 4*C*).

Figure 5 shows the microstructure of the solder joints at deformation rates of $5.6 \times 10^{-4}\ s^{-1}$, $2.8 \times 10^{-4}\ s^{-1}$, and $2.1 \times 10^{-4}\ s^{-1}$. At the fastest deformation rate, after 75 cycles, there is clear evidence of a heterogeneous coarsened band and a crack running through that coarsened region. The coarsening occurs parallel to the direction of imposed shear strain and cuts across microstructural features rather than following the colony boundaries. At the slower deformation rates, after 300 cycles, heterogeneous coarsening is observed only at the colony boundaries. Cracks form in the coarsened regions after 300 cycles, but are not nearly as extensive as at deformation rates of $5.6 \times 10^{-4}\ s^{-1}$ or faster.

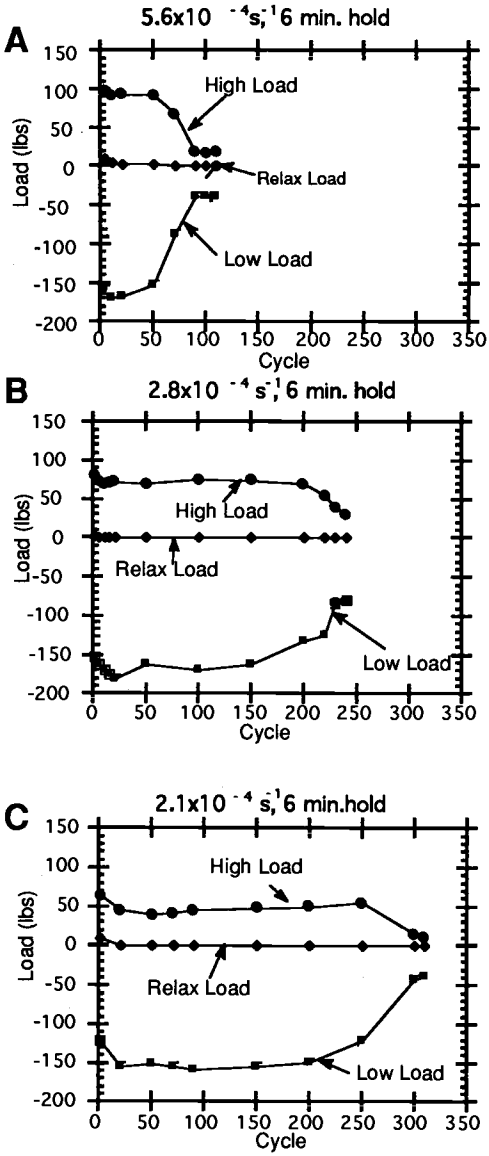

FIG. 4—*Plots of load versus the number of cycles for three deformation rates:* (A) $5.6 \times 10^{-4}\ s^{-1}$, (B) $2.8 \times 10^{-4}\ s^{-1}$, *and* (C) $2.1 \times 10^{-4}\ s^{-1}$.

Based upon the mechanical and microstructural results, there is a change in the damage mechanism in reducing the deformation rate from $5.6 \times 10^{-4}\ s^{-1}$ to $2.8 \times 10^{-4}\ s^{-1}$ and slower. At the slower deformation rate, the strain is accommodated within the solder at the eutectic colony boundaries. These boundaries are slightly coarsened upon solidification (they are the last regions of the joint to solidify). Following a Hall-Petch relationship, the coarsened regions are the weakest part of the microstructure. At the low-temperature portion of the thermal cycle, damage accumulates primarily at the colony boundaries and very little

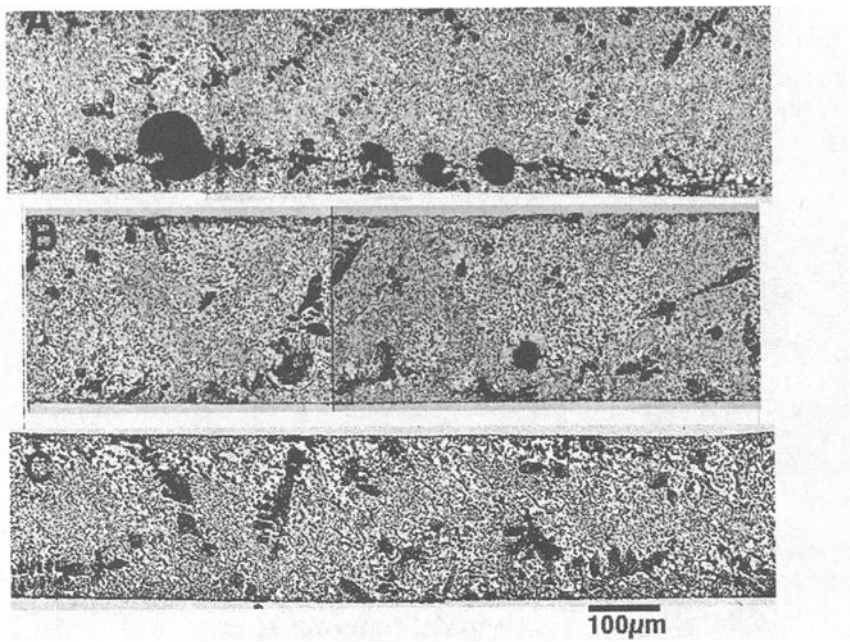

FIG. 5—*Optical micrographs of the 60Sn-40Pb solder joints for three deformation rates:* (A) *5.6* $\times$ 10^{-4} s^{-1} *(100 cycles),* (B) *2.8* $\times$ 10^{-4} s^{-1} *(300 cycles), and* (C) *2.1* $\times$ 10^{-4} s^{-1} *(300 cycles).*

in the rest of the solder. At the high-temperature portion of the thermal cycle, the damage is annealed out, which promotes coarsening of the colony boundaries. Subsequent cycles repeat the process until the joint fails by intergranular cracking of the coarsened tin-rich phase.

At the faster deformation rates (>5.6 $\times$ 10^{-4} s^{-1}), the strain is not accommodated primarily at the colony boundaries but at a region in the solder joint where there is a stress concentration parallel to the direction of imposed shear strain. In this case, the deformation is imparted to the solder too quickly to be accommodated at the colony boundaries, by colony sliding and rotation, and is imposed to a thin region in the solder joint where there is a stress concentration. The faster deformation rates have a shorter lifetime because the strain is concentrated into a much thinner region of the joint, rather than at colony boundaries, which accelerates the coarsening process and leads to a more rapid failure. It has been documented that eutectic Sn-Pb colonies can slide and rotate relative to one another [*6,7*]. Creep studies at elevated temperatures have shown that sliding and rotation in near eutectic solders occurs only at slower deformation rates [*20*]. The present work documents that this happens in thermomechanical fatigue at deformation rates of 2.8 $\times$ 10^{-1} s^{-1} or slower.

Effect of Hold Time

Thermomechanical fatigue tests can be dramatically accelerated by shortening the hold time at each temperature extreme. This effect was explored by performing thermomechanical fatigue tests at a deformation rate of 2.8 $\times$ 10^{-4} s^{-1} and hold times that increased in length until a time was found beyond which no additional changes to the microstructural and mechanical response were observed.

Figure 6 shows the load versus number of cycles for hold times of 0 (no hold time), 3, and 6 min. Solder joints that experienced no hold time did not fail, even after 500 cycles. Adding a hold time of 3 min resulted in a life of 250 cycles. An increase in hold time beyond 3 min had no significant effect on thermomechanical fatigue life.

Figure 7 shows the microstructure of the solder joints at 0, 3, and 6-min hold times after 500, 300, and 300 cycles, respectively. With no hold time there is no microstructural

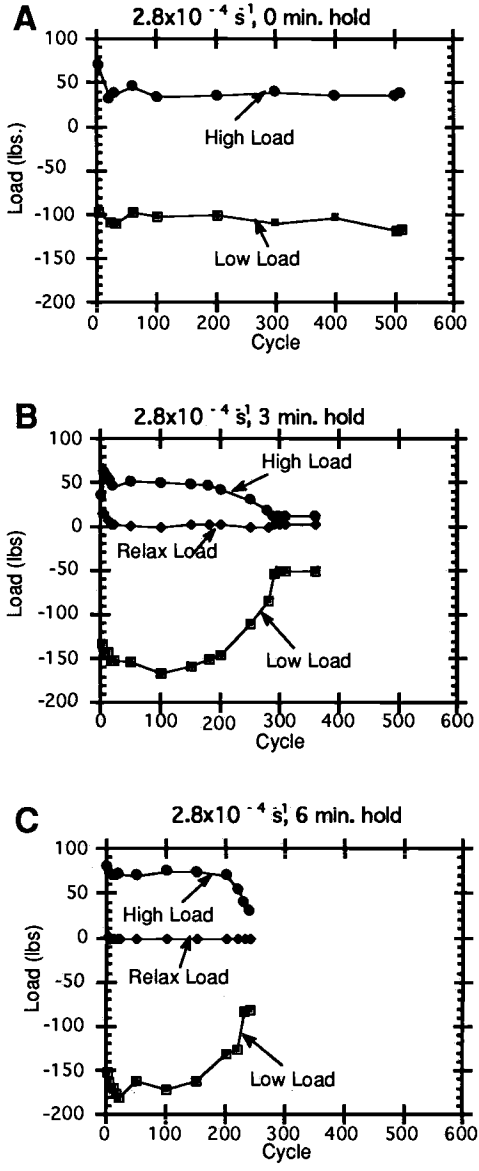

FIG. 6—*Plots of load versus the number of cycles for three different hold times:* (A) *0 min,* (B) *3 min,* (C) *6 min at a deformation rate of* $2.8 \times 10^{-4}\ s^{-1}$.

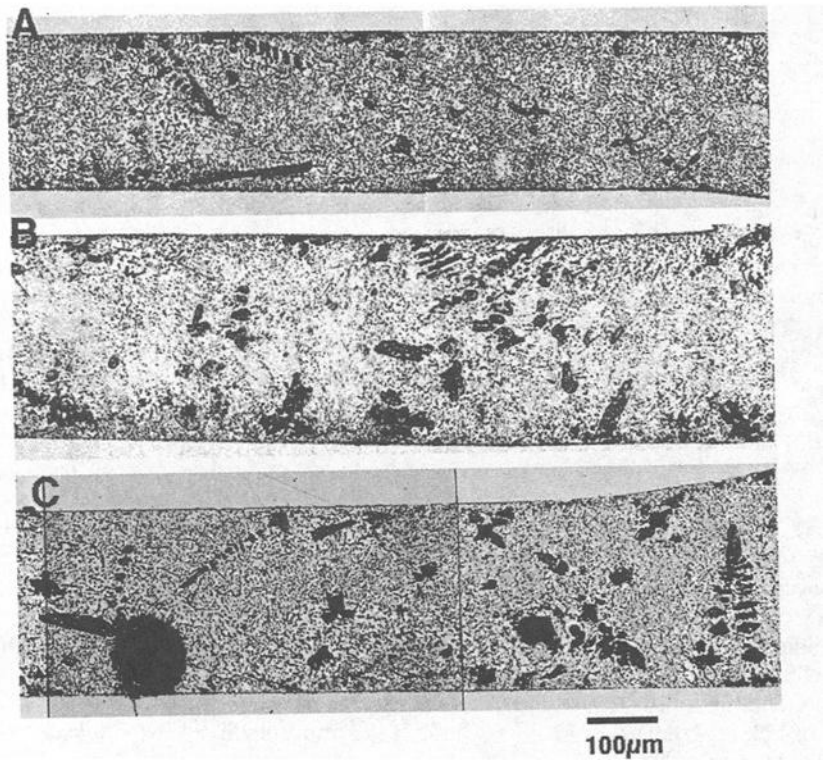

FIG. 7—*Optical micrographs of the 60Sn-40Pb solder joints for the three hold times:* (A) *0 min (500 cycles),* (B) *3 min (300 cycles), and* (C) *6 min (300 cycles).*

evolution or heterogeneous coarsening. After 3- and 6-min hold times the microstructure has a similar appearance with heterogeneous coarsening at the colony boundaries.

When there is no hold time, heterogeneous coarsening is limited because the solder does not have enough time at the elevated temperature to anneal out the damage. This is also found in the hysteresis behavior of the solder that shows no relaxation of the stress at either the low- or high-temperature portion of the thermal cycle. When a hold time is added to the thermal cycle, stress relaxation occurs at the high-temperature portion of the thermal cycle (125°C) and damage is annealed out. Negligible stress relaxation occurs at the low-temperature (−55°C) portion of the thermal cycle. Under the test conditions of the present study (temperature range of −55 to 125°C and 10% shear strain), relaxation to zero stress at the high-temperature portion of the thermal cycle occurs in just under 3 min. Hold times longer than 3 min do not change the material response because the strongest effect is the deformation-induced heterogeneous coarsening, not thermally induced homogeneous coarsening [*18*].

Results of the hold time tests show that a hold time just long enough to allow complete stress relaxation at the high-temperature portion of the thermal cycle can be used to accelerate the thermomechanical fatigue test. In tests over a temperature range of −55 to 125°C, a hold time of at least 3 min at 125°C is sufficient. No hold time is needed at −55°C. If

thermomechanical fatigue tests were to be performed at other temperature extremes, the hold time may vary. Hold times become necessary at the low-temperature portion of the thermal cycle if significant stress relaxation can occur during actual use conditions.

Isothermal versus Thermomechanical Fatigue Tests for Hold Time and Deformation Rate

Isothermal fatigue is often used as a mechanism to accelerate the conditions found for thermomechanical fatigue applications. It is reasonable to compare the thermomechanical fatigue results presented in this paper with that in the literature for isothermal fatigue to determine whether isothermal fatigue is a valid means to accelerate a test.

The deformation rate effect has been studied extensively for the isothermal fatigue behavior of 60Sn-40Pb [*21–24*]. Typically a sawtooth wave form was used, and deformation rate was changed by varying the frequency. Solomon [*21–23*] and others [*24*] observed that as frequency decreases, the isothermal fatigue life also decreases. This is caused by imparting additional damage to the solder joint by creep and stress relaxation processes at lower frequencies. These phenomena occur in isothermal fatigue because the damage mechanisms are the same throughout each fatigue cycle. During thermomechanical fatigue where there are large thermal cycles, however, there are two operative mechanisms: low-temperature damage accumulation and high-temperature annealing (coarsening). An isothermal fatigue cycle can experience only one of these mechanisms.

Fox et al. [*25*] observed the fatigue life to decrease with decreasing frequencies during thermomechanical fatigue of 60Sn-40Pb solder. However, Fox et al. used a sawtooth wave form with no hold times. As discussed above, the results of thermomechanical fatigue tests with no hold times differ greatly from those tests that incorporate hold times. Therefore, the result of Fox et al. is not surprising because, if the frequency in a sawtooth cycle is slowed sufficiently, damage can be annealed at the high-temperature portion of the cycle. Sawtooth waveforms should not be used for thermomechanical fatigue tests because this cycle is not representative of actual use conditions.

Stainless steels under conditions of thermomechanical fatigue also show that slower deformation rates shorten the fatigue life [*26*]. However, these stainless steel results cannot be used in the interpretation of solder results for several reasons. Stainless steels, at slower deformation rates, are prone to creep cavity formation and growth and 60Sn-40Pb solder does not form creep cavities in shear thermomechanical fatigue. Furthermore, there is extensive microstructural evolution in solders that is not found in steels. Therefore, a comparison between the two material results is not valid.

Effect of Environment

Solder joints that are not hermetically sealed can be exposed to environments that could degrade their fatigue life. Snowden [*27*], Berriche [*28*], and Lacey and Woodford [*29*] looked at the fatigue life of Pb and Sn-Pb alloys and found that the presence of oxygen dramatically reduces the isothermal fatigue life of solder joints. The environments of concern are oxygen and humidity. If environment is to be used to accelerate the thermomechanical fatigue tests, the effect of environment must be understood.

The effect of environment was characterized by exploring three atmospheric conditions. These environments included:

1. Oxygen-depleted nitrogen atmosphere.
2. Dry oxygen enriched air (measured at 40% oxygen).
3. Air containing 60% relative humidity.

Thermomechanical fatigue tests were performed at a deformation rate of $2.8 \times 10^{-1}\ s^{-1}$ with 3-min hold times at the temperature/strain extremes. Bulk solder samples, polished to a 0.1-μm finish, were also exposed to the same environments in order to characterize the oxidation processes with a confocal resonator.

Plots of the effect of oxygen and humidity on thermomechanical fatigue life are shown in Figs. 8 and 9. The thermomechanical fatigue life of joints in the presence of oxygen was slightly longer than in the inert environment. However, in a 60% RH atmosphere, the life decreased from the 250 cycles for the inert environment to 150 cycles in high humidity.

Figure 10 shows the microstructure of the joint after 250 cycles in dry oxygen (Fig. 10*A*) and 60% RH (Fig. 10*B*). In Fig. 10*A* (dry oxygen), the joint cracked through the heterogeneous coarsened region. However, the crack appears to have initiated in both the center of the

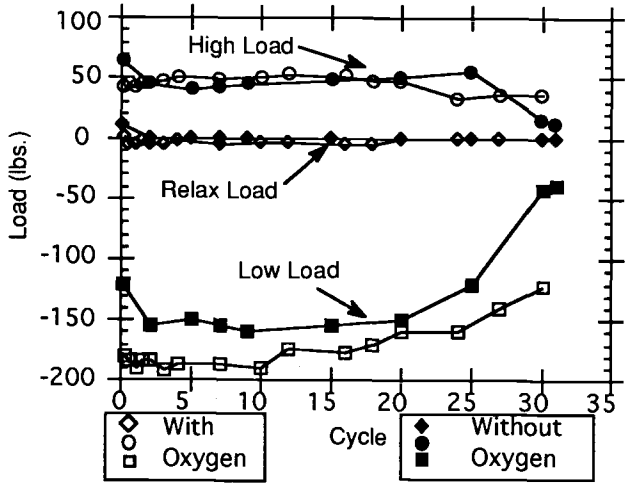

FIG. 8—*Plots of load versus the number of cycles for an inert environment and a 40% dry oxygen environment.*

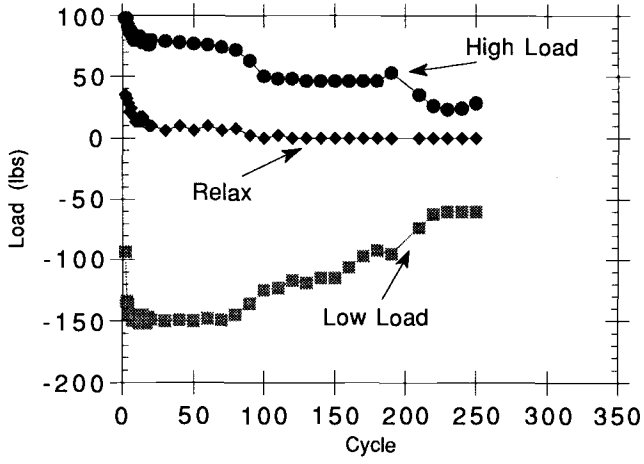

FIG. 9—*Plots of load versus the number of cycles for a 60% RH environment.*

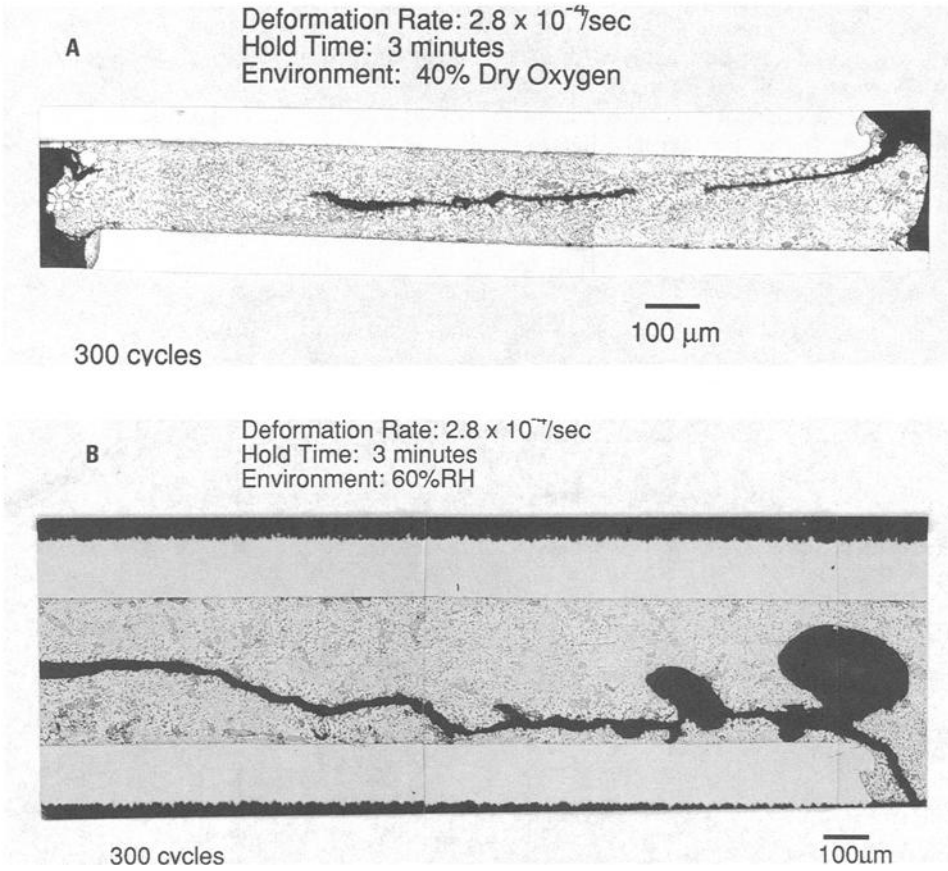

FIG. 10—*Optical micrographs of the 60Sn-40Pb solder joint at 250 cycles for:* (A) *40% dry oxygen, and* (B) *60% RH atmospheres.*

joint and at one of the edges. In Fig. 10*B* (60% RH), the joint also cracked through the coarsened bands, and cracks formed in two different regions in the joint, but initiation of the crack occurs on the surface of the joints.

These experiments indicate that dry oxygen has little, if any, effect on the thermomechanical fatigue life of the solder. There is some evidence that the crack initiation site changes from the surface of the joint to the interior. This could be caused by diffusion of oxygen into the solder at the surface, which suppresses grain coarsening by a pinning process. If the grains on the surface do not heterogeneously coarsen, the thermomechanical fatigue life increases. In a humid environment, a significant decrease in fatigue life was observed. This could be due to an atmospheric corrosion process. At humidity levels above 50% RH, the absorbed water vapor can begin to behave like a bulk electrolyte, which will enhance the corrosion (oxidation) process. Enhanced corrosion of the surface of the solder could lead to the formation of cracks that, if present near the heterogeneous coarsened band, could accelerate failure.

Confocal resonator measurements were made to determine the thickness and type of oxide present on the solder under the environmental conditions tested. Figure 11 shows the results of the oxidation experiments. Figure 11*A* shows the total oxide thickness as a function of

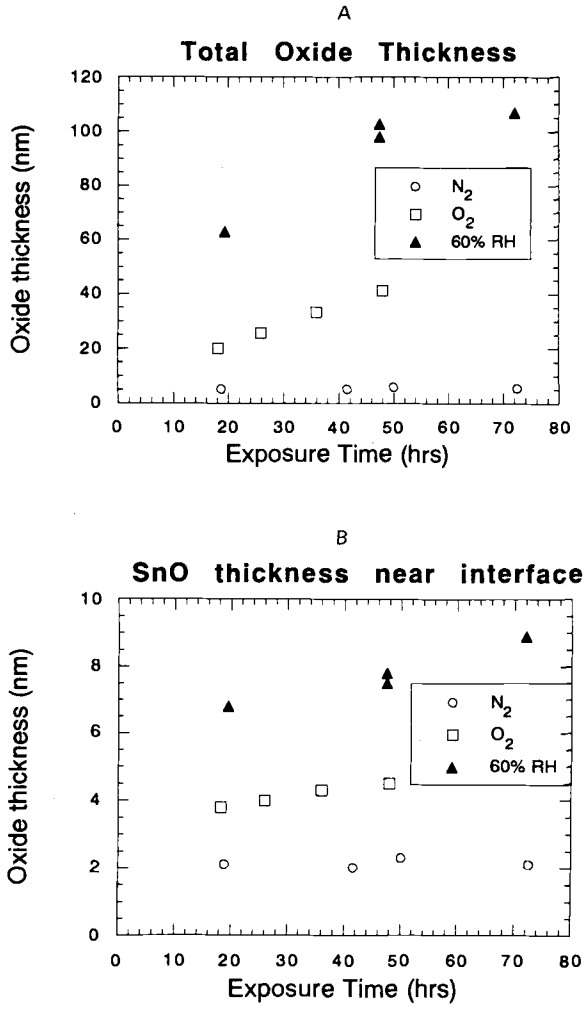

FIG. 11—*Plot of oxide thickness on solder as a function of exposure time for exposure to nitrogen, oxygen and humid air. Part* (A) *shows total film thickness and* (B) *presents thickness data for an inner SnO film at the metal film interface.*

exposure time for the three environments. In Fig. 11*B*, the thickness of an inner SnO layer, present at the metal-film interface, is shown. Testing in the nitrogen environment resulted in essentially no oxidation of the solder. The total oxide thickness, as well as the SnO layer, remained constant throughout the test. Subjecting the sample to oxygen caused a slight increase in the initial inner SnO layer, but the layer was stable and did not increase in thickness throughout the test. The outer layer, composed of SnO_2, exhibited continuous growth with apparently linear kinetics throughout the test. The samples exposed to elevated humidity had the thickest SnO layers, but remained fairly constant in thickness throughout the test. The outer layer was thicker than for the oxygen samples and exhibited what may be parabolic film growth kinetics.

From these tests, it is apparent that both oxygen and humidity accelerate oxidation of the solder. There is some evidence that the films formed are similar and that only the kinetics

have been increased. This is not unexpected since the primary function of humidity is to increase the thickness of the water film on the surface and allow the surface to undergo electrochemical, rather than gas phase, oxidation. Thus, one might expect that the film thickness would be similar for the two environments after extended exposure.

Based upon the results of the environmental thermomechanical fatigue tests, recommendations for accelerated testing can be made. It is clear that dry oxygen has the same effect on fatigue behavior as an inert environment and therefore is not an enhancement mechanism. High humidity does shorten the thermomechanical fatigue life. The damage mechanism in this case is associated with surface corrosion. The corrosion process has been accelerated by the presence of humidity. The composition of the oxide is similar to that formed in dry air and may reach a limiting thickness more rapidly. If oxidation of the solder contributes to the fatigue process experienced in the field, humidity may be a suitable accelerating factor for thermomechanical fatigue tests in the laboratory.

Thermomechanical Fatigue Test Recommendations

Valid accelerated thermomechanical fatigue tests can be performed over a temperature range of $-55°$ to 125°C with a nominal 10% shear strain if the following conditions are met:

1. The deformation rate must be $2.8 \times 10^{-4}\ s^{-1}$ or slower.
2. Hold times of sufficient length to relax the stress at the high-temperature portion of the thermal cycle (at 125°C for 3 min). If there is very limited relaxation at the low-temperature portion of the thermal cycle during use conditions, no hold time is needed at the low temperature.
3. Increasing the severity of the environment by adding water vapor to the atmosphere may be an accelerating factor provided that solder oxidation contributes to thermomechanical fatigue of solder joints in the field.

Summary and Conclusions

Tests were performed to determine the valid acceleration parameters for thermomechanical fatigue testing of solder joints. The parameters characterized were deformation rate, hold time, and environment. At deformation rates faster than $2.8 \times 10^{-4}\ s^{-1}$, the damage accumulates in the form of a heterogeneous coarsened band parallel to the direction of imposed shear strain independent of the microstructural features. The fatigue life at faster deformation rates results in a shorter number of cycles to failure. At deformation rates of $2.8 \times 10^{-4}\ s^{-1}$ and slower, damage occurs in the form of heterogeneous coarsening at colony boundaries. Reducing the deformation rates further has no effect on the thermomechanical fatigue process. Therefore a valid accelerated deformation rate is $2.8 \times 10^{-4}\ s^{-1}$.

If there is no hold time at the temperature/strain extremes, fatigue life is extended because heterogeneous coarsening does not have sufficient time to occur. Hold times at the elevated temperature portion of the thermal cycle sufficiently long to allow the stress to relax to zero results in the same number of cycles to failure as for longer hold times. For a thermal cycle of -55 to 125°C, a hold time of 3 min is a valid acceleration parameter.

The effect of dry oxygen and high-humidity atmospheres were explored as acceleration parameters. Dry oxygen results in a slight increase in the fatigue life due to diffusion of oxygen into the solder surface, limiting the heterogeneous coarsening. An increased level of humidity over 50% RH results in a decreased life due to a surface corrosion mechanism. A high-humidity environment may be an accelerating factor provided that solder oxidation

contributes to thermomechanical fatigue of solder joints in service. Further work is needed to clarify this point.

Acknowledgments

The authors would like to thank Jan Finch for performing the fatigue tests and Alice Kilgo for the metallography. This work, performed at Sandia National Laboratories, was supported by the U.S. Department of Energy under contract DE-AC04-76DP00789.

References

[1] Wild, R. N., *Welding Research Supplement,* Vol. 51, 1972, p. 521s.
[2] Bangs, E. R. and Beal, R. E., *Welding Research Supplement,* 1975, p. 377s.
[3] Frear, D. R., *IEEE Transactions on Composites, Hybrids, and Manufacturing Technology,* CHMT-12, 1989, pp. 492–501.
[4] Frear, D. R. and Jones, W. B., *Proceedings,* NEPCON West '90, 1990, p. 1340.
[5] Frear, D. R., *Proceedings,* 40th ECTC Conference, Vol. 40, 1990, p. 510.
[6] Frear, D. R., in *Solder Mechanics—A State of the Art Assessment,* D. R. Frear, W. B. Jones, and K. R. Kinsman, Eds., TMS Publications, Warrendale, PA, 1991.
[7] Lee, S. M. and Stone, D. S., *Proceedings,* 40th IEEE ECTS, Vol. 40, 1990, p. 491.
[8] Sandor, B. I., "Life Prediction of Solder Joints: Engineering Mechanics Methods," *Solder Mechanics—A State of the Art Assessment,* TMS publications, D. R. Frear, W. B. Jones, and K. R. Kinsman, Eds., 1991.
[9] Solomon, H. D., "Life Prediction and Accelerated Testing," *The Mechanics of Solder Alloy Interconnects,* S. N. Burchett, D. R. Frear, H. Morgan, and J. Lau, Eds., Van Nostrand Reinhold, New York, 1993.
[10] Coffin, L. F., Jr., *Transactions ASME,* Vol. 76, 1954, pp. 931–950.
[11] Manson, S. S., "Behavior of Materials Under Conditions of Thermal Stress," *Proceedings,* Heat Transfer Symposium, University of Michigan, 27–28 June 1952, University of Michigan Press; also NACA TN2933, July 1953.
[12] Manson, S. S., *Mechanical Design,* Vol. 32, No. 14, 1960, pp. 139–144.
[13] Coffin, L. F., Jr., in *Fracture 1969,* Chapman and Hall, London, 1969.
[14] Coffin, L. F., Jr., *Journal of Materials,* Vol. 6, 1971, pp. 388–402.
[15] Solomon, H. D., *Proceedings,* 38th Electronic Components Conference, Vol. 38, 1988, pp. 7–12.
[16] Kilinski, T. J., Lesniak, J. R., and Sandor, B. I., *Solder Joint Reliability,* J. H. Lau, Ed., Van Nostrand Reinhold, New York, 1991, pp. 384–405.
[17] Clech, J. P. and Augis, J. A., *Solder Joint Reliability,* J. H. Lau, Ed., Van Nostrand Reinhold, New York, 1991, pp. 545–587.
[18] Frear, D. R., Grivas, D., and Morris, J. W., Jr., *Journal of Electronic Materials,* Vol. 18, 1989, pp. 671–680.
[19] Martens, J. S., Sorenson, N. R., and Ginley, D. S., "A Novel Millimeter Wave Corrosion Detection Method," to be published in the *Journal of the Electrochemical Society.*
[20] Grivas, D., Ph.D. thesis, University of California, Berkeley, 1978.
[21] Solomon, H. D., *Electronic Packaging: Materials and Processes,* J. A. Sortell, Ed., American Society of Metals, Metals Park, OH, 1985, pp. 29–49.
[22] Solomon, H. D., in *Low Cycle Fatigue, ASTM STP 942,* American Society for Testing and Materials, Philadelphia, 1988, pp. 342–369.
[23] Solomon, H. D., *Journal of Electronics Packaging,* Vol. 111, 1989, pp. 75–90.
[24] Vaynman, S., Fine, M. E., and Jeannotte, D. A., in *Solder Mechanics—A State of the Art Assessment,* D. R. Frear, W. B. Jones, and K. R. Kinsman, Eds., TMS Publications, Warrendale, PA, 1991, pp. 155–189.
[25] Fox, L. R., Sofia, W., and Shine, M. C., *Proceedings, IEEE CHMT,* Vol. 8, 1985, pp. 275–282.
[26] Majumdar, S. and Jones, W. B., in *Solder Mechanics—A State of the Art Assessment,* D. R. Frear, W. B. Jones, and K. R. Kinsman, Eds., TMS Publications, Warrendale, PA, 1991, pp. 273–360.
[27] Snowden, K. U., *Acta Metallurgica,* Vol. 12, 1964, p. 295.
[28] Berriche, R., Vaynman, S., Fine, M. E., and Jeannette, D. A., *Electronic Packaging and Corrosion in Microelectronics,* M. E. Nicholson, Ed., American Society of Metals, Metals Park, OH, 1987, p. 169.
[29] Lacey, T. G. and Woodford, D. A., *Scripta Metallurgica,* Vol. 22, 1988, pp. 1543–1545.

James A. Wasynczuk,[1] *W. Dave Hanna,*[1] *Franklin D. Ross,*[1] *and Thomas A. Freitag*[1]

High-Cycle Fatigue of Kovar

REFERENCE: Wasynczuk, J. A., Hanna, W. D., Ross, F. D., and Freitag, T. A., **"High-Cycle Fatigue of Kovar,"** *Fatigue of Electronic Materials, ASTM STP 1153,* S. A. Schroeder and M. R. Mitchell, Eds., American Society for Testing and Materials, Philadelphia, 1994, pp. 110–122.

ABSTRACT: Kovar®, an austenitic Fe-29Ni-17Co alloy, was tested in monotonic tension and axial fatigue at stress ratios (minimum stress/maximum stress) of $R = -1$ and 0.1. Two annealed microstructures, having grain sizes of 14 and 65 μm, were tested. The strain-hardening exponent of tensile flow curves gradually increased with strain, and then remained constant at a value of 0.23. Long-life ($>10^8$ cycles) tests indicated that fatigue limit behavior, well known for ferritic steels, also exists in Kovar. Fatigue limits (defined as the highest stress amplitude that did not cause failure in $>10^7$ cycles) were found to be 276 MPa (53% of UTS) for the 14-μm grain size and 207 MPa (41% of UTS) for the 65-μm grain size, both at $R = -1$. These two data points suggest that the fatigue strength of Kovar may have a strong grain size dependence. The fatigue strength of the 65-μm grain-size material was strongly affected by stress ratio. The $R = 0.1$ fatigue limit of this material was found to be 103 MPa (21% of UTS). Sharply notched ($K_t = 6.8$, 0.04-mm notch root radius) 65-μm grain-size specimens were tested at $R = 0.1$. Metallographic evidence of a small nonpropagating fatigue crack was found at the notch root of a specimen that was tested to $>10^8$ cycles. Fracture surfaces with well-defined striations were produced when fatigue crack-growth rates were high.

KEYWORDS: austenitic alloys, crack growth, fatigue (materials), grain size, mean stress

Kovar® (a trademark of Carpenter Technology Corporation, Reading, PA) is an austenitic alloy with a nominal composition of Fe-29Ni-17Co (wt%). The composition range and a number of physical properties of this type of alloy are covered in the ASTM Standard Specification for Iron-Nickel-Cobalt Sealing Alloy (F 15-78). Because the thermal expansion coefficient of Kovar matches those of alumina and certain sealing glasses reasonably well, it is commonly used as a lead frame material in ceramic integrated circuit packages. Vibrations encountered in environmental tests and service can subject Kovar leads to fatigue. Thorough searches of the technical literature failed to locate appropriate fatigue data for Kovar. This study was initiated in order to provide data for design and failure analysis work.

Experimental Procedure

Annealed round bar stock (25.4 mm diameter) was purchased from Carpenter Technology Corporation. This material conformed to the ASTM F 15-78 specification for an iron-nickel-cobalt sealing alloy. The vendor certified the composition as being (wt%) 28.98 Ni/17.34 Co/0.012 C/0.25 Mn/0.11 Si/0.004 P/0.003 S/0.09 Cr/0.001 Mg/<0.002 Zr/0.008 Al + Mg + As + Ti. Metallographic sections were ground and polished by standard methods, and then etched with a solution of 10 mL HNO_3/20 mL HCl/10 mL glycerin. Grain size will be

[1]Member of the technical staff, The Aerospace Corporation, El Segundo, CA 90245-4691.

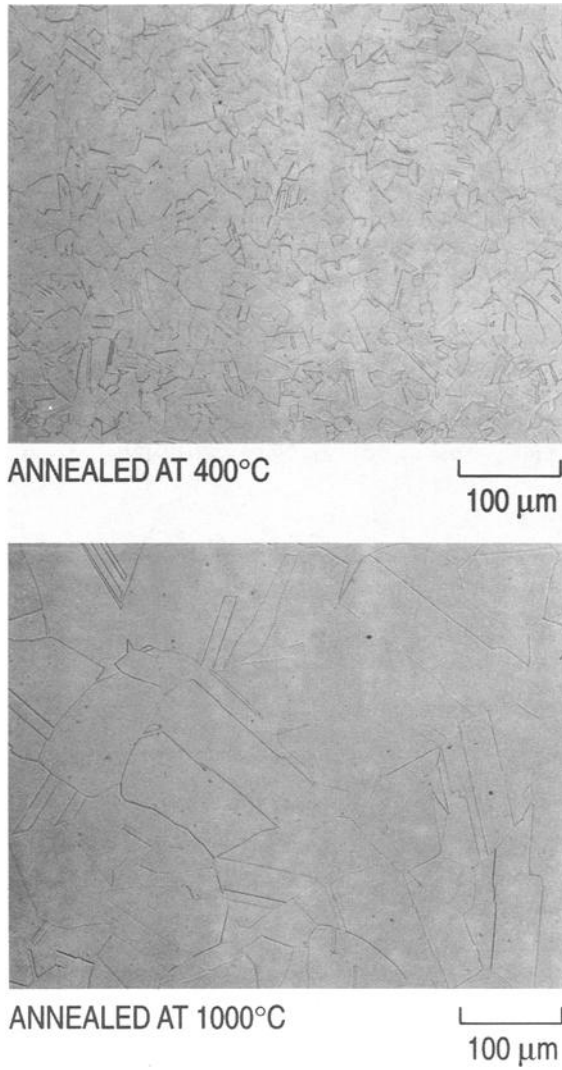

FIG. 1—*Optical micrographs of the annealed microstructures. These sections were etched with a HNO_3/HCl/glycerin solution.*

defined as the mean linear intercept diameter (test line length/number of intersections with boundaries). Because it was often difficult to distinguish between grain and twin boundaries, intersections with twin boundaries were included in all of our grain-size measurements. For each microstructure, our test lines contained an average of roughly 16 intersections. The microstructure of the as-received material consisted of equiaxed grains with a mean size of about 12 μm. Two annealed microstructures were tensile and fatigue tested. Annealing for 20 min at 1000°C produced equiaxed grains with a mean size of 65 μm. Annealing for 1 h at 400°C produced equiaxed grains with a mean size of 14 μm. Optical micrographs of the annealed microstructures are shown in Fig. 1. Tension tests were also performed on

annealed 0.32-mm-diameter Kovar wire that was purchased from California Fine Wire Co., Grover City, CA. The microstructure of this wire consisted of equiaxed grains with a mean size of 5 μm.

X-ray diffraction was used to ascertain the absence of any remnant cold work. A diffractometer (Philips model APD 3720) with a copper tube and a double-crystal monochrometer was used. For the annealed round bars, the samples were transverse metallographic cross sections that were given a chemical etch with a HF/H_2O_2 solution in order to remove any polishing damage. For the 0.32-mm-diameter wire, a sample was prepared by gluing several 1-cm-long segments, side by side, to a flat plastic platen. This sample was oriented such that the incident beam was normal to the wire axis. The diffraction peaks from all three microstructures exhibited well-resolved $K_{\alpha 1}/K_{\alpha 2}$ doublets. Clear resolution of $K_{\alpha 1}/K_{\alpha 2}$ doublets is indicative of well-annealed microstructures [*1*].

Diagrams of the unnotched and circumferentially V-notched fatigue specimens are shown in Fig. 2. After machining, all specimens received either the 20 min/1000 or the 1 h/400°C anneal, followed by furnace cooling. The reduced sections of the unnotched specimens were then centerless ground. Visual comparison with surface-roughness standards indicated an

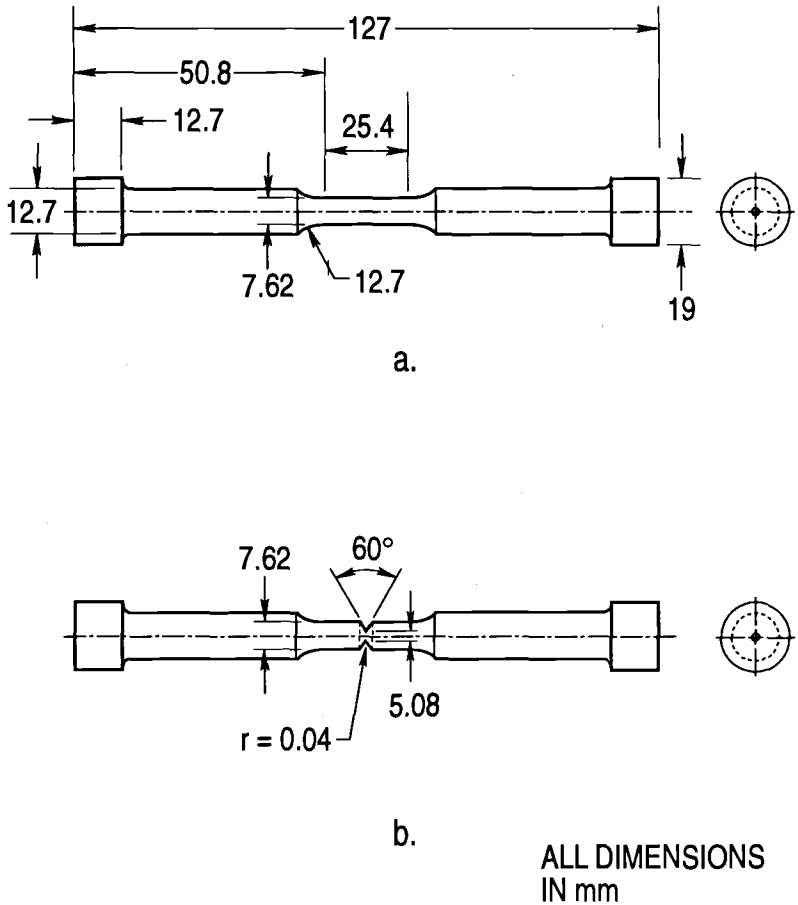

FIG. 2—*Schematic diagrams of the axial fatigue specimens:* (a) *unnotched,* (b) *notched.*

rms roughness of 0.4 μm. The circumferential V-notch was also produced by grinding. It had a root radius of 0.04 mm, a depth of 1.27 mm, and an included angle of 60°. The theoretical stress concentration factor, K_t, for this notch was approximately 6.8. It was estimated with the following equation [2]

$$K_t = 1/N[(a/r)\sqrt{(1 + a/r)} + ((1 + 2\nu)/2)(a/r) + (1 + \nu)(1 + \sqrt{(1 + a/r)}]$$

where a is the radius of the reduced section (a = 2.54 mm), r is the notch-root radius, ν is Poisson's ratio, and $N = (a/r) + 2\nu\sqrt{(1 + a/r)} + 2$. A value of $\nu = 0.32$ was used for Poisson's ratio [3].

Fatigue testing was performed on a servohydraulic testing machine that was operated under load control. Loading was sinusoidal, at frequencies ranging from 25 to 100 Hz. As indicated in the ASTM Practice for Constant Amplitude Axial Fatigue Tests of Metallic Materials (E 466), the fatigue behavior of most structural alloys is unaffected by such changes in the rate of loading. Tests were performed in laboratory air at approximately 50% relative humidity. The unnotched specimens were tested at stress ratios of $R = (S_{min}/S_{max}) = -1$ and 0.1, where S_{min} and S_{max} are the minimum and maximum applied stresses, respectively. One specimen was used for each test. Specimens that did not fail at low stress amplitudes were not retested at higher stress amplitudes. Only the large-grained microstructure was tested in the notched-bar configuration, and only at $R = 0.1$. For these notched specimens, the nominal applied stresses were based on the reduced cross section.

Tension tests were performed on screw-driven Instron machines that were operated at a crosshead speed of 1.27 mm min^{-1}. For the 65-μm grain-size material, the unnotched specimen geometry shown in Fig. 2*a* was used, and engineering strains were calculated from crosshead displacement data. The ASTM Standard Test Methods of Tension Testing of Metallic Materials (E 8) 12.7-mm round tension specimens were used for the 14-μm grain-size material. For these specimens, engineering strains were calculated from axial displacements that were measured with an Instron model 2620-524 clip gage with a 50.8-mm gage length. The results of the ASTM Standard Method of Verification and Classification of Extensometers (E 83-85) calibration experiments indicated that this is a class B-1 extensometer with a range of 10% engineering strain. Displacements associated with strains larger than 10% were measured by quickly collapsing the clip gage back to zero displacement when the end of its range was approached. True stress and true strain up to the maximum load were calculated using the relations: true strain = ln (1 + engineering strain) and true stress = engineering stress · (1 + engineering strain) [4]. Flow curves for the 14-μm grain-size material will be described in terms of true plastic strain, which was calculated as: true plastic strain = true strain − (true stress/Young's modulus determined from our true stress-true strain curve).

Results and Discussion

The results of the monotonic tension tests are listed in Table 1. Each value listed represents the average from at least two tests. A sample true stress–true plastic strain curve for a 14-μm grain-size specimen is plotted on linear scales in Fig. 3*a* and in a log-log format in Fig. 3*b*. The log-log plot makes it apparent that the simple power law $\sigma = K_1\epsilon_p^{n_1}$, where σ is the true stress, ϵ_p is the true plastic strain, K_1 and n_1 are constants (the dashed line in Fig. 3*b* is for $n_1 = 0.23$), fails to fit the experimentally determined curve below a true plastic strain of about 0.06. Behavior similar to this has been reported for stable austenitic stainless steels, and it has been attributed to the planar-slip character of these materials [5]. The equation $\sigma = K_1\epsilon_p^{n_1} + \exp(K_2 + n_2\epsilon_p)$, where K_1, n_1, K_2, and n_2 are constants, was

TABLE 1—*Monotonic tensile properties of annealed Kovar.*

Specimen	Condition	Yield Stress, MPa	UTS, MPa	Elongation, %	Reduction of Area, %
Unnotched bar	Annealed 1000°C 65-μm grain size	329	502	50[a]	80
Unnotched bar	Annealed 400°C 14-μm grain size	379	517	46[b]	85
0.32-mm diameter wire	Annealed 5-μm grain size	438	558	Not determined	Not determined

[a]2.54-cm gage length.
[b]5.08-cm gage length.

developed to describe such flow curves [5]. For true plastic strains above 0.008, the flow curve in Fig. 3 was well fit by this equation (the calculated values of true stress were within 0.5% of the measured values) when the constants had the following values: K_1 = 913 MPa, n_1 = 0.23, K_2 = 4.98, and n_2 = −63.7. At smaller values of true plastic strain, this equation underestimated true stress. Direct evidence for planar slip in Kovar was found in surface-slip lines. An example is shown in Fig. 4. We have performed similar slip-line

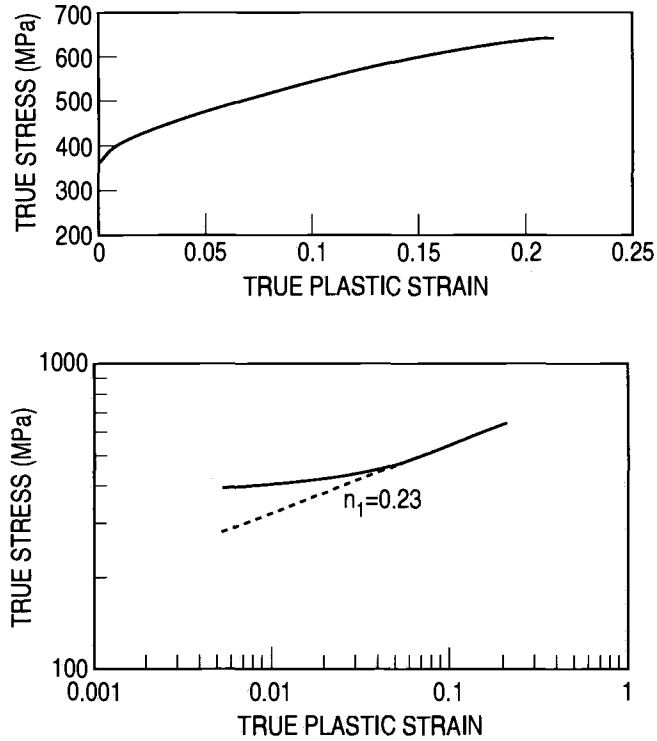

FIG. 3—*True stress–true plastic strain curves for annealed Kovar, 14-μm grain size:* (a) *linear plot,* (b) *the same curve plotted in a log-log format. The dashed line in* (b) *represents the simple power law* $\sigma = K_1\epsilon_p^{n_1}$, where σ = true stress, ϵ_p = true plastic strain, K_1 = *913 MPa, and* n_1 = *0.23.*

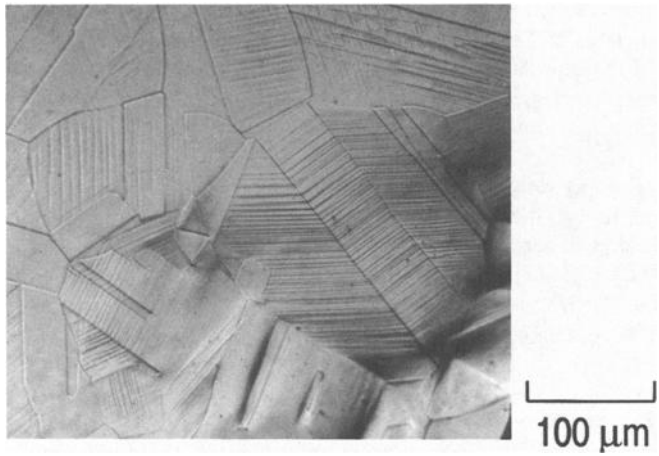

FIG. 4—*Optical micrograph showing surface slip lines in Kovar. The region shown is close to a Rockwell B hardness indentation on a polished surface.*

studies on AISI 316 stainless steel. The slip lines formed in Kovar tend to be at least as straight as those in AISI 316.

The fatigue data are plotted in semilog form in Fig. 5. Stress amplitude, $S_a = (S_{max} - S_{min})/2$, is used as the ordinate. Some specimens were tested for up to 10^8 cycles without failure. The results of these long-life tests indicate that fatigue-limit behavior, well known for ferritic steels, was also exhibited by the austenitic Kovar. The fatigue limit will be defined as the highest stress amplitude that did not cause failure in $>10^7$ cycles. For the

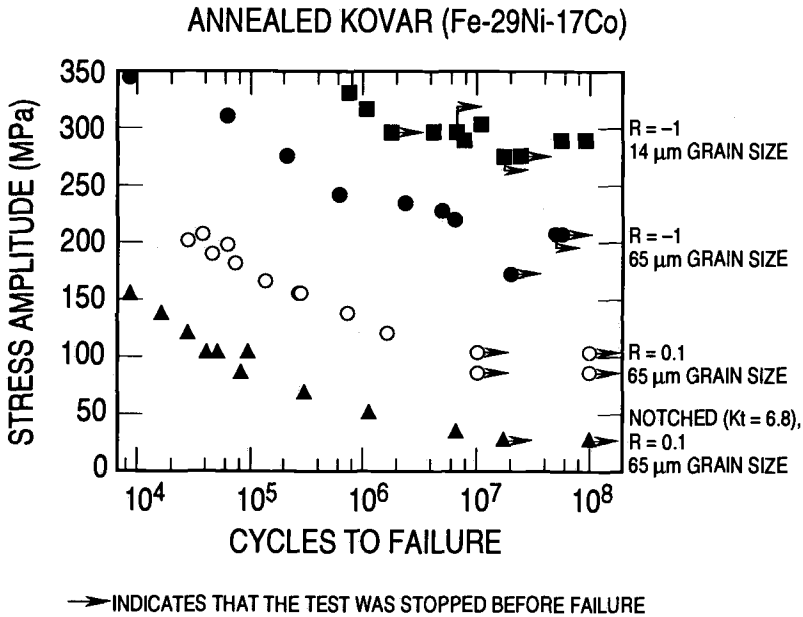

FIG. 5—S/N *curves for annealed Kovar.*

unnotched specimens tested at $R = -1$, the present data give fatigue limits of 207 MPa for the 65-μm grain size and 276 MPa for the 14-μm grain size. These $R = -1$ fatigue limits represent 41% of the ultimate tensile strength (UTS) for the 65-μm grain size and 53% of the UTS for the 14-μm grain size. Values ranging from 40 to 60% of UTS have been reported for ferritic structural steels, most of which were tested by beam-bending techniques [*6*].

The present values of yield stress (S_y), UTS, and $R = -1$ fatigue limit are plotted against the inverse square root of the grain size in Fig. 6. Although originally developed to describe the lower yield stress of ferritic alloys, the Hall-Petch relationship has also been used to fit UTS and fatigue data [*7–17*]. The present monotonic strength values are fit by the equations $S_y = 288$ MPa + $10.7/\sqrt{d}$ and UTS = 477 MPa + $5.6/\sqrt{d}$, where d is the grain size in millimetres. A line connecting the present two $R = -1$ fatigue limits is described by $S_f = 147$ MPa + $15.2/\sqrt{d}$.

Inverse relationships between high-cycle fatigue strength and grain size have also been observed in ferritic steels and 70Cu/30Zn alpha brass. Our analysis of data for alpha brass with grain sizes of roughly 20 μm and larger indicates that the fatigue limit scales as $S_f = 40$ MPa + $10.3/\sqrt{d}$ [*12,13*]. It has been shown that a low stacking fault energy and attendant planar slip are central to the grain-size sensitivity exhibited by this FCC alloy [*11*]. In aluminum and copper, FCC metals that have high stacking fault energies and readily exhibit cross slip, fatigue strength was practically unaffected by changes in grain size [*11*]. Extensive metallographic data on the number and length of fatigue cracks indicated that slip character had its primary effect on Stage I [*18*] crack growth and relatively little influence on crack initiation [*11*]. Since dislocations readily cross slip in low-carbon ferritic steels, the grain-size effects observed in these alloys have been explained in terms of the generation of dislocations from grain boundaries [*11*] and microstructural barriers to crack growth [*15*]. For reversed bending specimens with grain sizes of approximately 55, 21, and 8 μm, the fatigue limit of a normalized 0.2% C plain-carbon steel can be fit by $S_f = 107$ MPa +

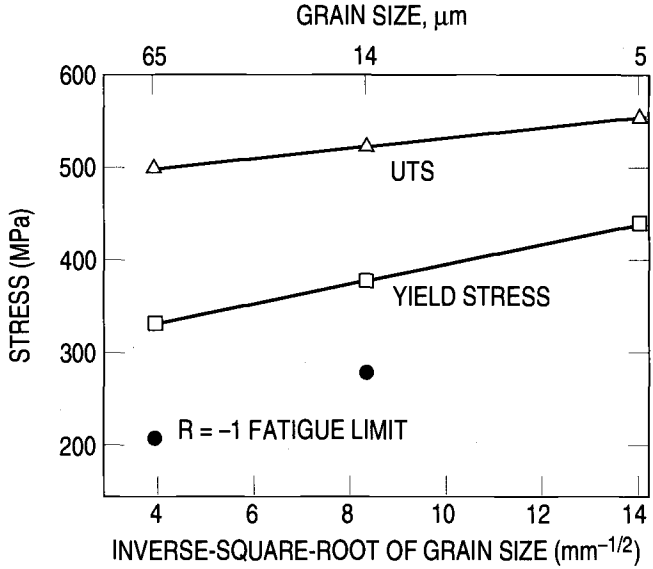

FIG. 6—*Hall-Petch-type plots of monotonic strengths and fatigue limits for annealed Kovar.*

$10.6/\sqrt{d}$ [15]. The slope of the line connecting the present two $R = -1$ fatigue limits suggests that the grain-size effect in Kovar might be more pronounced than those found for alpha brass and mild steel. Additional experiments are needed to substantiate this trend and to elucidate the fatigue strengthening mechanisms operative in Kovar.

When tested at $R = 0.1$, the unnotched 65-μm grain-size specimens gave a fatigue limit of 103 MPa, about half the value obtained at $R = -1$. This measured value is substantially smaller than the 167 MPa predicted by the well-known Soderberg relation, $S_a = S_{a,R=-1}(1 - S_m/S_y)$, where S_a is the fatigue strength when the mean stress is not zero, $S_{a,R=-1}$ is the fatigue strength at zero mean stress, S_m is the mean stress, and S_y is the monotonic yield stress [4]. Other, more general, empirical relations have been developed for applications where the cumulative fatigue damage resulting from variable stress amplitudes and mean stresses have to be considered. For axial fatigue data, *Mil Handbook 5E* recommends that the mean stress be accounted for in terms of an equivalent stress parameter, $S_{eq} = S_{max}(1 - R)^m$, where S_{max} is the maximum stress and m is an optimized constant determined from data obtained at different load ratios [19]. A similar sort of empirical formula has been developed by Topper and Sandor [20]. For nominally elastic material behavior, $S^* = S_a + (S_m)^\alpha$, where S^* is the equivalent fully reversed stress amplitude that would give the same life as a stress amplitude S_a coexisting with a mean stress S_m, and α is an optimized constant. An analogous formula, written in terms of strain amplitudes, includes inelastic material behavior [20]. For fatigue lives greater than 10^5 cycles, the present $R = -1$ and $R = 0.1$ data for the 65-μm grain-size material could be coalesced by either the relation given by Topper and Sandor with $\alpha = 1.1$, or that given in *Mil Handbook 5E* with $m = 0.17$.

The shape of high-cycle *S/N* curves can often be described by the empirical relation proposed by Basquin, $S_a = \sigma_f(N_f)^b$, where S_a = the stress amplitude at $R = -1$, σ_f = the fatigue strength coefficient, and b = the fatigue strength exponent [4]. Above the unnotched $R = -1$ fatigue limit, regression analysis gave Basquin exponents of $b = -0.07$ for the 65-μm grain size and -0.02 for the 14-μm grain size. It has been reported that values ranging from -0.05 to -0.12 are typical for engineering alloys [4]. A value of $b = -0.12$ was found for the unnotched $R = 0.1$ data. This greater slope is almost certainly due to the higher maximum stresses employed in the $R = 0.1$ tests. Most of those data represent maximum stresses that exceeded the monotonic yield stress. It is therefore reasonable that the slope of the $R = 0.1$ curve be closer to those encountered in low-cycle fatigue studies [4]. This trend is even more pronounced for the notched specimen data, for which a Basquin exponent of $b = -0.23$ was found. For much of these data, substantial fractions of the specimen's cross sections must have been deforming plastically.

The $R = 0.1$ fatigue limit for the notched ($K_t = 6.8$) 65-μm grain-size specimens was found to be 28 MPa. Optical and SEM examinations of the specimen that was tested for more than 10^8 cycles at this fatigue limit revealed that it was cracked at its notch root. An example is shown in Fig. 7. These surface observations indicated that notch-root cracking was confined to a roughly 2-mm-long segment of the notch-root circumference, which measured $5.08\ \pi = 15.96$ mm.

Attempts to map the depth profile of these cracks by acoustic microscopy met with limited success. Our most reliable measurements were obtained by serial metallographic sectioning. An example is shown in Fig. 8. These data indicate the presence of a roughly thumbnail-shaped crack, roughly 2 mm wide and 0.06 mm long. Although this specimen was not monitored for crack initiation throughout the test, a substantial body of published data supports the assumption that the crack shown in Figs. 7 and 8 initiated relatively early in the fatigue test, and then grew at rates that decreased to negligible values. Such cracks are commonly referred to as nonpropagating fatigue cracks. They have been observed in sharply notched specimens of numerous other engineering alloys [21–24].

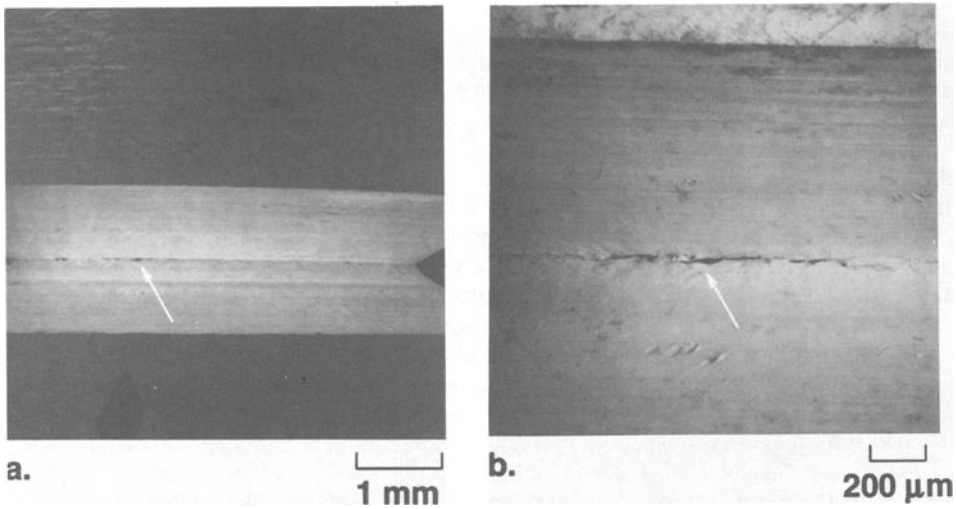

FIG. 7—*SEM images showing a fatigue crack at the root of a notch. The specimen received more than 10^8 cycles at its fatigue limit. The same crack is shown in* (a) *and* (b).

Fatigue cracks initiate readily at sharp notches, and fracture mechanics concepts have been used to describe their growth. Data for 316 stainless steel [*25*] and a low-strength (124 MPa yield stress) mild steel [*26*] indicate that the number of cycles required to initiate a fatigue crack decreases with notch-root radius, but becomes constant for notches with root radii that are below a critical value, which was found to be approximately 0.25 mm for both alloys. Below this critical radius, notches behaved the same as sharp cracks [*26*]. Mean stress had little effect on this behavior [*26*]. At stress amplitudes above the fatigue limit of sharply notched specimens, cracks exhibit growth rates that decrease to some minimum value and thereafter increase [*21*]. At the fatigue limit, cracks emanating from sharp notches decelerate to arrest. When linear elastic fracture mechanics has been used to describe the growth of small cracks that emanated from sharp notches, it has been found that the growth rates exhibited during deceleration are considerably higher than those of long (greater than a couple of mm) cracks at equivalent values of alternating stress intensity factor ΔK [*21–24,27*]. Similarly, the values of ΔK at which these small cracks became nonpropagating were found to be considerably less than the threshold alternating stress intensity factor for long fatigue cracks ΔK_{th} [*21–24*]. Explanations for this sort of small-crack behavior include crack closure effects [*22,24*] and a reduced constraint for plasticity of near-surface grains [*21*]. Although it has been reported that the differences between the threshold values of long and small cracks can be reconciled by measurements of effective ΔK_{th}, which allow for crack closure [*22*], other data indicate that the differences may not be solely attributable to closure effects [*24*]. The differences between long and small cracks have also been explained by phenomenological theories that employ effective crack lengths for small cracks [*21,23*].

If the present circumferential V-notch is treated as a sharp crack, then the alternating stress intensity factor may be calculated as $\Delta K = \Delta S_{net}\sqrt{\pi a} \cdot F_1(a/b)$, where ΔS_{net} is the net section stress range, a is the radius of the net section, and $F_1(a/b)$ is a function of the net and gross section radii [*28*]. At the $R = 0.1$ fatigue limit, the nominal stress range ($2S_a$) for the notched Kovar specimens was found to be 56 MPa. The corresponding value of ΔK calculates to approximately 1.8 MPa$\sqrt{m}$. The presence of the 0.06-mm-long thumbnail crack at the notch root causes little change in this value. The long-crack threshold alternat-

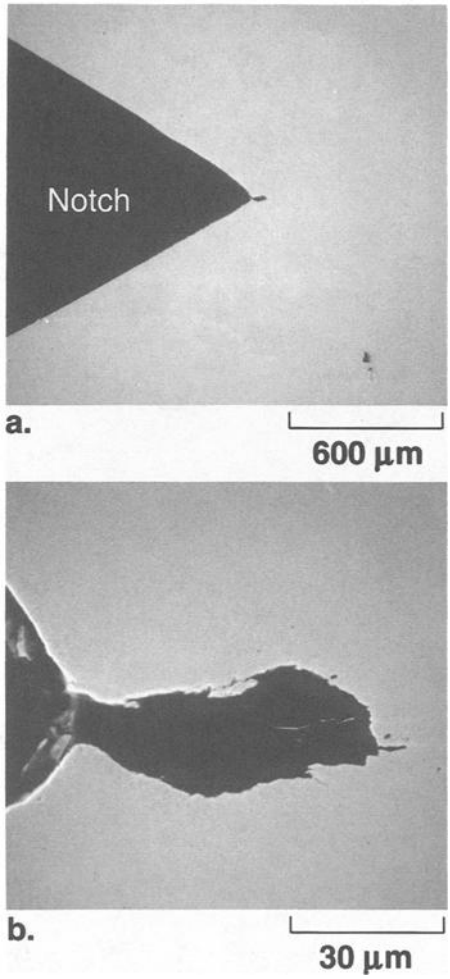

FIG. 8—*SEM images of a longitudinal cross section of a notched specimen that received more than 10^8 cycles at its fatigue limit. The same crack is shown in* (a) *and* (b).

ing stress intensity factor for Kovar is unknown. However, it is reasonable to assume that it is similar to the values of 3 to 9 MPa$\sqrt{m}$ that have been reported for 316 stainless steel at $R = 0.1$ [*29*]. Although additional experimental work will be needed to accurately determine the differences between long- and small-crack threshold behavior in Kovar, the present data agree with the generally observed trend that values of ΔK_{th} for small cracks are lower than those for long cracks. The present finding of only a microstructurally small [*27*] (less than one grain diameter long) nonpropagating crack at the fatigue limit may also indicate a similarity to the small-crack behavior that has been reported for AISI 304 stainless steel [*22*]. Regardless of the fully reversed ($R = -1$) stress amplitude that was applied, cracks that emanated from the roots of sharply notched specimens of AISI 304 exhibited deceleration, but no arrest. The absence of nonpropagating fatigue cracks in this material was attributed to crack-closure effects [*22*].

SEM examinations of fractured 14-μm grain-size specimens indicated that surfaces with

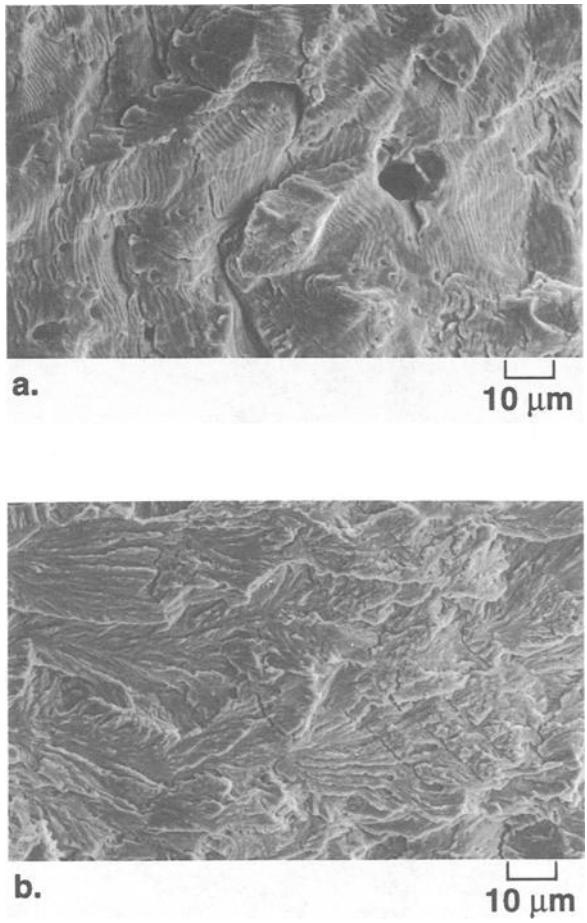

FIG. 9—*SEM images of fatigue fracture surfaces produced in annealed 14-μm grain-size Kovar at* R = *0.1:* (a) *a region exhibiting well-defined striations,* (b) *a region representing low Stage II crack-growth rates.*

well-defined striations were produced when crack-growth rates were high. An example is shown in Fig. 9*a*. Striations with apparent spacings as wide as 1.2 μm can be seen in this image. This type of fatigue fracture surface was produced just before failure by tensile overload. At low Stage II fatigue crack-growth rates, fracture surfaces like that shown in Fig. 9*b* were produced. This image is representative of regions close to the origin of Stage II fatigue crack growth. The results of limited SEM examinations indicate that fracture surfaces similar to those in Fig. 9 were also produced in the 65-μm grain-size specimens.

Conclusions

Monotonic tensile and axial fatigue tests have been performed on annealed Kovar having mean linear intercept grain diameters of 14 and 65 μm. The data obtained support the following conclusions.

1. Annealed Kovar does not exhibit simple power-law strain-hardening behavior. For the 14-μm grain-size material, the strain-hardening exponent gradually increased with strain, and then remained constant at a value of 0.23.

2. Long-life ($>10^8$ cycles) fatigue tests indicated that fatigue limit behavior, well known for ferritic steels, also exists in Kovar. Fatigue limits at $R = -1$ were found to be 276 MPa (53% of UTS) for the 14-μm grain size and 207 MPa (41% of UTS) for the 65-μm grain size. These two data points suggest that the fatigue strength of Kovar may have a strong grain-size dependence.

3. The effect of mean tensile stress on the fatigue strength of annealed Kovar is stronger than that predicted by the Soderberg relation. For the 65-μm grain-size material, the $R = 0.1$ fatigue limit was found to be 103 MPa.

4. After testing at its fatigue limit, a sharply notched 65-μm grain-size specimen exhibited a small nonpropagating fatigue crack. The value of ΔK applied to this crack (approximately 1.8 MPa$\sqrt{\text{m}}$) agrees with the generally observed trend that values of ΔK_{th} for small cracks are lower than those of long cracks.

5. Fracture surfaces with well-defined striations can be produced in Kovar when fatigue crack growth rates are high.

Acknowledgments

This work was funded by Aerospace Sponsored Research. The tension tests and many of the $R = 0.1$ fatigue tests of the large-grained specimens were performed by G. Fuchs. The X-ray diffraction experiments were performed by P. Adams. Metallography and some SEM work were done by J. Marcus, C. N. Su, and R. Brose.

References

[1] Cullity, B. D., *Elements of X-Ray Diffraction,* 2nd ed., Addison-Wesley, 1978, p. 288.
[2] Neuber, H., *Kerbspannungslehre,* 2nd ed., 1958, Springer, Berlin, p. 100.
[3] Harner, L., "The Use of Fe29Ni17Co Alloy in the Electronics Industry," *ASM/TMS Materials Week,* November 1992, American Society for Metals, Metals Park, OH.
[4] Hertzberg, R. W., *Deformation and Fracture Mechanics of Engineering Materials,* 2nd ed., John Wiley & Sons, New York, 1983.
[5] Ludwigson, D. C., "Modified Stress-Strain Relation for FCC Metals and Alloys," *Metallurgical Transactions,* Vol. 2, October 1971, pp. 2825–2828.
[6] Dolan, T. J., "Basic Concepts of Fatigue Damage in Metals," *Metal Fatigue,* G. Sines and J. L. Waisman, Eds., McGraw-Hill, New York, 1959, pp. 39–67.
[7] Hirth, J. P., "The Influence of Grain Boundaries on Mechanical Properties," *Metallurgical Transactions,* Vol. 3, December 1972, pp. 3047–3067.
[8] Armstrong, R. W., "The Influence of Polycrystal Grain Size on Several Mechanical Properties of Materials," *Metallurgical Transactions,* Vol. 1, May 1970, pp. 1169–1174.
[9] Johnston, T. L. and Feltner, C. E., "Grain Size Effects in the Strain Hardening of Polycrystals," *Metallurgical Transactions,* Vol. 1, May 1970, pp. 1161–1166.
[10] Scott, J. A. and Spruiell, J. E., "Grain Refinement of Wrought Austenitic Steels by Rapid Heating," *Metallurgical Transactions,* Vol. 5, January 1974, pp. 255–259.
[11] Thompson, A. W. and Backofen, W. A., "The Effect of Grain Size on Fatigue," *Acta Metallurgica,* Vol. 19, July 1971, pp. 597–606.
[12] Sinclair, G. M., "Some Metallurgical Aspects of Fatigue," *Fatigue—An Interdisciplinary Approach,* J. J. Burke, N. L. Reed, and V. Weiss, Eds., Syracuse University Press, 1964, pp. 63–81.
[13] Sinclair, G. M. and Craig, W. J., "Influence of Grain Size on Work Hardening and Fatigue Characteristics of Alpha Brass," *Transactions of the American Society for Metals,* Vol. 44, 1952, pp. 929–948.
[14] Forrest, P. G. and Tate, A. E. L., "The Influence of Grain Size on the Fatigue Behavior of 70/30 Brass," *Journal of the Institute of Metals,* Vol. 93, 1964–65, pp. 438–444.
[15] Taira, S., Tanaka, K., and Hoshina, M., "Grain Size Effect on Crack Nucleation and Growth in

Long-Life Fatigue of Low-Carbon Steel," *Fatigue Mechanisms, ASTM STP 675,* J. T. Fong, Ed., American Society for Testing and Materials, Philadelphia, 1979, pp. 135–173.

[16] Phillips, W. L. and Armstrong, R. W., "The Influence of Specimen Size, Polycrystal Grain Size, and Yield Point Behavior on the Fatigue Strength of Low-Carbon Steel," *Journal of the Mechanics and Physics of Solids,* Vol. 17, 1969, pp. 265–270.

[17] Klesnil, M., Holzmann, M., Lukas, P., and Rys, P., "Some Aspects of the Fatigue Process in Low-Carbon Steel," *Journal of the Iron and Steel Institute,* Vol. 203, January 1965, pp. 47–53.

[18] Laird, C., "The Influence of Metallurgical Structure on the Mechanisms of Fatigue Crack Propagation," *Fatigue Crack Propagation, ASTM STP 415,* American Society for Testing and Materials, Philadelphia, 1967, pp. 131–180.

[19] *MIL-HDBK-5E,* 1 June 1987.

[20] Topper, T. H. and Sandor, B. I., "Effects of Mean Stress and Prestrain on Fatigue—Damage Summation," *Effects of Environment and Complex Load History on Fatigue Life, ASTM STP 462,* American Society for Testing and Materials, Philadelphia, 1970, pp. 93–104.

[21] El Haddad, M. H., Topper, T. H., and Smith, K. N., "Prediction of Non Propagation Cracks," *Engineering Fracture Mechanics,* Vol. 11, 1979, pp. 573–584.

[22] Ogura, K., Miyoshi, Y., and Nishikawa, I., "Threshold Behavior of Small Fatigue Crack at Notch Root in Type 304 Stainless Steel," *Engineering Fracture Mechanics,* Vol. 25, No. 1, 1986, pp. 31–46.

[23] Miller, K. J., "Fatigue of Notches," *Advances in Fatigue Science and Technology,* C. M. Branco and L. G. Rosa, Eds., Kluwer Academic Publishers, Norwell, MA, 1989, pp. 3–21.

[24] Ritchie, R. O. and Yu, W., "Short Crack Effects in Fatigue: A Consequence of Crack Tip Shielding," *Small Fatigue Cracks,* R. O. Ritchie and J. Lankford, Eds., The Metallurgical Society, Warrendale, PA, 1986, pp. 167–189.

[25] Saanouni, K. and Bathias, C., "Study of Fatigue Crack Initiation in the Vicinity of Notches," *Engineering Fracture Mechanics,* Vol. 16, No. 5, 1982, pp. 695–706.

[26] Jack, A. R. and Price, A. T., "The Initiation of Fatigue Cracks from Notches in Mild Steel Plates," *International Journal of Fracture Mechanics,* Vol. 6, No. 4, December 1970, pp. 401–409.

[27] Ritchie, R. O. and Lankford, J., "Overview of the Small Crack Problem," *Small Fatigue Cracks,* R. O. Ritchie and J. Lankford, Eds., The Metallurgical Society, Warrendale, PA, 1986, pp. 167–189.

[28] Tada, H., Paris, P. C., and Irwin, G. R., *The Stress Analysis of Cracks Handbook,* Del Research Corp., Hellertown, PA, 1973, p. 27.1.

[29] Mills, W. J. and James, L. A., "Near-Threshold Fatigue Crack Growth Behavior for 316 Stainless Steel," *Journal of Testing and Evaluation, JTEVA,* Vol. 15, No. 6, November 1987, pp. 325–332.

Anatoliy Parnas[1]

Thermal Stresses in Cooled Heat-Releasing Elements of Electronic Devices

REFERENCE: Parnas, A., **"Thermal Stresses in Cooled Heat-Releasing Elements of Electronic Devices,"** *Fatigue of Electronic Materials, ASTM STP 1153,* S. A. Schroeder and M. R. Mitchell, Eds., American Society for Testing and Materials, Philadelphia, 1994, pp. 123–132.

ABSTRACT: Numerical and analytical methods for calculating thermal stresses and deformations in a flat plate connected to a cooled wall with an intermediate layer of solder or adhesive are proposed. In the numerical method, the nonisothermal flow theory for layer material was used. In the analytical method, the layer material was elastic if shear stresses were less than yield limit and ideal-plastic if they exceeded it. The plate and the wall were elastic in both methods. Specific computations were performed for the ferrite plate soldered to the metal wall of a high-power waveguide. Results showed the length of the plastic zone in the layer could be large not only in operation (when heat in the plate was releasing), but also after cooling in a plate-to-wall connecting process. The less accurate but simple analytical method can be useful for estimations of thermal stress and cooling rate, which can provide the necessary temperature and strength of both the plate and the layer. To calculate a deflection of the plate due to the thermal gradient in its cross section, the Bubnov's-Galyorkin's approximate method was used. It was shown that the deflection is small if a layer is made of solder and could be significant if the layer is adhesive.

KEYWORDS: thermal stress, plastic deformations, electronic devices, waveguides, ferrites, plates, elastic base, solders, adhesives

Nomenclature

plate	Heat releasing plate
layer	Intermediate layer (made of metal solder or of adhesive)
x, y, z	Coordinates (Fig. 1)
α	Linear coefficient of thermal expansion
c	Thermal conductivity
θ	Function of the free change in volume
δ	Thickness
L	½ length of the plate along the x axis
a	½ length of the plate along the z axis
K	Bulk modulus of elasticity
p	Proportionality factor between load and deformation of the elastic base
f and f_t	Maximum thermal deflections of a plate on the elastic base and the same free plate, respectively
S	Normal stress
T	Shearing stress
S_t	Stress in a plate due to temperature gradient
S_w	Stress in a plate due to a wall influence

[1]Senior researcher, American Combustion, Inc., 4476 Park Dr., Norcross, GA 30093.

S_s and T_s Tensile and shearing yield strengths of a layer material
R Displacement of the plate relative to the wall in the x-direction
ϵ Strain
S_i Stress intensity (effective stress)
ϵ_i Strain intensity (effective strain)
Δ Value increment
t Temperature
μ Poisson's ratio
E Longitudinal modulus of elasticity
G Shearing modulus of elasticity of a layer
D Plate stiffness, $E\delta/12(1 - \mu)$

Subscripts

av Average along the y axis
pL Plate
La Layer
w Wall
0 Initial value
x, y, z Along axis x, y, z
melt Melting
m Main (maximum) value
p Plasticity state
t Temperature

Superscript

* Value at the previous step of computation

Thermal stresses caused by cooling after the bonding process in an elastic brittle plate bonded to a metallic wall were calculated in Ref *1*. This important work explained the nature of typical cracks in semiconductors having smaller expansivity than the metal substrate. The cracks usually entered a plate near its ends at the angle close to or less than 45°. But experience with electronic device operations showed that a fracture of the plate-layer-wall structure could also happen after a successful bonding. After some number of thermal cycles, cracks appeared in any cross section of the plate, or sometimes the plate was completely or partly separated from the wall. Calculations based on the assumptions of layer elasticity [*1*] couldn't explain this observation. The calculated maximum stresses in the layer were located at the plate ends and usually exceeded by many times the tensile strength of the layer material. Therefore as used in Ref *1*, the theory of elasticity became invalid for the layer. It was necessarily to develop a model in which layer material behavior was described more correctly.

In this work, material of a layer is assumed to be elastic-plastic, and a plate and a wall are elastic. Two models for the layer were used:

1. Nonisothermal plastic flow for the medium with slight strengthening and von Mises yielding condition.
2. Ideal-plastic material with shear stress yielding condition.

The plastic flow model usually describes real materials better. To obtain an analytical solution, a more simple ideal-plastic model was used.

Thermal stresses in both the plate and the layer were analyzed for the state after bonding (the plate, the layer, and the wall were cooled and had equal temperatures) and for the operation (after bonding and cooling, when heat in the plate was releasing and removing through the wall).

Problem Formulation

General Relationships

It is assumed that the plate dimension along the z axis (Fig. 1) is quite large to consider the x-y plane strain case. The relationship between thicknesses is: $\delta_{La} \ll \delta_{pL} \ll \delta_w$, and bending deformations are neglected.

It is convenient to express the stress in a plate as the sum

$$S_{pL}(x,y) = S_t(x,y) + S_w(x,y) \tag{1}$$

where S_t is a stress in the plate due to the temperature gradient

$$S_t(x,y) = [E/(1-\mu)][\epsilon_{t,av}(x) - \epsilon_t(x,y)] \tag{2}$$

$$\epsilon_t(x,y) = \alpha_{pL}\Delta t(x,y); \quad \epsilon_{t,av}(x) = \left[\int_0^{\delta_{pL}} \epsilon_t(x,y)dy\right] \Big/ \delta_{pL} \tag{3}$$

$$\Delta t(x,y) = t(x,y)_{pL} - t(x,y)_{pL0} \tag{4}$$

and S_w is a stress due to wall influence. A plate strain is

$$\epsilon(x,y) = \epsilon_t(x,y) + [(1-\mu)/E]S(x,y)_{pL} \tag{5}$$

If R depends only on x, it's easy to show that S_w and ϵ also do not depend on Y, and that the next relationship is valid

$$\epsilon(x) = \epsilon_{tav}(x) + [(1-\mu)/E]S_w(x) \tag{6}$$

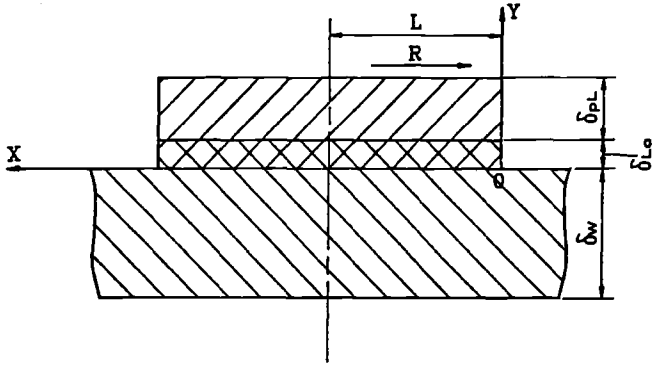

FIG. 1—*Coordinate system and structure sketch.*

The wall strain equation is analogous with Eq 6. The wall stress is small and can be neglected.

The plate point displacement relative to the wall can be obtained by integration over the x axis the difference in strain between the plate and the wall. Taking Eq 5 for the plane $y = 0$, assuming that initial temperatures of the plate and the wall are equal, and neglecting the temperature drop across the layer, the result of integration can be expressed in the form

$$R = R_t + R_w \tag{7}$$

where R_t is the free plate temperature displacement

$$R_t(x) = \int_x^L \Delta\alpha\Delta t(x,0)dx \tag{8}$$

and R_w is the displacement due to wall influence

$$R_w(x) = [(1 - \mu)/E] \int_x^L S_{pL}dx \tag{9}$$

Taking into account that $\int_0^{\delta_{pL}} S_t dy = 0$, the forces balance equation for the arbitrary cross section of the plate is

$$S_w\delta_{pL} = -\int_0^x Tdx \tag{10}$$

The relationship between the displacement, R, and the stress, T, can be obtained after the layer material behavior analysis.

Use of the Plastic Flow Model for the Layer Material

The nonisothermic plastic flow theory equations are used in the form convenient for numerical calculations [*2*]

$$S_x = A_1\Delta\epsilon_x + A_2\Delta\epsilon_y + \eta_x \tag{11}$$

$$S_y = A_1\Delta\epsilon_y + A_2\Delta\epsilon_x + \eta_y \tag{12}$$

$$T = S_{xy} = A_3\Delta\epsilon_{xy} + \eta_{xy} \tag{13}$$

$$S_z = [(\phi - K)/(2\phi + K)](S_x + S_y) + [3/(2\phi + K)][\Delta\epsilon_z - \Delta\theta + (S_z/2G)^* + S_{av}(K - 1/2G)^*] \tag{14}$$

where

$$\begin{aligned} &A_1 = (\phi + 2K)/(3\phi K), \quad A_2 = (\phi - K)/(3\phi K), \quad A_3 = 1/\phi \\ &\eta_x = A_1 b_x + A_2 b_y, \quad \eta_y = A_1 b_y + A_2 b_x, \quad \eta_{xy} = A_3 b_{xy} \\ &S_{av} = (S_x + S_y + S_z)/3, \quad \text{and} \quad \phi = 1/(2G + \Delta U) \end{aligned} \tag{15}$$

where ΔU is a function of the material plastic state

$$\Delta U = \begin{cases} 0, & F = (S_i)^2 - (S_s)^2 < 0 \\ 1.5\Delta\epsilon_{ip}/S_i > 0, & F = 0, dF = 0 \end{cases} \tag{16}$$

Here $F > 0$ is prohibitive.

$$S_i = \sqrt{\{0.5[(S_x - S_y)^2 + (S_x - S_z)^2 + (S_y - S_z)^2 + 6T^2]\}} \tag{17}$$

$$\epsilon_i = \sqrt{\{2[(\epsilon_x - \epsilon_y)^2 + (\epsilon_x - \epsilon_z)^2 + (\epsilon_y - \epsilon_z)^2 + 6\epsilon_{xy}]/9\}} \tag{18}$$

$$b_x = (S_x/2G)^* - [3\phi/(2\phi + K)]\{\Delta\theta + (S_{av})^*(1/2G - K)^* + [(K - \phi)/3\phi](S_z/2G)^* + [(K - \phi)/3\phi]\Delta\epsilon_z\} \tag{19}$$

$$b_y = (S_y/2G)^* - [3\phi/(2\phi + K)]\{\Delta\theta + (S_{av})^*(1/2G - K)^* + [(K - \phi)/3\phi](S_z/2G)^* + [(K - \phi)/3\phi]\Delta\epsilon_z\} \tag{20}$$

$$b_{xy} = (T/2G)^*, \quad K = (1 - 2\mu)/E_{La}, \quad \Delta\theta = \alpha_{La}\Delta t \tag{21}$$

As δ_{La} is small, let $(S_y)_{La}$ be constant along y axis and

$$\Delta\epsilon_{xLa}(x,y) = \alpha_w\Delta t + \Delta\epsilon(x,\delta_{La})y_{La}/\delta_{La} \tag{22}$$

S_y has to satisfy the following equation

$$\iint_{F_{pL}} S_y\,dxdz = -\iint_{F_{pL}} p(x,z)\,dxdz \tag{23}$$

where $p(x,y)$ is an external pressure on the surface $F_{pL} = 4aL$. Usually $p(x,y)$ is much less than S, and in this paper $p(x,y) = 0$ was assumed. From the plane strain state, it follows that $\Delta\epsilon_z = \alpha_w\Delta t$. To solve the problem, it's necessary to know the temperatures of all the parts of the structure, i.e., to know the quantity of heat emitted by the internal sources per unit volume of the plate and per unit time. It was assumed that heat transfer to the free plate surface is small. The next approximate relationship was used in this work

$$t(x,y)_{pL} = k(x)t(y) \tag{24}$$

where

$$k(x) = 1, x > \delta_{pL}, \quad \text{and} \quad k(x) = (x/\delta_{pL}), x <= \delta_{pL}$$

The substantiation of Eq 24 represents the known phenomenon: temperature of the plate end drops due to cooling effect of the large wall. The solution of the problem at the plate ends is physically correct but, of course, approximate. To analyze the stress distribution at the plate ends, the theory of elasticity or plasticity has to be used not only for the layer but for the plate material also.

In this paper, results of calculations for a homogenous heat sources distribution are given. In this case the steady-state distribution of the plate temperature is

$$t(y) = t(0) + wy(\delta_{pL} - y/2) \tag{25}$$

$$t_{av} = t(0) + w(\delta_{pL})^2/2 \tag{26}$$

Equations 7 through 10 give the relation between R and T. They are solvable by quadratures if we assume that T is the known function of R. This is valid if R doesn't change its sign along the integration range. To provide it, steps of integration have to be quite small.

Consider these equations as a relationship between increments ΔT and ΔR. After differentiating Eq 7 twice, and taking into account Eqs 8 through 10, we obtain

$$d^2(\Delta R)/dx^2 = f(R) \tag{27}$$

where

$$f(\Delta R) = -B + [(1 - \mu_{pL})/(E_{pL}\delta_{pL})]\Delta T(\Delta R)$$
$$B = \alpha_{pL}\Delta t_{av}/\delta_{pL}, x < \delta_{pL}; \quad B = 0, x > \delta_{pL} \tag{28}$$

Nonlinear Eq 27 is well known in mechanics. Its solution can be obtained if the equation is multiplied through by a derivative $d(\Delta R)/dx$ and then integrated with boundary conditions

$$\Delta R(x) = 0, x = L; \quad d(\Delta R)/dx = \Delta\alpha\Delta t + k(x)\alpha_1(\Delta t)_{av} \tag{29}$$

The solution of Eq 27 is

$$x = L - \int_0^{\Delta R} d(\Delta R)/\sqrt{\{\Delta\alpha\Delta t + k\alpha_1(\Delta t)_{av} - 2\int_{\Delta R}^{\Delta R_0} [(1 - \mu)\Delta T/E\delta_{pL} - B]d(\Delta R)\}} \tag{30}$$

The value of $\Delta R(0)$ in Eq 30 is defined by Eq 29, and $\Delta T(\Delta R)$ in Eq 30 can be calculated if the total accumulated displacement R is known for any point under examination. To calculate ΔR at specified points x, the next iterative procedure was developed. The solution of Eq 7 obtained with the negligible elastic deformation in the layer was used as the initial approximation. Then at the every next temperature change step the values of the previous step were used. Therefore the procedure was [*3*]:

1. The initial $\Delta R(x)$ distribution for the plate was obtained and used as a boundary condition for the layer plastic flow problem (Eqs 11 through 23).
2. Stresses and strains in the layer were defined by iteration procedure [*2*] with the iteration parameter ϕ.
3. Obtained values of $\Delta T(x,0)_{La} = \Delta T(x,0)_{pL}$ were used to refine values of $\Delta R(x)$.
4. Steps 1 through 3 were being repeated until the difference between assumed and obtained values of ΔR was less than an adopted accuracy.
5. Normal stresses in the plate were calculated with Eqs 1, 2, and 10.
6. Maximum stresses were calculated. If stress S_y was small, the next formula was used

$$S_m = 0.5\{S_x + \sqrt{[(S_x)^2 + 4T^2]}\} \tag{31}$$

Use of the Ideal-Plastic Model for the Layer Material

The analytical solution of the problem was obtained with use of the more simple ideal-plastic model for the layer material. In this case the relationship between R and T is

$$T = GR/\delta_{La}, x > x_s; \quad |T_m| = T_s, x <= x_s \tag{32}$$

where

$$T_s = T_m = \sqrt{(T^2 + S_x^2/4)} \tag{33}$$

and x_s is the coordinate separating elastic and plastic zones of the layer. Equations 7 through 10 and 32 could be solved analytically. Assume that after bonding and cooling the length of plastic zone was x_{s0}, and that $T_0 > 0$ and $x_s < x_{s0}$. The solution is a superposition of the

initial solution (for cooling after bonding) and the solution for operation (the yielding condition is $T_m = -2T_s$). It was assumed that the temperature drop in the layer cross section is negligible.

To simplify the analytical procedure it was also assumed that normal stress S_x can be omitted in the plasticity condition Eq 33. In this case $T_s = T$, and α_{La} becomes insignificant. Solution for elastic zone was obtained in the form

$$T = [M/N] \sinh [N(1 - x/\delta_{pL})]/\cosh [N(1 - x_s/\delta p_{pL})], \quad x > x_s \tag{34}$$

where

$$N = \sqrt{[G(1 - \mu_{pL})/(E_{pL}\delta_{pL}\delta_{La})]} \tag{35}$$

$$M = G[k(x)\Delta\alpha\Delta t(x,0) + k(x)\alpha_w(t(x,y)_{pL} - t(x,0)_{pL})_{av} + (1 - \mu)x_sT_s/(E_{pL}\delta_{pL} + (1 - \mu)\int T_0dx/(E_{pL}\delta_{pL})]/\delta_{La} \tag{36}$$

S_t may be calculated with Eqs 2 through 4. Then S_w is defined from Eq 10 as

$$S_w = \begin{cases} 2xT_s/\delta_{pL}, & x \leq x_s \\ 2xT_s/\delta_{pL} - (M/(N^2\delta_{pL})\{1 - \cosh[N(L - x)]/\cosh[N(L - x_s)]\}, & x > x_s \end{cases} \tag{37}$$

Displacement, R, can be calculated with Eqs 7 through 9. After stresses S and T are obtained, maximum stresses can be defined using one of the known strength theories. If heat release in the plate and the plastic zone length in the layer are negligible, $X_s = 0$, and the ideal-plastic model results agree with the results obtained in Ref *1*.

If the length of the plastic zone is large, the problem can be simplified by neglecting the elastic zone deformations. It means that $R = 0$, if $x > x_s$, and stresses in the elastic zone of the plate are described with the well-known formulas for bimetal plates.

Deflection of Heating Elements

Previous results were obtained with the assumption that the influence of plate bending is negligible. Therefore a special analysis was fulfilled to estimate values of a deflection and stresses in the plate due to bending [*4*]. The plate was thought of as a thin plate and the layer as an elastic base. Bubnov's-Galyorkin's approximate method was used. In the case of a square plate, the simple formula for a maximum deflection was obtained

$$f/f_t = 1 - 1/(1 + 6.93D)/(pL^4) \tag{38}$$

where thermal deflection of the free plate, f_t, can be taken from any thermal stresses manual.

Calculations with Eq 38 show that, if the layer material is metal solder, deflections of the plates in real devices are usually very small. If the layer is made of adhesive, plate deflections can be noticeable.

Results of Calculations

Thermal stresses in ferrite plates soldered or bonded with adhesive to the brass waveguide wall were calculated using both the plastic flow and ideal-plastic models. Typical results for

the tin-lead alloy used as a solder material are presented in this paper. The yield limit of the alloy depends on temperature and is used in the form of the empirical equation

$$T_{s,La}(t) = T_{s,La}(0)(1 - t/t_{\text{melt}}) \tag{39}$$

where

$$T_{s,La}(0) = 1.82*10^5\ \text{N/m}^2, \quad t_{\text{melt}} = 220°\text{C}$$

Dimensions of the ferrite plate and the layer are: $L = 20$ mm, $\delta_{pL} = 0.5$ mm, $\delta_{La} = 0.05$ mm. It is supposed that after bonding the system was cooled down to 20°C, and that the wall temperature in operation is $t_w = 53°\text{C}$. Heat release in the plate is 10^9 W. Ferrite properties are: $c_{pL} = 3.2$ W/(m°C), $\alpha_{pL} = 9.4 \times 10^{-6}$ 1/°C, $E_{pL} = 8.3 \times 10^6$ N/m^2. Brass parameters were standard.

The comparison of results for the two models is made on Fig. 2. As ferrite tensile strength is approximately ten times less than its compression ultimate strength, only the principal tensile stresses in the plate are shown on the graph. The calculated length of a plasticity zone in the solder is approximately $L/2$ in the ideal-plastic model and equals L in the plastic flow model. Values of shear stresses, T_{La}, are close in both models. The plate stresses in operation

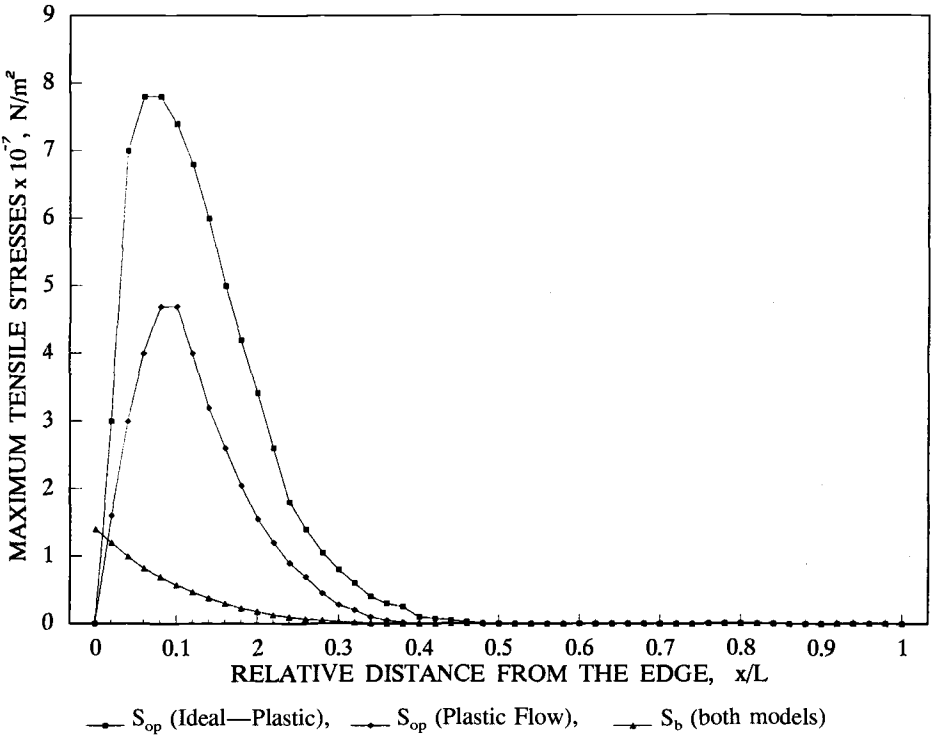

FIG. 2*a*—*Comparison of results: maximum tensile stresses in the ferrite plate.* *SUBSCRIPTS: b = stresses after bonding and cooling;* op = *stresses in operation.*

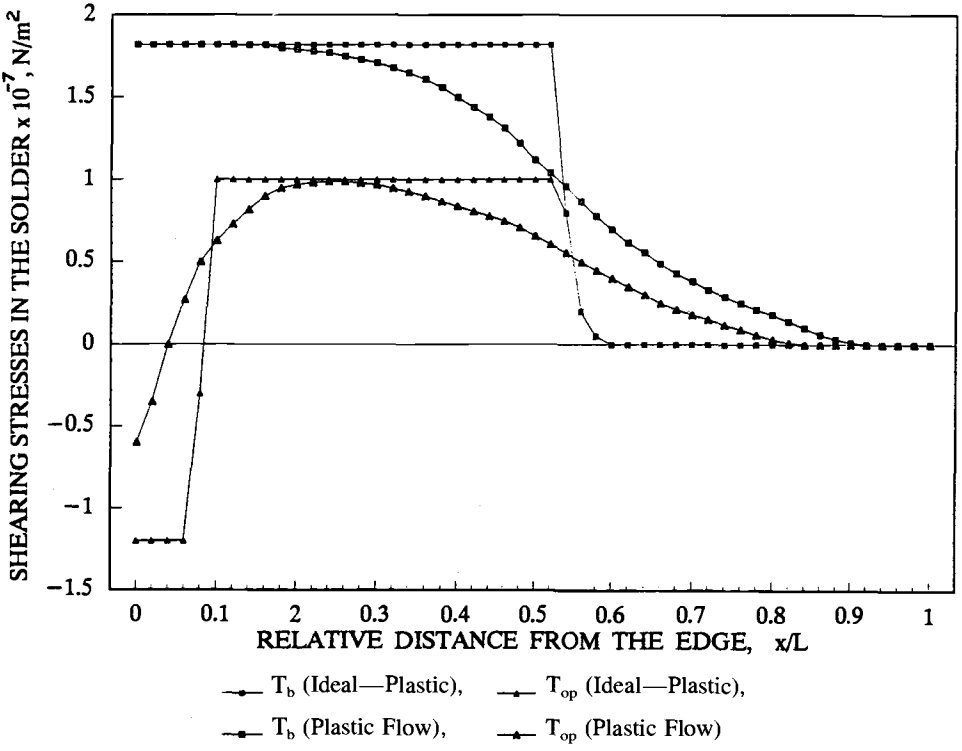

FIG. 2*b*—*Comparison of results: shearing stresses in the solder.* SUBSCRIPTS: *b* = *stresses after bonding and cooling;* op = *stresses in operation.*

obtained with the ideal-plastic model are larger than stresses obtained with the plastic flow model mainly because of neglecting S_x in Eq 33. Let's examine it in more detail.

Normal stress, $S_{x,La}$, in the central part of the solder depends mainly on the wall displacement, i.e., on the difference $(\alpha_w - \alpha_{La})$. For the state after bonding and cooling, the stress can be estimated with the well-known formula for bimetal plates. Then the possible maximum value of elastic stress, T, in the x-direction can be obtained from Eq 33

$$T_m = \sqrt{\{T_s^2 - 0.25[(\alpha_w - \alpha_{La})(t - t_{\text{melt}})E_{Ld}/(1 - \mu)]^2\}} \tag{40}$$

Equation 40 shows that the value of T_m can be much less than T_s. This means that sometimes the entire layer can be transformed from elastic into a plastic state. Therefore, to examine the layer material state, the normal stress in a layer should be taken into account. It means that of the two models, the numerical model is preferable.

Thermal stresses in the layer after bonding and cooling, calculated with the plastic flow model, are shown in Fig. 3. It is interesting that in the middle part of the layer, stresses S_x and S_z are tensile and larger than the solder yield limit. Nevertheless, this is consistent with the model because the plasticity condition $S_i = S_s$ is satisfied.

Some calculations were made for thermal cycling operation (heat release in the plate was being switched on and off many times). Temperature fluctuations caused the stresses sign change at least in the part of the plastic zone of the layer and therefore could initiate cracks after some number of cycles.

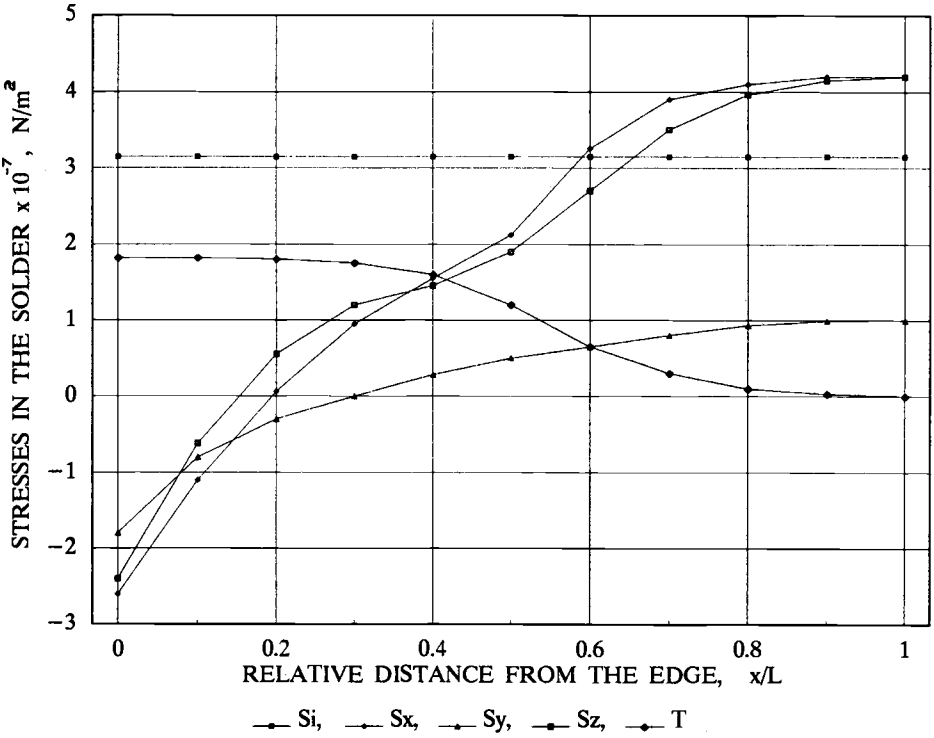

FIG. 3—*Stresses in the solder after bonding and cooling.*

Conclusion

Numerical and analytical methods for calculating thermal stresses in a flat plate and a connecting layer of solder or adhesive are proposed. Computational results are given for the ferrite plate soldered to the metal wall of a high-power waveguide. They show that stresses both in the plate and in the layer could exceed the yield limits and force the rupture immediately or after some number of thermal cycles. Not only do the used models need improvement but additional experimental data are desirable. The most important data needed are more reliable stress-deformation and creep relationships for the entire temperature interval under consideration.

References

[*1*] Taylor, T. C. and Yuan, F. L., "Thermal Stress and Fracture in Shear-Constrained Semiconductor Device Structures," *IRE Transactions on Electronic Devices,* Vol. 9, No. 3, May 1962, pp. 303–308.

[*2*] Makhnenko, V. I., "Computational Methods for the Investigation of Welding Stresses Kinetics," *Naukova Dumka,* Kiev, 1976 (in Russian).

[*3*] Parnas, A. L., "Thermal Stresses in Cooled Heat-Releasing Elements of Electronic Devices," *Heat and Mass Transfer in Electronic and Microelectronic Systems Technology and Use,* Materials of International School-Seminar, Part 1, Minsk, 1989, pp. 79–89 (in Russian).

[*4*] Parnas, A. L., Bashtovaya, E. A., and Parnas, I. A., "Thermal Strains and Stresses in a Rectangular Plate on the Elastic Base," *Injenerno-Physitcheskiy Journal,* Vol. 53, No. 6, 1987 (in Russian).

Dale A. Wilson[1] *and Anbazhagan Katherisan*[1]

Stress and Thermal Analysis of Resistance Temperature Detectors

REFERENCE: Wilson, D. A. and Katherisan, A., **"Stress and Thermal Analysis of Resistance Temperature Detectors,"** *Fatigue of Electronic Materials, ASTM STP 1153,* S. A. Schroeder and M. R. Mitchell, Eds., American Society for Testing and Materials, Philadelphia, PA, 1994, pp. 133–146.

ABSTRACT: In many industries the failure of temperature devices such as resistance temperature detectors (RTDs) are of significance to process control. Therefore, a study was instituted to evaluate these failures. RTDs from various manufacturers were monitored and periodically calibrated until failure. Sensors that developed open circuits were then examined. Upon examination of the sensors, it was found that failures were occurring at or near the solder connection between the platinum lead-out and copper wire. A two-dimensional (2-D) finite element analysis of this joint was then developed.

Finite element models were created to evaluate stresses at 100, 200, and 300°C. The thermal expansion mismatch between the wires joined by the solder results in high-stress gradients at the corners of the solder joint. Photomicrographs were produced of the joint failures with a scanning electron microscope to study the crack nucleation and propagation. Aging of the solder due to long-term temperature exposure may also play a key role in the fracture behavior. The need for improved joint design and special coating materials is of primary importance to improve the life of the solder joints in many applications. This will improve the reliability of the components.

KEYWORDS: electronic materials, finite-element-analysis, solder joint, fracture, high temperature, resistance temperature detectors, platinum wire, copper wire, thermal stresses

Temperature is one of the most important quantities in science and industry. Often, it is the most important quantity in a process or an experiment. Therefore, temperature measurement must be convenient, accurate, and reliable. The most commonly used sensors are resistance temperature detectors (RTDs) and thermocouples (TCs). The RTDs are inexpensive, durable, and easy to handle. Manufacturers certify the accuracy of RTDs, but they are not guaranteed after a long-term temperature exposure to process conditions. Additionally, there are only a few realistic studies that have been done to evaluate their calibration performance under process conditions.

To alleviate this oversight, a long-term sensor evaluation project was conducted at the University of Tennessee at Knoxville to study and to develop a better understanding of the decalibration behaviors of RTDs under typical process conditions. To aid this objective, a test group of 101 RTDs was used.

The RTDs were inspected to determine the physical condition and were tested to provide a reference for comparison prior to the installation in the furnaces. The RTDs were then subjected to simulated process conditions (200°C isothermal, 300°C isothermal, and cycled 200 to 300°C every 6 h) and were removed and checked for calibration shifts after 6 h, 12 h,

[1]Professor and graduate student, respectively, Department of Mechanical Engineering, Tennessee Technological University, Cookeville, TN 38505-5014.

1 day, 1 week, and then subsequently for months. Finally, the work performed since the initiation of the project, the problems encountered with the RTDs, the techniques used for the test, and the results are collected in the form of data for future research [*1*].

The determination of the causes for decalibration of RTDs with long-term temperature exposure would be a significant contribution for the improvement of the stability of industrial temperature sensors. The calibration of the sensor plays an important role in the stability. Apart from calibration, the factors that lead to decalibration are diffusion, high-temperature annealing, rough handling, vibration, and long-term temperature exposure. The cross section of the RTD with the area of interest being the solder joint is shown in Fig. 1. The solder joint will be studied with a 2-D finite element model and compared with scanning electron microscope (SEM) fractographs. However, the problem of thermal failure in solder joints is as complex as any failure problems that have been researched. Adding to

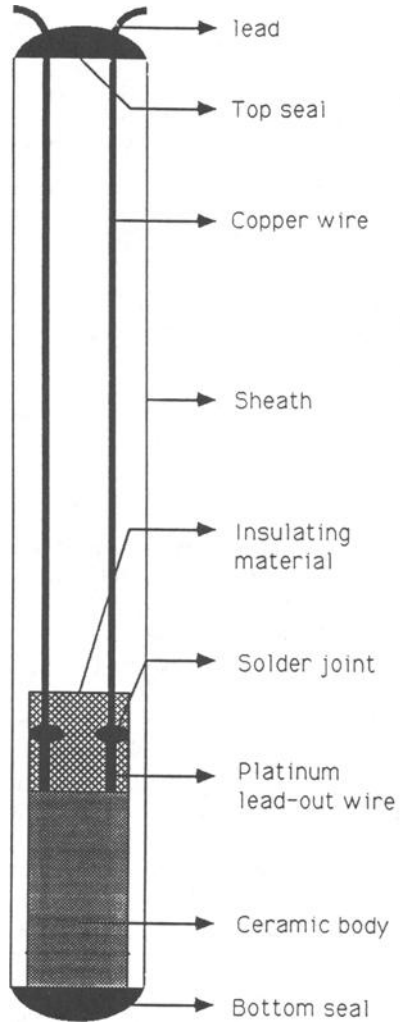

FIG. 1—*Cross section of an RTD.*

this complexity are the cycling temperatures the solders are subjected to in most of the cases. In this research the 2-D finite element analysis is confined to steady state conditions. The steady state analysis gives us a start to understand the magnitude of the thermal stresses.

Technical Discussion

Standard RTDs are the prescribed interpolating instrument used to serve as reference standards for calibration. The birth of RTDs as useful instruments occurred in 1887, when H. L. Callender reported that RTDs exhibited the prerequisite stability and reproducibility if they were properly constructed and treated with sufficient care [*2*]. The international scale has been redefined both to take advantage of these measurements and to bring the scale more nearly into agreement with the thermodynamic scale. The platinum resistor shall be very pure annealed platinum supported in such a manner that the resistor remains as strain-free as possible; the value of $R(100)/R(0)$ shall not be less than 1.3925 or defined as $R(100) - R(0)$, not less than 0.003925.

The insulation material that supports the resistor and leads must not contaminate the platinum during the annealing of an assembled RTD, nor when subjected for extended periods of time to temperatures to which the RTD is normally exposed [*3*]. An RTD is a mechanically delicate instrument. As discussed before, the platinum wire cannot be rigidly supported and at the same time be free to expand and contract with the temperature changes. Care is taken to prevent such damages [*4–7*]. Shock, vibration, or any other form of acceleration may cause the wire to bend between and around its supports, thus producing strains that change its temperature-resistance characteristics.

The solder contacts used in the RTD provide both mechanical and electrical connection. Solders of different composition are often used for the different levels of contact. The most common type of RTD used is the wire-wound platinum-resistance temperature detector. The platinum leads are connected to the copper wire by a solder contact. The mechanical integrity of the solder contacts in the RTDs has become a serious concern. The problems arise because of the thermal expansion mismatch between the wires joined by the solder.

The industrial need to guarantee reliability in solder contacts involves two problems, both of which have a strong metallurgical content. The first problem is the development of a computer model to guide and verify the designs. The design of a general model requires the identification and accurate scaling of the metallurgical mechanisms that determine the life of the solder joint. The second problem is the design of fatigue-resistant solder that can survive the severe conditions that will be experienced.

Experimental Procedures

Sensor Identification and Inspection

Before subjecting the RTDs to test conditions, an aluminum identification tag was attached to each, and the following were recorded: the sheath length, sheath diameter, sheath material, number of lead wires and its length, optional range, and the manufacturer. Other information was found in the manufacturers' catalogs. The RTD was inspected for visible cracks or holes on the head insulation and the surfaces.

Lead Wire Test

The lead wire resistance was measured at room temperature. The measurements were made with a Fluke precision multimeter (Model 8505 A).

Insulation Resistance Test

To evaluate the condition of the RTDs' inner packing material, the sheath insulation resistance was measured using a General Radio Megohm bridge meter (Model 1644 A). A resistance less than 200 MΩ is considered low.

X-Ray Inspection

An X-ray examination was done to selected RTDs if any of the following were true:

1. The insulation resistance was low.
2. During measurement of the insulation resistance, it was difficult to null the megaohm bridge as the needle fluctuated.
3. The measurement showed that the RTD was shorted.
4. During the measurement, the sensor became too hot to touch.

Several others were selected at random. Two pictures, at 0 and 90° about the long axis, were used to determine element structure, size, and position.

Calibration

Calibrations were used to determine change in performance of an RTD. Every RTD was calibrated before being subjected to any high-temperature environment. Three points were used to calibrate each sensor. A reference thermometer (Minco Model S 7929) was used to verify the temperature at each point. The RTDs were exposed to 0°C, 100°C, and the freezing point of lead, 327.5°C.

Industrial Condition

Three furnaces were built to simulate the industrial process conditions. These temperatures were determined in accordance with the manufacturer's recommendations. Overheating was prevented with a Eurotherm voltage cutoff system, Model RB11.

Results

The two RTDs from each process condition that failed were analyzed. All the RTDs except one at 200°C were open circuited. The dimensions and classifications of each of the RTDs used in the analysis along with the data are explained in the next section. By visual examination the open circuit was found to be near the solder joint. Scanning electron microscope (SEM) fractographs of the solder joint along with the 2-D steady state finite element analysis helped the research to understand the thermal cracks and stresses experienced near the solder joint.

Analysis on the Solder Joint

The calibration and recalibration of the RTD involves heating and cooling. Heating the device strains the solder contact in shear; cooling or decreasing the temperature reverses the strain. Since the solder is mechanically soft and is used at a high temperature (a large fraction of its melting point), deformation is introduced by plasticity and creep (stress relaxation). The long-term behavior is further complicated by the microstructural changes that inevitably occur in the solder as it is cycled and aged. The solder alloy compositions are confidential to each manufacturer.

TABLE 1—*Dimensions of RTD A1 and A2.*

RTD No.	Length of the RTD, mm	Diameter of the Sheath, mm	Length of the Ceramic, mm	Diameter of the Ceramic, mm
A1	431.80	6.350	30.276	3.962
A2	311.15	6.375	25.400	3.099

TABLE 2—*Decalibration data of RTD A1 and A2.*

Test Period	RTD A1 Temperature Drift, °C	RTD A2 Temperature Drift, °C
Original	0.000	0.000
6 h	−0.049	0.029
12 h	−0.055	0.036
24 h	−0.073	0.055
1 week	−0.055	0.065
30 days	...	...
60 days	5.270	250.800
90 days	Open circuit	101.900
120 days	Open circuit	54.100
150 days	Open circuit	−29.000
240 days	Open circuit	0.999
330 days	Open circuit	2.650
390 days	Open circuit	−259.900
420 days	Open circuit	2.770
480 days	Open circuit	2.680

TABLE 3—*Dimensions of RTD B1 and B2.*

RTD No.	Length of the RTD, mm	Diameter of the Sheath, mm	Length of the Ceramic, mm	Diameter of the Ceramic, mm
B1	381.00	6.299	25.40	3.124
B2	317.50	6.248	25.40	3.175

Dimensions and Classifications of RTD

The RTDs at 200°C isothermal are named A1 and A2, at 300°C isothermal as B1 and B2, cycled 200 to 300°C every 6 h as C1 and C2. The dimensions of RTD A1 and A2 are tabulated in Table 1. The decalibration data of RTD A1 and A2 are shown in Table 2. The dimensions of RTD B1 and B2 are tabulated in Table 3. The decalibration data of RTD B1 and B2 are shown in Table 4. The dimensions of RTD C1 and C2 are tabulated in Table 5. The decalibration data of RTD C1 and C2 are shown in Table 6.

The platinum lead-out connects the bridge wire by a solder joint. The solder joint forms a part of the measured resistance and also a mechanical connection. It is protected by an insulating material. The insulating material used will help to determine the type. In Type 1 the insulating material used is an insulating cloth, and in Type 2 a ceramic tube is used as an insulating material. A hook-on type of connection is established between the platinum lead-out and copper wire in Type 3.

TABLE 4—*Decalibration data of RTD B1 and B2.*

Test Period	RTD B1 Temperature Drift, °C	RTD B2 Temperature Drift, °C
Original	0.000	0.000
6 h	0.084	0.016
12 h	0.039	0.029
24 h	0.021	0.039
1 week	0.026	0.083
30 days	0.018	0.465
60 days	0.031	0.504
90 days	0.018	0.540
120 days	0.005	0.535
150 days	−0.005	0.584
180 days	0.005	0.595
210 days	0.055	0.522
240 days	0.037	0.675
300 days	−0.028	0.665
350 days	0.003	0.608
500 days	−0.098	Open circuit
550 days	−0.057	Open circuit
650 days	...	Open circuit
680 days	Open circuit	Open circuit

TABLE 5—*Dimensions of RTD C1 and C2.*

RTD No.	Length of the RTD, mm	Diameter of the Sheath, mm	Length of the Ceramic, mm	Diameter of the Ceramic, mm
C1	311.15	6.375	25.40	3.099
C2	304.80	6.325	25.40	3.073

TABLE 6—*Decalibration data of RTD C1 and C2.*

Test Period	RTD C1 Temperature Drift, °C	RTD C2 Temperature Drift, °C
Original	0.000	0.000
6 h	...	...
12 h	...	...
24 h	...	...
1 week	0.003	−0.010
30 days	0.039	0.018
60 days	0.088	0.034
90 days	0.216	...
150 days	0.146	Open circuit
450 days	Open circuit	Open circuit
480 days	Open circuit	Open circuit

Finite Element Model of Solder Joint

In this study, a SUN workstation was used together with a finite element program developed by Structural Dynamics Research Corporation (SDRC) called Integrated Design Engineering Analysis System (I-DEAS) [*8*]. The fourth version of the program was used in the steady state thermal analysis of the solder joint.

Two types of models are used in this analysis to study the variation in thermal stresses with the increase in contact point of the solder with the platinum lead-out and copper wire. The shape of the solder joint was modeled by scaling down the SEM fractographs obtained with a higher magnification. The dimensions of Model 1 are shown in Fig. 2. In Model 2 the contact surface is increased by 0.254 mm. A 2-D model is used in this steady state thermal analysis. The purpose of this analysis was to identify the initial stress field and was not intended to quantify the stress relaxation in the joint. The RTD is subjected to a constant temperature bath except when it is calibrated and recalibrated at certain intervals. Hence a steady state analysis is done on the model to study the thermal stress distribution. Future research is recommended to analyze the thermal stresses due to cycling temperatures, taking into consideration the effect due to calibration and recalibration. The material properties used in the model are given in Table 7.

Mesh Generation

The 2-D finite element model was used due to the axisymmetric geometry of the joint. The type of mesh used in these analyses is three-node linear triangular elements. Both of the models have a total of 500 elements and 288 nodes.

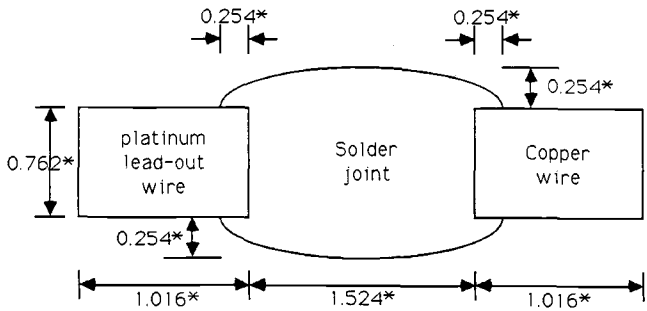

FIG. 2—*Dimensions of Model 1 of the solder joint.*

TABLE 7—*Material properties of the finite element model.*

S. No.	Type of Material	Young's Modulus $\times 10^4$, MPa	Poisson's Ratio, ν	Density, g/cm^3	Coefficient of Thermal Expansion $\times 10^{-6}$, μmm/mm K
1	Platinum lead-out	17.36	0.39	21.45	9.10
2	Solder joint	4.06	0.37	11.34	29.08
3	Copper wire	11.55	0.34	8.90	16.40

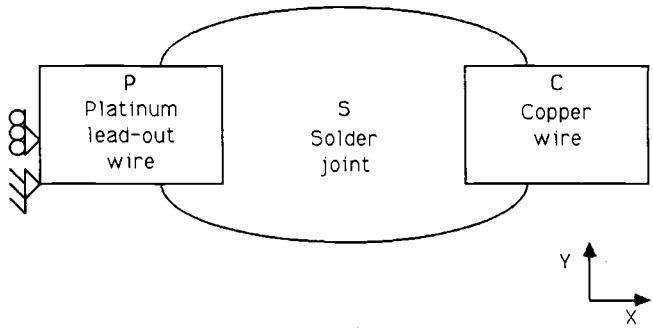

FIG. 3—*Restraints used in the finite element model.*

Application of Thermal Loads and Boundary Conditions

The boundary conditions and thermal loads in the finite element model must be applied in such a way that the model structure simulates the actual working condition. In the model the platinum end, P, is fixed at X and $Y = 0$. This restraint satisfies the condition needed for the analysis of the model. The node above the fixed end is fixed in the X-direction and let free in the Y-direction. These restraints are shown in Fig. 3.

The thermal loading condition for the model is simulated by loading each of the nodes at 100, 200, and 300°C. The reference temperature used in both the models is 25°C. In the analysis of the cycling condition, at present, the experimental data and SEM fractographs are used.

Finite Element Analysis Results

The stress and displacement contours of Model 1 and Model 2 at 100, 200, and 300°C are identical with different magnitudes of thermal stresses and displacements. However, the results are tabulated in Tables 8*a* and 8*b* and Tables 9*a* and 9*b*. The thermal stresses in the X-direction approach zero near the ends of platinum lead-out wire and copper wire. Since heating strains the solder contact in shear, it is important to find the maximum shear stress of the model. The shear stress is concentrated near the corners of the solder joint. The normal XY shear stress also indicates that the stresses are concentrated near the corners. For analysis and design purpose it is convenient to define the Von Mises stress. The distortion energy theory which leads to Von Mises stresses predicts the failure more accurately.

The Van Mises stress contours of Model 1 and Model 2 solder joints at 200°C are given in Figs. 4 and 5. The minimum and maximum stresses of Model 1 solder joint at 200°C varies from 0.536 MPa (tension) to 137.90 MPa (tension) as shown in Fig. 4. The stresses near the

TABLE 8a—*Finite element results of Model 1 solder joint.*

S. No.	Temperature, °C	Principal Stress, MPa		Principal Stress, X-Direction, MPa		Principal Stress, Y-Direction, MPa	
		Max	Min	Max	Min	Max	Min
1	100	41.23	−6.30	14.14	−53.97	40.25	−30.31
2	200	93.80	−14.35	32.20	−123.20	91.70	−69.16
3	300	147.00	−22.40	50.26	−192.50	143.50	−107.80

TABLE 8b—*Finite element results of Model 1 solder joint.*

S. No.	Shear Stress, *XY*-Direction, MPa		Shear Stress, MPa		Von Mises Stress, MPa		Displacement, mm	
	Max	Min	Max	Min	Max	Min	Max, $\times 10^{-5}$	Min, $\times 10^{-15}$
1	16.80	−16.94	30.94	0.199	60.34	0.235	55.88	30.48
2	38.29	−38.64	70.70	0.272	137.90	0.536	127.25	52.32
3	59.78	−60.34	109.90	0.425	214.90	0.840	198.62	132.59

TABLE 9a—*Finite element results of Model 2 solder joint.*

S. No.	Temperature, °C	Principal Stress, MPa		Principal Stress, *X*-Direction, MPa		Principal Stress, *Y*-Direction, MPa	
		Max	Min	Max	Min	Max	Min
1	100	50.96	−56.70	19.32	−57.19	50.12	−29.54
2	200	116.20	−129.50	43.96	−130.20	114.10	−67.27
3	300	181.30	−201.61	68.67	−203.70	178.50	−105.00

TABLE 9b—*Finite element results of Model 1 solder joint.*

S. No.	Shear Stress, *XY*-Direction, MPa		Shear Stress, MPa		Von Mises Stress, MPa		Displacement, mm	
	Max	Min	Max	Min	Max	Min	Max, $\times 10^{-5}$	Min, $\times 10^{-15}$
1	23.52	−22.54	34.44	0.14	67.34	0.083	56.90	89.92
2	53.55	−51.38	78.40	0.32	153.30	1.897	129.54	65.53
3	84.00	−80.50	122.50	0.50	240.10	2.961	202.18	116.58

corners of the solder joint vary from 39.69 MPa (tension) to 137.59 MPa (tension) at 200°C. Increasing the contact of the solder joint also increased the stress levels of Model 2. The minimum and maximum stresses at 200°C and of Model 2 solder joint vary from 1.90 MPa (tension) to 153.30 MPa (tension) as shown in Fig. 5. These stresses are found to be concentrated near the solder joint as seen in Model 1. The yield strength of the solder decreases with the increase in temperature. For the common solder (60Sn-40Pb) the yield strength decreases from 47.25 MPa at 20°C to 18.27 MPa at 125°C. Since the solder is mechanically soft, deformation is introduced by plasticity and creep (stress relaxation). Added to this deformation are the microstructural changes that occur near the solder contact as it is aged. The effects due to these deformations can be seen in the SEM fractographs taken near the solder joint. Designing a fatigue-resistant solder that can survive these severe conditions can increase the life of the solder and eventually the life of the RTD.

Legend

Contour line	MPa
1	0.536 to 20.1
2	20.1 to 39.7
3	39.7 to 59.3
4	59.3 to 79.1
5	89.1 to 118.3
6	118.3 to 137.9

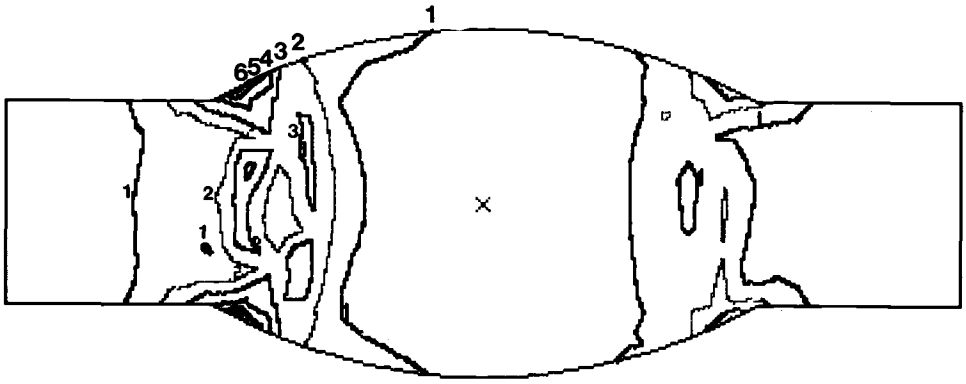

FIG. 4—*The Von Mises stress contours on Model 1 at 200°C.*

Scanning Electron Micrograph of the Solder Joint

The location of the open circuit was found by visual examination. All the RTDs examined failed near the solder joint except RTD A2 at 200°C. Each RTD carries two platinum lead-out wires and hence two solder joints. Due to high temperatures the solder joint may get fused to the insulating material; hence, some RTDs are left with only one solder joint for analysis. The RTDs subjected to 200°C are A1 and A2. A1 has a Type 3 solder joint where the platinum lead-out wire is connected to the copper wire by a hook mechanism. One of the two platinum lead-out wires is fused to the insulating material, and the other joint magnified at ×50 exhibits severe thermal damage on the platinum lead-out and copper wire as shown in Fig. 6. The open circuit is caused due to the severe thermal damage that has occurred to the fused joint. Finite element analysis was not performed because it is not a common-type joint, and hence the magnitude of the thermal stresses involved in this type is left for future research. A2 has a Type 1 solder joint, and both of the solder joints exhibit thermal damages near the joints. This type of joint failure will be shown later. However, the RTD did not open circuit. On both of the solder joints the copper wire is being extensively damaged compared to the platinum lead-out wire; hence, extra protection is required on the copper wire to prevent any failure near the solder joint connected to the copper wire. This extra protection can prevent failure of the copper wire. Since fewer failures will be due to exposure to high temperature, it is expected to observe more failures due to the thermal stresses in the solder joint.

As the temperature increases, the magnitude of the thermal stresses also increases, and these results can be seen in the finite element analysis. It is also evident that higher temperature means a large fraction of the solder's melting point is being used. For a

Legend

Contour line	MPa		
1	1.897	to	23.6
2	23.6	to	45.2
3	45.2	to	66.9
4	66.9	to	88.2
5	88.2	to	131.6
6	131.6	to	153.3

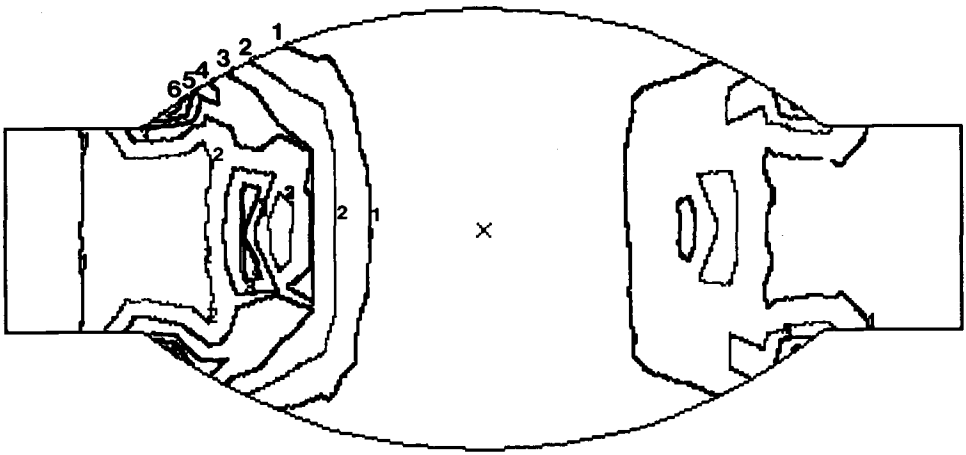

FIG. 5—*The Von Mises stress contours on Model 2 at 200°C.*

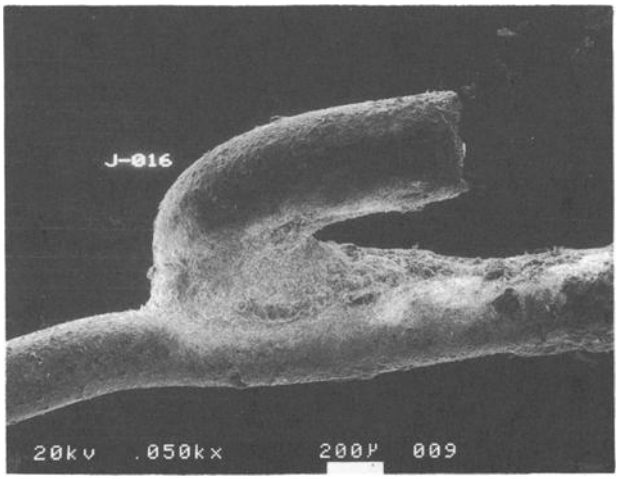

FIG. 6—*Lead-out wire of Sensor A1 with a Type 3 solder joint subjected to 200°C (×50). The platinum wire is on the left.*

temperature of 300°C a Pb-Sn solder must have a composition of less than 5% Sn to prevent melting. More deformation is introduced by plasticity and creep, increasing crack nucleation, and crack propagation near the solder joint. The RTDs subjected to 300°C are B1 and B2. The platinum lead-out wire of both solder joints shows that the outer surface of the solder is peeling off. This is not visible at 200°C. Extra protection is recommended to the platinum lead-out, solder joint, and copper wire. This can be achieved by coating the platinum lead-out wire, solder joint, and copper wire with temperature-resistant ceramic.

In a thermal cycling condition the deformation observed can be more than the simple thermal expansion mismatch that is observed in the steady state analysis. To analyze the stresses, nonlinear elastic/plastic solder properties at different temperatures and a steady state creep law are recommended to characterize the deformation. In this research, only SEM pictures are available to assess the damage to the solder joint due to cycling temperature. Sensor C2 has both the solder contacts available as shown in Fig. 7 and Fig. 8, respectively. It is of Type 1, and both the joints are magnified at ×40. Evidence of fatigue

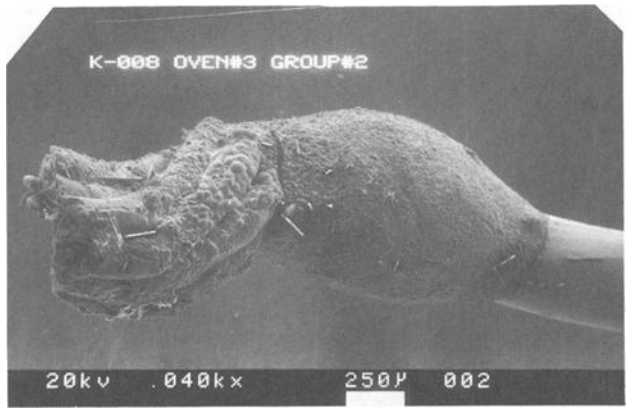

FIG. 7—*Lead-out 1 wire of Sensor C2 with a Type 1 solder joint subjected to a cycling temperature or 200 to 300°C (×40). The platinum wire is on the right.*

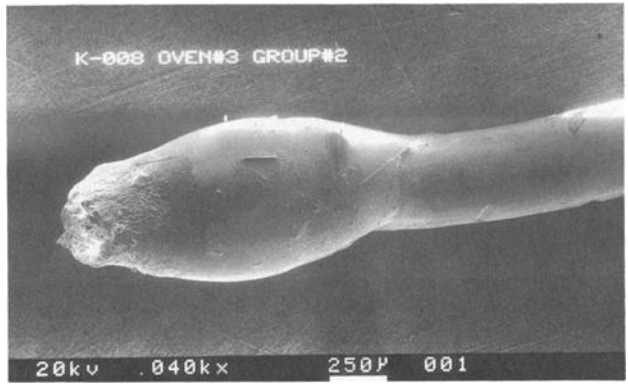

FIG. 8—*Lead-out 2 wire of Sensor C2 with a Type 1 solder joint subjected to a cycling temperature of 200 to 300°C (×40). The platinum wire is on the right.*

crack nucleation and propagation is seen near the copper solder contact as shown in Fig. 7. This is due to thermal expansion mismatch and plastic deformation accumulated due to thermal cycling [*9*]. The failure did occur in the copper wire, and there was also visible thermal damage of the solder and copper wire. As seen in Fig. 8, the copper wire has been sheared off the solder joint, showing evidence of a thermal fatigue condition due to the cycling temperature.

From the micrographs it is evident that the type of solder joint used has an effect on the open circuit problem. The finite element results show high thermal stresses, and the photomicrographs show severe thermal damage at high temperature, crack nucleation, and propagation on both isothermal and cycling temperatures. The photomicrographs show that most cracks are nucleated near the corners of the solder joint. Improving the quality of the protecting sheath (high-temperature-resistant ceramic) along with the special coating material can prevent damage due to steady-state and cycling temperatures. The finite-element models do represent high thermal stresses showing signs of plastic deformation, but the effects due to nonlinearity (such as the change in geometry with plastic deformation and its subsequent change in material property due to change in temperatures) are not taken into account in this steady state analysis.

Analysis and Future Research

The steady-state analysis gives an idea of the location of the thermal stresses and the temperature at which the plastic deformation starts. Once these two factors are determined the creep characteristics are introduced into the solder joint using temperature and rate/time-dependent properties. At the same time, temperature-dependent elastic models are used for materials which exhibit negligible plastic deformation at the temperature range considered. The nonreversible deformation occurring during the heating-hold and cooling-hold time that occurs during the calibration and recalibration process must also be considered. The final stresses depend on the shape of the finite element model after plastic deformation, and these deformations depend on the creep law. The creep law is determined by the experimental measurement of steady-state creep of the solder at different temperatures. Along with this analysis it is more likely that a more complicated fatigue life prediction model will be necessary to deal with the complexity of the thermal stresses involved in the nonlinear analysis instead of an average value determined usually by the Coffin-Mason equation [*10*]. A promising approach to access the life of the solder involves applying fracture mechanics and fractographic methods to measure crack propagation [*11–14*]. The fracture mechanics approach estimates the fatigue life based on the initial defect or crack state, the environmental stress state, and the growth of the crack (analytical equations can be used to describe the crack propagation). However, many assumptions such as initial crack size, existence of voids, inter- or trans-granular crack propagation, microstructural changes, etc. required with the current level of understanding make the fracture mechanics approach of limited accuracy at this time. In the fractographic method, metallurgical techniques are used to evaluate the crack growth rate microscopically. This could contribute a precise measurement of crack propagation which could be used to validate the fracture mechanics approach. Both provide a more complete physical understanding of the failure and life prediction compared to the uniform shear theory given by the Coffin-Mason equation.

Conclusion

As seen in this research the solder joint played an important role in the open circuit problem. The finite element model and the SEM micrographs have helped identify the cause

of failure near the joints. The FEM results indicated that there was a stress increase at the corners of joint between solder and wire. This stress increase was due to the thermal expansion mismatch at the elevated temperature. This high stress under elevated temperature was the main cause of the large plastic deformation and creep. This led to an increased probability of crack nucleation and propagation near the wire-solder joint.

The magnitude of the thermal stresses obtained by the steady-state analysis do not represent the actual stress level due to the fact that nonlinear characteristics such as plastic deformation and creep law were not introduced in the analysis. A nonlinear finite element program using temperature and rate/time-dependent properties for a creep law in this type of solder joint will help the future research to determine the actual thermal stress distribution.

References

[1] Katz, E. M., Kerlin, T. W., Yu, D., Hurst, A., and Klein, T., "Long-Term Drift of Industrial Sensors," progress report, University of Tennessee, Knoxville, 1986–1988.

[2] Callender, H. L., "On the Practical Measurement of Temperature: Experiments Made at the Cavendish Laboratory," Cambridge, *Philosophical Transactions,* Vol. 178, 1887, pp. 161–230.

[3] Rosebury, F., *Handbook of Electron Tube and Vacuum Techniques,* Addison-Wesley Publishing Co., Inc., Reading, MA, 1965, p. 371.

[4] Barber, C. R., "Platinum Resistance Thermometers of Small Dimensions," *Journal of Scientific Instruments,* Vol. 27, 1950, pp. 47–49.

[5] Barber, C. R., "Platinum Resistance Thermometers for Use at Low Temperatures," *Journal of Scientific Instruments,* Vol. 32, 1955, pp. 416–417.

[6] Barber, C. R., *Platinum Thermometers for Low Temperatures in Progress in Cryogenics,* K. Mendelssohn, Ed., Academic Press, New York, 1960, pp. 147–171.

[7] Barber, C. R. and Blanke, W. W., "A Platinum Resistance Thermometer for Use at High Temperatures," *Journal of Scientific Instruments,* Vol. 38, 1961, pp. 17–19.

[8] "I-DEAS Supertab Pre/Post Processing Engineering Analysis User's Guide," Version 4.0, Structural Dynamics Research Corporation, Milford, OH, 1988.

[9] Pan, T.-Y., "Thermal Cycling Induced Plastic Deformation in Solder Joints, Part I: Accumulated Deformation in Surface Mount Joints," ASME winter annual meeting, 90-WA/EEP-13, 25–30 Nov. 1990, Dallas, TX, ASME, New York.

[10] Jeannotte, D. A., Goldmann, L. S., and Howard, R. T., "Package Reliability," *Microelectronics Packaging Handbook,* R. R. Tummala and E. J. Raymaszewski, Eds., Van Nostrand Reinhold, New York, 1989.

[11] Engelmaier, W., "Surface Mount Solder Joint Long-Term Reliability: Design, Testing, Prediction, Soldering and Surface Mount Technology," *Circuits Manufacturing,* Vol. 28, No. 12, December 1988, pp. 16–17.

[12] Wong, B., Helling, D. E., and Clark, R. W., "A Creep-Rupture Model for Two-Phase Eutectic Solder," *IEEE Transactions on Components, Hybrids, and Manufacturing Technology,* Vol. 11, No. 3, 1988, pp. 284–290.

[13] Yamada, S. E., "A Fracture Mechanics Approach to Soldered Joint Cracking," *IEEE Transactions on Components, Hybrids, and Manufacturing Technology,* Vol. 12, No. 1, March 1989, pp. 99–104.

[14] Yamada, S. E., "Stress Analysis of Partially Yielded Soldered Joint for Surface Mount Connectors," *IEEE Transactions on Components, Hybrids, and Manufacturing Technology,* Vol. CHMT-10, No. 2, 1987, pp. 236–241.

ISBN: 0-8031-1994-1